SAPIENZA
UNIVERSITÀ DI ROMA

FACULTY OF INFORMATION ENGINEERING, INFORMATICS AND STATISTICS
DEPARTMENT OF INFORMATION ENGINEERING, ELECTRONICS AND TELECOMMUNICATIONS

DOCTORATE (PHD) IN
INFORMATION AND COMMUNICATIONS TECHNOLOGIES

Atmospheric remote sensing and radiopropagation: from numerical modeling to spaceborne and terrestrial applications

Candidate
Luca Milani

Supervisor
Prof. Frank Silvio Marzano

DOCTORATE CYCLE XXXII
(OCTOBER 2019)

Ai miei fantastici Nonni,
alla mia Famiglia,
agli Amici veri.

Abstract

The remote sensing of electromagnetic wave properties is probably the most viable and fascinating way to observe and study physical media, comprising our planet and its atmosphere, at the same time ensuring a proper continuity in the observations. Applications are manifold and the scientific community has been importantly studying and investing on new technologies, which would let us widen our knowledge of what surrounds us. This thesis aims at showing some novel techniques and corresponding applications in the field of the atmospheric remote sensing and radio-propagation, at both microwave and optical wavelengths.

The novel Sun-tracking microwave radiometry technique is shown. The antenna noise temperature of a ground-based microwave radiometer is measured by alternately pointing toward-the-Sun and off-the-Sun while tracking it along its diurnal ecliptic. During clear sky the brightness temperature of the Sun disk emission at K and Ka frequency bands and in the under-explored millimeter-wave V and W bands can be estimated by adopting different techniques. Parametric prediction models for retrieving all-weather atmospheric extinction from ground-based microwave radiometers are tested and their accuracy evaluated. Moreover, a characterization of suspended clouds in terms of atmospheric path attenuation is presented, by exploiting a stochastic approach used to model the time evolution of the cloud contribution.

A model chain for the prediction of the tropospheric channel for the downlink of interplanetary missions operating above Ku band is proposed. On top of a detailed description of the approach, the chapter presents the validation results and examples of the model-chain online operation. Online operation has already been tested within a feasibility study applied to the BepiColombo mission to Mercury operated by the European Space Agency (ESA) and by exploiting the Hayabusa-2 mission Ka-band data by the Japan Aerospace Exploration Agency (JAXA), thanks to the ESA cross-support service. A preliminary (and successful) validation of the model-chain has been carried out by comparing the simulated signal-to-noise ratio with the one received from Hayabusa-2.

At the next ITU World Radiocommunication Conference 2019, Agenda Item 1.13 will address the identification and the possible additional allocation of radio-frequency spectrum to serve the future development of systems supporting the fifth generation of cellular mobile communications (5G). The potential impact of International Mobile Telecommunications (IMT) deployments is shown in terms of received radio frequency interference by ESA's telecommunication links. Received interference can derive from several radio-propagation mechanisms, which strongly depend on atmospheric conditions, radio frequency, link availability, distance and path topography; at any time a single mechanism, or more than one may be present. Results are shown in terms of required separation distances, i.e. the minimum distance between the earth station and the IMT station ensuring that the protection criteria for the earth station are met.

Finally a novel remote sensing technique applied to optical wavelengths is presented, consisting of an anomaly detection and estimation method, using a pixel-based modified version of the Kalman temporal filter. In order to detect anomalies of the observed variable, the proposed Kalman-based anomaly masking (KAM) algorithm relies on background state models of the expected measurement cycle of each pixel in nominal (abnormal) conditions. If the measurement significantly deviates from its expected value as predicted by a-priori state, an anomaly is identified. The algorithm also provides an a-priori estimate of the nominal scenario, exploiting the previous Kalman filter states. The product is an equivalent clear-air observation, expected to be measured in absence of anomaly (e.g., in absence of cloud coverage). The KAM algorithm exhibits a general applicability, since its estimates are empirically computed from pixel-based models and its thresholds can be set independently from the area of interest. An application of the KAM algorithm to clear-air nominal scenarios is shown using multispectral imagery from the geostationary Spinning Enhanced Visible and Infrared Imager, having 12 visible-infrared channels and repeat cycle of 15 minutes, on-board of the Meteosat Second Generation satellite.

Acknowledgments

First, I would like to sincerely thank my supervisor, Professor Frank Marzano, for his continuous support and all the enormous passion he has passed on to me, from both a professional and a human perspective.

I also want to thank everyone I have been working with for the last years, especially all the colleagues of the Sapienza University of Rome, CETEMPS University of L'Aquila, Progressive Systems, and the European Space Agency. The list would be huge and I am very glad I had the chance to interact with so many valuable and competent people: all of this would not have been possible without you.

Headlines

Table of contents

List of figures

List of tables

Chapter 1. Introduction

The remote sensing of electromagnetic wave properties is probably the most viable and fascinating way to observe and study physical media, comprising our planet and its atmosphere, ensuring a proper continuity in the observations. Applications are manifold and the scientific community has been studying and investing on new technologies, which would let us widen our knowledge of what surrounds us.

This thesis aims at showing some novel techniques and corresponding applications in the field of the atmospheric remote sensing and radio-propagation, at both microwave and optical wavelengths. Radiopropagation channel conditions are indeed correlated directly to the remote sensed characterization of atmospheric quantities, relationship mainly governed by the so-called radiative transfer theory. Furthermore, from a telecommunication point of view, different propagation phenomena affect radio waves and understanding the effects of varying conditions on radio propagation has many practical applications: from choosing frequencies for international shortwave broadcasters, to designing reliable space communication systems, to radio navigation and operation of radar systems.

The dissertation is structured as follows:

Chapter 2 provides a collection of key concepts in the field of atmospheric remote sensing and radio-propagation, at both microwave and optical frequencies. The section is largely complemented by a number of historic and modern literature references.

Chapter 3 is devoted to ground based microwave radiometric applications. In particular, the novel Sun-tracking microwave radiometry technique is shown. The antenna noise temperature of a ground-based microwave radiometer is measured by alternately pointing toward-the-Sun and off-the-Sun while tracking it along its diurnal ecliptic. During clear sky the brightness temperature of the Sun disk emission at K and Ka band and in the unexplored millimeter-wave frequency region at V and W band can be estimated by adopting different techniques. Using a unique dataset collected during 2015 through a Sun-tracking multifrequency radiometer, the Sun brightness temperature shows a decreasing behavior with frequency with values from about 9000 K at K band down to about 6600 K at W band. In the presence of precipitating clouds the Sun-tracking technique can also provide an accurate estimate of the atmospheric extinction up to about 32 dB at W band with the current radiometric system. Parametric prediction models for retrieving all-weather atmospheric extinction from ground-based microwave radiometers are then tested and their accuracy evaluated. Moreover, chapter 3 also addresses the characterization of suspended clouds in terms of atmospheric path attenuation. Well-known radiative models are adopted to provide an estimate of the equivalent clear-air path attenuation contribution, exploiting surface weather measurements and making several assumptions on their vertical stratification over the troposphere. However, the attenuation contribution due to non-precipitating clouds cannot be easily modelled by only using in-situ measurements, i.e. surface boundaries are not able to provide

enough information about the whole atmospheric status for a given instant. A stochastic approach is used to model the time evolution of the cloud contribution. Physically-based prediction models for all-weather path attenuation estimation at 32 GHz are applied to the measured radiometric brightness temperatures. The cloud contribution is then extrapolated and modelled as a log-normal stochastic process as a result of a detailed analysis in both amplitude and time domains.

In chapter 4, a model chain for the prediction of the tropospheric channel for the downlink of interplanetary missions operating above Ku band is proposed. On top of a description of the approach, the chapter contains details on the validation and some examples of online operation of the model-chain. The latter has been already tested within a feasibility study applied to the BepiColombo mission to Mercury operated by the European Space Agency (ESA) and by exploiting the Hayabusa-2 mission Ka-band data by the Japan Aerospace Exploration Agency (JAXA) thanks to the ESA cross-support service. Three main modules compose the model-chain. A weather forecast module for the prediction of the atmospheric state expected during the downlink transmission. A radiopropagation module to simulate radiopropagation variables generated by the predicted atmospheric state. A downlink budget module for the statistical optimization of the satellite-to-Earth link. The latter exploits the spatial grid domain and the temporal evolution of the predicted radiopropagation variables to compute statistics and uncertainties of the outputs operational parameters to use during the transmission. A preliminary (and successful) validation of the model-chain has been carried out by comparing the simulated signal-to-noise ratio with the one received from Hayabusa-2.

Chapter 5 recaps some studies performed in the context of International Telecommunication Union (ITU) activities of ESA. In particular, at the next ITU World Radiocommunication Conference 2019, Agenda Item 1.13 will address the identification and the possible additional allocation of radio-frequency spectrum to serve the future development of the International Mobile Telecommunications (IMT) for 2020 and beyond, mainly focused on systems supporting the fifth generation of cellular mobile communications (5G). The frequency range of interest goes from 24.25 to 86 GHz, which fully covers all millimeter bands used or planned by the European Space Agency's space missions for high data rate transmissions. The chapter shows the potential impact of IMT deployments in terms of received radio frequency interference by ESA's telecommunication links in frequency bands allocated to the Earth Exploration-Satellite Service and to the Space Research Service. Received interference can derive from several propagation mechanisms including line-of-sight propagation, diffraction, scatter, ducting, reflection/refraction, etc. which strongly depend on atmospheric conditions, radio frequency, link availability, distance and path topography; at any time a single mechanism or more than one may be present. Particular focus is given to the ESA's tracking network and to the earth stations located in New Norcia (Australia), Cebreros (Spain), Malargüe Sur (Argentina) and Kiruna (Sweden). Results are shown in terms of required separation distances, i.e. the minimum distance between the earth station and the IMT station ensuring that the protection criteria for the earth station are met by the emissions of an IMT base station or user equipment.

A novel remote sensing technique applied to optical wavelengths is depicted in chapter 6. It consists of an anomaly detection and estimation technique, using a pixel-based modified version of the Kalman temporal filter. In order to detect anomalies of the observed variable, the proposed Kalman-based anomaly masking (KAM) algorithm relies on background state models of the expected measurement cycle of each pixel in nominal (abnormal) conditions. If the measurement significantly deviates from its expected value as predicted by a-priori state, an anomaly is identified. The KAM algorithm also provides an a-priori estimate of the nominal scenario, exploiting the previous Kalman filter states. The product is an equivalent clear-air observation, expected to be measured in absence of anomaly (e.g., in absence of cloud coverage). The KAM algorithm exhibits a general applicability, since its estimates are empirically computed from pixel-based models and its thresholds can be set independently from the area of interest. An application of the KAM algorithm to clear-air nominal scenarios is shown using multispectral imagery from the geostationary Spinning Enhanced Visible and Infrared Imager, having 12 visible-infrared channels and repeat cycle of 15 minutes, on-board of the Meteosat Second Generation satellite. The area of interest covers West Africa for a test period of three months (December 2015 until February 2016). This results in a massive amount of processed pixels (i.e., 1530x880 pixels for 96 timeslots per day). A validation of the clear-air KAM algorithm is presented by inter-comparing the detection results with the well-known EUMETSAT cloud mask product. The validation shows constant percentages of matching around 90% over the entire period of analysis.

Finally, chapter 7 draws the conclusions plus considerations on future work and possible developments.

Chapter 2. Atmospheric Remote Sensing and Propagation fundamentals

2. I. Introduction

Substantial information on the Earth's environment is gained from the remotely sensed properties of electromagnetic waves that interact with the observed target [1]. The basic quantities involved in the information acquisition process are the electromagnetic field vectors, the associated power and their statistical parameters. On its side, the target exerts the imprinting on the waves according to the electric properties of the constitutive matter, which are therefore key elements to trace the physical features of interest from the measured data. The electromagnetic energy always transfers through parts of the terrestrial environment. The traversed medium consists of the atmosphere and of the layers of other materials that the wave has to cross along the path between source of radiation, target under observation, and observing platform. Wave propagation affects the performance of the Earth Observation (EO) systems not only because it changes the amplitude of the field, but also because it modifies the phase, which carries its own peculiar information.

From a telecommunication point of view, radio waves are also affected by the phenomena of reflection, refraction, diffraction, absorption, polarization, and scattering [2]. Understanding the effects of varying conditions on radio propagation has many practical applications, from choosing frequencies for international shortwave broadcasters, to designing reliable mobile telephone systems, to radio navigation, to operation of radar systems.

Generally speaking, the energy emanating from a medium can be measured by a sensor. That measurement is used to construct an image of the landscape beneath the platform or retrieve an associated product or information (e.g. useful to characterize radio-propagation channel, atmospheric quantities, etc.). The energy can be reflected sunlight so that the image recorded is, in many ways, similar to the view we would have of the earth's surface from an airplane, although the wavelengths used in remote sensing are often outside the range of human vision. As an alternative, the upwelling or downwelling energy can be from the earth (and its atmosphere) itself acting as a radiator because of its own temperature. Finally, the energy detected could be scattered from the observed medium as the result of some illumination by an artificial energy source such as a laser or radar on the platform.

In principle, remote sensing systems could measure emanating energy in any sensible range of wavelengths [3]. However, technological considerations, the selective opacity of the earth's atmosphere, scattering from atmospheric particulates and the significance of the data provided exclude certain wavelengths. The major ranges utilized for earth resources sensing are between about 0.4 and 12 μm (the visible/infrared range) and between about 30 to 300 mm (the microwave range). At microwave wavelengths it is more common to use frequency rather than wavelength to describe ranges of importance. Thus, the microwave range of 30 to 300 mm corresponds to

frequencies between 1 GHz and 10 GHz. For atmospheric remote sensing, frequencies in the range 20 to 200 GHz are often used. The significance of these different ranges lies in the interaction mechanism between the electromagnetic radiation and the materials being examined. In the visible/infrared range, the energy measured by a sensor depends upon properties such as the pigmentation, moisture content and cellular structure of vegetation, the mineral and moisture contents of soils and the level of sedimentation of water. At the thermal end of the infrared range, it is heat capacity and other thermal properties of the surface and near subsurface that control the strength of radiation detected. In the microwave range, using active imaging systems based upon radar techniques, the roughness of the cover type being detected and its electrical properties, expressed in terms of complex permittivity (which in turn is strongly influenced by moisture content) determine the magnitude of the reflected signal. In the range 20 to 60 GHz, atmospheric oxygen, water vapor and liquid water have a strong effect on transmission and thus can be inferred by measurements in that range. Thus, each range of wavelength has its own strengths in terms of the information it can contribute to the remote sensing process. Consequently, systems are built and optimized to operate and provide data captured in specific spectral ranges.

The chapter is structured as follows: section 2.II provides some background on the dielectric properties of the air, at both microwave and optical frequencies; section 2.III provides an overview on microwave radiometry, from the fundamentals governing phenomena to a description of the radiometric systems. Section 2.IV is devoted to the description of terrestrial microwave propagation phenomena, often used for the prediction of the potential for interference among terrestrial systems; finally section 2.V recaps some concepts on optical remote sensing. All sections are well complemented by a large literature survey.

2. II. Dielectric behavior of the air

The time-domain Maxwell's equations can be expressed in terms of a system of differential equations in the space variables alone by assuming quasi-monochromatic fields [4]. Narrow-band fields are of particular interest in Earth observation, since they are apt to approximately represent both artificial (e.g., radar) signals and the natural radiation passing through radiometric channels, which separate the spectral components. It is indeed recognized that, the radiation is the result of a mixture of several sinusoidal oscillations generated by the energy conversion process, taking place in the source. For this particular reason, the spectrum of the electromagnetic field does not consist of a single line, rather it extends over a range of frequencies. The frequency spectra S of the electromagnetic radiation considered in practical applications have narrow bands, that is, they differ appreciably from zero in a narrow frequency range Δf about a central frequency f0. Maxwell's equations in the frequency domain represented by analytic vectors and scalars become as follows

$$\nabla \, x \, \boldsymbol{E} = -j\omega\mu\boldsymbol{H} - \boldsymbol{J_{ms}} \tag{2.1}$$

$$\nabla \, x \, \boldsymbol{H} = j\omega\epsilon\boldsymbol{E} + g\boldsymbol{E} + \boldsymbol{J_s} \tag{2.2}$$

$$\nabla \cdot \epsilon\boldsymbol{E} = \rho_s \tag{2.3}$$

$$\nabla \cdot \mu \boldsymbol{H} = 0 \tag{2.4}$$

Where $\boldsymbol{E}$ and $\boldsymbol{H}$ are the electric and magnetic fields, ρ_s is the charge density and $\boldsymbol{J_s}$ and $\boldsymbol{J_{ms}}$ are the electric and magnetic source currents, respectively
Equations (2.1)–(2.4) interconnect electric and magnetic fields with the sources, taking into account the effects of the materials, represented by their dielectric permittivity ϵ, electrical conductivity g and magnetic permeability μ. The coefficients of the equations depend on these electromagnetic parameters, therefore the fields clearly carry the imprinting by the material.

A wide range of values of permittivity and conductivity are encountered in common terrestrial materials, while their magnetic permeability is usually quite close to that of vacuum ($\mu \approx \mu_0$).

The atmosphere is of utmost importance in Earth observation, since:

- it is a relevant observable component of the Earth's environment, directly interacting with the human activity;
- it interacts with any incoming or outgoing radiation, and thus it needs to be taken into account even when it is not direct subject of observation, e.g. in sensing surface based targets from elevated platforms.

The atmosphere essentially consists of nitrogen (78.1%) and oxygen (20.9%), a small amount of water vapor and minor quantities of other gases, among which carbon dioxide, methane, and ozone. Because of the low polarizability of nitrogen, the permittivity of the air mainly results from the dielectric polarization of the other molecular species, of which the water vapor, being polar, is particularly active.

Real and imaginary parts of the permittivity are expressed as the superposition of the contributions by the N_{H_2O} individual interaction modes of single H_2O molecules and the N_{O_2} modes of O_2 molecules, plus additional contributions [5]-[6].

2. II.A. Microwave behavior

At microwaves, the main interactive air gases are oxygen and, especially, water vapor, which determine the dominant trend with frequency of the real and imaginary parts of the air permittivity [8]-[9]-[10].
Figure 2-1 shows the trends of the real ($\tilde{\epsilon}_r$) and imaginary ($|\tilde{\epsilon}_j|$) parts of the dielectric permittivity for frequencies up to the millimeter-wave range, of the reference atmosphere, assumed at pressure 1013 hPa (sea level), temperature 20 deg C and relative humidity 70 %. The shapes are mainly governed by:

- Oxygen, which has a set of resonant lines resulting in the peak of $|\tilde{\epsilon}_j|$ around 61.2 GHz and a line at about 118.8 GHz;
- Water vapor, with lines at 22.2 GHz and 183.3 GHz.

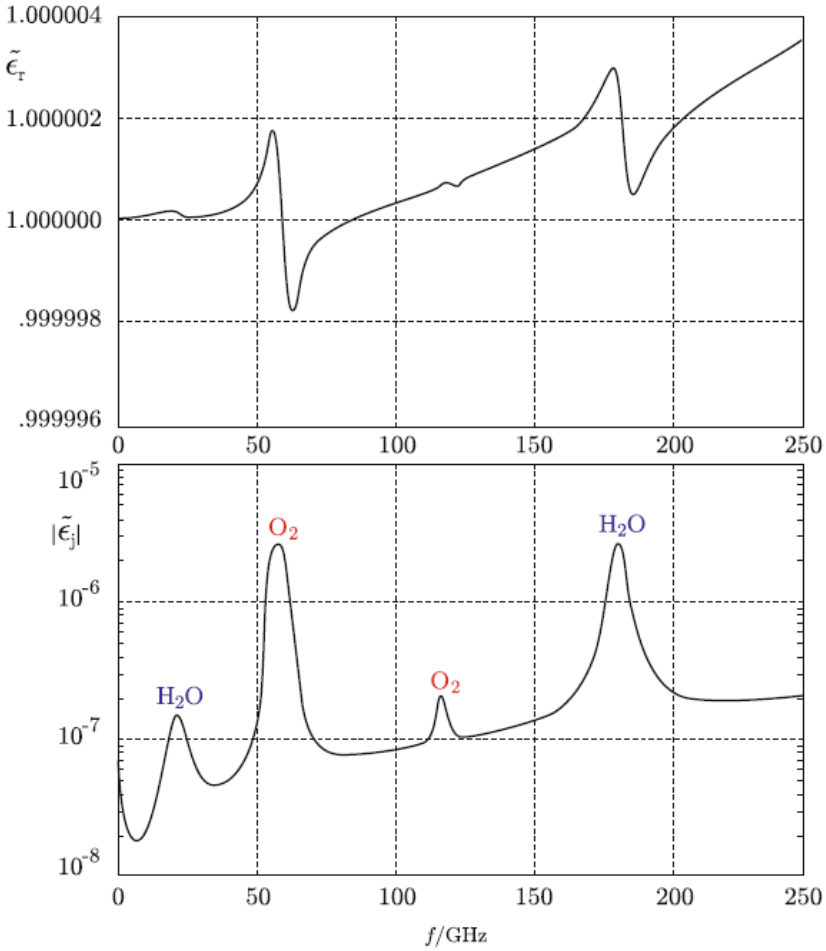

Figure 2-1: Real ($\tilde{\epsilon}_r$) and imaginary ($|\tilde{\epsilon}_j|$) parts of relative permittivity of air at standard conditions modeled [7] as a function of microwave frequency f (diagram from [1])

The diagrams show that the Lorentzian line shapes of the single molecular species are superimposed to the pedestal (the continuum) which increases smoothly with frequency. The continuously raising trend is attributed to the far wings of broadened resonant lines at higher frequencies [11], as well as to clusters of two (dimers) or more water vapor molecules in the air [12]-[13]-[14]-[15].
It is common practice to assume two main contributors to the air relative microwave permittivity:

- The Dry term accounting for the total amount of all polarizable molecules and linked to the total atmospheric pressure;
- The Wet term, accounting for the density of the highly polarizable water molecules directly linked to water vapor partial pressure.

For given total atmospheric and water vapor pressures, the permittivity decreases with the temperature, because increasing temperature enhances thermal agitation that hinders the action of the field in inducing oriented dipoles. On the other hand, the water vapor density in the air increases considerably with temperature, hence an overall growth of permittivity with the increase

of temperature actually occurs. To summarize, the dry term is higher, but more stable, whereas the wet term has lower values but with high variations, given the considerable dependence of vapor density on temperature and on the type of air mass.

It is worth to point out that both real and imaginary parts of the dielectric permittivity change with altitude, following pressure variation with height. In fact, the decreasing air density lowers the number of molecules per unit volume. The height-decreasing pressure also changes the overall shape of the imaginary part of air permittivity in the neighborhood of the 60-GHz oxygen resonant complex [16]. Indeed, pressure broadening has the effect of merging single lines into a relatively smooth function of frequency, which characterizes $|\tilde{\epsilon}_j|$ at low altitudes. As pressure decreases with altitude, the individual lines tend to separate.

Figure 2-1 indicates that real and imaginary parts of the air permittivity keep a generally increasing trend with increasing frequency beyond the microwave range. The growing trend is caused by the superposition of numerous resonant lines of atmospheric constituents located at higher frequencies. The high number of resonances of the atmospheric gases has the general effect of increasing the imaginary part of air permittivity especially in the infrared. In particular, the water molecule keeps contributing strongly to the air susceptibility, given the large number of resonances corresponding to rotational and roto-vibrational transitions that fall in the sub-mm wave band and in the infrared [17].

2. II.B. Optical behavior

In the optical domain, i.e., near infrared and visible, the resonances of atmospheric constituents rarefy and decrease in intensity, so that at the frequencies corresponding to visible wavelengths the air susceptibility is again approximately real. Modeling of permittivity in the visible and near infrared spectral range takes account of the main air constituents and water vapor, as well as of carbon dioxide [18].

It can be observed that the water vapor contribution, which is strong at microwaves, is quenched in the optical frequency range. Finally, at the high frequency end, that is, in the ultraviolet of interest to Earth observation, real and imaginary parts of the air susceptibility keep increasing with increasing frequency, given the approaching electronic resonances. It is worth mentioning that an additional analysis of the fine effects of the atmospheric constituents and of the physical parameters of air is needed when enhanced accuracy of the optical permittivity estimations is required by particular applications [19].

2. III. Microwave radiometry fundamentals

The microwave spectral range (between 1 and 100 GHz) offers a unique opportunity to derive a nearly complete picture of the atmospheric thermodynamical state. Water vapor and several other gases as well as water in its liquid form emit microwave radiation making this spectral range particularly interesting to provide information on the cloudy atmosphere both from the ground and from satellite [20]. Most of the concepts reported in this section are extracted from [20] and complemented with a number of literature references.

Ground-based microwave radiometer (MWR) measurements of atmospheric thermal emission are useful in a variety of environmental and engineering applications, including meteorological observations and forecasting, communications, geodesy and long-baseline interferometry, satellite validation, climate, air-sea interaction, and fundamental molecular physics. One reason for the utility of these measurements is that with careful design, microwave radiometers can be operated in a long-term unattended mode in nearly all weather conditions. An important feature is the nearly continuous observational capability on time scales of seconds to minutes [21]-[22]-[23].

The following sections, 2.II.A and 2.II.B, are devoted to provide some background information on the radiative transfer theory of the atmosphere, with particular focus on the properties of atmospheric gases and hydrometeors, which determine atmospheric brightness temperatures and the weighting function at the different microwave frequencies. Section 2.II.C briefly describes microwave radiometer systems, together with a small survey on instrument calibration techniques.

2. III.A. Fundamentals of Radiative Transfer

The basic ideas of radiative transfer and thermal emission are described, among others, by [25]-[26]. Their application to microwave radiometric remote sensing is outlined in [24]-[27]-[28].

➢ *Emission*

An ideal blackbody absorbs all incident radiation and re-emits all of the absorbed radiation as a function of its temperature and frequency. The spectral distribution of a blackbody emission at temperature T [K] and frequency ν [Hz]. $B_\nu(T)$ can be calculated from Planck's law to:

$$B_\nu(T) = \frac{2h\nu^3}{c^2}\frac{1}{e^{\frac{h\nu}{kT}}-1} \quad [\mathrm{W}\cdot\mathrm{sr}^{-1}\cdot\mathrm{m}^{-2}\cdot\mathrm{Hz}^{-1}] \tag{2.5}$$

where h is the Planck's constant, k is Boltzman's constant and c is the speed of light. This radiance expresses the emitted power per unit projected area, per unit solid angle and per unit frequency. Note the higher the temperature, the higher the emitted radiation. Most emitters, however, show a lower emission compared to that of a blackbody at the same temperature, i.e. the so-called "grey" body. If the fraction of incident energy from a certain direction absorbed by the grey body is e_ν, then the amount emitted is $e_\nu B_\nu(T)$. For a perfectly reflecting or transmitting body e_ν is zero and incident energy may be redirected or pass through the body without being absorbed. For an

upward-looking radiometer viewing a non-scattering medium, the equation that relates the actually observed radiance I_ν to the atmospheric state is the radiative transfer equation (RTE) [27]:

$$I_\nu = B_\nu(T_c)e^{-\tau_\nu} + \int_0^\infty B_\nu\big(T(s)\big)\,\alpha_\nu(s)\;\; e^{-\int_0^s \alpha_\nu(s')ds'}\;\; ds \tag{2.6}$$

where s is path length in m, $T(s)$ is the temperature in K at point s, T_C the cosmic background noise of 2.725 K, τ_ν the opacity or total optical depth:

$$\tau_\nu = \int_0^\infty \alpha_\nu(s)\, ds \tag{2.7}$$

where $\alpha_\nu(s)$ is the absorption coefficient (m^{-1} or Np/km) at the point s. The first term in Eq. (2.6) describes the transmitted part of the cosmic background radiation and is mostly much smaller than the second term that describes the atmospheric emission. The use of the blackbody source function in (2.6) is justified by the assumption of local thermodynamic equilibrium in which the population of emitting energy states is determined by molecular collisions and is independent of the incident radiation field. For a plane parallel atmosphere, s and the height z are related by $z = s \cdot \sin\theta$, where θ is the elevation angle of the measurement. In order to simplify the unit of measurement, Planck's law can be solved for T. In case of a "grey" emitter T will not be identical to the physical temperature of the emitter. Thus, this temperature is defined as the Planck-equivalent brightness temperature T_b. If the Rayleigh-Jeans limit holds ($h\nu << kT$) radiances $I_\nu = B_\nu(T_b)$ can easily be converted to brightness temperatures via $T_{B_{RJ}} = (c^2/2\nu^2 k)\, I_\nu$ and are identical to the Planck equivalent. Using this definition, the RTE becomes:

$$T_{B_\nu} = T_c e^{-\tau_\nu} + \int_0^\infty T(s)\,\alpha_\nu(s)\;\; e^{-\int_0^s \alpha_\nu(s')ds'}\;\; ds \tag{2.8}$$

By introducing the mean atmospheric temperature T_{mr}, defined as:

$$T_{mr} = \frac{\int_0^\infty T(s)\,\alpha_\nu(s)\;\; e^{-\tau(0,s)}\;\; ds}{\int_0^\infty \alpha_\nu(s)\;\; e^{-\tau(0,s)}\;\; ds} \tag{2.9}$$

Eq. (2.8) can be simplified as follows:

$$T_B = T_c e^{-\tau} + T_{mr}(1 - e^{-\tau}) \tag{2.10}$$

where we have omitted the frequency dependence for convenience. Note, that α_ν is a function of pressure, temperature, water vapor and cloud liquid. Information on these meteorological variables is obtained from measurements of T_B as a function of ν and/or θ.

➢ *Scattering*

For frequencies below 100 GHz scattering by small atmospheric particles, i.e. molecules, aerosols and cloud droplets can be neglected. However, for larger precipitating particles scattering effects need to be taken into account. For an upward-looking microwave radiometer the RTE approximation from the former section can be generalized, e.g., [29]-[30]-[31]-[32], to:

$$I_\nu = B_\nu(T_c)e^{-\tau_\nu} + \int_0^\infty J(s)\ \alpha_\nu(s)\ \ e^{-\int_0^s \alpha_\nu(s')ds'}\ \ ds \tag{2.11}$$

where the pseudo-source function J is given by:

$$J(s) = \frac{\omega(s)}{4\pi}\int_{4\pi} P(s,\Omega,\Omega')\, I_\nu(\Omega)\, d\Omega' + \ \big(1-\omega(s)\big)\, B_\nu\big(T(s)\big) \tag{2.12}$$

with ω the single scattering albedo, P the scattering phase function (normalized to 1) and Ω the solid angle. The single scattering albedo is the ratio of scattering to total extinction. i.e. the sum of absorption and scattering. In case of a non-precipitating atmosphere scattering is negligible for frequencies below 100 GHz and ω becomes zero. Under this condition, equations (2.6) and (2.11) become equal. For a scattering medium the single scattering properties need to be known to compute the brightness temperatures. In case of spherical particles this can be done exactly using Mie-theory. Larger rain drops flatten at the bottom due to frictional forces and their scattering behavior can be calculated assuming rotational symmetric, e.g., using the T-Matrix method in [33]. [34]-[35] show the importance of taking into account the realistic shape of rain drops, and that the scattering signature of non-spherical precipitation sized particles can be detected by using dual-polarized ground-based observations during rain at 19 GHz. Scattering by larger snow particles becomes noticeable at 90 GHz. Here, the computation of scattering properties becomes rather complicated as shape, density, aspect ratio, orientation and mass-size relation need to be considered [36].

The simulation of T_B (forward modelling) is typically used in inverse problems and parameter retrieval applications, in which meteorological and/or propagation information is inferred from measurements of T_B. For forward modeling the knowledge on the atmospheric absorption characteristics is fundamental. In order to evaluate the gas absorption models that provide α_ν the relevant meteorological variables are measured by radiosondes and the calculated brightness temperatures are then compared to measured ones. The simulation of T_B is also useful for determining the effects of instrument noise on parameter retrieval or for determining optimal measurement configurations, such as ν and θ.

2. III.B. Microwave absorption and emission of the troposphere

The principal sources of atmospheric microwave emission and absorption are water vapor, oxygen, and cloud liquid (Figure 2-2). In the frequency region from 20 to 100 GHz, water-vapor absorption arises from the weak electric dipole rotational transition at 22.235 GHz, and a much stronger water vapor line at 183.31 GHz that is used at dry conditions [47]-[48]. The so-called continuum

absorption of water vapor most likely arises from the far wing contributions of higher-frequency resonances that extend into the infrared region. Oxygen absorbs due to a series of magnetic dipole transitions centered around 60 GHz and the isolated line at 118.75 GHz. Because of pressure broadening, i.e. the effect of molecular collisions on radiative transitions, both water vapor and oxygen absorption extend outside of the immediate frequency region of their resonant lines. There are also resonances by ozone that are important for stratospheric sounding [49]. In addition to gaseous absorption, scattering, absorption, and emission also originate from hydrometeors in the atmosphere. For liquid water, the emission is roughly proportional to the frequency squared.

➢ *Gaseous absorption models*

J. H. Van Vleck first published detailed calculations of absorption by water vapor and oxygen in [50]-[51]. The quantum mechanical basis of these calculations, including the Van Vleck-Weisskopf line shape, together with laboratory measurements, has led to increasingly accurate calculations of gaseous absorption. Currently, there are several absorption models that are widely used in the propagation and remote-sensing communities. Starting with laboratory measurements that were made in the late 1960s and continuing for several years, H. Liebe developed and distributed the computer code of his Microwave Propagation Model (MPM). One version of the model [52] is still used extensively and many subsequent models are compared with this one. Liebe later made changes to both water-vapor and oxygen models, especially to parameters describing the 22.235 GHz water vapor line and the continuum [53].

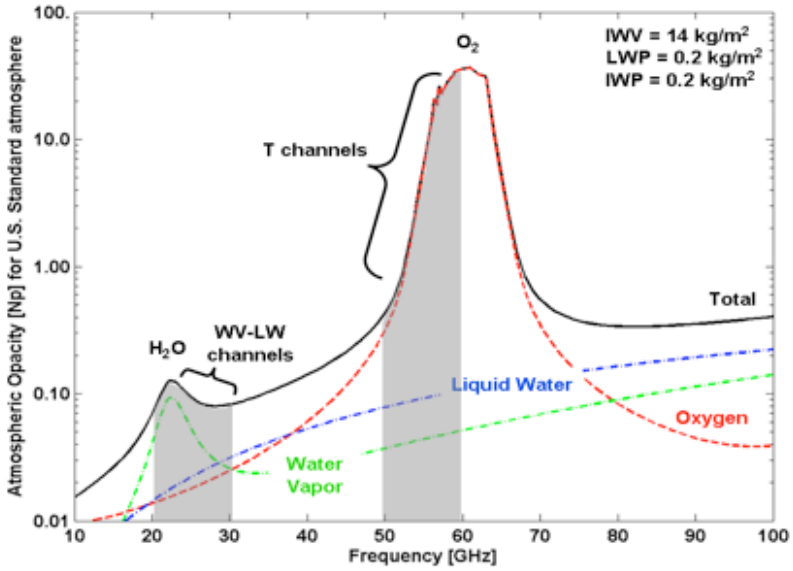

Figure 2-2: Atmospheric opacity for U.S. standard atmosphere with liquid and ice water clouds. The ice water contribution is below 0.01 Np throughout the 10-100 GHz range. The spectral range of commercially available water vapor (WV; K-band 20-30 GHz) and temperature (V-band 50-60 GHz) microwave profilers is indicated (figure from [20]).

Rosenkranz, in [55]-[56], developed an improved absorption model that also is extensively used in the microwave propagation community. However, there are many issues in the determination of

parameters that enter into water vapor absorption modeling, and a clear discussion of several of these issues is given in [54]. Relevant to the discussion is the choice of parameters to calculate the pressure-broadened line width, which in the case of water vapor, is due to collisions of H_2O with other H_2O molecules (self-broadening), or from collisions of H_2O molecules with those of dry air (foreign broadening). In fact, Rosenkranz [55] based his model on Liebe and Layton's [52] values for the foreign-broadened component, and those from [53] for the self-broadened component. The most recent version of Rosenkranz's model [57] is described in [58]. A RTE model that is used extensively in the US climate research community is the Line by Line Radiative Transfer Model (LBLRTM) by S. Clough and his colleagues [59]-[60]. An extension of the model, called MONORTM, is most appropriate for millimeter wave and microwave radiative transfer studies [60]. MONORTM has been compared extensively with simultaneous radiation and radiosonde observations near 20 and 30 GHz. Important refinements of absorption models have occurred and are occurring in the last decade, additional details can be found in [20].

➢ *Extinction due to hydrometeors*

For spherical particles, the classical method to calculate scattering and absorption (i.e., extinction) is through the Lorenz-Mie Equations [29]-[65]-[66]. When calculating absorption for non-precipitating clouds the Rayleigh approximation is used, for which the liquid absorption depends only on the total liquid amount and does not depend on the drop size distribution and scattering is negligible. The Rayleigh approximation is valid when the scattering parameter $\beta = |n(2\pi r / \lambda)| << 1$ [29]. Here, r is the particle radius, λ is the wavelength, and n is the complex refractive index.

An important physical property for the calculations is the complex dielectric constant of the particle. This dielectric constant of liquid water is described by the dielectric relaxation spectra of Debye [67]. The strong temperature dependence of the relaxation frequency is linked to the temperature dependent viscosity of liquid water. Therefore, the cloud absorption coefficient also shows significant temperature sensitivity. Above 0 °C the dielectric constant can be well measured in the laboratory and a variety of measurements have been made from 5 to 500 GHz [147]. However for super-cooled water below 0 °C, the situation is less certain and models of [68]-[69]-[147] differ by 20 to 30% in this region. This is relevant for cloud remote sensing, because measurements of super-cooled liquid are important for detection of aircraft icing [70]. A more detailed literature survey, also addressing the ice characterization, can be found in [20].

For rain and other situations for which the β is greater than roughly 0.1, the full Mie equations, combined with a modeled (or measured) size distribution, must be used. Generally for a given wavelength and particle, the single particle contribution is calculated and the total extinction are then obtained by integration over the size distribution of particles. Due to the non-spherical shape of ice hydrometeors, the situation is more complicated when scattering plays a role. For larger snow particles scattering becomes significant at frequencies above 60 GHz and realistic models of the snow particle shape together with techniques like the *Discrete Dipole Approximation* need to be used to calculate the scattering properties [71]. Special situations occur when ice particles start to melt.

A very thin skin of liquid water can be sufficient to cause significant absorption and thus emission. Usually, these conditions apply to precipitating clouds in the so-called radar "bright band".

2. III.C. Radiometric systems

Today, microwave radiometers measuring downwelling thermal emission at the ground are routinely operated in unattended 24h/7days a week mode at many sites worldwide. Commercial systems include multi-channel systems for the retrieval of IWV and LWP and temperature and humidity profilers (e.g., [37]-[38]-[39]). Elevation scanning is often used for boundary layer profiling [40]-[41]. Also, radiometers scanning in both azimuth and elevation are used to observe hemispheric variations of water vapor and clouds [42]-[43].
The fundamentals of microwave radiometers are clearly discussed in [24]-[44]. Radiometers used to observe the atmosphere are comprised of a highly directional antenna, a sensitive receiver, followed by a detector unit and a data-acquisition system. To produce meteorologically important information, the total system requires calibration.

➢ *Hardware*

In order to treat the observation as a pencil beam, a highly directional antenna with a beam width, commonly defined as Full Width at Half Maximum (FWHM), in the order of a few degrees is needed. In the microwave spectral range the diffraction limit causes the antenna size to become relatively large. Symmetric beam patterns of Gaussian shape (typically between 1 and 6°) are achieved with corrugated feed horns which are sometimes illuminated by a scanning system. Because many remote-sensing systems perform scanning in a vertical plane, low side lobes are required to minimize contamination from ground emission. Because surface-based antennas are deployed in rain and snow, protection from and reduction or elimination of environmental effects is of primary concern. This is typically achieved by using hydrophobic radome material covering the antenna that is further kept clean by a heated blower.

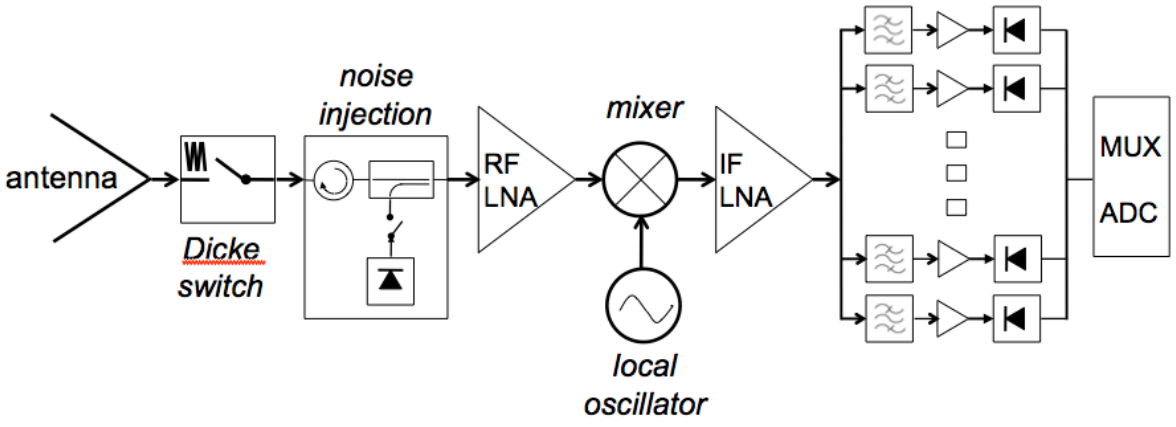

Figure 2-3: Schematic view of a multi-frequency heterodyne microwave receiver. Low noise amplifiers (LNA) are implemented in the radio frequency (RF) and intermediate frequency (IF). After the signal splitting band pass filtering, amplification and detection takes place in the individual channels. The analogue signals are combined by a multiplexer (MUX) and converted by analogue digital converters (ADC) to digital counts (figure from [20]).

Because of the low radiances emitted in this spectral range microwave radiometers need to amplify the signal received at the antenna by about 80 dB. Throughout the last decade, low noise amplifiers (LNA) have become available for frequencies up to 100 GHz. Therefore, several radiometers are based on direct detection techniques, while heterodyne receivers are still widely implemented (Figure 2-3). In a heterodyne receiver, the radio frequency (RF) from the atmosphere is down-converted to an intermediate frequency (IF) by a mixer using a frequency stable local oscillator (LO). In principle two sidebands with $\nu_{RF} = \nu_{LO} \pm \nu_{IF}$ are converted to the IF. This is often exploited when observations along a single symmetric absorption line are performed. In this case the LO is set to the line centre frequency and contributions from equally distant frequencies on both sides of the line are combined into a single channel. Thus, a single LO can be used for several frequency channels along the line and respective profiling. This double side band approach increases the signal-to-noise ratio by a factor of two. If this technique is used for window channels, low IF center frequencies have to be used to realize typical channel bandwidths of a few GHz. If only one frequency band shall be received, a single sideband filter, for example of Martin-Puplett or Fabry Perot type, has to be implemented.
Multi-channel microwave radiometers typically split the IF signal into the different channels by band pass filters (Figure 2-3). Each channel's signal is further amplified, detected, and finally converted to digital counts. For detection the radiometer use a square law detector, in which the output voltage is proportional to the input power; i.e., the voltage U is proportional to the brightness temperature T_B.

➢ *Calibration*

For accurate observations of brightness temperatures, the signal calibration is of uttermost importance. To convert the radiometer's output voltages U into brightness temperatures, T_B, the measurement process can be modelled via:

$$U_a = g(P_r + P_a)^{\alpha} \tag{2.13}$$

Here, g is the gain, α the nonlinearity factor and P_r the noise power of the receiver itself that can be related to the receiver temperature T_r via inverting the Planck-formula in (2.5). In the same sense, $P_a(T_a)$ denotes the power received at the antenna (antenna temperature) either by the atmosphere or from an external target. The sum of receiver and antenna temperature gives the system noise temperature $T_{sys} = T_r + T_a$. A low system noise is desired because T_{sys} together with the integration time Δt and the frequency bandwidth $\Delta\nu$ determine the minimum detectable brightness temperature change:

$$\Delta T_B = \frac{T_{sys}}{\sqrt{\Delta t\, \Delta\nu}} \tag{2.14}$$

Typical values of ΔT_B for state-of-the-art microwave systems reach 0.1 K.

A common simplification in the design of calibration systems for receivers is the assumption of a linear radiometer response. In this case $\alpha = 1$ and only two calibration parameter need to be

determined. A seemingly straightforward calibration method is to view two external blackbody targets that are kept at two widely separated temperatures [44]. Preferably, the target temperatures bracket the range of antenna temperatures emitted from the scene. In addition, it is important to construct targets with high emissivity such that reflections from external sources are negligible, and to have the targets sufficiently large that at least 1½ to 2 projected antenna diameters are captured by the target system.

Targets are frequently constructed with a surface having high thermal conductivity covered with a thin layer of very absorbing material. Many times, a corrugated pyramidal surface with wavelength-dependent spacing and depth ratios is constructed to reduce reflections and hence to increase emissivity, i.e. to realize a blackbody. For calibration, it is important to know the physical temperature of the target with high accuracy. Therefore, often measurements of target temperatures at several locations within the target are performed [45]. Another approach is to cancel thermal gradients across the load by venting of air that is very efficient for ambient temperature targets.
For realizing a calibration point at a lower temperature blackbody targets immersed in cryogenic fluids, such as liquid nitrogen (LN_2), are commonly used. Hereby, one must carefully considers the reflection of the ambient scene as well as the reflection coefficient of the cryogen. The boiling point of the liquid nitrogen and thus the physical temperature of the cold load depends on the barometric pressure p. A practical challenge is to avoid formation of condensed water on the parts of the outer calibration setup of the radiometer, through which the received radiation is to be transmitted or by which it is reflected.

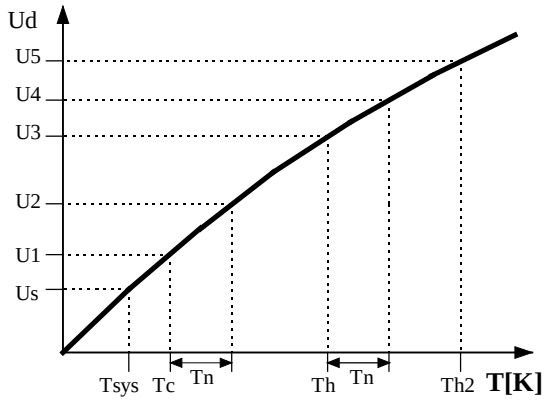

Figure 2-4: Detector response as a function of input noise T. T_c is the total noise when the radiometer is terminated with a cold load (e.g. liquid nitrogen cooled absorber) and T_h the corresponding noise temperatures for the ambient load, T_n the additionally injected noise.

Accurate noise injection measurements have shown that the assumption of linear system response is not valid in general. Calibration errors of 1-2 K have been observed at brightness temperatures in between the two calibration target temperatures. This system nonlinear behavior is mainly caused by detector diodes needed for total power detection, and becomes important when low noise systems are concerned. The problem is to determine g, α and T_r experimentally within a so-called absolute calibration as three unknowns cannot be calculated from a measurement on two

reference targets. A solution is to generate four temperature points by additional noise injection of temperature T_n, which leads to four independent equations with four unknowns (2.13). T_n is the equivalent brightness temperature of a noise diode that is coupled into the input of each receiver to inject a reference signal. Noise diodes generate stable white noise with Gaussian characteristics and can be switched on and off rapidly. They do not provide an absolute reference and must be calibrated against an external reference. Once burnt in, however, they can provide a stable secondary standard.

Calibration experiments with commercially available state-of-the-art radiometer systems have shown that LN_2 calibrations have an absolute accuracy of approximately 1 K at optically thin channels [106]. These results were obtained by successively performing multiple calibrations within a time window of hours and by subsequently applying the different sets of calibration parameters to one and the same time series of voltages measured during characteristic clear-sky situations. The spread in the obtained brightness temperatures lies within +/-1 K for channels in the K band and in the optically thin V band underlining the repeatability of the calibration procedure. The absolute accuracy decreases to the accuracy of the internal ambient reference target when moving towards optically thick frequency channels. In order to obtain this retrieval accuracy, the calibration procedure as outlined by the manufacturer must be strictly followed.

Even if a system is well thermally stabilized, gain fluctuations typically occur on shorter time scales than variations in T_{sys}. Therefore, Dicke-type radiometer use magnetically controlled Dicke switches to direct the receiver input alternately to the antenna or an internal reference load (see Figure 2-3). This reduces the integration time by a factor of two but with a cycling of several Hz gain fluctuations can be minimized effectively. Such a relative calibration – though on longer time scales (couple of minutes compared to milliseconds) – can also be realized by regularly pointing the antenna to an internal ambient temperature target.

In the transmission windows from 20 to 45 GHz or from 70 to 150 GHz, clear-sky brightness temperatures can be in the 10 to 50 K range and, hence, operational deployment of targets whose temperatures are in this range is difficult. In this low transmission case, the so-called tipping-curve calibration method can give a high degree of accuracy [46] and has been commonly used throughout the microwave community. In this method, brightness temperatures are measured as a function of elevation angle θ, and are then converted to opacity $\tau(\theta)$ using the mean radiating temperature approximation in (2.9). For each angle θ, an angular-dependent mean radiating temperature $T_{mr}(\theta)$ is used to derive the optical depth $\tau(\theta)$ by

$$\tau(\theta) = \ln\left(\frac{T_{mr}(\theta) - T_{cos}}{T_{mr}(\theta) - T_B(\theta)}\right) \tag{2.15}$$

In Equation (2.15), the antenna temperature T_a has been adjusted to $T_B(\theta)$. If the system is well calibrated, then the linear fit of $\tau(\theta)$ as a function of (normalized) air mass $m = \csc(\theta)$, will pass through the origin; conversely, if $\tau(m) = \tau(1)m + b$ does not pass through the origin, then a single parameter in the radiometer equation is adjusted until it does. Note, that when the calibration is achieved, then the slope of the line is equal to the zenith opacity. Several of the factors affecting the accuracy of tipping calibrations were analyzed in [46]. The most serious of these errors

are those caused by non-stratified atmospheric conditions and can occur due to clouds and horizontal variations in the water vapor field. Various criteria, based on symmetric scans, are available to determine the quality of a tipping calibration [46]. Other problems arise from non-correct levelling of the instrument, and effects of the earth curvature and antenna beamwidth. Especially when pointed at low elevation angles, the antenna beamwidth can pose a problem as the signals received at the lower and higher angles than the nominal pointing do not cancel out, and low side lobes are required to minimize contamination from ground emission. Due to the finite antenna beam width, the airmass-angle relationship is no longer correctly given by $m = \csc(\theta)$, which is applicable for a radiometer with an infinitely small beam width. Also, errors increase with the increase of airmass [46]. These problems may give rise to absolute uncertainties larger than 1 K if not dealt within in a consistent way.

2. IV. Terrestrial microwave propagation for interference prediction

Congestion of the radio-frequency spectrum has made necessary the sharing of many frequency bands between different radio services, and between the different operators of similar radio services. In order to ensure the satisfactory coexistence of the terrestrial and Earth-space systems involved, it is important to be able to predict with reasonable accuracy the interference potential between them, using propagation predictions and models which are acceptable to all parties concerned, and which have demonstrated accuracy and reliability.

Many types and combinations of interference path may exist between stations on the surface of the Earth, and between these stations and stations in space, and prediction methods are required for each situation. Interference may arise through a range of propagation mechanisms whose individual dominance depends on climate, radio frequency, time percentage of interest, distance and path topography. At any one time a single mechanism or more than one may be present. The principal interference propagation mechanisms are as follows [61]:

- *Line-of-sight* (Figure 2-5): The most straightforward interference propagation situation is when a line-of-sight transmission path exists under normal (i.e. well-mixed) atmospheric conditions. However, an additional complexity can come into play when sub path diffraction causes a slight increase in signal level above that normally expected. Also, on all but the shortest paths (i.e. paths longer than about 5 km) signal levels can often be significantly enhanced for short periods of time by multipath and focusing effects resulting from atmospheric stratification (see Figure 2-6).

- *Diffraction* (Figure 2-5): Beyond line-of-sight (LoS) and under normal conditions, diffraction effects generally dominate wherever significant signal levels are to be found. For services where anomalous short-term problems are not important, the accuracy to which diffraction can be modeled generally determines the density of systems that can be achieved. The diffraction prediction capability must have sufficient utility to cover smooth-earth, discrete obstacle and irregular (unstructured) terrain situations.

- *Tropospheric scatter* (Figure 2-5): This mechanism defines the "background" interference level for longer paths (e.g. more than 100-150 km) where the diffraction field becomes very weak. However, except for a few special cases involving sensitive receivers or very high power interferers (e.g. radar systems), interference via troposcatter will be at too low a level to be significant.

- *Surface ducting* (Figure 2-6): This is the most important short-term propagation mechanism that can cause interference over water and in flat coastal land areas, and can give rise to high signal levels over long distances (more than 500 km over the sea). Such signals can exceed the equivalent "free-space" level under certain conditions.

- *Elevated layer reflection and refraction* (Figure 2-6): The treatment of reflection and/or refraction from layers at heights up to a few hundred meters is of major importance as these mechanisms enable signals to overcome the diffraction loss of the terrain very effectively under favorable path geometry situations. Again the impact can be significant over quite long distances (up to 250-300 km).

- *Hydrometeor scatter* (Figure 2-6): Hydrometeor scatter can be a potential source of interference between terrestrial link transmitters and earth stations because it may act virtually omnidirectionally, and can therefore have an impact off the great-circle interference path. However, the interfering signal levels are quite low and do not usually represent a significant problem.

A basic problem in interference prediction (which is indeed common to all tropospheric prediction procedures) is the difficulty of providing a unified consistent set of practical methods covering a wide range of distances and time percentages; i.e. for the real atmosphere in which the statistics of dominance by one mechanism merge gradually into another as meteorological and/or path conditions change. Especially in these transitional regions, a given level of signal may occur for a total time percentage which is the sum of those in different mechanisms.
In recommendation ITU-R P.452 [61], the clear-air method consists of separate models for diffraction, ducting/layer-reflection, and troposcatter. All three are applied for every case, irrespective of whether a path is LoS or trans-horizon. The results are then combined into an overall prediction using a blending technique that ensures for any given path distance and time percentage that the signal enhancement in the equivalent notional line-of-sight model is the highest attainable. On the other hand, the hydrometeor-scatter interference prediction is defined in [61] as a completely separate method.

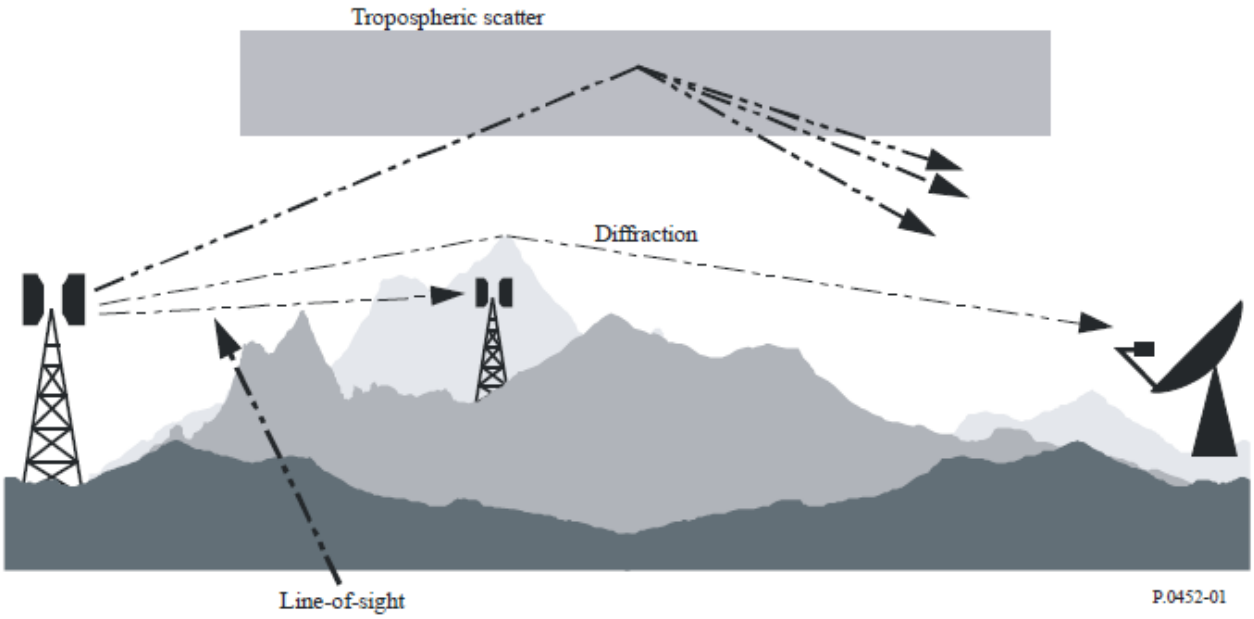

Figure 2-5: Long-term interference propagation mechanisms (image from [61])

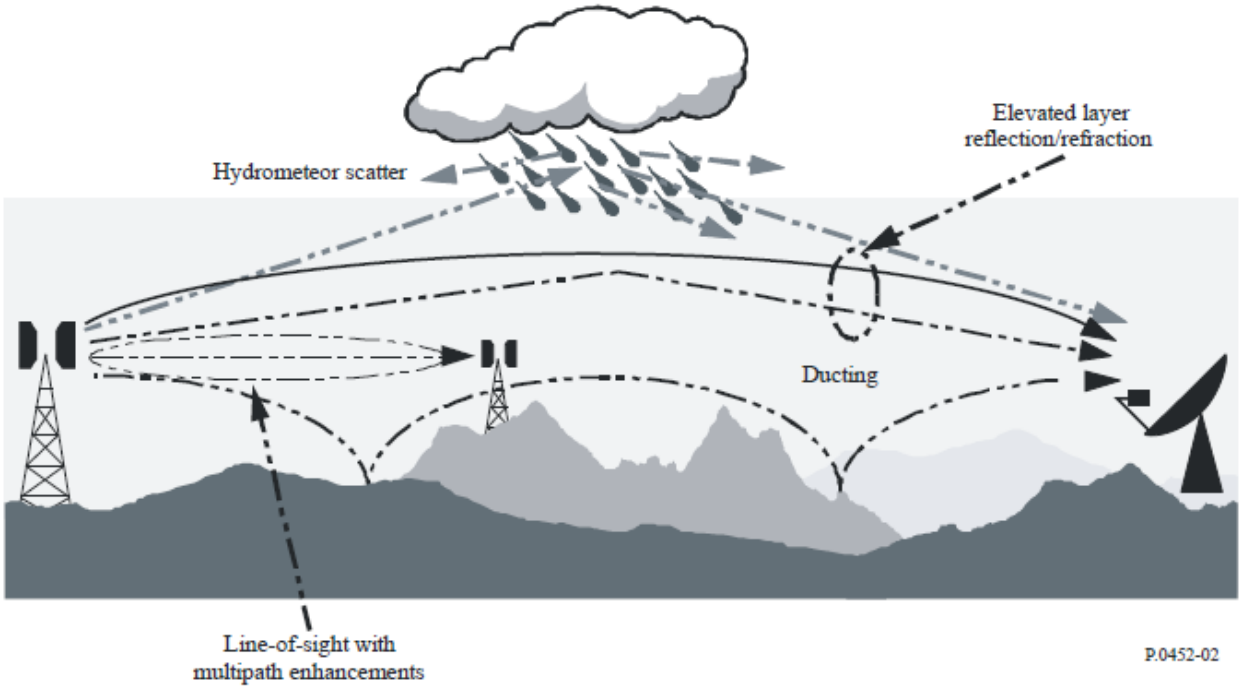

Figure 2-6: Anomalous (short-term) interference propagation mechanisms (image from [61])

2. V. Optical remote sensing

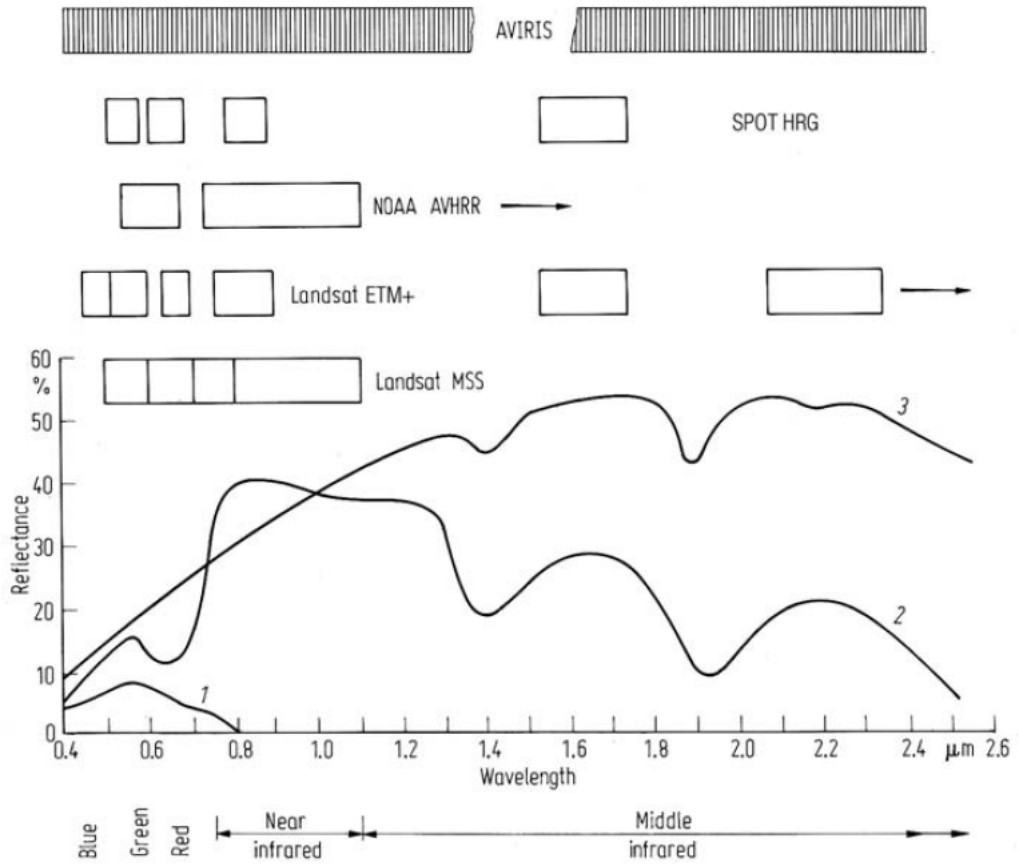

Figure 2-7: Spectral reflectance characteristics of common earth surface materials in the visible and near-to-mid infrared range. 1=Water, 2=vegetation, 3=soil. The positions of spectral bands for common remote sensing instruments are indicated (image from [3]).

Figure 2-7 depicts how the three dominant earth surface materials of soil, vegetation and water reflect the Sun's energy in the visible/reflected infrared range of wavelengths [3]. It is seen that water reflects about 10% or less in the blue-green range, a smaller percentage in the red and certainly no energy in the infrared range. Should the water contain suspended sediments or should a clear water body be shallow enough to allow reflection from the bottom then an increase in apparent water reflection will occur, including a small but significant amount of energy in the near infrared range. This is a result of reflection from the suspension or bottom material. Soils have a reflectance that increases approximately monotonically with wavelength, however with dips centered at about 1.4 μm, 1.9 μm and 2.7 μm owing to moisture content. These water absorption bands are almost unnoticeable in very dry soils and sands. In addition, clay soils also have hydroxyl absorption bands at 1.4 μm and 2.2 μm.

The vegetation curve is considerably more complex than the other two. In the middle infrared range it is dominated by the water absorption bands at 1.4 μm, 1.9 μm and 2.7 μm. The plateau between about 0.7 μm and 1.3 μm is dominated by plant cell structure while in the visible range of

wavelengths it is plant pigmentation that is the major determinant. The curve sketched in Figure 2-7 is for healthy green vegetation. This has chlorophyll absorption bands in the blue and red regions leaving only green reflection of any significance. This is why we see chlorophyll pigmented plants as green. An excellent review and discussion of the spectral reflectance characteristics of vegetation, soils, water, snow and clouds can be found in [62] and [63]. This includes a consideration of the physical and biological factors that influence the shapes of the curves, and an indication of the appearances of various cover types in images recorded in different wavelength ranges.

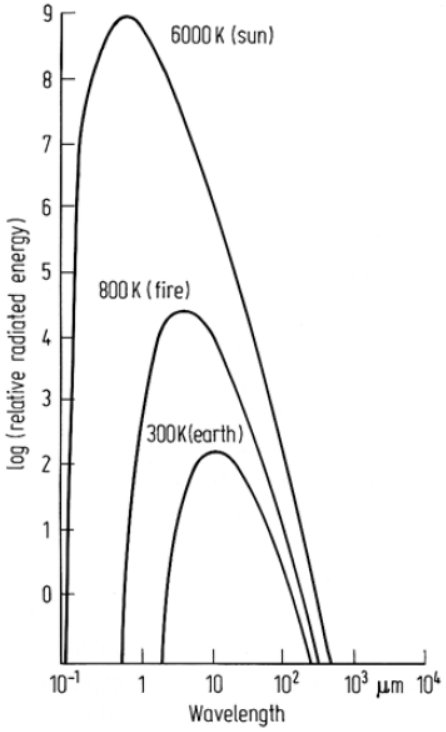

Figure 2-8: Energy from perfect radiators (black bodies) as a function of wavelength (image from [3]).

In wavelength ranges between about 3 and 14 μm, the level of solar energy actually irradiating the earth's surface is small. This is due to both the small amount of energy leaving the sun in this range by comparison to the higher levels in the visible and near infrared range (Figure 2-8), and the presence of strong atmospheric absorption bands between 2.6 and 3.0 μm, 4.2 and 4.4 μm, and 5 and 8 μm [64]. Consequently, much remote sensing in these bands is of energy being emitted from the earth's surface or objects on the ground rather than of reflected solar radiation.

Figure 2-8 shows the relative amount of energy radiated from perfect black bodies of different temperatures. As seen, the sun at 6000 K radiates maximally in the visible and near infrared regime but by comparison generates little radiation in the range around 10 μm. The earth, at a temperature of about 300 K has its maximum emission around 10 to 12 μm. Thus, a sensor with sensitivity in this range will measure the amount of heat being radiated from the earth itself. Hot bodies on the

earth's surface, such as bushfires, at around 800 K, have a maximum emission in the range of about 3 to 5 μm. Indeed, to map fires, a sensor operating in that range would be used. Real objects do not behave as perfect black body radiators but rather emit energy at a lower level than that shown in Figure 2-8. The degree to which an object radiates by comparison to a black body is referred to as its emittance. Thermal remote sensing is sensitive therefore to a combination of an object's temperature and emittance, the last being wavelength dependent.

Chapter 3. Ground-based microwave radiometry for Earth-satellite attenuation retrieval

3. I. Introduction

Since the beginning of the wireless telecommunications history, the exploration of new frequency regions has been always aimed to find allocation for a plenty of new services (e.g.: radio navigation, radio astronomy, remote sensing, telecommunication to cite some examples). Both telecommunication and space exploration systems continuously demand increasing uplink and downlink capabilities able to satisfy specific requirements and the use of frequencies at K-band and above seems to be the only way forward. Such frequency bands offer several performance advantages, provided by larger available bandwidth and higher gain for the same antenna size. Because of the Shannon–Hartley theorem [82], larger bandwidth is directly proportional to higher data transfer rates which is a particular attractive feature for those applications and telecommunications protocols that require high data transfer rates (e.g. video, deep space, internet of things data streaming, etc.). Additionally, a larger bandwidth enables capabilities like wideband spread-spectrum techniques [83] that allow to further reduce for impairments caused, for example, by multipath, clutter and radio frequency interferences. In addition, smaller antenna sizes for a fixed gain, fostered by the use of higher frequencies, is an appealing characteristic for space born applications due to size constrains. For the reasons previously exposed, accompanied by the fact that the today's spectrum use is crowded and it does not permit to allocate additional services, an interest to improve spectrum usage gained attention from the research community as well as private companies. A particular focus is in the exploitation of extreme high frequency bands or millimeter wave bands (wavelength and frequency in the range from 1 mm to 10 mm and from 30 GHz to 300 GHz, respectively) to meet global radio communication needs [84]. At millimeter wave frequencies, wavelengths shrink by an order of magnitude (if compared to centimeter microwave frequencies) and became comparable with hydrometeors sizes. Indeed, propagation impairments get more severe as the frequency increases, i.e. the impact of radio-meteorological factors degrading the link availability gets quite relevant [72]-[73]. Not only the impact of rain significantly affects the channel performances [72], but also the contributions of atmospheric gases and non-precipitating clouds are not negligible [24]-[77]-[78]. This elevates the importance of having accurate propagation models. The latter aim at predicting, in statistical terms, the level of the signal to noise ratio expected at the receiver station for a given path [87] thus aiding Earth-to-Earth or a satellite-to-Earth link budget design as well as to deliver a better quality to remote sensing data. By resorting to the Friis transmission equation in presence of path attenuation [76], the signal to noise ratio can be described in terms of atmospheric optical thickness / attenuation (A) undergone by the transmitted signal during its travel and the brightness temperature (T_B) that accounts for the self-emission of the atmosphere delivered to the receiving antenna in the form of thermal noise

[87]. Thus, A and T_B become key quantities in designing a propagation model especially at the underexplored millimeter wave bands.
Beacon campaigns and microwave radiometry are the most interesting techniques used to characterize both physical and statistical characteristics of the atmosphere, despite very limited and constrained [79]-[80]. If no radio-frequency observations are available for a given antenna ground station site, the Earth-space radiocommunication systems design needs to rely on other information sources to estimate the propagation conditions.

3. II. Sun-Tracking Microwave Radiometry

The Sun-tracking (ST) microwave (MW) radiometry technique consists in spatially varying the observation angle on and off the Sun by means of a ground-based radiometer antenna [81]-[85]. In this respect, ST uses the Sun as a signal source of radiation transmitting through the atmosphere [81]. The interest of the ST microwave radiometry is typically twofold. First, by properly choosing the switching time interval and taking into account the main lobe aperture under clear-sky conditions, it is possible to estimate the effective brightness temperature of the Sun, which is a valuable data in radio astronomy [86]. Secondly, the ST technique allows the retrieval of the atmospheric extinction in all weather conditions with an upper limit depending on the radiometric accuracy [80].
In radio astronomy, MW observations of the Sun are dominated by large multi-element arrays [89], which have the advantage of high spatial resolution, high sensitivity and ability to make maps on very short timescales, discriminating the rather weak signal of the quiet Sun from the strong active region signals [90]. Indeed, most solar radio observations have focused on active region phenomena such as flares and coronal mass ejections, demonstrating powerful diagnostic capabilities of large microwave arrays to address open issues regarding the quiet Sun [91], [92]. At sub-millimeter frequencies Sun observations have historically been performed with single-dish antennas thus showing comparatively a poorer spatial resolution [93]. Solar measurements at multiple frequencies are useful as the emitted brightness arises from different layers of the solar atmosphere. For instance, the lower chromosphere is typically detected at frequencies of 100–1000 GHz, the middle chromosphere at 20–100 GHz, and the upper chromosphere at frequencies of 2–20 GHz. The solar corona is usually measured at frequencies of 2 GHz and below [86].
The application of a ST microwave radiometry technique for the retrieval of the atmospheric properties was envisaged in early works to complement Sun observations with radio telescopes [94]. In the seventies Hogg and Chu [95] proposed the ST technique as an independent way to measure rain attenuation with a good dynamic range. Shimada et al. [96] proposed a method to provide clear-sky absorption statistics. The potential of ground-based MW radiometry in radiopropagation and remote sensing applications has been also demonstrated by Marzano et al. [80], [97], who proposed to develop and validate retrieval models for estimating the total atmospheric extinction due to precipitation and its associated rainfall rate [98]-[100]. However, the difficulty to assess the capability of ground-based MW radiometry for atmospheric parameter estimation is typically linked to the lack of collocated beacon measurements at the same observation frequency [101]. In this respect, ST microwave radiometry is a self-consistent approach

where atmospheric path attenuation estimates can be also verified in almost all weather conditions and even in the unexplored range of millimeter and sub-millimeter wavelengths.

The Sun-tracking operation mode considers a constant elevation angle (θ in Figure 3-1) between two relatively close TB measurements, which are taken only varying the azimuth angle by first pointing the antenna toward the Sun source (φ_1 in Figure 3-1) and then measuring the atmospheric contribution without the Sun (φ_2 in Figure 3-1) [127]. A value at elevation θ is retrieved exploiting the difference between the brightness temperature toward the Sun and one without the Sun. This operation mode allows removing possible brightness temperature biases when atmospheric optical thickness is estimated.

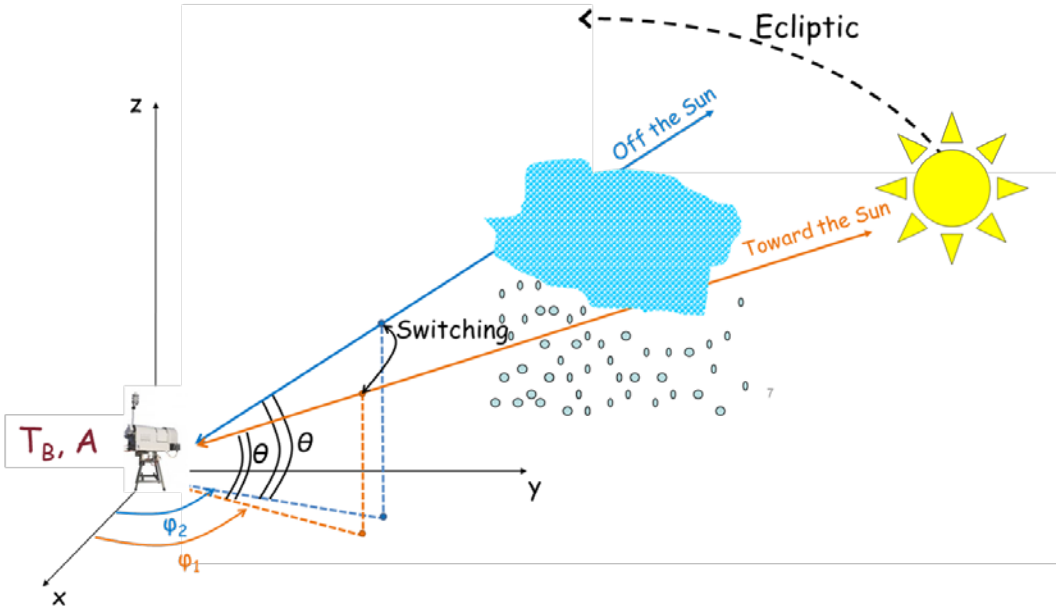

Figure 3-1: ST-MWR operation: the radiometer tracks the Sun during its motion considering a constant elevation angle θ between two close measurements taken varying the azimuth from toward-the-Sun φ_1 to off-the-Sun φ_2.

Few operational ST multi-frequency microwave radiometers are currently operational. One of these is the system installed in Rome (NY, USA) at Air Force Research Laboratory (AFRL) [117]. This AFRL Sun-tracking microwave radiometer (ST-MWR) has four channels with receivers at K band (23.8 GHz), Ka (31.4 GHz), V band (72.5 GHz) and W band (82.5 GHz) and is a modified version of a commercial water-vapor and cloud-liquid microwave radiometer series, to allow an automatic Sun-switching and tracking operation mode. A unique relatively long dataset has been collected by the AFRL Sun-tracking MWR in 2015. These data represent an opportunity to test ground-based single-antenna ST for both radio astronomy and radiopropagation. Moreover, as an additional application, ST microwave radiometry can be used as a system calibration tool to determine receiving systems noise temperature [102] as well as antenna boresight pointing errors [103].

This chapter has several purposes: i) to summarize the basics of ST microwave radiometry and investigate the issues of antenna pattern beam-filling, error sensitivity and expected limitations; ii) to illustrate the data processing of the AFRL available measurements in 2015 and the need to apply proper radiometric approaches to exploit ST potential; iii) to estimate the brightness temperature of the Sun at K, Ka, V and W band using the collected dataset at AFRL in 2015 and comparing with available radio astronomical data; iv) to propose the parametric retrieval of the atmospheric extinction at K, Ka, V and W band due to precipitating clouds and validating it with ST measurements in different weather conditions.
The sub-chapter is structured as follows. In Section 3.II.A two different techniques, based on elevation scanning and surface meteorological data, are rigorously proposed to estimate the Sun brightness temperature and the atmospheric extinction from ST-MWR measurements. Section 3.II.B is devoted to the description, quality control and processing of the available ST-MWR data. Section 3.II.C describes the application of the two methodologies for the Sun brightness temperature estimate and discusses the results. Section 3.II.D shows the retrieval of atmospheric extinction in cloudy and precipitating conditions. Sensitivity and error budget analyses are carried out in the Appendix A, with respect to antenna pattern, beam filling, atmospheric attenuation uncertainties, and instrument spectral response.

Appendix B shows an application of Sun-Tracking radiometry by inter-comparing measurements with several radiative transfer simulation sources. The objective is to characterize the atmospheric radiometeorological parameters (optical thickness and brightness temperature) at centimeter and millimeter waves. To this aim, we have exploited two radiative transfer models: a 3-dimensional model (3D-RTM), driven by numerical weather forecasts, and a stochastic 1-dimensional model (1D-RTM), fed by a synthetic clouds dataset. We have compared the radiative transfer simulations with measurements from two ground-based microwave radiometers: a profiler and a Sun-tracking radiometer. The comparisons between simulations and measurements provide satisfactory results that assess the reliability of the 3D-RTM with some biases, in terms of brightness temperature, that should be investigated. 3D-RTM turns out to be able to successfully reproduce correlations between brightness temperature and optical thickness and correlations among the different frequency channels. This confirms the potential of the combined use of weather forecast models and physically-based radiative transfer models. On the other hand, 1D-RTM reveals to be able to reproduce frequency-channel correlation trends, though additional climatological set-up are needed to make the model exploitable for the computation of statistics of atmospheric optical thickness. These comparisons also highlight some possible calibration errors in the Sun-tracking radiometer that must be fixed.

3. II.A. Theoretical background

Considering ground-based observations, the measured antenna noise temperature T_A along the radiometer antenna pointing angle (θ_0, φ_0) is the convolution between the received sky brightness temperature and the normalized antenna power radiation pattern $F_n(\theta_0, \varphi_0, \theta, \varphi)$ [24]:

$$T_A(\theta_0, \varphi_0) = \frac{\int_{4\pi} T_B(\theta, \varphi) F_n(\theta_0, \varphi_0, \theta, \varphi) d\Omega}{\int_{4\pi} F_n(\theta_0, \varphi_0, \theta, \varphi) d\Omega} \quad (3.II.1)$$

With

$$\int_{4\pi} F_n(\theta_0, \varphi_0, \theta, \varphi) d\Omega = \Omega_{Pant} \tag{3.II.2}$$

where Ω_{Pant} is the antenna radiation-pattern solid angle. All the involved parameters are also dependent on frequency, which is neglected in the formulations in favor of geometric considerations.
When pointing out-of-the-Sun (ooS), the sky brightness temperature T_{BooS}, impinging upon the antenna along the zenith angle θ and azimuth φ [24], can be written as

$$T_{BooS}(\theta, \varphi) = T_{mr}(\theta, \varphi)\left[1 - e^{-\tau(\theta,\varphi)}\right] + T_{cos} e^{-\tau(\theta,\varphi)} \tag{3.II.3}$$

where T_{mr} is the sky mean radiative temperature (that can be defined in all-weather conditions [101], [79]), τ is the atmospheric optical thickness (in Neper) and T_{cos} is the brightness temperature of the cosmic background (equal to about 2.73 K).
When pointing at the Sun, the toward-the-sun (twS) sky brightness temperature T_{BtwS} is given by the sum of two components, the Sun brightness temperature T_{Bsun}, attenuated by the atmosphere, and the brightness temperature of the sky

$$T_{BtwS}(\theta, \varphi) = T_{Bsun} e^{-\tau(\theta,\varphi)} + T_{mr}(\theta, \varphi)\left[1 - e^{-\tau(\theta,\varphi)}\right] + T_{cos} e^{-\tau(\theta,\varphi)} \tag{3.II.4}$$

According to (3.II.1), the computation of the antenna noise temperature T_{AtwS}, measured observing the Sun, implies that the T_{BtwS} is observed by the antenna within the solid angle Ω_{sun} subtended by the Sun. Therefore, it holds:

$$\begin{aligned} T_{AtwS}(\theta_0, \varphi_0) = \frac{1}{\Omega_{Pant}} \int_{\Omega_{sun}} & \left[T_{Bsun} e^{-\tau(\theta,\varphi)} + T_{mr}(\theta, \varphi)\left(1 - e^{-\tau(\theta,\varphi)}\right)\right. \\ & \left. + T_{cos} e^{-\tau(\theta,\varphi)}\right] F_n(\theta_0, \varphi_0, \theta, \varphi) d\Omega \\ + \frac{1}{\Omega_{Pant}} \int_{4\pi - \Omega_{sun}} & \left(T_{mr}(\theta, \varphi)\left[1 - e^{-\tau(\theta,\varphi)}\right] + T_{cos} e^{-\tau(\theta,\varphi)}\right) \\ & \cdot F_n(\theta_0, \varphi_0, \theta, \varphi) d\Omega \end{aligned} \tag{3.II.5}$$

which can be rewritten as

$$\begin{aligned} T_{AtwS}(\theta_0, \varphi_0) = & \frac{1}{\Omega_{Pant}} \int_{\Omega_{sun}} T_{Bsun} e^{-\tau(\theta,\varphi)} \cdot F_n(\theta_0, \varphi_0, \theta, \varphi) d\Omega \\ & + \frac{1}{\Omega_{Pant}} \int_{4\pi} \left(T_{mr}(\theta, \varphi)\left[1 - e^{-\tau(\theta,\varphi)}\right] + T_{cos} e^{-\tau(\theta,\varphi)}\right) F_n(\theta_0, \varphi_0, \theta, \varphi) d\Omega \end{aligned} \tag{3.II.6}$$

It is useful to introduce the beam-filling factor f_Ω as the ratio between the Sun radiation-pattern solid angle Ω_{Psun} and the antenna beamwidth radiation-pattern solid angle Ω_{Pant}, it holds

$$f_\Omega = \frac{\int_{\Omega_{sun}} F_n(\theta_0, \varphi_0, \theta, \varphi) d\Omega}{\Omega_{Pant}} = \frac{\Omega_{Psun}}{\Omega_{Pant}} \tag{3.II.7}$$

In ground-based radiometry, it is also commonly assumed that the atmospheric contribution is constant within the main beam and T_{AooS} is approximated by the T_{BooS} at (θ_0, φ_0). If it is assumed that the Sun has a uniform brightness temperature within the beam (e.g., Ω_{sun} is much smaller than the antenna main beam half-power solid angle), then, using (3.II.7), we can approximate (3.II.6) as

$$T_{A_{twS}}(\theta_0, \varphi_0) \cong f_\Omega T_{Bsun} e^{-\tau(\theta_0, \varphi_0)} + T_{mr}(\theta_0, \varphi_0)\left[1 - e^{-\tau(\theta_0, \varphi_0)}\right] + T_{cos} e^{-\tau(\theta_0, \varphi_0)} \tag{3.II.8}$$

Analogously, for the ooS mode, we can simplify

$$\begin{aligned} T_{AooS}(\theta_0, \varphi_1) &= \frac{1}{\Omega_{Pant}} \int_{4\pi} \left(T_{mr}(\theta, \varphi)\left[1 - e^{-\tau(\theta, \varphi)}\right] + T_{cos} e^{-\tau(\theta, \varphi)}\right) F_n(\theta_0, \varphi_1, \theta, \varphi) d\Omega \\ &\cong T_{mr}(\theta_0, \varphi_1)\left[1 - e^{-\tau(\theta_0, \varphi_1)}\right] + T_{cos} e^{-\tau(\theta_0, \varphi_1)} \end{aligned} \tag{3.II.9}$$

In the ST technique, the radiometer antenna is pointing alternatively on and off the Sun, and between these two measurements, the elevation angle θ_0 is kept constant, while the azimuth angle is switched from φ_0 (twS) to φ_1 (ooS). Then, after a few observations, the elevation angle is varied, in accordance with the Sun movement along its diurnal ecliptic.
The ST antenna noise temperature difference for each pointing angle can then be expressed by:

$$\Delta T_A(\theta_0, \varphi_0, \varphi_1) = T_{AtwS}(\theta_0, \varphi_0) - T_{AooS}(\theta_0, \varphi_1) \tag{3.II.10}$$

If the switching between ooS and twS observation modes is fast enough and the azimuth distance is chosen so that the Sun is just outside the field of view of the instrument, it can be assumed that the mean radiative temperature and optical thickness do not change between the two observation modes (i.e. $T_{mr}(\theta_0, \varphi_0) \cong T_{mr}(\theta_0, \varphi_1)$ and $\tau(\theta_0, \varphi_0) \cong \tau(\theta_0, \varphi_1)$). Substituting (3.II.8) and (3.II.9) into (3.II.10) we obtain:

$$\Delta T_A(\theta_0, \varphi_0) \cong f_\Omega T_{Bsun} e^{-\tau(\theta_0, \varphi_0)} \tag{3.II.11}$$

The previous equation gives the basis for estimating T_{Bsun} and the atmosphere path attenuation, as described in the following subsections.

➢ *Estimation of Sun brightness temperature in clear sky*

During clear-sky conditions, the ST technique can be used to estimate the brightness temperature T_{Bsun} emitted by the Sun. Two different approaches can be applied: i) the Langley elevation-based self-consistent method and ii) the Tmr-based meteorologically-oriented method. Both methods are

able to provide reliable results with the availability of radiometric measurements in clear air conditions, when T_{Bsun} estimates are less affected by the atmosphere variability. In both methods, a plane-parallel horizontally stratified and azimuthally homogeneous atmosphere is assumed and the "secant law" is applied to describe the elevation angle dependence of the optical thickness.
The Langley technique is commonly used in sun-photometry for determining the Sun radiance at the top of the atmosphere with ground-based instruments [81], [85]. It exploits the antenna noise temperature difference in (3.II.11) according to:

$$ln[\Delta T_A(\theta_0)] = \ln[f_\Omega T_{Bsun}] - \tau(\theta_0) = \ln[T^*_{Bsun}] - \tau_z\, m(\theta_0) \tag{3.II.12}$$

where T^*_{Bsun} is the brightness temperature of the Sun weighted by the filling factor f_Ω and $m(\theta_0)$ stands for atmospheric air mass, equal to $sec(\theta_0)$. Under the plane-parallel atmosphere assumption, it holds that $ln[\Delta T_A(\theta_0)]$ is linearly dependent on the air mass $m(\theta_0)$ and we can estimate T^*_{Bsun} through the exponential of the intercept of the linear best-fitting curve. Finally, exploiting the beam-filling factor f_Ω, as given in (3.II.7), the sun brightness temperature T_{Bsun} is computed:

$$ln[\Delta T_A(\theta_0)] = a + b\, m(\theta_0) \;\rightarrow\; T_{Bsun} = \frac{T^*_{Bsun}}{f_\Omega} = \frac{\exp(a)}{f_\Omega} \tag{3.II.13}$$

The meteorological technique is based on the radiometer equation (3.II.9) in clear air [81], [117]. In a horizontally-stratified clear air, we can obtain the atmospheric extinction $\tau(\theta_0)$ according to:

$$\tau(\theta_0) = \ln\left[\frac{T_{mr}(\theta_0) - T_{cos}}{T_{mr}(\theta_0) - T_{AooS}(\theta_0)}\right] \tag{3.II.14}$$

In (3.II.14), the mean radiating temperature T_{mr} of the atmosphere is needed. It can be interpolated from concurrent radiosonde observation (RaOb) or estimated directly from surface temperature T_s, pressure p_s and relative humidity RH_s in clear air [104]-[105]. Details on the computation of the T_{mr} are given later in this section. From (3.II.11), using the ST measurements, the Sun brightness temperature is computed according to:

$$T_{Bsun} = \frac{T^*_{Bsun}}{f_\Omega} = \frac{1}{f_\Omega}\left(\Delta T_A(\theta_0) \cdot e^{\tau(\theta_0)}\right) \tag{3.II.15}$$

Note that, with respect to the Langley technique, which provides one estimate from the fitted regression line, the meteorological technique provides a time series of T_{Bsun}.
In order to compute T_{Bsun}, the filling factor f_Ω in (3.II.7) must be evaluated. Note that the Sun radiation-pattern solid angle Ω_{Psun} can be computed according to (3.II.7):

$$\Omega_{Psun} = \int_{\Omega_{sun}} F_n(\theta_0, \varphi_0, \theta, \varphi)\, d\Omega \tag{3.II.16}$$

A typical assumption is that $F_n(\theta_0, \varphi_0, \theta, \varphi) \cong 1$ over Ω_{sun}, so that the effect of the radiometer antenna pattern can be neglected. In this case the filling factor is given by $f_\Omega \cong \Omega_{sun}/\Omega_{ant}$ being $\Omega_{Psun} \cong \Omega_{sun}$. The Sun solid angle Ω_{sun} can be then obtained from:

$$\Omega_{sun} \cong \frac{\pi}{4}\Theta_{sun}^2 \cong \frac{\pi r_{sun}^2}{R_{ES}^2} \tag{3.II.17}$$

where r_{sun} is the radius of the Sun, approximated as a circular disk, and R_{ES} is the Earth-Sun average distance, and Θ_{sun} is the zenithal-plane angle subtended by the Sun. The last right-hand side term of (3.II.17) is obtained by approximating the solid angle as the ratio between the object cross area and its square distance.
However, if the antenna beamwidth cross-section is comparable with the diameter of the Sun, such assumption is no longer valid. To account for it, a Gaussian shape has been used to model the radiometer antenna normalized pattern F_{nML} main beam, as suggested by the radiometer manufacturer [106]. Thus, we can express F_{nML} as [111]:

$$F_{nML}(\theta, \varphi) = e^{-\ln(2)\left(2\frac{\theta}{\Theta_{\mathrm{ML}}}\right)^2} \tag{3.II.18}$$

where Θ_{ML} is the half-power beamwidth of the antenna main beam. Then, assuming $sin\theta \cong \theta$:

$$\Omega_{Psun} = \int_0^{2\pi}\int_0^{\frac{\Theta_{sun}}{2}} F_{nML}(\theta, \varphi)\, sin\theta d\theta d\varphi \;\cong \frac{\pi}{4\ln(2)}\Theta_{\mathrm{ML}}^2\left[1 - e^{-\ln(2)\left(\frac{\Theta_{sun}}{\Theta_{\mathrm{ML}}}\right)^2}\right] \tag{3.II.19}$$

The antenna radiation-pattern solid angle Ω_{Pant} can be obtained from (3.II.2) by considering the antenna main beam efficiency η_{ML} and calculating the antenna main lobe radiation-pattern solid angle Ω_{PML} for the Gaussian-shape beam in (3.II.18):

$$\begin{aligned}\Omega_{Pant} &= \frac{\Omega_{PML}}{\eta_{ML}} = \frac{\int_{4\pi} F_{nML}(\theta, \varphi) d\Omega}{\eta_{ML}} \cong \frac{1}{\eta_{ML}}\frac{\pi}{4\ln(2)}\Theta_{\mathrm{ML}}^2\left[1 - e^{-\ln(2)\left(\frac{2\pi}{\Theta_{\mathrm{ML}}}\right)^2}\right] \\ &\cong \frac{1}{\eta_{ML}}\frac{\pi}{4\ln(2)}\Theta_{\mathrm{ML}}^2\end{aligned} \tag{3.II.20}$$

where η_{ML} is defined as the ratio between the main lobe radiation solid angle and the antenna one. It is possible to neglect the exponential term for Θ_{ML} values up to 20°.
Summarizing, the expression of the filling factor f_Ω is obtained from the following expression:

$$f_\Omega = \eta_{ML}\left[1 - e^{-\ln(2)\left(\frac{\Theta_{sun}}{\Theta_{\mathrm{ML}}}\right)^2}\right] \tag{3.II.21}$$

using (3.II.19) and (3.II.20). The possible effects of antenna pattern side lobes are modeled and discussed in the Appendix A.

➢ *Atmospheric extinction in precipitating clouds*

Starting from (3.II.11), provided that estimates of T^*_{Bsun} are available for instance from ST measurements obtained during clear sky, the extinction A_{ST} (in dB) in all weather conditions can be retrieved from the ΔT_A differences between ooS and twS measurements, according to

$$A_{ST}(\theta_0, \varphi_0) = 4.343\ \tau(\theta_0, \varphi_0) = 4.343 \ln\left[\frac{T^*_{Bsun}(\theta_0, \varphi_0)}{\Delta T_A(\theta_0, \varphi_0)}\right] \tag{3.II.22}$$

In the presence of clouds or precipitation, as the atmospheric extinction significantly increases, the Sun signal is also increasingly attenuated, and therefore the antenna noise temperature difference between the two measurement modes ooS and twS decreases. For heavy precipitation, the contribution of the Sun is completely masked by the rain attenuation and the ΔT_A differences are only dependent on the radiometer noise and the atmosphere variability, providing an upper limit to the application of the technique for the retrieval of rain attenuation [80].

3. II.B. Measurement Dataset

The available dataset consists of 163 days of measurements collected by the ground-based AFRL ST-MW radiometer from May to October 2015 in Rome, NY, USA (43.2°N, 75.4°W) at angles between 20° and 70°. The AFRL ST-MWR has four channels with receivers at 23.8, 31.4, 72.5 and 82.5 GHz and is a modified version of the RPG LPW-U72-82 water-vapor and cloud-liquid microwave radiometer [106], [112]. It is provided with an azimuth positioner allowing a scan step of 0.15° in elevation and 0.1° in azimuth. The track of the Sun along the ecliptic is based on input data (latitude, longitude, time) and it is performed in a Sun-switching operation mode, keeping the elevation angle θ_0 constant, and varying the azimuth angle from φ_0 (twS) to φ_1 (ooS) according to (3.II.10). The integration time of each measurement is set to 1 second and the azimuth positioner switches every 6 seconds in order to perform the integration with fixed antenna position. The worst-case root-mean-square noise of 0.15 K is to be expected for a scene temperature of 300 K, assuming the overall bandwidth of 230 MHz and 1 second integration time. Therefore, 1-second integration time is enough for our purposes. One could theoretically integrate for up to 5-6 seconds (elevation and azimuth angles are constant for about 6 seconds), however it is not recommended since the Sun's position could vary within the mentioned interval. The processing and quality-control procedures applied to the radiometer data are described in the following.

➢ *Clear-air data discrimination*

Both Langley and meteorological techniques need measurements in clear-sky to estimate T_{Bsun}. The discrimination has been carried out through a scalar quantity named Status Sky Indicator (SSI), purely based on the measured brightness temperatures. The method has been successfully applied in several applications with ground-based radiometers [113],[114]. SSI is defined as

$$SSI(\theta_0) = \frac{T_{AooS(31.4\ GHz)}(\theta_0) - c(\theta_0)}{T_{AooS(23.8\ GHz)}(\theta_0)} \tag{3.II.23}$$

with

$$c(\theta_0) = -0.13\, m^2 \; + \; 6.3\, m \; + \; 2.1 \tag{3.II.24}$$

where c is a parameter dependent on air mass $m \; = sec(\theta_0)$ and θ_0 is the elevation angle. A clear air condition is assumed if SSI is less than a given threshold SSI_{th} given by

$$SSI_{th}(\theta_0) = -0.00012\, m^2 \; + \; 0.0066\, m \; + \; 0.31 \tag{3.II.25}$$

A clear-sky day is assumed if the number of measurements for which the SSI value is below the threshold is larger than the 98% of available samples (neglecting the non-clear-air samples in the T_{Bsun} estimation).
Table 3-1 details the available measurement dataset providing a monthly classification in terms of clear, cloudy and rainy days. The clear-air days have been identified by using the SSI criterion as described before, whereas the discrimination of rainy days has been carried out by looking at the rain flag directly provided by the radiometer.

TABLE 3-1: MONTHLY CLASSIFICATION OF CLEAR, CLOUDY AND RAINY DAYS DURING AFRL ST-MWR AVAILABLE MEASUREMENTS

MONTH	CLEAR	CLOUDY	RAINY	TOTAL
May 2016	5	13	4	22
June 2016	0	19	10	29
July 2016	2	22	7	31
August 2016	0	21	6	27
September 2016	1	21	8	30
October 2016	7	12	5	24

➢ *Radiosounding dataset*

SSI parameterization in (3.II.23) has been set up by performing radiative transfer simulations of brightness temperatures at 23. 8 and 31.4 GHz at several elevation angles applied to a long-term available radiosonde observation (RaOb) dataset. The closest RaOb site to Rome, NY, is located at Albany County Airport, NY, USA (WMO station ID code 72518, WBAN ID code 14735), about 140 km from the radiometer. RaOb data belonging to the period 1994-2012 have been collected for this study. Downwelling brightness temperatures have been generated using a plane parallel radiative transfer equation (RTE) scheme [115] with an updated version of Rosenkranz [56] for gas absorption and a cloud model as given in [116].
The RaOb dataset has been also used to generate corresponding mean radiating temperatures T_{mr} at the same frequencies and angles. Monthly regression coefficients for each frequency and angle were computed to relate T_{mr} values to the surface temperature T_s, pressure p_s and relative humidity RH_s provided by the radiosondes:

$$T_{mr}(\theta_0) = a_0(\theta_0) + a_1(\theta_0)T_s + a_2(\theta_0)p_s + a_3(\theta_0)RH_s \tag{3.II.26}$$

where the regression coefficients a_i are dependent on the elevation angle θ_0 (one set for each considered frequency). Finally, the regression coefficients have been fitted with respect to air mass m to provide the final coefficients a_i. Those coefficients were then applied to the concurrent surface measurements from the meteorological sensors that are part of the radiometer equipment.

➢ *Filtering toward-the-Sun observations in clear air*

The maximum $T_{A_{twS}}$ values were held on for each elevation angle to compute T_{Bsun} with both Langley and Meteorological technique. AFRL-MWR sun-tracking mode maintains a constant elevation for a certain time and the Sun does not remain stationary during that period. The best matching observation corresponds to the maximum value, where the Sun disk is centered with respect to the antenna beamwidth. Only for the Langley technique, a binning average with respect to air mass (steps of 0.1) was performed to achieve an equal distribution of samples with airmass and not to influence the linear regression in (3.II.13).

➢ *Evaluation of antenna beamwidth*

The AFRL MWR antenna is a feed-horn/parabola system shaped to reduce the sidelobes to less than -30 dB at K-band and less than -40 dB at V and W band [106]. The antenna radiation pattern results approximately Gaussian, following the approximation given in (3.II.18). In order to evaluate the filling factor in (3.II.21), both the Sun disk angle Θ_{sun} and the half-power beamwidth $\Theta_{3\mathrm{dB}}$ values must be retrieved [117]. Higher accuracy is needed in knowing Θ_{ML} exact values with respect to the ones provided by RPG LPW-U72-82 technical specifications (3.7°, 3.3°, 1.3° and 1.3°, at 23.8, 31.4, 72.5 and 82.5 GHz, respectively). The radiation pattern has been measured by scanning the radiometer across the Sun, i.e. letting the Sun drift across the radiometer path. From the known ephemeris, it has been possible to determine the relative angular position of the sun assuming a uniform disk Θ_{sun} of 0.533° arch. Finally, the measured brightness temperatures have been fit to a Gaussian profile convolved with the sun to obtain Θ_{ML} measurements for each frequency. The AFRL full-width half-power beamwidth values are equal to 3.74°, 2.97°, 1.47°, and 1.30° at 23.8, 31.4, 72.5 and 82.5 GHz, respectively with a main beam efficiency η_{ML} of 0.969 at Ka band and 0.979 at V and W band [108]. In appendix A, detailed theoretical sensitivity analysis and error budget have been reported, with particular emphasis on side lobe contributions.

3. II.C. Sun brightness temperature estimates

The analysis of the measured antenna noise temperature time series can give an insight on the ST concept and MW radiometric data behavior. Figure 3-2 shows the time series of ST T_A measurements of both ooS (lower curves) and twS (upper curves) for the case study of October 10, 2015 at the four AFRL-MWR available frequencies. The trend observed at 23.8 and 31.4 GHz with respect to time and so to elevation (Figure 3-2a) is similar for both T_{AooS} and $T_{A_{twS}}$: at the beginning of the daily Sun-tracking, higher T_A values are observed at low elevation due to a larger atmospheric contribution, reaching their minimum at the solar noon (i.e. maximum tracking elevation).

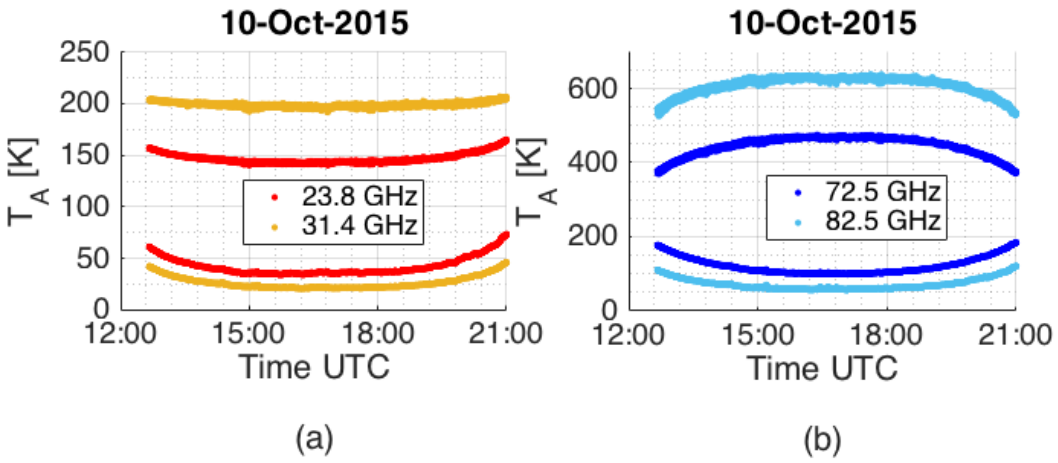

Figure 3-2: Time series of ST-MWR measurements in terms of antenna noise temperatures for a case studies referring to a clear air (October 10, 2015) at the 4 AFRL-MWR available frequencies: a) 23.8 and 31.4 GHz; b) 72.5 and 85.5 GHz.

In Figure 3-2b, the time series at 72.5 and 82.5 GHz show an opposite trend with elevation for T_{AooS} and $T_{A_{twS}}$, with the latter reaching their maximum values at the solar noon. Such behavior is explained by recalling (3.II.8) and the increasing impact of T^*_{Bsun} contribution at K, Ka and V, W band, because of the increasing filling factor f_Ω. At K and Ka band, the atmospheric contribution with air mass still dominates over that one due to the Sun, whereas in V and W band it is the reverse. The behavior in the presence of clouds or precipitation is described in Section II.D.
Figure 3-3 shows the estimate of T^*_{Bsun} using the Langley technique for each frequency and for the case study of October 10, 2015, exploiting the natural logarithm of the antenna noise temperature difference versus air mass. The fitted linear regressions are shown as black dashed lines, and R-squared statistics are also given. As discussed in Section II.A, T^*_{Bsun} is computed according to (3.II.13) from the intercept of the fitted line, while the slope is an estimate of the daily average atmospheric zenith extinction. Figure 3-4 shows the estimate of T^*_{Bsun} for October 10, 2015, by using the meteorological technique for each frequency. The average values of T^*_{Bsun} are also shown as black dashed lines.

Daily T^*_{Bsun} estimates obtained by the two techniques for all the available clear-sky dataset are given in Table 3-2. Then, T_{Bsun} values were computed by dividing those estimates by the Sun filling factor f_Ω. The average estimates for both T^*_{Bsun} and T_{Bsun} are given in Table 3-3. The values of the estimated beam filling factors are also reported; these were computed using AFRL-derived values described in Section II.B.
Table 3-4 reports minimum and maximum deviations with respect to the daily mean of the fifteen examined clear-air days for both techniques. A standard deviation over the daily time series has been carried out to provide the Meteorological technique deviation. To put deviations on a comparable scale, the Langley deviations have been computed supposing a Normal-distributed percentile associated to the linear regression in (3.II.13). By evaluating the 68.27% confidence intervals we are able to obtain deviation values equivalent to the Meteorological ones.

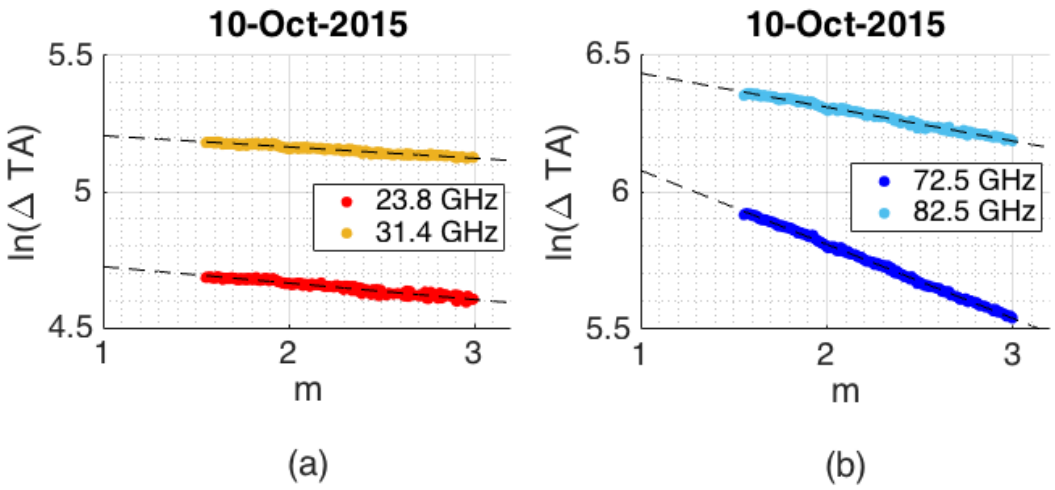

Figure 3-3: Application of the Langley technique to estimate T^*_{Bsun} (128 samples equally spaced in terms of air mass), as discussed in sect. II.B, for each frequency on October 10, 2015: a) 23.8 (R^2=0.9367) and 31.4 GHz (R^2=0.9630); b) 72.5 (R^2=0.9984) and 85.5 GHz (R^2=0.9909).

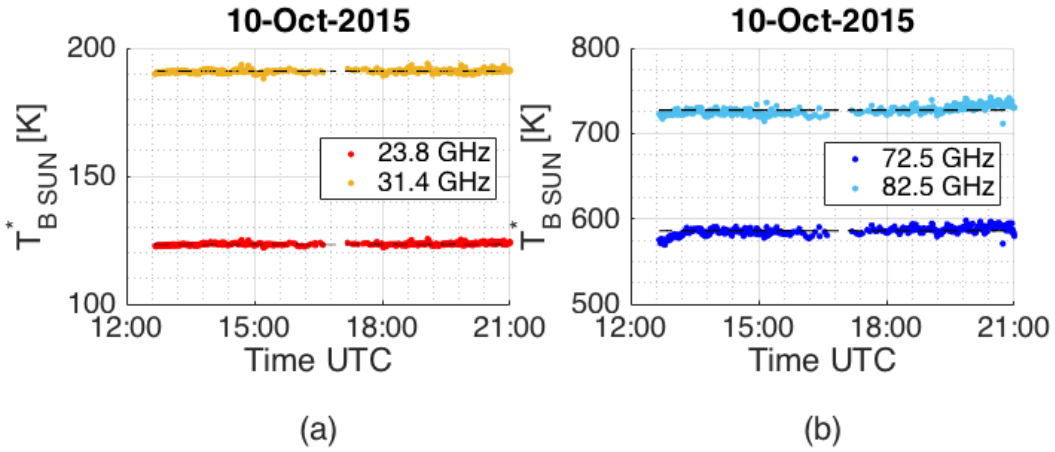

Figure 3-4: Estimates of T^*_{Bsun} using the meteorological technique for each frequency on October 10, 2015.

TABLE 3-2: LANGLEY AND METEOROLOGICAL DAILY ESTIMATES OF T^*_{Bsun}

LANGLEY T^*_{Bsun}[K]

	23.8 GHz	31.4 GHz	72.5 GHz	82.5 GHz
06/05/15	121.70	185.99	590.18	745.83
08/05/15	120.54	182.17	573.24	716.34
21/05/15	122.16	184.11	578.43	727.40
23/05/15	120.71	182.49	563.58	703.72
24/05/15	117.69	179.05	545.31	681.66
03/07/15	122.04	181.61	559.67	710.62
16/07/15	118.18	178.29	566.02	711.41
26/09/15	122.19	191.52	586.17	729.72
02/10/15	122.45	189.36	578.12	706.84
08/10/15	122.59	193.28	586.96	727.22
10/10/15	119.79	189.91	571.63	702.97
11/10/15	122.56	193.01	587.58	728.51
15/10/15	122.70	192.86	587.14	727.15
23/10/15	120.76	186.50	572.84	698.24
26/10/15	121.74	188.88	582.65	712.93

METEOROLOGICAL T^*_{Bsun}[K]

	23.8 GHz	31.4 GHz	72.5 GHz	82.5 GHz
06/05/15	124.05	189.68	564.22	704.09
08/05/15	121.64	185.33	570.65	710.55
21/05/15	119.84	184.21	571.80	709.88
23/05/15	119.66	184.29	570.71	707.81
24/05/15	119.62	183.63	567.61	707.61
03/07/15	120.44	184.48	565.26	705.74
16/07/15	119.74	184.19	564.30	703.32
26/09/15	123.86	191.05	589.66	730.19
02/10/15	124.26	190.89	592.92	723.28
08/10/15	123.59	191.30	582.63	726.86
10/10/15	123.47	190.93	585.69	727.18
11/10/15	124.56	192.41	593.56	734.70
15/10/15	124.56	191.80	581.76	729.38
23/10/15	124.17	190.58	602.84	735.99
26/10/15	123.77	190.03	586.08	726.32

When comparing the Langley and the meteorological methods, we note that they provide very similar results. Differences exist because of the assumptions underlying their applicability. In the Langley technique, the daily attenuation variability affects the slope estimations and in turns the intercept (ideally, it should be independent as air mass is extrapolated to zero). As such, only the most stable days in clear-sky can be used for the estimate. Conversely, the meteorological technique has fewer constraints, with the price that it provides much larger uncertainty to the associated average value. The advantage of the Langley technique is that it is a stand-alone method, without the need of resorting to RTE models or the need of additional ancillary measurements.

TABLE 3-3: LANGLEY AND METEOROLOGICAL AVERAGE ESTIMATE INTER-COMPARISON

		Langley		Meteorological	
f [GHz]	f_Ω	T^*_{Bsun}[K]	T_{Bsun}[K]	T^*_{Bsun}[K]	T_{Bsun}[K]
23.8	0.0136	121.19	8942	122.48	9037
31.4	0.0214	186.60	8719	188.32	8799
72.5	0.0853	575.30	6741	579.31	6788
82.5	0.1078	715.37	6638	718.86	6670

TABLE 3-4: LANGLEY AND METEOROLOGICAL ESTIMATE DEVIATIONS INTER-COMPARISON

	Langley deviation		Meteorological deviation	
f [GHz]	Min [K]	Max [K]	Min [K]	Max [K]
23.8	0.30	0.91	0.48	1.19
31.4	0.31	0.82	0.70	1.90
72.5	1.22	5.57	3.05	11.34
82.5	1.62	8.97	4.34	16.33

The estimated T_{Bsun} values decrease with increasing frequency ranging from about 9000 K down to about 6600 K. These values are consistent with those from radiotelescope observations [89], [102], and models [118]. T_{Bsun} values at W band agree with a radiation originating from the Sun lower chromosphere. In particular, K-band measurements are available in previous researches: i) comparing the result at 23.8 GHz in Table 3-3 with respect to the results at 20.7 GHz in [109] and [110], we have obtained percentage deviations of 14.2% and 20.9%, respectively; ii) comparing the result at 31.4 GHz in Table 3-3 with respect to the results at the same frequency in [109] and [110], we have obtained percentage deviations of 4.0% and 11.7%, respectively. It is pointed out here that in the ST technique, at frequencies above 10 GHz, the Sun appears as a rather uniform disk [86] and the solar activity in our observations has little effect due to a large field of view of the radiometer antenna main-beam. Therefore, the Sun can be considered as a constant source in our application, apart from multi-year solar cycles.

3. II.D. Extinction estimates in precipitating clouds

Sun brightness temperatures have been set to fixed values according to Table 3-3, in particular the Langley results have been taken into account during the following analysis.
Figure 3-5 shows the time series of the ST-MWR measurements of both *ooS* (lower curves) and *twS* (upper curves) antenna noise temperatures for the case study of September 29, 2015 at the four AFRL-MWR available frequencies. With respect to the clear-sky case shown in Figure 3-2, it is shown how in the presence of clouds or precipitation, the brightness temperature difference between the two measurement modes *ooS* and *twS* decreases as the atmospheric extinction significantly increases, this behavior being more dominant at V and W band than at K and Ka band. Indeed, the *ooS* brightness temperature increases because of the contributing emission from clouds and precipitation while correspondingly the Sun signal is attenuated in the *twS* brightness temperature. The decrease in T_A due to the cloudy/rainy atmosphere is clearly evident at V- and W-band, where the Sun provides the larger contribution (also due to the difference in beam filling factors, much smaller at V- and W-band). Conversely at K band, where the atmosphere signal is also providing a strong contribution, the *twS* noise temperatures also increases, although with less impact.

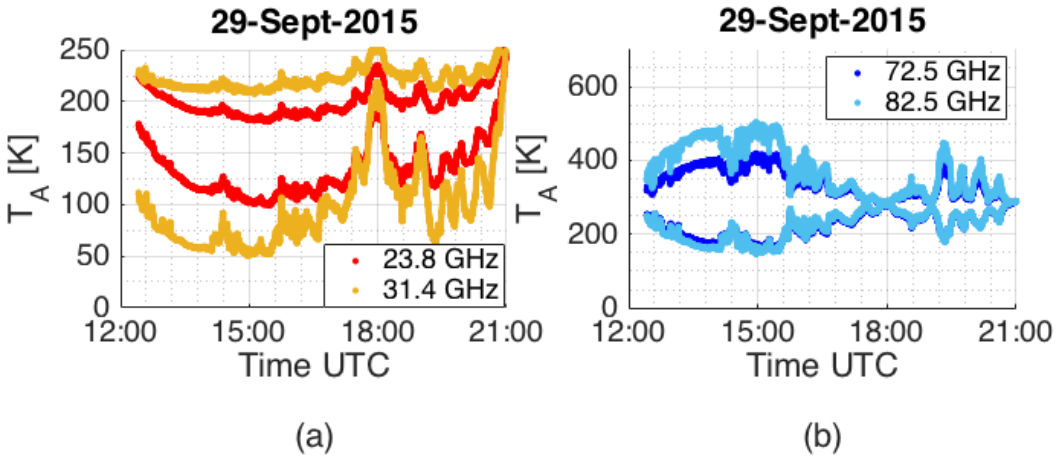

Figure 3-5: Time series of ST-MWR measurements in terms of antenna noise temperatures for a case studies in presence of clouds or precipitation (29 September 2015) at the 4 AFRL-MWR available frequencies: a) 23.8 and 31.4 GHz; b) 72.5 and 85.5 GHz.

The ST-MW radiometry technique is able to estimate a valid atmospheric extinction, according to (3.II.22), only if consistent antenna noise temperature differences are available. During intense rain events ΔT_A differences can reach zero or even negative, which limits the application of this technique. The maximum atmospheric extinction value A_{STmax} depends on both considered frequency and standard deviation std(ΔT_A) and it can be computed from (3.II.22). By considering a measurement deviation equal to the MW radiometric brightness temperature absolute accuracy (equal to 0.5 K at K-band and 1 K at W-band), we can evaluate the standard deviation (std) of the noise temperature difference from (3.II.10) according to:

$$\mathrm{std}(\Delta T_A) = \sqrt{\mathrm{var}(T_{AooS}) + \mathrm{var}(T_{AtwS})} \tag{3.II.27}$$

where "var" stands for the noise variance equal to the square of the absolute accuracy. By properly substituting $\mathrm{std}(\Delta T_A)$ values (0.7 at K and Ka band and 1.4 at V W band) in (3.II.22), the maximum atmospheric extinction values result about 22 dB, 24 dB, 26 dB and 27 dB, at 23.8, 31.4, 72.5 and 82.5 GHz, respectively. The percentages of ΔT_A values lower than its standard deviation result less than 0.1% at K and Ka band and 0.6% at V and W band, taking into account the entire available dataset described in Section II.B.

As described in [80] and [97], the ST-MW radiometry technique can offer a very interesting framework to validate parametric retrieval models, especially at frequency bands above K band due to the unavailability of satellite-to-Earth beacon campaigns. Previous works already proposed physically-based prediction models (PPM) for estimating atmospheric parameters based on the non-linear regression fit of numerical simulations [101], [79]. Sky-noise Eddington radiative transfer model (SNEM) has been considered in an absorbing and scattering medium such as gaseous, cloudy and rainy atmosphere [120], [115]. The exploitation of the closest RaOb dataset has been used to statistically characterize the local meteorology in terms of temperature, pressure and humidity average and standard-deviation profiles. The latter statistics is then imposed in the Monte Carlo pseudo-random generation of vertical cloud structures where average profiles and cross-correlation among hydrometeor concentration are imposed [79]-[120].

The PPM general approach has been adapted for Rome (NY, USA) using our available radiosonde dataset described in II.B and performing SNEM simulations at 23.8, 31.4, 72.5 and 82.5 GHz and for 8 elevation angles between 20° and 90° in terms of both brightness temperature and atmospheric extinction.

The multi-frequency PPM-PolDEx model [80] is based on a polynomial regression on SNEM dataset, reinforced with a double exponential single-frequency term, able to achieve better results in heavier rainy cases. This multi-frequency weighted polynomial approach is able to balance the use of two different models depending on the weather conditions. The PPM-PolDEx atmospheric extinction estimates are given by:

$$A_{PolDEx}(f) = m \cdot \{(1 - SSI + h)A_{Pol}(f) + (SSI - h)A_{DEx}(f)\} \tag{3.II.28}$$

where

$$A_{Pol}(f) = \sum_{i=1}^{4} a_i \, T_{AooS}(f_i) + \, b_i \, T_{AooS}^2(f_i) \tag{3.II.29}$$

$$A_{DEx}(f) = \left[c_1 \cdot \mathrm{e}^{c_2 \cdot T_{AooS}(f)} + d_1 \cdot \mathrm{e}^{d_2 \cdot T_{AooS}(f)}\right] \tag{3.II.30}$$

where $f_{i=1,2,3,4}$=23.8,31.4,72.5,82.5 GHz and f is one of 4 available frequencies fi, whereas the coefficients are all function of the air mass m. A first comparison is here performed among all-weather conditions available from the six months of measurements. Table 3-5 quantifies the comparison in terms of average error (AvE) and root-mean-square-error (RMSE), with the error defined as the difference between attenuation from the PPM model and the ST time series. We can clearly note how the PPM-PolDEx parametric model shows solid results at all frequencies and for

the entire range of elevation angles. In order to stress the last consideration, the correlation coefficient (CC) and the index of agreement (IA) have been also considered to better evaluate the percentage accuracy. IA is a standardized measure of the degree of model prediction error and it varies between 0 and 1. An agreement index score of 0 suggests no agreement between the PPM model and the SNEM dataset, while an agreement score of 1 suggests complete match between the model and the dataset [121]. For the PPM-PolDEx model in Table 3-5, IA goes from about 0.99 at 23.8 GHz to about 0.98 at 72.5 GHz.

Measurements, described in Section II.B, are available at different elevation angles since the ST technique is intrinsically based on a variable antenna pointing in order to follow the Sun movement along its ecliptic. Both ST and PPM-PolDEx estimates are able to provide valid results for a wide range of elevation angles. In particular, the measurements result equally distributed with about 33.9% between 70° and 54°, 43.1% between 53° and 38° and 22.5% between 37° and 20° in elevation. In order to focus the emphasis on cloudy and rainy conditions, the threshold criterion described in Section II.B has been used to define the total percentage of clear-air samples (30.5%), as well as the one of cloudy/rainy situations (69.5%).

TABLE 3-5: ATMOSPHERIC EXTINCTION INTER-COMPARISON BETWEEN ST-MWR AND PPM-POLDEX MODEL FOR THE AVAILABLE DATASET IN 2015 IN ROME, NY ALL-WEATHER CASES

f [GHz]	AvE[dB]	RMSE[dB]	CC	IA
23.8	0.0069	0.1721	0.9800	0.9893
31.4	-0.0500	0.2441	0.9846	0.9860
72.5	0.0593	0.7061	0.9791	0.9793
82.5	0.0513	0.6242	0.9808	0.9861

TABLE 3-6: ATMOSPHERIC EXTINCTION INTER-COMPARISON BETWEEN ST-MWR AND PPM-POLDEX MODEL FOR THE AVAILABLE DATASET IN 2015 IN ROME, NY CLOUDY AND RAINY CASES

f [GHz]	AvE[dB]	RMSE[dB]	CC	IA
23.8	0.0093	0.2014	0.9778	0.9881
31.4	-0.0315	0.2820	0.9848	0.9864
72.5	0.0933	0.8421	0.9790	0.9780
82.5	0.0893	0.7425	0.9796	0.9849

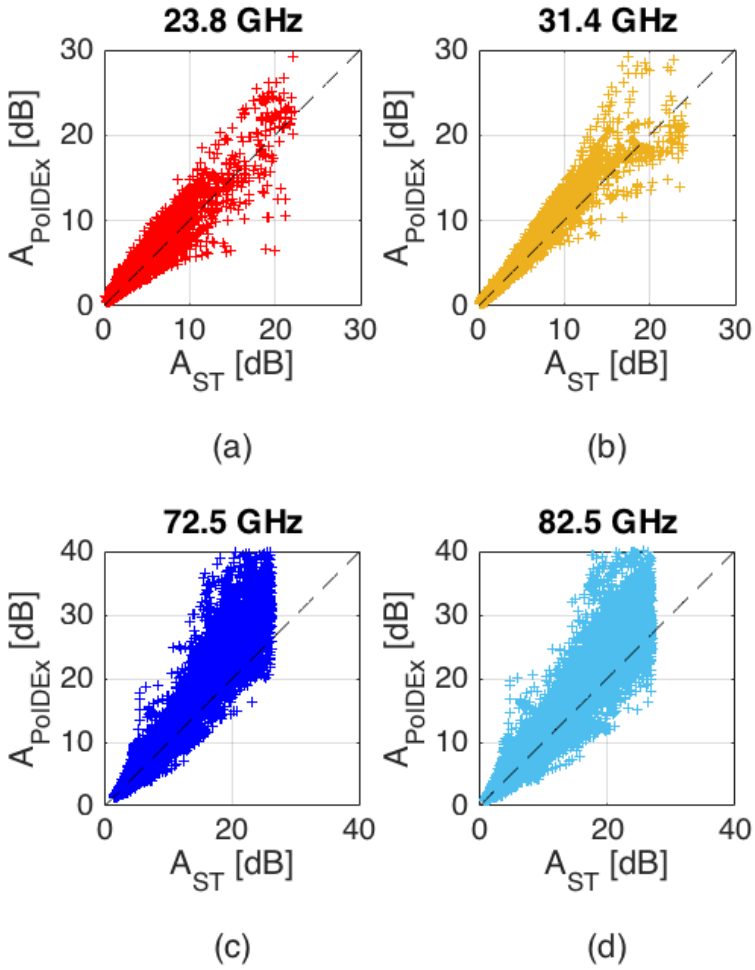

Figure 3-6: Scatterplot of ST-MWR atmospheric extinction for each frequency versus extinction estimates from PPM-PolDEx for all cloudy/rainy conditions.

Figure 3-6a-d shows the scatterplot of PPM-PolDEx model atmospheric extinction estimates for each frequency versus the corresponding ST-MWR ones for all the available dataset for only cloudy/rainy situations. A saturation effect is shown in the ST extinction retrieval, especially at V and W-band, attesting the limits of the ST technique in terms of the maximum attainable extinction. It generally occurs for heavy rain at K-band, but it may occur for light rain at 72.5 and 82.5 GHz. In such conditions antenna noise temperature differences ΔTA between twS and ooS are minimal and can go below the noise level.

Table 3-6 quantifies the comparison in terms of average error (AvE) and root-mean-square-error (RMSE), correlation coefficient (CC) and the index of agreement (IA). Both scatterplots and numerical results confirm that the exclusion of the clear-air samples in the comparison has a minimum impact on the comparison and the PolDEx approach shows a good correlation with respect to ST data for all frequencies in cloudy/rainy situations.

3. III. Cloud attenuation stochastic characterization and Parametric Prediction models at Ka-band

In this work, well-known radiative models are adopted to provide an estimate of the equivalent clear-air path attenuation contribution, exploiting surface weather measurements and making several assumptions on their vertical stratification over the troposphere [24]-[107]. However, the attenuation contribution due to non-precipitating clouds cannot be easily modelled by only using in-situ measurements, i.e. surface boundaries are not able to provide enough information about the whole atmospheric status for a given instant. This work aims at characterizing the behavior of suspended clouds in terms of atmospheric path attenuation. A stochastic approach is used to model the time evolution of the cloud contribution [75]. Both the probability density function and the power spectral density are retrieved by exploiting measurements from the RPG-HATPRO radiometer installed in Cebreros, Spain at the European Space Agency's Deep Space Antenna site. Physically-based prediction models for all-weather total path attenuation estimation at 32 GHz are applied to the measured radiometric brightness temperatures [97]-[127]. The cloud contribution is then extrapolated and modelled as a log-normal stochastic process as a result of a detailed analysis in both amplitude and time domains.

The section is organized as follow: section III.A describes the available data and defines physically-based prediction models for all-weather atmospheric path attenuation estimates at 32 GHz; section III.B recaps the models used to retrieve the integrated path attenuation starting from the available surface data and eventually exposes the cloud attenuation stochastic model characterization.

3. III.A. Path Attenuation Retrieval from Microwave Radiometric Data

➢ *Microwave Radiometer dataset*

The available dataset consists of sparse measurements collected by the ground-based microwave radiometer (MWR) from December 2014 to December 2015 at the ESA deep space antenna located at Cebreros, Spain (40°27'13''N, 04°22'04''W). The ESA-MWR is a RPG-HATPRO profiler (built by the German company Radiometer Physics GmbH) and has a total of 14 channels with receivers at K-Band (22.24, 23.04, 23.84, 25.44, 26.24, 27.84 and 31.4 GHz) and V-Band (51.26, 52.28, 53.86, 54.94, 56.66, 57.3 and 58.0 GHz) [106]. Measurements are always taken at zenith. The instrument system also includes in-situ measurements of air temperature, relative humidity, pressure, and rain intensity.

➢ *Parametric prediction model for path attenuation retrieval*

The parametric prediction model (PPM) approach is based on non-linear regression fitting of numerical simulations, derived from the sky-noise Eddington radiative-transfer model (SNEM) in an absorbing and scattering medium such as gaseous, cloudy and rainy atmosphere [120], [114]. Radiosounding datasets are used to statistically characterize the local meteorology in terms of temperature, pressure and humidity average and standard-deviation profiles. The latter statistics is then imposed in the Monte Carlo pseudo-random generation of vertical cloud structures where

average profiles and cross-correlation among hydrometeor concentration are imposed [120]-[79]. The PPM general approach has been adapted for ESA deep space antenna at Cebreros (Spain) using radiosounding profiles obtained at the closest WMO RAOB station at Madrid/Barajas airport (about 60 km distance from the radiometer). By extracting the meteorological statistics, SNEM simulations have been performed at zenith (90° of elevation angle) in order to compute both brightness temperature and path attenuation. The multi-frequency PPM-*PolDEx* model has been already proposed and applied in previous works [80]-[97]-[127] for different antenna sites. It is based on a combination between a polynomial term and a double exponential single-frequency term, properly tuned by the Sky Status Indicator *SSI* and a tuning parameter h_0. This multi-frequency weighted approach is able to balance the use of two different models depending on the weather conditions: the polynomial during clear-air situations and the double exponential for cloudy/rainy cases. The PPM-*PolDEx* atmospheric attenuation estimates are given by:

$$A_{PolDEx}(\theta_0) = \csc\theta_0 \{(1 - SSI + h_0)A_{Pol} + (SSI - h_0)A_{DEx}\} \tag{3.III.1}$$

where θ_0 is the elevation angle of interest and csc is the cosecant. SSI stands for Status Sky Indicator (SSI), an atmospheric index purely based on the available radiometric measurements and successfully applied in several MWR campaigns [116], [81].

$$\text{SSI} = \frac{BT_3 - r_0}{BT_1} \tag{3.III.2}$$

$$A_{Pol} = \sum_{i=1}^{4} a_i\, BT_i + b_i\, BT_i^2 \tag{3.III.3}$$

$$A_{DEx} = [c_1\, \mathrm{e}^{c_2\, BT_3} + d_1\, \mathrm{e}^{d_2\, BT_3}] \tag{3.III.4}$$

The SSI is defined in (3.III.2), the polynomial term A_{Pol} is given in (3.III.3), while (3.III.4) provides the expression of the double exponential single-frequency term. $BT_{i=1,2,3,4}$ are the zenithal brightness temperatures $BT_{23.84GHz}$, $BT_{26.24GHz}$, $BT_{31.40GHz}$, $BT_{51.26GHz}$. Table 3-7 recaps the PPM coefficients to be used to estimate the atmospheric path attenuation at 32 GHz.

TABLE 3-7: PPM-POLDEX MODEL COEFFICIENTS AT 32 GHZ

a_1	4.582E-03	b_1	-1.229E-04
a_2	-7.262E-03	b_2	2.412E-04
a_3	2.198E-02	b_3	-3.060E-05
a_4	-5.553E-04	b_4	-4.169E-06
c_1	5.575E-01	c_2	1.303E-02
d_1	1.110E-11	d_2	9.525E-02
h_0	3.231E-01	r_0	6.768E+00

➢ *Cloudy conditions discrimination*

In order to select instants purely representative of cloudy conditions, we consider the following two criteria:

- To exclude rainy conditions, surface measurements of the rain flag provided by the radiometric system are considered. We discarded all the measurements taken during rain events, i.e. when the rain flag was equal to 1.
- To filter out clear-air conditions, we implemented a threshold mechanism on the SSI by setting a fixed zenithal parameter. If SSI is below the SSI_{th}, a clear air condition is assumed. Parameterization has been set up by performing radiative transfer simulations applied to long-term available radiosonde observations [116]-[81].

3. III.B. INTEGRATED PATH ATTENUATION DUE TO CLOUDS

Considering a horizontally stratified atmosphere with the lowest level at $z = h_s$ (site altitude) and the top height at $z = H$, the atmospheric integrated path attenuation A in dB may be computed according to:

$$A(f, \theta_0) = \frac{10}{\ln 10} \int_{h_s}^{H} \kappa_e(f, z) \csc \theta_0 \, dz \tag{3.III.5}$$

where e is the Neper number, θ_0 is the elevation angle and κ_e is the extinction coefficient at height z above the surface in Np/km. Starting from (3.III.5), we can consider the extinction coefficient defined by $\kappa_e = \kappa_a + \kappa_s$, where κ_a and κ_s are the absorption and scattering coefficients, respectively:

$$A(f, \theta_0) = \frac{10}{\ln 10} \int_{h_s}^{H} [\kappa_a(f, z) + \kappa_s(f, z)] \csc \theta_0 \, dz = A_a(f, \theta_0) + [A_C(f) + A_R(f, \theta_0)] \tag{3.III.6}$$

In (3.III.6), A_a stands for the clear-air contribution due to absorption and the scattering contribution is split into two main attenuation terms: the cloud contribution A_C and the rain contribution A_R. In this contribution, we do not consider the rain contribution but we only focus on the cloud-specific attenuation contribution.

➢ *Clear-air atmospheric path attenuation retrieval from surface data*

Considering a horizontally stratified atmosphere under clear-air conditions, the atmosphere may be considered a non-scattering medium ($\kappa_s = 0$) and the extinction coefficient κ_e results equal to the absorption coefficient κ_a. Considering the Earth's atmosphere in the microwave spectrum, water vapor and oxygen result the main constituents with relevant absorption effects [24]. Assuming the absorption coefficients be $\kappa_{a(H_2O)}$ and $\kappa_{a(O_2)}$ in Np/km, the atmospheric integrated path attenuation A_a in dB under clear-air conditions can be computed from (3.III.6) by setting κ_a as the sum of the two coefficients above mentioned, water vapor and oxygen respectively. Existing literature provides several formulations of the absorption coefficients of interest, which mainly

depend on considered frequency, and vertical profiles of meteorological parameters as temperature, water vapor density and atmospheric pressure. In particular, we have used models contained in [24], exploiting well-known formulations for the water vapor [77] and oxygen absorptions [148]-[78]. Eventually, we have considered standard profiles of meteorological quantities [107]-[149] as approximation, making use of the surface measurements of temperature, relative humidity and pressure available from the weather station.

➢ *Cloud attenuation stochastic characterization*

A stochastic approach is used to model the time evolution of the cloud additive contribution A_C in (3.III.6). Radiometric measurements of cloudy atmosphere are selected by using the criteria defined in section 3.III.A and the clear-air contribution is then subtracted using the clear-air attenuation estimate described in the previous section. The resulting time series of A_C is used for the analysis.

In order to characterize a stochastic process, we need to define both the probability density function and the power spectral density. The time series of A_C can be represented with a reasonable accuracy by adopting a log-normal distribution. Therefore, we have considered a probability density function ζ_{A_C} as follow

$$\zeta_{A_C}\{A_C(f)|\,\mu_C(f),\sigma_C(f)\} = \frac{\exp\left[\frac{-\left(\ln[A_C(f)]-\mu_C(f)\right)^2}{2\sigma_C^2(f)}\right]}{\sqrt{2\pi}\,A_C(f)\,\sigma_C(f)} \tag{3.III.7}$$

where μ_C, σ_C are the so-called location parameter and scale parameter of the Log-normal distribution [75]. By evaluating the Fourier transform of the autocorrelation function $R_{AA}(\tau)$, and assuming a real power signal A_C, we have obtained the power spectral density $\widetilde{\mathrm{A}_c}(f)$, where the half-power bandwidth B_C of the stochastic process is given by $\left|\widetilde{\mathrm{A}_c}(B_C)\right| \equiv 1/\sqrt{2}$.

Once defined the location parameter and scale parameter of the probability density function and the half-power bandwidth B_C, we are able to reconstruct the same stochastic process by synthetizing samples of cloud attenuation A_C. Figure 3-7 shows the inter-comparison between the real radiometric measurements (red curve) and the simulated stochastic process (blue curve) in terms of both probability density function and cumulative distribution function. We can note as the two pairs of curves show a very good agreement.

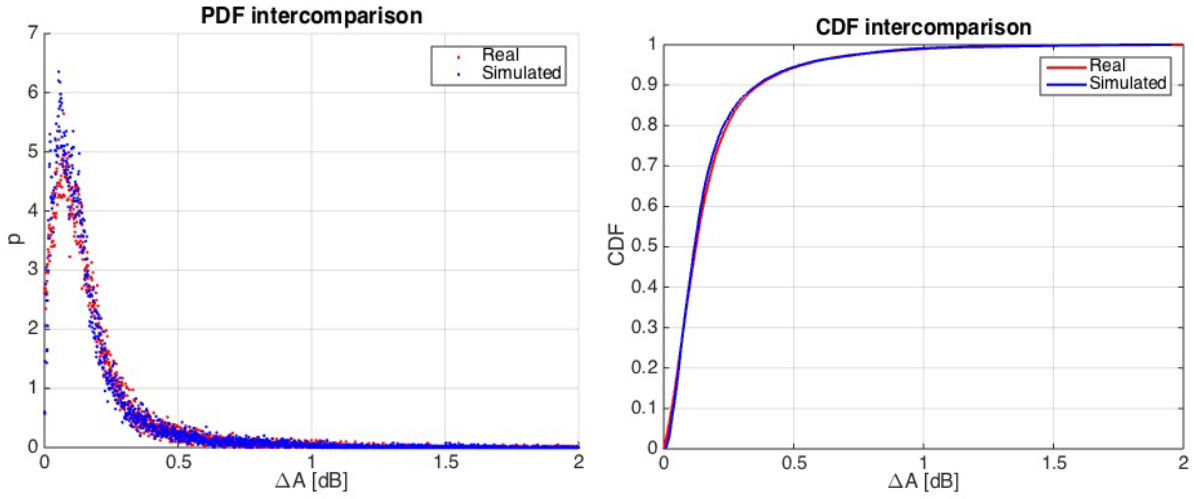

Figure 3-7: Probability density function (PDF) and Cumulative distribution function (CDF), inter-comparison between real measurements and simulated stochastic process

On the other hand, Figure 3-8 shows the same comparison in terms of time series, where the red curve corresponds to the real radiometric measurements and the blue curve to the simulated ones. The time variations of the simulated stochastic process are able to simulate the behavior of a real cloud attenuation contribution in a good manner even in time domain.

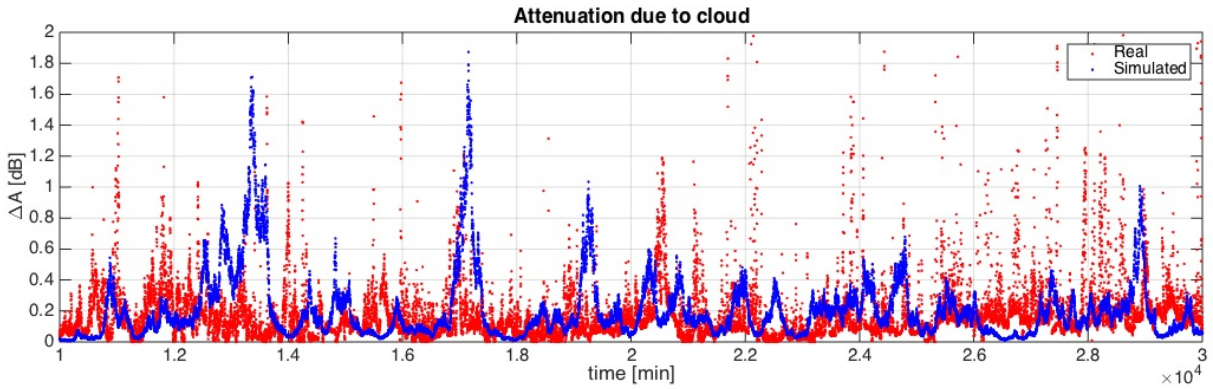

Figure 3-8 Time domain comparison between real measurements and simulated stochastic process

Chapter 4. Model-based prediction of data rate for deep-space satellite missions

4. I. Introduction

Typical frequency bands for space missions range from around 2 GHz (L and S band) to around 8 GHz (X band). Deep space missions have a satellite-Earth distance larger than 2.0 10^6 km and are aimed at exploring the solar system. The increasing number of deep space missions is making the bands allocated for space exploration oversubscribed. Moreover, the necessity of increasing the transmission data-rate, connected to the need of a wider channel bandwidth, is pushing deep space missions toward higher link frequencies such as 32 GHz (Ka band) [150]. The counterpoint is that signals propagating at such frequencies are more affected by atmospheric degrading effects [151]. Indeed, in addition to convective rainfall, which is the preponderant meteorological event at frequencies lower than 10 GHz, also non-precipitating clouds and moderate precipitation produced by stratiform rain events must be considered in the link-budget design [152].

Traditional link budget techniques typically design the link in a conservative way by maximizing transmitted data with a fixed percentage of channel availability (e.g., 90%). More recent techniques aims at maximizing data return while keeping data losses under a fixed threshold (e.g., 5%) and by properly varying the transmission data-rate during the transmission period [153]. Those techniques rely on climatological statistics of atmospheric attenuation (on monthly or even yearly time-scale) derived from historical measurements collected during several years in the past [153]. Such approaches could turn to be too conservative, especially for links operating at Ka-band frequencies [153]. A way to overpass this problem is to resort to weather forecast (WF) models that allow optimizing the link budget on the basis of the predicted atmospheric channel conditions expected during the satellite-to-Earth transmission period [150], [154]. Only few studies can be found in literature concerning the use of WF for the link budget design. One of the most important is the study proposed in [155] where the presented results were interesting but not enough decisive to be operationally adopted for the Ka-band data transfer links in DS missions. In [156] a technique for the link budget optimization exploiting WF numerical models coupled with radiopropagation models is proposed. WF models provide forecasted meteorological variables that are converted into radiopropagation parameters by an accurate radiative transfer model (in contrast to semi-empirical relations typically adopted by traditional link budget techniques). Such WF-based model chain allows designing the link-budget using statistics of the radiopropagation parameters that are physically based and dynamically correlated to the evolving weather scenario. The design and optimization of the link-budget leads to the computation of the operational parameters used to set-up the satellite-to-Earth downlink (which determine the predicted transferred data-volume).

Two applications of the weather-forecast based link budget optimization technique are described in this chapter:

- A feasibility study of the model-chain proposed in [156] through the simulation of the satellite-to-Earth transmission conditions of the BepiColombo mission to Mercury [157]
- An application to JAXA Hayabusa-2 mission Ka-band data provided by the ESA cross-support service

BepiColombo is a mission of the European Space Agency (ESA) launched in October 2018. The two reference ground stations for the mission are the ESA Deep Space stations in Cebreros (Spain) and in Malargüe (Argentina). The test-case scenario that we have simulated in [156] was relative to one transmission year operating at Ka-band and considering the receiving ground-station in Cebreros. We have performed the link-budget design of the satellite-to-Earth transmission comparing different optimization techniques that exploit statistics of atmospheric attenuation derived from two different meteorological datasets: weather-forecast and climatological. As previously stated, the advantage of using a weather-forecast model relies in the possibility of dynamically adapt the satellite link to the evolving meteorological scenario expected during the satellite transmission period. On the contrary, climatological archives (used in the classical link-budget design techniques) provides static information derived from meteorological measurements collected in several years in the past. Results obtained in [156] have highlighted that the proposed WF-based approach (which exploits atmospheric statistics derived by a weather forecast coupled with a radiopropagation model) can provide a gain of more than 20% in terms of yearly received data-volume if compared to traditional optimization techniques (which exploits atmospheric statistics derived from climatological archives). Although results in [156] were promising, the unavailability of meteorological measurements prevented any kind of tuning and validation of numerical models and predicted data-volumes. Moreover, those results were relative to a specific transmission year and a specific receiving ground station (Cebreros) operating at Ka band (i.e., 32 GHz).

In order to fill the gap in [156], the aim of the present work is to improve and assess the proposed WF-based technique. The first strength of this work is the availability of several meteorological measurements such as radiosounding observations and microwave radiometric measurements. We have exploited these measurements for the fine-tuning, set-up and validation of both WF and radiopropagation models (see [158] for details about the WF-model tuning). Once tuned and validated the two models of the WF-based chain, to assess and prove the reliability of the results in [156], we have enlarged the simulation period from 1 to 4 years of transmission thus analyzing 4 different yearly meteorological trends that influence the relative yearly transferred data-volume. To confirm the general applicability of the proposed WF-based model chain, we have performed the transmission simulations for both Cebreros and Malargüe receiving ground stations and for transmissions operating at both X and Ka band. The use of the WF-based approach allowed the development of a technique for the estimation of the uncertainty associated to the transferred data volume. This aspect is crucial from an operative point of view: if predicted data volume with the associated uncertainty does not satisfy the mission constraints, in some cases the schedule of the downlink transmission can be changed by switching the downlink frequency and/or the receiving ground-station. Finally, the availability of radiometric measurements allowed the validation of the entire model-chain through the comparison of the transferred data volumes predicted with the WF-based technique with the ones computed exploiting atmospheric radiometric measurements.

Moreover, it is presented a preliminary operational validation of the model chain applied to the Hayabusa2 mission to the asteroid 162173 Ryugu (that was launched in 2014 by the Japan aerospace exploration agency, JAXA, and reached the asteroid in June 2018). We have run our model-chain to operatively provide JAXA with the optimized transmission parameters for the Hayabusa2 downlink and compared our simulations with measurements provided by JAXA and ESA. The results confirm the reliability and the efficiency of our model-chain.

The chapter is organized as follows: section 4.II describes the model chain composition, section 4.III briefly summarizes the results of the feasibility study on the BepiColombo mission and finally section 4.IV presents the preliminary verification with Hayabusa-2 cross-support data.

4. II. Methodology and Weather-Forecast chain description

The model chain is composed by three modules: weather forecast, radio propagation and down-link budget module. The weather forecast module produces numerical weather predictions of the atmospheric state expected during the satellite transmission. The radiopropagation module converts the predicted atmospheric state into radiopropagation variables (i.e., atmospheric path attenuation and brightness temperature) by taking into account the gaseous absorption and the microphysical properties of cloud droplets and hydrometeors. The last downlink-budget module exploits the predicted radiopropagation variables to perform the optimization of the satellite-to-Earth link with a stochastic approach. The latter provides the optimal prediction of the operational parameters of the satellite mission in terms of transmission data-rate and expected transferred data-volume or signal-to-noise ratio at the receiving ground-station antenna. The downlink optimization is accomplished in a statistical framework: spatial-grid domain of simulated radiopropagation variables is exploited to derive statistics and uncertainties of the temporal evolution of the predicted signal-to-noise ratio expected when operating with the predicted optimized operational parameters. Classical link budget optimizations are realized exploiting climatological statistics of radiopropagation variables (e.g., statistics retrieved by meteorological measurements collected during several years of measurements in the past) [152]. At frequencies above the Ku band such techniques turn out to be too conservative [153]. On the contrary, the advantage of the approach proposed in this work, derived by the coupling of weather forecast and radiopropagation models, is that the predicted radiopropagation variables are physically-based and dynamically correlated to the evolving weather scenario expected during the downlink transmission period.

Figure 4-1 shows the model-chain block-scheme deeply described in [87]. The weather forecast module (WFM) is a regional scale model (initialized by a global-scale model) that produces numerical weather predictions of the atmospheric state. The model runs over two-way nested domains (where the inner domain has a finer spatial resolution) centered on the geographical area of our interest and for the considered downlink transmission period. The predicted atmospheric state is described by the 3-dimensional time-evolution of microphysical variables (e.g., pressure, temperature, humidity, wind velocity and orientation) and thermodynamic variables (e.g.,

atmospheric particle concentration of water clouds and aerosol dispersions). The radiopropagation module (RPM) converts the atmospheric state vector computed by the WFM into radiopropagation variables. The latter are the atmospheric attenuation and brightness temperature for the considered link-frequency and the considered ground-station antenna elevation angle (which, in general, changes during the transmission period due to reciprocal motion of satellite and Earth) for each pixel of the inner grid-domain generated by the WFM. RPM implements a sky-noise Eddington model to solve the radiative transfer problem for the computation of the atmospheric attenuation (L_{atm}) and brightness temperature (T_B) along the signal slant-path taking into account the gas absorption and the hydrometeors multiple scattering with five hydrometeor distributions (cloud, rain, ice, snow, graupel) [120]. Note that, the signal slant-path is determined by the elevation angle θ of the ground station antenna pointing to the satellite. Finally, the downlink budget module (DBM) exploits the radiopropagation variables computed by the RPM to optimize the satellite-to-Earth link. The optimization is done in a statistical framework in order to maximize the received data and minimize the losses.

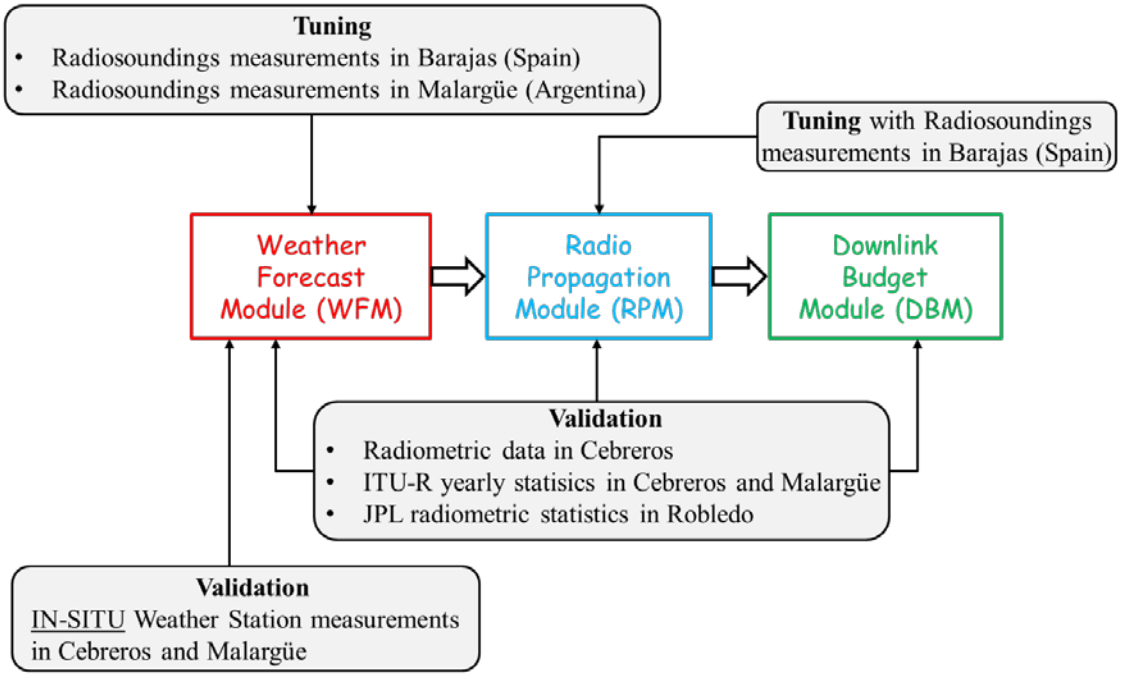

Figure 4-1: Model chain: weather forecast (red), radiopropagation (blue) and downlink budget (green) modules. Grey blocks are measurements and statistics used for tuning and validating the three modules.

Note that, in this work, we adopt daily forecasts from the WFM. This means that the atmospheric state expected during the transmission period is predicted 24 hours before the start of the transmission itself. The transmission period is defined by the visibility (line of sight) between satellite and receiving ground station. The spatial and temporal resolutions of the whole model chain are imposed by the WFM resolutions. Each single model was tuned and validated with external data source during the feasibility study [158]. I manly contributed to the radio-propagation and link-budget modelling and data analysis, as well supporting the fine tuning and validation of

the whole chain.

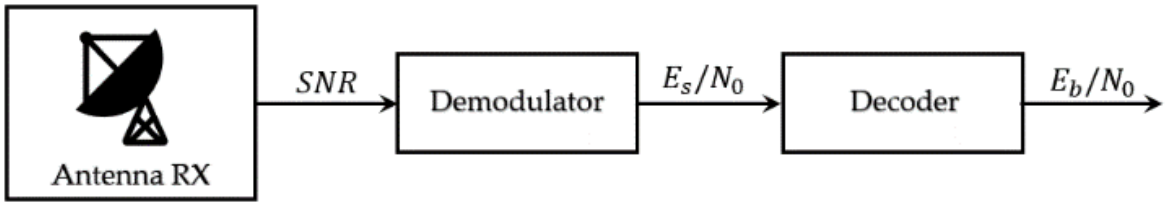

Figure 4-2: Receiving system block-scheme.

The setup of the three modules must be adapted in function of the space mission specifics and will be described in the next sections. In particular, the link-budget optimization technique implemented by the DBM, is strictly related to the mission's objectives and the transmission characteristics. We can use the generic scheme of a receiving system in Figure 4-2 for some considerations.
Referring to Figure 4-2, depending on the section of the receiving system, we can define the following quantities:

$$\frac{S}{N} = \frac{EG_R}{L_{FS}L_{atm}(\theta)kT_{sys}(\theta)\Delta f} \quad \text{[adim]} \tag{4.1}$$

$$\frac{E_s}{N_0} = \frac{EG_R}{L_{FS}L_{atm}(\theta)kT_{sys}(\theta)R_S L_{mod}L_{tech}} \quad \text{[adim]} \tag{4.2}$$

$$\frac{E_b}{N_0} = \frac{EG_R}{L_{FS}L_{atm}(\theta)kT_{sys}(\theta)R_b L_{mod}L_{tech}} \quad \text{[adim]} \tag{4.3}$$

The symbol legend for (4.1)-(4.3) is reported in Table 4-1.

TABLE 4-1 SYMBOL LEGEND

S	Total signal power [W]	T_{sys}	System noise temperature [K]
N	Total noise power [W] in the bandwidth Δf	E_s	Energy per symbol [J]
Δf	Frequency bandwidth [Hz]	N_0	Noise spectral density [W/Hz]
E	Effective isotropic radiative power (EIRP) of the spacecraft antenna [W]	E_b	Energy per bit [J]
		R_b	Bit rate [bit/s]
G_R	Receiving antenna gain [adim]	R_s	Symbol rate [sym/s]
L_{FS}	Free space loss [adim]	L_{mod}	Modulation/demodulation losses [adim]
L_{atm}	Atmospheric path attenuation [adim]	L_{tech}	Technological loss of the receiver [adim]
k	Boltzmann constant [$1.38 \cdot 10^{-23}$ J/K]	θ	Antenna elevation angle [deg]

With respect to Figure 4-2, (4.1) is the downlink signal-to-noise ratio (SNR) received by the antenna that is the input of the demodulator. After the demodulator we have the estimation of the energy-

per-symbol to noise-density ratio derived with (4.2). Finally, we can calculate the energy-per-bit to noise-density ratio at the output of the decoder using (4.3).
Note that, in (4.1)-(4.3), T_{sys} is directly related to T_B [K]:

$$T_{sys}(\theta) = T_n(\theta) + \left(\frac{1}{L_{fr}}\right) \cdot T_B(\theta) \tag{4.4}$$

Where T_n [K] includes all noise contributions from passive and active elements of the whole antenna system, referenced at Low Noise Amplifier input, including elevation-dependent ground noise and L_{fr} [adim] represents the feed losses.
The DBM optimization allows the computation of the operational parameters to setup the transmission operations. Such parameters, which are the data-rates (R_b or R_s) and the best instant to start transmitting (within the visibility period), are computed through the maximization of the received data that passes through the computations (4.1) - (4.3).

4. III. Feasibility study: ESA BepiColombo mission test-case

The model chain presented in section 4.II was tested within a feasibility study done on the BepiColombo mission test case. BepiColombo is Europe's first mission to Mercury, the smallest and least explored terrestrial planet of our Solar System. The satellite was launched by the ESA (in collaboration with JAXA) in October 20, 2018 and will arrive at Mercury in 2025. BepiColombo will be the first European deep-space mission using the Ka band (32 GHz) for the downlink of telemetry data. The downlink transmission will occur once per day with transmission periods of about 7 to about 12 hours (depending on the period of the year, i.e., on the reciprocal distance between Mercury and Earth) and reference ground stations for the Ka band downlink will be in Cebreros (Spain) and Malargüe (Argentina), both from the ESA Deep Space Network.

We have simulated the BepiColombo transmission phase with its operative specifics. The setup of the three modules in Figure 4-1 is the following [158]:

- WFM is realized with the Mesoscale Model 5 [159] initialized with analysis data provided by the global model of the European Centre for Medium-Range Weather Forecast with horizontal resolution of 0.25°. The model is run over two nested-grid domains centered on the considered receiving site (Cebreros or Malargüe): the first domain has 57×69 grid points and the second domain has 46×52 grid points with spatial resolutions of 18 and 6 km, respectively. The vertical structure is composed of 22 vertical pressure levels (with finer resolution in the lower levels near the surface). Daily weather forecast are produced with a release time of 1 hour.

- RPM is formed by the Satellite Data Simulator Unit [160] that simulates radiopropagation variables as measured by meteorological satellites and it has been adapted to ground-based view. We have setup microphysical parameterizations of spherical particles using WFM outputs per each grid point and considering five hydrometeors distributions: water, ice,

rain, snow and graupel. RPM runs are set to produce L_{atm} and T_B at 32 GHz and at several elevation angles (ranging from 10° to 90° with 10° step) in each point of the inner grid-domain.

- DBM realizes an optimization of the received data volume with statistical techniques. Such techniques are applied to daily statistics of L_{atm} and T_B directly computed from the time series produced by the RPM and relative to the specific day in which the transmission will occur. The optimization is based on the maximization of the received data while keeping the losses under a given threshold [156]. Such threshold is given by the retransmission protocol of the satellite transmitter and is set to 5% in our case. Data volume is computed in terms of frames, then converted into bits, and is directly derived by the E_b/N_0 (4.3) through the frame error rate function, which depends on the adopted coding scheme [156]. The operational parameters computed by the DBM are: Rb and the minimum elevation angle at which start and stop the transmission.

First, we have tuned and validated each module with several meteorological measurements (as indicated in Figure 4-1) available from sites near the two receiving ground stations: radiosounding observations, weather stations, radiometric measurements. We have also made statistical comparisons with yearly statistical models of the radiocommunication sector of the international union of telecommunications (ITU-R) and with climatological statistics available from NASA jet propulsion laboratory (JPL). These comparisons confirmed the reliability of the model chain [158].

Then, we have run the optimization model chain over a period of four transmission years (from 2012 to 2015) on both Cebreros and Malargüe stations. We have compared the optimized data-volume with the one obtained with two classical link-budget techniques based on monthly climatological statistics from JPL (which are the actual adopted techniques) that we have called "standard" and "advanced" techniques. The results of this study are in [158]. As an example, Figure 4-3 from [158] shows the results for the transmission to Cebreros ground station (we have similar results for Malargüe). We have demonstrated that the use of our model chain for the link budget optimization allows a potential increase of the yearly-received data-volume of 20% to 24% with respect to classical link budget techniques without losing additional frames (lost frames percentage remains below the 5% threshold).

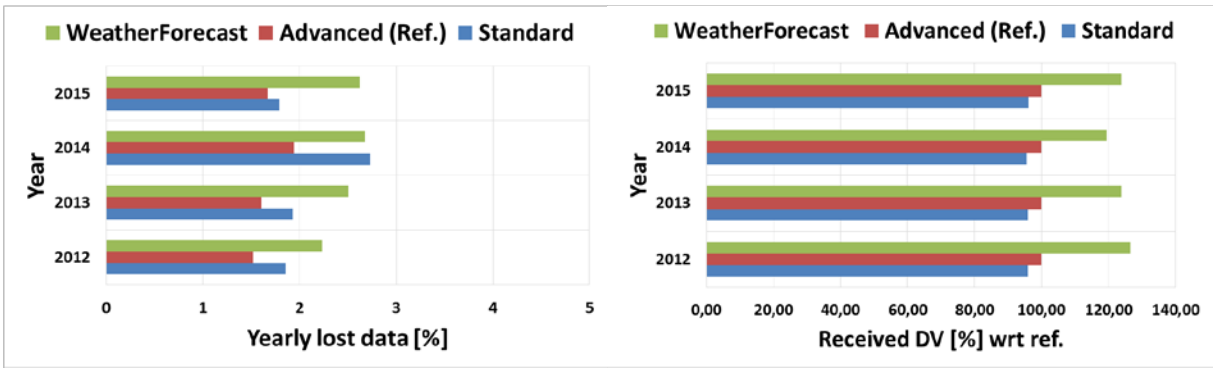

(a) (b)

Figure 4-3: Yearly lost (a) and received (b) data volume (DV) in Cebreros at Ka band. Note that received data are expressed in percentage with respect to reference *advanced* technique (from [158]).

A detailed description of the analyses performed (and obtained results) in the framework of the BepiColombo feasibility study can be found in [158]. I manly contributed to the radio-propagation / link-budget modelling and data analysis, as well supporting the fine tuning and validation of the whole chain. Moreover, I took care of the processing and analysis of all available radiometric measurements.

4. IV. Preliminary validation and online operation with JAXA Hayabusa-2 mission support data

After the feasibility study presented in section 4.III, we are operationally validating the model chain with Hayabusa2 mission to the asteroid 162173 Ryugu. Hayabusa2 was launched in 2014 by JAXA and reached the asteroid in June 2018. The Ka-band (32 GHz) downlink transmission occur once per week: each Saturday, typically from 14:00 to 22:00 (but the transmission window depends on the period of the year and on the availability of the receiving ground stations that are shared among several missions). The reference ground stations are the same of BepiColombo mission: Cebreros and Malargüe. For the model chain validation JAXA, with ESA collaboration, provided us with E_s/N_0 estimated by the Telemetry, Tracking and Command Processor (TTCP) of the receiving antenna and the corresponding R_s used during each transmission period. With respect to the BepiColombo mission test-case, we have updated the modules in Figure 4-1 with the current state-of-the-art models:

- for the WFM, the Mesoscale Model 5 was updated with the Weather Research and Forecasting model [161] initialized with data from the Global Forecast System model produced by the National Centers for Environmental Prediction. The space and time resolutions are the same used for the BepiColombo mission.

- the Satellite Data Simulator Unit of the RPM was changed with the latest Goddard- Satellite Data Simulator Unit [162] that, among several updates, considers the contribution of non-spherical particles. L_{atm} and T_B are produced at 32 GHz and at elevation angles ranging from 10° to 90° with 10° step in each point of the inner grid-domain.

- Differently from BepiColombo mission, Hayabusa2 does not support any retransmission protocol and losses must be avoided at all. Thus, the objective of the DBM statistical optimization is to keep the E_s/N_0, computed with (4.2), above a given threshold (i.e., 2.06 dB). In this case, as described in the following, the statistics are derived exploiting the spatial grid domain of the forecasted radiopropagation variables. The output of the DBM is the optimum Rs to use during the transmission.

Figure 4-4 shows the horizontal surface section of the inner-grid domain of the model chain: each point corresponds to a pixel with given latitude and longitude coordinates. WFM model computes temporal evolution of the vertical profile of the atmospheric state per each grid-point. RPM computes the slant-path values of radiopropagation variables through the slant-integration of the atmospheric state in each grid-point (and per each temporal instant). The result is a 2-dimensional map (with 6 km spatial resolution) of slant-path radiopropagation variables per each point of the grid and per each temporal instant (with 1-hour time sampling). We have realized the statistical approach of the DBM through the computation, for a given R_s value, of E_s/N_0 ratio (4.2) over a 7x7 sub-grid centered on the considered ground station (Figure 4-4). This computation is accomplished per each temporal instant of the transmission period. The result is, for a given R_s value, a distribution of E_s/N_0 values (one per each pixel of the 7x7 sub-grid) available per each temporal instant. Such distribution can be converted into a probability density function, as shown in Figure 4-5, from which we can extract a median value with an error-bar determined by its 25th and 75th percentile. Note that Figure 4-5 is just an example but, in general, the probability density function of E_s/N_0 is not symmetrical and the 25th and 75th percentile are not equidistant from the median.

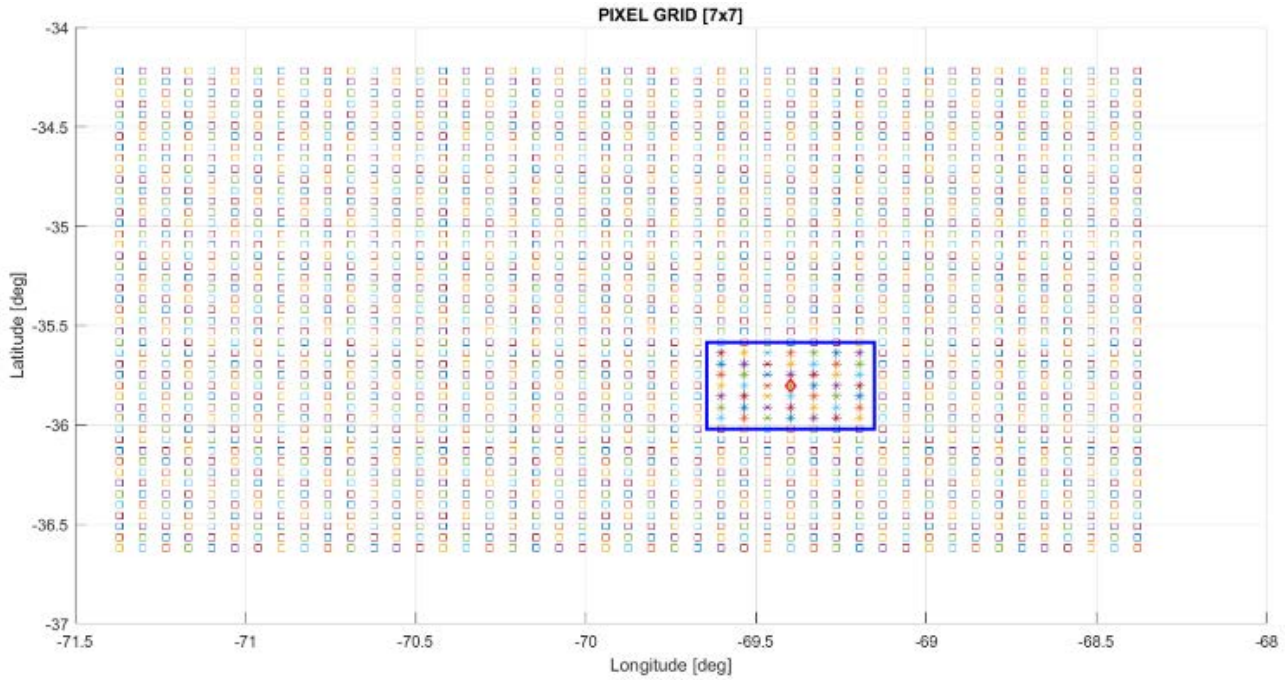

Figure 4-4: Inner domain and 7x7 pixels sub-grid (blue rectangle) centered on ground-station antenna (indicated with a diamond).

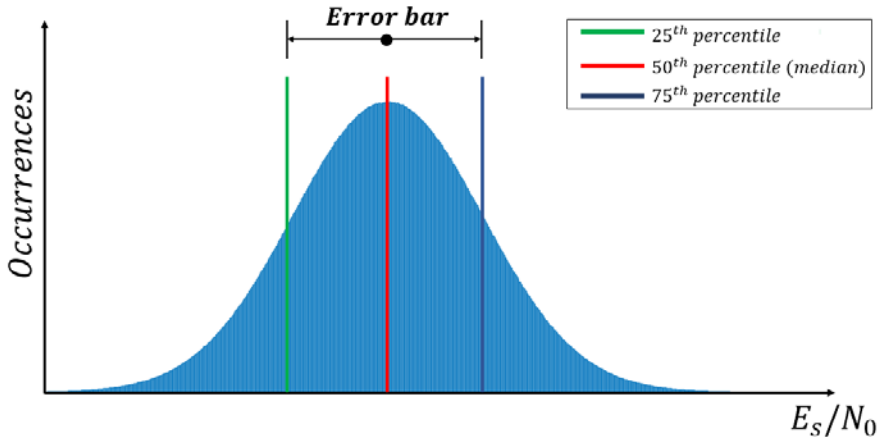

Figure 4-5: E_s/N_0 probability density function for a given temporal instant and a given R_s value: median value (red) with error-bar determined by its 25th (green) and 75th (blue) percentile.

Using this approach, we have tested the model-chain. The validation case is the transmission of August 11, 2018 to Malargüe station: we have compared the E_s/N_0 measured by the TTCP with the one computed with our model chain considering the R_s actually adopted by Hayabusa2 during the transmission. The result of the comparison is in Figure 4-6: blue line is the E_s/N_0 from the TTCP and the pink line is the one simulated by the model-chain (with the corresponding error-bar), the red line is the E_s/N_0 threshold. Note that, for graphical purposes, we have accomplished a linear interpolation of the E_s/N_0 simulated per each hour. The validation shows an excellent agreement between the simulated and measured curves with an average error of about 0.16 dB. Note that the

step down occurring about at 14:40 UTC (that can be observed in both measured and simulated curve) is due to the switch of the transmission from non-coherent to coherent mode that always happen within the first hour of transmission.

For the DBM optimization, we have applied a statistical approach to the R_s computation. Per each of the 7x7 sub-grid point and per each temporal instant we have chosen the highest R_s that allows E_s/N_0 higher than the minimum threshold $E_s/N_0|_{th}$:

$$R_{s_{opt}} = \max_{R_s}\left\{\frac{E_s}{N_0} > \frac{E_s}{N_0}\Big|_{th}\right\} \tag{4.5}$$

Where $R_{s_{opt}}$ is chosen among the list of data-rates of Hayabusa2 and $E_s/N_0|_{th}$ = 2.06 dB. The E_s/N_0 in (4.5) is computed with (4.2) following the statistical approach described above and using L_{atm} and T_B provided by the RPM for the considered pixel and hour. After this computation, we have a 7x7 grid of R_s optimized values per each hour of transmission. To select the optimum R_s of each hour we consider the mode (i.e., the most frequent R_s value occurring in the 7x7 sub-grid) instead of considering the single pixel corresponding to the receiving station. This technique, as it will be clarified in the following, allows to compensate for the potential double-penalty error of the meteorological forecasting model, which consists in the space-time delocalization of a predicted meteorological phenomenon.

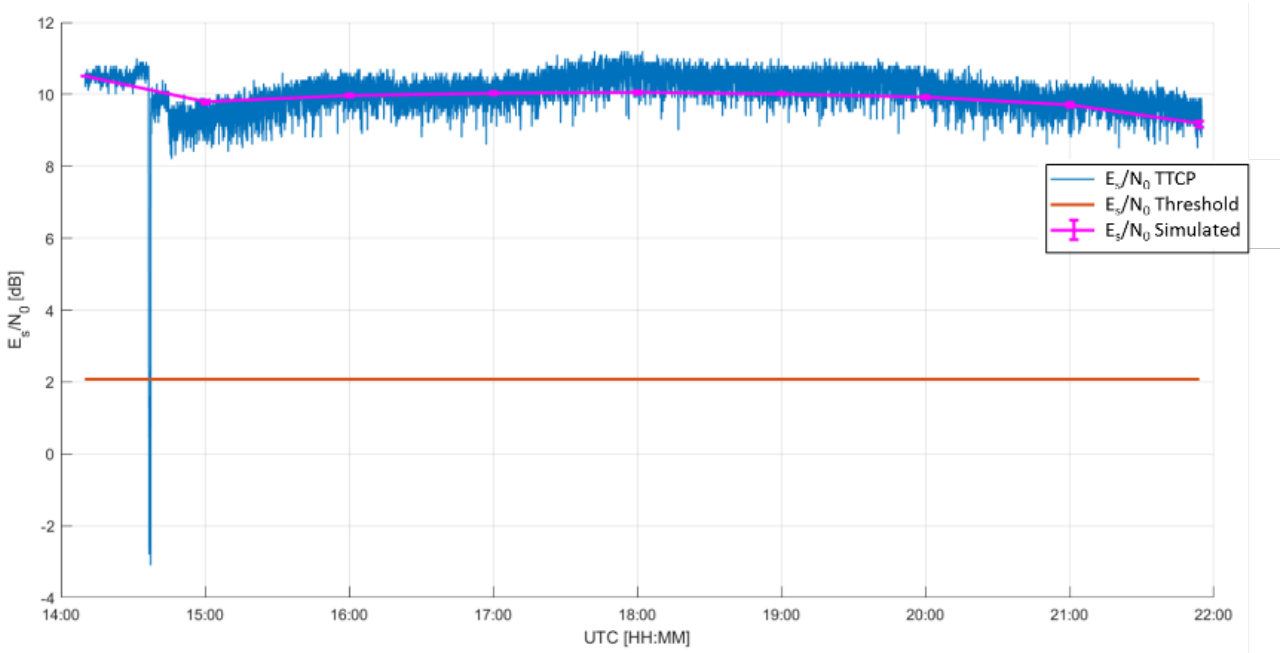

Figure 4-6: Model-chain validation (August 11, 2018, Malargüe)

We have tested the model-chain in an operative context: the operation case is the transmission of November 10, 2018 to Malargüe. On the day before the transmission (i.e., November 9), we have run our model-chain with daily forecasts for the day of 10 November and provided the optimized

R_s with the corresponding E_s/N_0 to the JAXA team. The upper panel of Figure 4-7 shows the comparison of R_s produced by our optimization and the one actually used by Hayabusa2. For the first 2 hours of transmission, Hayabusa2 operated at 8192 symbols per seconds (sps). Since our prediction suggested that the data-rate could be increased up to 32768 sps, from the third hour of transmission JAXA decided to switch from 8192 to 16348 sps. The lower panel of Figure 4-7 shows the E_s/N_0 measured by the TTCP (operating with the "R_s HYB2" of panel a) and the one that would be obtained using our optimized values ("R_s opt." of panel a). As expected, our predicted E_s/N_0 is lower than the one measured, because it corresponds to higher data-rate (i.e., higher transmitted and received data), but is higher than the minimum threshold. This confirms that our optimization would allow a more efficient transmission with higher received data and, at the same time, a level of E_s/N_0 above the minimum threshold. Note that in the lower panel of Figure 4-7 there are two steps down of the E_s/N_0. The first one (occurring at about 14:40 UTC) appears on both TTCP and Optimization curves and is due to the switch from non-coherent to coherent transmission (as previously explained). The second step down occurs at about 15:00 in the TTCP curve and is due to the switch of R_s from 8192 to 16348 sps. If R_s had been further switched to 32768 sps, the TTCP line would be at the same level of the simulated Optimization line.

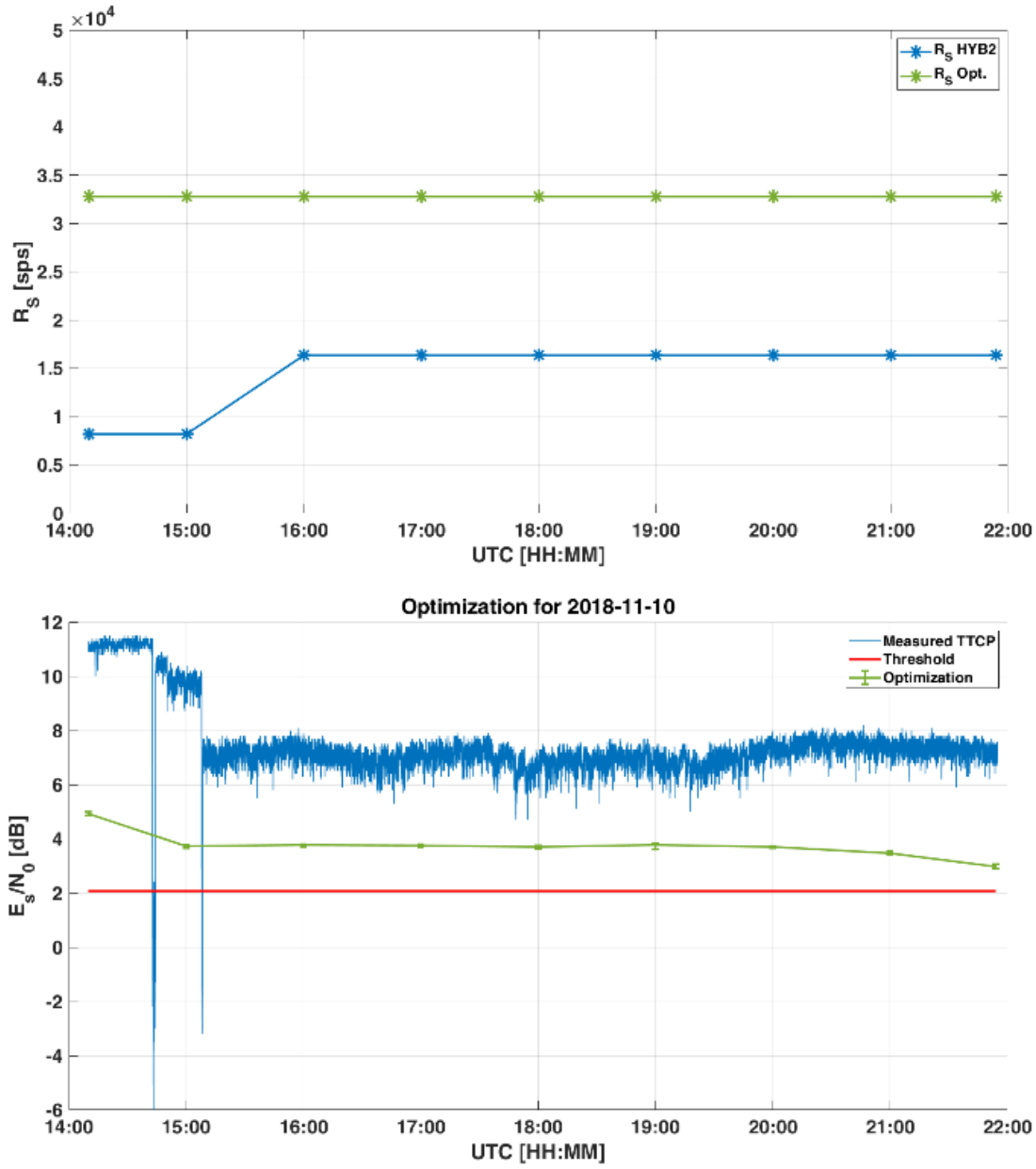

Figure 4-7: Model-chain operation on November 10, 2018, Malargüe: optimized R_s (Opt., green) vs R_s actually adopted by Hayabusa2 (HYB2, blue)

To conclude, Figure 4-8 shows time series of attenuation computed by the RPM per each of the 7x7 pixel during the transmission of November 10, 2018. The picture highlights that our model-chain "sees" a meteorological event (i.e., a humidity peak probably due to a cloud and causing excess attenuation) in the Malargüe pixel at 18:00 UTC and in some surrounding pixels and hours. After the transmission we have checked radiometric measurements (available from the ESA zenithal pointing radiometer sited in Malargüe) and found that no meteorological events where registered on the vertical above Malargüe station during the pass. This means that, probably, the event predicted by our WFM actually occurred in a different position (i.e., in a different pixel): this is an

example of double-penalty error. If we had designed the link using the Malargüe pixel to select the optimal R_s (instead of considering the mode R_s from the 7x7 sub-grid), we would have overestimated the attenuation and undersized the link at 18:00 UTC. This suggests that the proposed statistical approach for the R_s and E_s/N_0 optimization would be a powerful solution to overpass potential model errors, however further analysis on more passes would be required to confirm the findings.

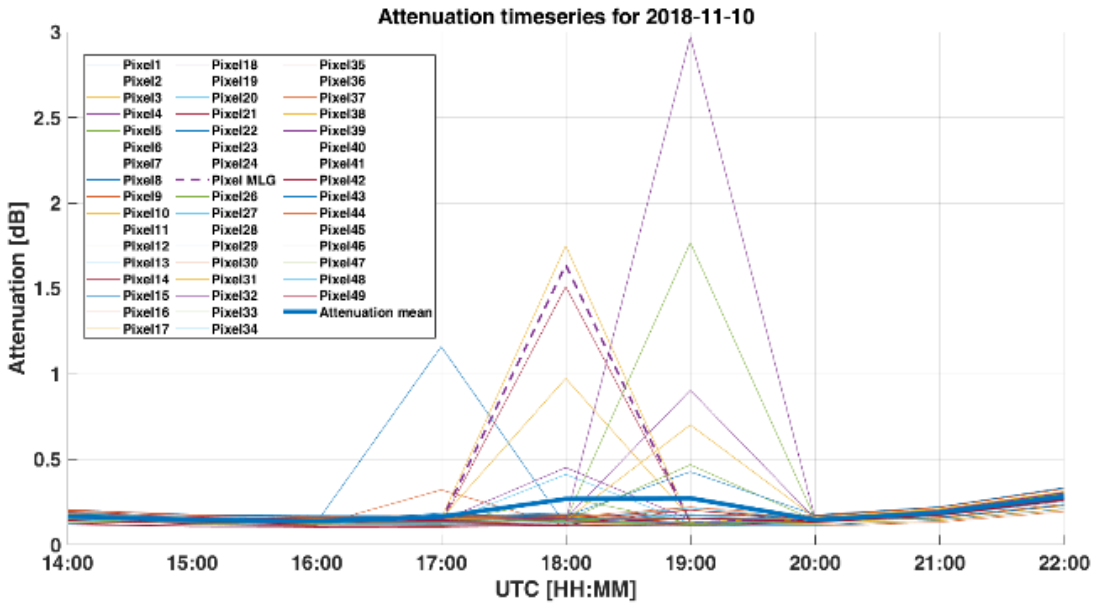

Figure 4-8: Attenuation time-series in Malargüe for each of the 7x7 pixels of the sub-grid domain (10 Nov. 2018). Pixel 1 corresponds to Malargüe.

Chapter 5. Microwave interference source modelling and terrestrial applications

5. I. Introduction

In the framework of the World Radiocommunication Conference 2019 (WRC-19) of the International Telecommunication Union (ITU), Agenda Item 1.13 (AI 1.13) will address the identification and the possible additional allocation of radio-frequency spectrum to the mobile services on a primary basis. Such identification and allocation are required to serve the future development of the International Mobile Telecommunications (IMT) for 2020 and beyond, mainly focused on systems supporting the fifth generation (5G) of cellular mobile communications. The frequency range of interest goes from 24.25 to 86 GHz, which fully covers all the high-frequency bands used or planned by the European Space Agency's space missions for high data rate transmissions.

The use of frequencies at millimeter waves is a key interest of the agency, as these high frequency bands are not as congested as the lower bands and provide several performance advantages. Hence, the need of ensuring a proper protection from the future IMT systems in terms of received radio frequency interference (RFI) has become one of the crucial tasks of the ESA's frequency management office in preparation for the upcoming WRC-19. In addition to data transmission from space, it is necessary to ensure the protection of the adjacent frequency bands used by many earth observation missions equipped with passive sensors. The impact of high levels of unwanted emissions from IMT-2020 devices is a potential threat for such sensitive instruments and could compromise the data quality of future missions.

This chapter shows the potential impact of IMT deployments presenting an in-band spectral overlap with ESA's missions using or planning to use frequency bands allocated to the Earth Exploration-Satellite Service (EESS) and to the Space Research Service (SRS) as follow:

- 25.5-27.0 GHz, allocated to EESS (space-to-Earth) and SRS (space-to-Earth) – already used by EDRS and planned for use by EUCLID, PLATO, WFIRST, MTG, MetOp-SG and many other missions in the near future;
- 31.8-32.3 GHz, allocated to SRS Deep Space (space-to-Earth) – already used by BepiColombo, Hayabusa2 and several NASA missions, and planned for Juice;
- 37.0-38.0 GHz, allocated to SRS (space-to-Earth) – earmarked for future lunar manned missions like the international moon village.

Particular focus is given to the ESA's tracking network and to the earth station (ES) sites located in New Norcia (Australia), Cebreros (Spain), Malargüe Sur (Argentina) and Kiruna (Sweden). The high performance of the deep space stations makes them very sensitive to a potential interference source on ground. Results are shown in terms of required separation distances, i.e. the minimum distance between the earth station and the IMT station ensuring that the protection criteria for the

earth station are met by the emissions of an IMT base station (IMT-BS) or user equipment (IMT-UE).

It is to be noted that transmission media of radiowaves include all possible routes between a radio transmitter and a receiver consisting of free space and atmospheric propagation as well as electromagnetic interaction with the ground surface and surrounding medium. Received interference can derive from several propagation mechanisms including line-of-sight propagation, diffraction, scatter, ducting, reflection/refraction, etc. which strongly depend on climate, radio frequency, link availability, distance and path topography; at any time any of these mechanisms may be present. For this, the ESA analysis adopts the terrestrial propagation modelling of the latest version of Recommendation ITU-R P.452 [61] "Prediction procedure for the evaluation of interference between stations on the surface of the Earth at frequencies above about 0.1 GHz" as the method to assess the interference potential between the IMT terrestrial networks and Earth-to-space receiving stations, and to ensure a satisfactory coexistence.

The chapter is organized as follows: section 5.II recaps all the assumptions for both the ESA's earth stations and the IMT-2020 terrestrial systems, section 5.III describes the adopted methodology and section 5.IV summarizes the compatibility study results.

5. II. Assumptions

5. II.A. ESA's earth stations

To ensure RFI free operations of the receiving earth stations operated by ESA and other space agencies, it is necessary that the emissions of IMT-2020 mobile networks as seen by the earth station be compliant with the relevant ITU recommended protection criteria for SRS and EESS. The criteria mainly depend on the mission type and on the sensitivity of the receiver and are usually expressed as maximum permitted interference density level received by the victim for a given probability of time. Table 5-1 recaps the ITU-R criteria adopted by ESA in the compatibility studies at 26, 32 and 37 GHz.

The knowledge of the earth station characteristics is crucial when performing RFI assessment, as the results vary depending on the antenna performance. In particular, at least the following parameters shall be available when performing this kind of compatibility studies:

1. Maximum antenna gain [dBi] and antenna radiation pattern;
2. Local horizon profile around the station [deg], referred to the antenna radiation center of phase height;
3. Minimum elevation angle [deg] and minimum separation angle [deg]. The latter is defined as the angular difference between the local horizon as seen from the ES and the minimum elevation angle to be considered in a certain direction.

TABLE 5-1: ITU-R RECOMMENDED PROTECTION CRITERIA FOR SRS AND EESS EARTH STATIONS

Space-to-Earth frequency band and service	**ITU-R Rec.**	**Permissible interference level**	**Probability**
26 GHz (EESS non-geostationary)	SA.1027 [163]	*Long-term* –143 dB(W/10MHz) *Short-term* –116 dB(W/10MHz)	*Long-term* 20 % *Short-term* 0.005 %
26 GHz (SRS)	SA.609 [164]	-156 dB(W/MHz)	0.1 % (unmanned missions) 0.001 % (manned missions)
32 GHz (SRS deep space)	SA.1157 [165]	-217 dB(W/Hz)	0.001 %
37 GHz (SRS)	SA.1396 [166]	-217 dB(W/Hz)	0.1 % (unmanned missions) 0.001 % (manned missions)

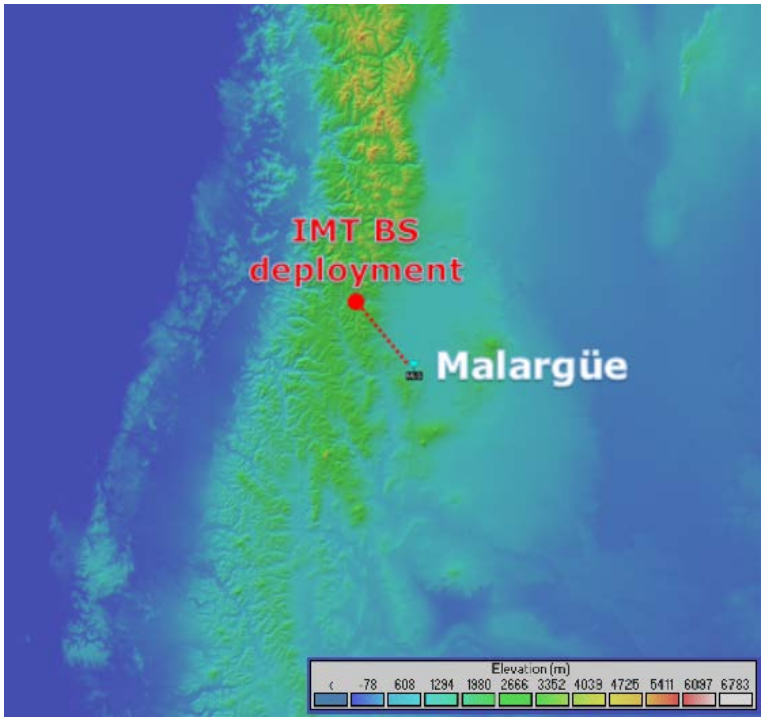

Figure 5-1: Example of Terrain heights map around the Malargüe Deep Space station in Argentina

These parameters are necessary to compute the receiving gain towards the horizon in a given direction (azimuth cut). Moreover, the ES-related information below is required to predict the propagation channel behavior:

4. Absolute antenna radiation center of phase height [m];
5. Terrain heights map, covering any possible path between the considered station and any given points where IMT deployments are expected. The data collected by the Shuttle Radar Topography Mission (SRTM) have been used, in particular the 1-arcsec resolution terrain profile data, with a projected ground resolution of about 30 m. Figure 5-1 shows an example of terrain heights map around the ESA's Deep Space Antenna located in Argentina, close to the city of Malargüe.

In the compatibility studies, the earth station system is considered as a static element, i.e. the antenna is modelled with a fixed static gain towards the local horizon for each considered azimuth cut. This assumption is required given the fact that the considered ESs support a wide variety of space missions (EESS and SRS). Indeed, the trajectory of a spacecraft varies considerably from one mission to another. In particular, all types of missions can be envisaged for SRS (near Earth), ranging from low Earth orbits (LEO) to missions around one of the Lagrange points, and including geo-synchronous Earth orbits (GEO), highly elliptical orbits (HEO) or lunar missions. Similarly, SRS (deep space) missions generally target planets in the ecliptic plane, but can stay for an extended period in near earth orbits, or depart from the ecliptic plane when chasing comets, asteroids or other bodies.

5. II.B. IMT-2020 Base Stations

Relevant expert groups provided the IMT network specifications, which were then formalized by the ITU study groups and universally adopted in compatibility studies. The IMT base stations will exploit Massive Multiple-Input & Multiple-Output (MIMO) techniques, able to serve more than one user at the same time by adopting beamforming antenna arrays with highly directional antennas. Figure 5-2 shows an example of the IMT 5G antenna pattern at 24.25 - 33.40 GHz, when assuming zero tilt (both mechanical and electrical). The beamforming antenna array is modelled in the recommendation ITU-R M.2101 [167]. It consists of a number of identical radiating elements with a fixed separation distance, identical radiation patterns and having maximum directivity along the same axis. A weighting function is used to direct the beam in various directions. The total antenna gain is the sum (logarithmic scale) of the array gain and the element gain.

The elevation angle θ is defined between "$\theta_{min} = -90° - \theta_{mtilt}$" (down) and "$\theta_{max} = 90° - \theta_{mtilt}$" (up), where $\theta = 0°$ is the horizon and θ_{mtilt} is the perpendicular angle to the array antenna aperture, i.e. the mechanical tilt. The azimuth angle is denoted as φ and it is defined between −180° and 180°.

Network topology and IMT-BS characteristics differ among the following deployment scenarios, as defined by the relevant IMT experts [169]:

- outdoor suburban open space,
- outdoor suburban,

- outdoor urban,
- indoor.

This study addresses all possible scenarios at the three considered frequency bands (26, 32 and 37 GHz), except for indoor, which is expected to be the less critical in terms of risk for interference. Dynamic aggregated analysis and sensitivity analyses were also considered to assess the impact of any possible future deployment. For what concerns interference due to User Equipment (UE) emission, analyses have shown that the latter does not contribute much to the aggregate interference because of a high clutter loss value and the indoor/outdoor attenuation, which would limit the impact of indoor transmitters.
The following subsections aim at describing the IMT-2020 parameters, split in three different categories: static, dynamic and aggregation parameters.

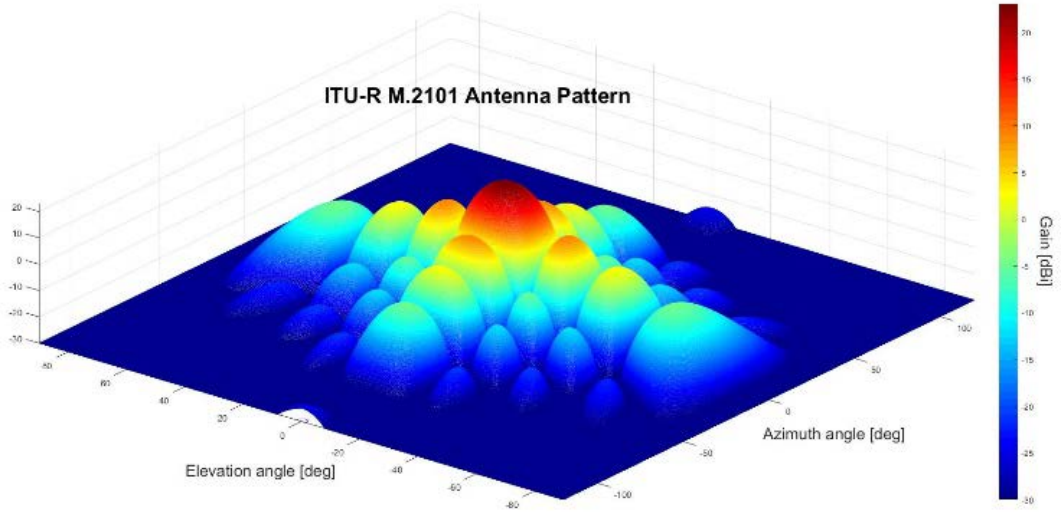

Figure 5-2: IMT-2020 5G antenna pattern at zero tilt (24.25 - 33.40 GHz)

➢ *Static parameters*

Table 5-2 recaps the static parameters considered in the compatibility studies. Basic assumption of the study is to consider the IMT-BS antenna panel pointing towards the ES, i.e. having a mechanical azimuth-pointing equal to 0 deg. This assumption is crucial to reproduce the worst-case scenario in terms of IMT-2020 deployments around the considered ground station.

TABLE 5-2: IMT-2020 CHARACTERISTICS – STATIC PARAMETERS (OUTDOOR SUBURBAN/URBAN HOTSPOTS [169])

Parameter		**Value**	**Unit**
BS antenna height (radiation center)	h_{BS}	6 or 15	m
UE antenna height	h_{UE}	1.5	m
Mechanical tilt (in elevation)	θ_{mtilt}	-10.0 or -15.0	deg
BS maximum coverage angle in azimuth		120	deg
Antenna pattern	ITU-R M.2101	[167]	-
Element gain	$G_{E,max}$	5	dBi
Horizontal 3 dB beamwidth of single element	φ_{3dB}	65	deg
Vertical 3 dB beamwidth of single element	θ_{3dB}	65	deg
Horizontal front-to-back ratio	A_m	30	dB
Vertical front-to-back ratio	SLA_v	30	dB
Horizontal radiating element spacing	d_H/λ	0.5	m/m
Vertical radiating element spacing	d_V/λ	0.5	m/m
Frequency range		**24.25 - 33.40**	**GHz**
Array configuration (rows × columns)	$N_V \times N_H$	8 × 8	-
Power per element	P_E	10	dBm
Total array power	P_{array}	28	dBm
Ohmic losses	L_{array}	3	dB
Maximum array gain	$G_{TX,max}$	23	dBi
Maximum EIRP	$EIRP_{max}$	48	dBm
Associated bandwidth	BW	200	MHz
Frequency range		**37.00 - 43.50**	**GHz**
Array configuration (rows × columns)	$N_V \times N_H$	8 × 16	-
Power per element	P_E	8	dBm
Total array power	P_{array}	29	dBm
Ohmic losses	L_{array}	3	dB
Maximum array gain	$G_{TX,max}$	26	dBi
Maximum EIRP	$EIRP_{max}$	52	dBm
Associated bandwidth	BW	200	MHz

➢ *Dynamic parameters*

The nature of the IMT-2020 systems suggests not considering the IMT-BS as a fully static element in the studies. It is indeed recognized that the gain (and EIRP) of the IMT-BS varies in time, due to the fact the antenna array will not be pointing towards a fixed direction. This implies considering dynamic scenarios and simulations, which shall represent a real environment by considering the electrical pointing of the IMT-BS antenna, i.e. the movement of the IMT-UE inside the coverage area. In this respect, a gain (or EIRP) probability distribution has to be defined to statistically model such behavior.

The azimuth electrical beam pointing φ_{escan} is assumed normal distributed in azimuth $\mathcal{N}(\mu, \sigma^2)$; the elevation tilt $\theta_{\mathrm{tilt\,TOT}}$ distribution is derived from the distribution in distance of the IMT-UE from the IMT-BS, and such distance is assumed to be:

- Log-normal distributed for an Outdoor Suburban Open Space base station;
- Rayleigh distributed for an Outdoor Suburban/Urban Open Space base station.

Figure 5-3 explains the definition of the total tilt, as combination of a static mechanical tilt and a varying electrical tilt.

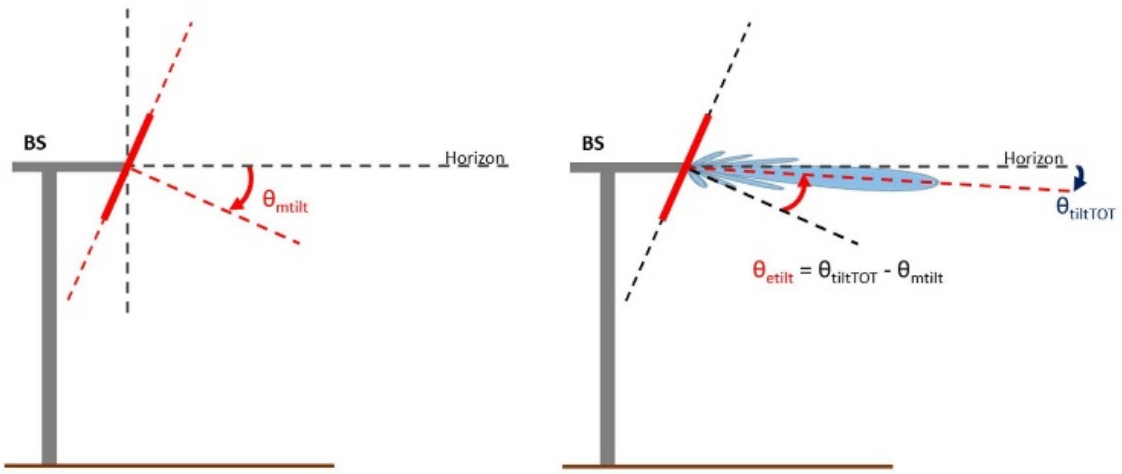

Figure 5-3: IMT-2020 BS (Suburban hotspot) – Definition of total tilt $\theta_{\mathrm{tilt\,TOT}}$

It is assumed to have only one single UE per BS, without considering the system as multi-beamforming MIMO. Taking into account a single beam is considered a worst-case assumption, due to the fact that in MIMO scenarios the gain would not correspond to the maximum obtainable value of the array.

From these assumptions, it is possible to determine the antenna gain distribution towards the victim earth station, using the antenna pattern from recommendation ITU-R M.2101 [167]. The distribution is assumed the same for each considered azimuth since it has been computed assuming a flat terrain, i.e. horizon 0 deg. The latter is a worst-case assumption given that higher horizon angles would provide lower antenna gain values (the antenna is mechanically pointing towards ground).

The IMT-2020 5G networks will be based on a Time Division Duplex (TDD) transmission form. TDD refers to duplex communication links where uplink is separated from downlink by the allocation of different time slots in the same frequency band. It is a transmission scheme that allows asymmetric flow for uplink and downlink data transmission. Users are allocated time slots for uplink and downlink transmission. Additionally, a network loading factor (NLF) was considered, defined as the ratio of the time between the actual usage time of the network and the total time that it could be in use.
Considering the two aforementioned characteristics, the EIRP probability density function can be obtained by convolving the transmit power probability density function with the transmitter gain distribution under the assumption of statistical independency among all variables.

➢ *Aggregation parameters*

Aggregated scenarios are to be considered as examples only, since they have been simulated by considering a series of approximations and assumptions. In particular, clutter loss modelling is strongly dependent on the deployment location and its surroundings. Proper aggregated analyses shall be considered on a case-by-case basis during actual coordination processes.

Taking into account the maximum density of IMT-2020 base stations per km^2 for a given deployment scenario, the aggregated emission of IMT-BS clusters is computed by adopting a Monte-Carlo simulation method and assuming the following:

- One-year simulation time with a 10-sec sampling time;
- Each IMT-BS is modelled by taking into account static and dynamic parameters above-mentioned;
- Dynamic parameters referring to a single simulated IMT-BS are assumed uncorrelated among themselves (electrical azimuth pointing, IMT-UE distance from BS, TDD and NLF);
- Distributions are recomputed from scratch from one IMT-BS to another, assuming full uncorrelation among IMT-BSs;
- The generated random processes are assumed white, i.e. with no correlation among realizations;
- The final aggregated EIRP distribution is obtained by convolving the individual IMT-BS distributions accordingly;
- The equivalent emission of the cluster is assumed to be compressed in a single point on ground, representing the equivalent contribution given by a cluster occupying an area of 1 km^2.

5. III. Methodology

The determination of the coordination area is based on the concept of the permissible interference power at the antenna terminals of a receiving terrestrial station, i.e. earth station. Hence, the path attenuation associated to the terrestrial propagation channel is required to limit the level of interference between a transmitting terrestrial station (IMT-2020 system) and a receiving station. This is represented by the "minimum required loss" to ensure that the interference power level is below the maximum permitted interference density level received by the victim for a given probability p% of time. Such required loss can be easily converted into a minimum separation distance d_{sep} [km], which ensures no risk for interference for the analysed earth stations (EESS or

SRS), i.e. the IMT-2020 terrestrial systems being compliant with the relevant ITU-R recommended protection criteria.

Instead of exploiting the propagation channel behavior for facilitating the communication, it is used to assess the interference potential between the terrestrial and Earth-space systems, predicted with reasonable accuracy to ensure the satisfactory coexistence of both. The many propagation mechanisms considered by ITU-R P.452 [61] are included in the analysis, since at any time more than one may be present. The final combined loss is basically equal to the smallest propagation component taken into account.

Dynamic analyses, in which some of the variables are assumed to be variant in time (see section 5. II), have been performed following the so-called Time Variant Gain (TVG) methodology as defined in Appendix 7, Annex 6.4, ITU Radio Regulations, Appendices, Edition 2016 [168]. The Time-Variant Gain (TVG) method ideally requires the cumulative distribution of the time-varying horizon antenna gain. If compared with the Time-Invariant Gain (TIG) method, the TVG method usually produces smaller distances, but requires greater computational effort as well as the determination of the horizon gain cumulative distribution for each propagation path to be considered. The TVG method closely approximates the convolution of the distribution of the time-varying quantity of interest with the propagation mode path loss. TVG may however produce slightly smaller distances than those obtained by an ideal convolution; and the latter cannot be implemented due to the limitations of the current model for propagation channel prediction. The TVG method can be applied considering the IMT-2020 5G base station transmitter antenna gain (IMT-BS tracking the IMT-UE) with a Time-Variant Gain. The propagation mode required distance, at the azimuth under consideration, is taken as the largest distance developed from a set of calculations, each of which is based on the following equation:

$$L_{req}(p_v) = P_t + G_t(p_n) + G_r - I(p) \tag{5.1}$$

where

- P_t is maximum available transmitting power level (dBW) in the reference bandwidth at the terminals of the antenna of a transmitting terrestrial station, i.e. IMT-BS;
- $I(p)$ is the permissible interference level (dBW) in the reference bandwidth to be exceeded for no more than p% of the time at the terminals of the antenna of a receiving earth station that may be subject to interference;
- $G_t(p_n)$ is the horizon gain of the transmitting antenna (dBi) that is exceeded for p_n% of the time on the azimuth under consideration;
- G_r is gain towards the physical horizon on a given azimuth (dBi) of the victim earth station antenna;
- $L_{req}(p_v)$ is the propagation mode minimum required loss (dB) for p_v% of the time; this loss must be exceeded by the propagation mode predicted path loss for all possible p_v% values retrieved from the considered gain complementary cumulative distribution function. p_v is the time percentage that approximates the convolution between the variable horizon gain and the propagation mode path loss and is given by

$$p_v = \begin{cases} 100\dfrac{p}{p_n} & \text{if } p_n \geq 2p \\ 50 & \text{if } p_n < 2p \end{cases} \tag{5.2}$$

The values of the percentages of time, p_n, to be used are determined in the context of the complementary cumulative distribution of the horizon antenna gain. This distribution needs to be developed for a predetermined set of values of horizon antenna gain spanning the range from the minimum to the maximum values for the azimuth under consideration. In other words, p_n is the percentage of time that the horizon antenna gain exceeds the n-th horizon antenna gain value. For each value of p_n, $G_r(p_n)$ is used in the equation to determine a propagation mode minimum required loss. The propagation mode predicted path loss is to exceed this propagation mode required loss for no more than p_v% of the time. The propagation mode required distance is then the maximum distance in the series of propagation mode distances that are obtained for any value of p_n.

Alternatively, a modified version of the Time Variable Gain (TVG) methodology given in [168] can be used to approximate the convolution of the distributions of the transmitter antenna gain (IMT-BS tracking the IMT-UE), the transmitting power (TDD and NLF) and the propagation model. Equation (5.2) can be rewritten as follow:

$$L_{req}(p_v) = EIRP(p_n) + G_r - I(p) \tag{5.3}$$

where $EIRP(p_n)$ is the EIRP (dBW) in the reference bandwidth at the terminals of the antenna of a transmitting terrestrial station that is exceeded for p_n% of the time on the path under consideration.

Note that the use of the presented methodology allows to cover all possible orbits from the victim receiver point of view and consider, at the same time, the variability in terms of electrical pointing of IMT-2020 BS systems.

5. IV. Results

Terrestrial radio-propagation simulations have been run following the methodology described in section 5. III, given the assumptions in section 5. II and applying ITU-R P.452 [61]. Figure 5-4 shows a detailed example of a 26-GHz simulation for a sample azimuth cut (339 deg) around the Malargüe Deep Space Station in Argentina. The top panel shows the terrain height profile (blue curve) taken into account for the computation of the propagation path loss, while the bottom panel shows the required path loss (green curve), together with the obtained path loss (red curve). For this particular case, the minimum separation distance has to be larger than 91.6 km, as this is the last point in distance which obtained propagation loss exceeding the required one. It can be noted how the obtained propagation loss does not simply correspond to the free space propagation loss (cyan dotted curve) and, under special circumstances, the actual propagation conditions could be more advantageous (as evident at ~15 km distance, where the red curve goes below the free space baseline).

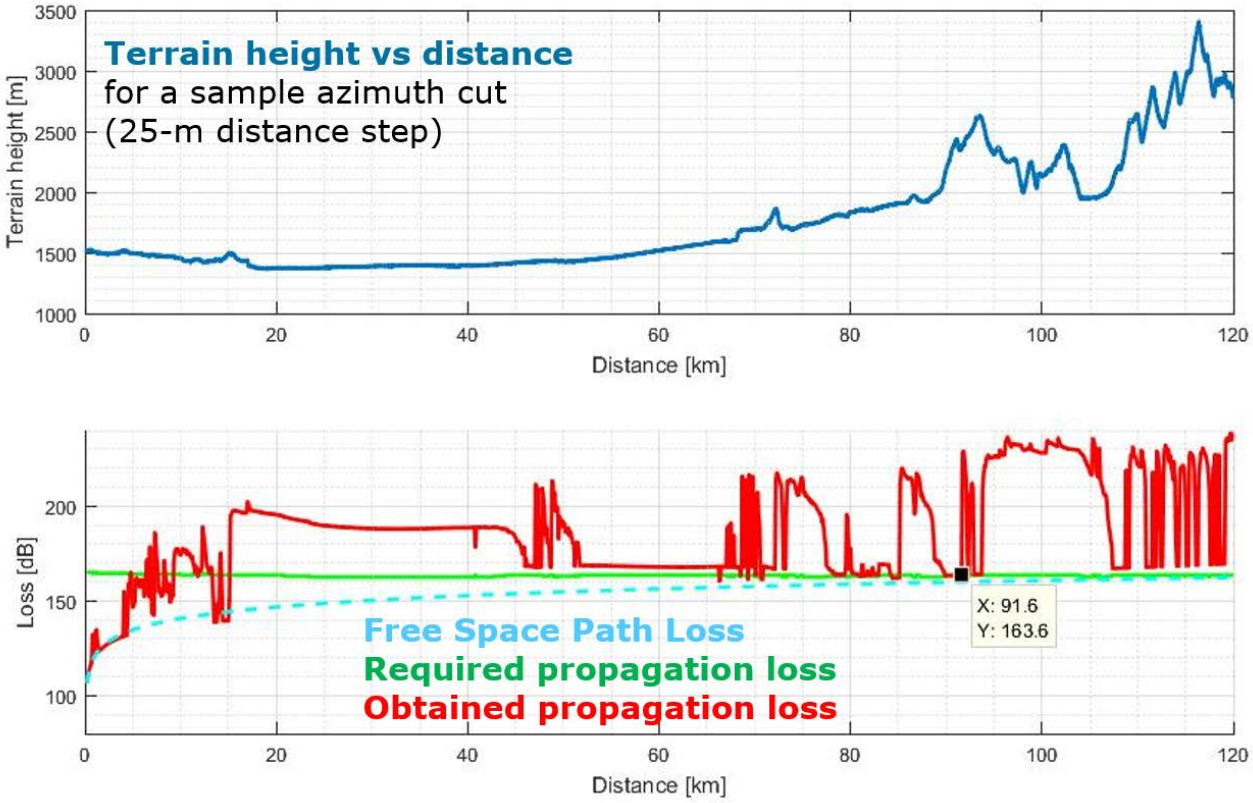

Figure 5-4: Simulation example at 26 GHz for an azimuth cut around the Malargüe Deep Space Station in Argentina (Outdoor Suburban IMT deployment, single entry)

Figure 5-5 shows another simulation example in terms of coordination contour (minimum separation distances) around the Malargüe Deep Space Station in Argentina (Outdoor Suburban IMT deployment, single entry IMT-BS with variable transmitter gain). Grey circles indicate distances from the Malargüe Deep Space Station at 10 km step. IMT-BS stations outside the contour would meet the earth station protection criteria. Inside the contour, the figure also shows the protection level violations around the station, where the violation is defined as the difference between the required and the obtained propagation losses. The map displays colored areas where the protection criterion is exceeded, i.e. when the required losses are larger than the obtained ones. If the criterion is respected, the areas are displayed in white. IMT-BS stations inside but close to the contour may meet the earth station protection criteria for specific azimuth mechanical pointing of the BS, while IMT-BS closer to the ES would not meet the criteria in any case, thus defining an exclusion zone or contour.

The variability of the obtained separation distances along the considered directions (1-deg step azimuth cuts) is mainly due to the following:

- the specific terrain heights for the considered cut, which lead to different radio-propagation loss along the signal path;

- the local horizon profile as seen from the antenna radiation center of phase height, which impacts the horizon antenna gain to be accounted for in (5.1) and (5.3).

Table 5-3 finally shows the maximum obtained coordination distances for all ESA's earth stations considered in the compatibility studies. As mentioned above, the results highly vary among stations, as they strongly depend on the antenna horizon mask and the local terrain profile along the considered direction. It is therefore clear that no generic coordination contour can be defined for a given ground station type, and ad-hoc studies must be carried out to determine the minimum distance required for a specific station to ensure an acceptable risk for interference, i.e. compliance with the ITU-R recommended levels in Table 5-1.

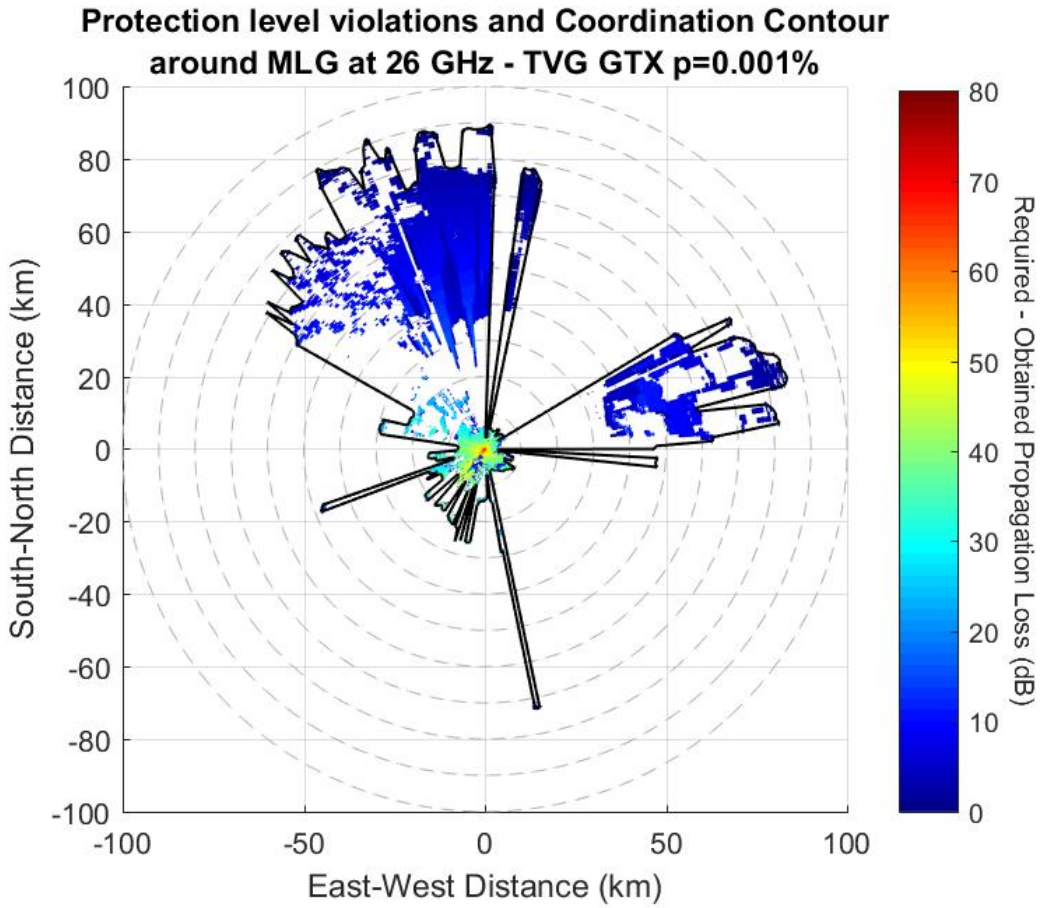

Figure 5-5: Simulation example at 26 GHz – Separation distances (coordination contour) around the Malargüe Deep Space Station in Argentina (Outdoor Suburban IMT deployment, single entry)

TABLE 5-3: MAXIMUM COORDINATION DISTANCES FOR THE ESA'S EARTH STATIONS CONSIDERED IN THE COMPATIBILITY STUDIES

Space-to-Earth frequency band and service	**Maximum coordination distance**			
	Kiruna, Sweden	**New Norcia, Australia**	**Cebreros, Spain**	**Malargüe, Argentina**
26 GHz (EESS non-GEO)	5 km	-	-	-
26 GHz (SRS)	40 km	79 km	31 km	92 km
32 GHz (SRS deep space)	-	51 km	31 km	67 km
37 GHz (SRS)	-	79 km	31 km	101 km

Chapter 6. Clear-Sky dynamical detection from geostationary infrared imagery

6. I. Introduction

Hazard and meteorological applications continuously rely on remote sensing techniques and, in the past decades, the international scientific research community has recognized the satellites to be vital in detecting and monitoring natural and environmental phenomena. In several countries or critical situations of emergency, satellite observations are the only economically feasible way to detect and track these phenomena and eventually mitigate the repercussions [170].
Space borne radiometers offer the possibility to sense the environment by exploiting thermal infrared and optical channels [173]-[174]. These measurements are obtained from both geosynchronous-Earth-orbit (GEO) and low-Earth-orbit (LEO) satellites, thus offering different spatial and temporal resolutions [173]-[185]. This translates into having different and complementary advantages, and the instrument to be used depends on the considered application [180].

For nearly real-time applications, geostationary platforms often are a mandatory choice as they are able to observe the same Earth scene with a rapid and continuous sampling rate [171]. However, given the large distance from Earth, they have the disadvantage of a low spatial resolution (typically larger than a few kilometers). On the other hand, for LEO payloads, the revisit time may be even longer than 12 hours but the spatial resolutions vary from several kilometers down to meters, depending on the wavelength [173].

Many operational services require short time resolutions with relatively short data latency in order to operate in near real-time. Many works stated the importance of operational meteorological satellites for the retrieval of routine products and long-term analyses [170], showing the possibility of developing detection algorithms exploiting GEO satellites [170]-[172]-[198]. Most of these approaches are designed on spatially-based algorithms, i.e. they consider a set of spatial thresholds to be contextually applied in absolute or differential way with respect to the averaged scene around the pixel of interest [173]-[174]-[191]. Following a purely spatial contextual algorithm could be disadvantageous in certain conditions, as the temporal trend information is not exploited to add robustness to the system (especially when a time correlation exists between two consecutive observations) [199]-[203].

This chapter aims at defining a generalized remote sensing technique, which implements a modified version of the well-known Kalman filter [177]-[179], [181]. Roughly speaking, the Kalman filter is a recursive algorithm able to estimate the true state of a system on the basis of noisy measurements and has long been considered the optimal solution to many tracking and data prediction tasks [181], providing linear, unbiased estimations of the states of a system. It has been used in a large variety of applications, [181]-[179]-[204], and it is still a very popular solution in

several science fields, such as supervisory management systems [175], as well as data fusion [176], among the most recent examples. The Kalman filter typically works in a time-based domain and is able to take into account multiple representations of the same observed scene (e.g. multispectral measurements). In this chapter, we provide a detailed formulation of a Kalman-based anomaly masking (KAM) technique, which can suit most of the Earth Observation and remote sensing applications characterized by recurrent observations of the same scene in a reasonably short time-interval [182]-[183]. The possibility of exploiting the time-evolution information of the observations is indeed one of the elements of novelty of the presented approach, adding robustness to the detection algorithm when persistent anomaly conditions are observed for a relatively large area in space (critical condition for spatial–based detection algorithms, e.g. [174]- [191]).

As real example of application, the KAM approach is applied to detect clear-air anomalies, making use of visible-infrared (VIS-IR) passive measurements from the Spinning Enhanced Visible and Infrared Imager (SEVIRI) aboard the GEO Meteosat Second Generation satellite. We follow a purely temporally-based approach in order to detect abnormal behaviors of the spectral radiance [182]. The clear-air KAM estimate relies on a background model of the daily measurement cycle of the considered pixel in pure clear-sky conditions. If the measurement significantly deviates from its expected value as predicted by the algorithm (a-priori state), the system identifies the presence of an anomaly, which is classified as a non-clear air scenario. The difference between the actual scenario and the corresponding a-priori Kalman estimates is therefore the main driver. Practically speaking, a clear-air classification only happens if the measurements strictly satisfy several multispectral conditions, which refer to the a-priori estimates and the pixel models. The filter updates the a-posteriori states depending on the detection outcome: the clear-sky model dominates only in presence of an anomaly, otherwise, the filter follows the actual measurements.

An important add-on value of the KAM approach is to be able to provide a-priori estimates of the scenario, exploiting the previous Kalman filter states and making use of the pixel models. This allows to have an equivalent clear-air radiance which is expected to be measured in absence of anomaly (for instance, in absence of cloud coverage). In such a way, the algorithm results globally applicable, since the estimates are computed from the pixel models and the thresholds can be set independently from the area of interest.

The chapter is structured as follow. Section 6.II presents the mathematical formulation of the modified Kalman filtering technique, which can be easily tailored to accommodate several applications. Section 6.III describes GEO measurements used to test and validate the approach, whereas section 6.IV provides detailed information on the actual filter tailoring for clear-air masking. Eventually, section 6.V shows an inter-comparison in terms of clear-air detection with respect to a highly assessed Cloud-Mask product using the same input measurements.

6. II. Modified Temporal Kalman Filter

Hereby we present a modified version of the well-known Kalman filter [181]. Such filter can theoretically suit most of the Earth Observation and remote sensing applications characterized by recurrent observations of the same scene in a reasonably short time interval. The proposed KAM filter works in a time-based domain and is able to take into account multiple representations of the same observed scene (e.g., multispectral measurements).

In the following paragraphs we assume time-discrete observations equally spaced by a constant time sampling T_s. Moreover, a daily cycle T_c is assumed. The index k indicates the considered time step $k = 1, \dots , T_s/T_c$. The filter can be easily adapted to operational situations in which the time-sampling is not uniform, as long as the measurements are recurrent, i.e. the correlation between two consecutive observations is not null. The Kalman nomenclature and the adopted vector notation are summarized in Table 6-1.

TABLE 6-1: MODIFIED TEMPORAL KALMAN FILTER, SUMMARY OF VARIABLES AND THEIR DEFINITIONS WITH N THE NUMBER OF AVAILABLE OBSERVATIONS SPANNED BY THE INDEXES I=1,…,N; J=1,…,N

Variable	Definition	Dimension
$\boldsymbol{z}_k$	True observation vector	(n×1)
$\hat{\boldsymbol{z}}_k$	Actual observation vector (known)	(n×1)
$\boldsymbol{\varepsilon}_k$	Associated observational error	(n×1)
$\boldsymbol{R}_k$	Observation noise covariance matrix (known)	(n×n)
$\boldsymbol{m}_k$	Background model vector (known)	(n×1)
$\boldsymbol{\sigma}_k^m$	Background deviation vector (known)	(n×1)
$\boldsymbol{A}_k$	State transition matrix	(n×n)
$\boldsymbol{Q}_k$	Process noise covariance matrix	(n×n)
$\boldsymbol{x}_k^-$	Kalman a-priori state vector	(n×1)
$\boldsymbol{x}_{k-1}^+$	Kalman a-posteriori state vector	(n×1)
$\boldsymbol{P}_k^-$	Kalman a-priori error covariance matrix	(n×n)
$\boldsymbol{P}_{k-1}^+$	Kalman a-posteriori error covariance matrix	(n×n)
$\boldsymbol{K}_k$	Kalman gain matrix	(n×n)
$\boldsymbol{t}_k$	Anomaly threshold dynamic vector	(n×1)
$\boldsymbol{t}_m$	Maximum threshold vector	(n×1)
$\boldsymbol{\sigma}^t$	Anomaly confidence interval vector	(n×1)

6. II.A. Kalman theoretical background

We consider a number of n representations of the same scenario (e.g., a multispectral characterization of the scene with n observations). The actual observation vector $\hat{\boldsymbol{z}}_k$ (n×1) is composed by the observed values of the scene at the instant k (e.g., measured radiances at n different frequencies as measured by the sensors):

$$\hat{\boldsymbol{z}}_k = \boldsymbol{z}_k + \boldsymbol{\varepsilon}_k = \begin{pmatrix} z_1 + \varepsilon_1 \\ z_2 + \varepsilon_2 \\ z_3 + \varepsilon_3 \\ \vdots \\ z_n + \varepsilon_n \end{pmatrix}_k = \begin{pmatrix} \hat{z}_1 \\ \hat{z}_2 \\ \hat{z}_3 \\ \vdots \\ \hat{z}_n \end{pmatrix}_k \tag{6.1}$$

where $\boldsymbol{z}_k$ (n×1) is the true observation vector, containing the true values of the scene, whereas $\boldsymbol{\varepsilon}_k$ represents the observational error associated to each measurement. By definition, the measurements $\hat{\boldsymbol{z}}_k$ are affected by various error sources (random and/or systematic) and thus deviate from their true value $\boldsymbol{z}_k$ with possibly cross-correlated errors [189]. Hence, the need of defining the covariances among noise pairs at the timeslot k, forming the observation noise covariance matrix $\boldsymbol{R}_k$ (n×n) defined as

$$\boldsymbol{R}_k = \begin{pmatrix} R_{11} & R_{12} & R_{13} & \cdots & R_{1n} \\ R_{21} & R_{22} & R_{23} & \cdots & R_{2n} \\ R_{31} & R_{32} & R_{33} & \cdots & R_{3n} \\ \vdots & \vdots & \vdots & \ddots & \vdots \\ R_{n1} & R_{n2} & R_{n3} & \cdots & R_{nn} \end{pmatrix}_k \tag{6.2}$$

The covariances among noise pairs, i.e. elements $\{R_{ij}\}_k$, are defined as follows:

$$\{R_{ij}\}_k = \{E[(\hat{z}_i - z_i)(\hat{z}_j - z_j)]\}_k \tag{6.3}$$

where $\hat{z}_{i,j}$ and $z_{i,j}$ are elements of the actual and true observation vectors, respectively. The operator E is the expected value operator and the indexes $i = 1 \div n$ and $j = 1 \div n$ refer to rows and columns of the matrix, respectively. In other words, the observation noise covariance matrix $\boldsymbol{R}_k$ defines possible mutual correlations among mean observational errors, associated to the measurements.

The state transition matrix $\boldsymbol{A}_k$ (n×n), also known as fundamental matrix, defines how two consecutive states are linked to each other [181]. There are several ways to define and retrieve the best fundamental matrix for a given application, often making use of Laplace transforms or Taylor-series expansions. Once we have the fundamental matrix $\boldsymbol{A}_k$ that fits our application, we can simply propagate states forward by matrix multiplication, by properly taking into account the sampling time [177]. For polynomial Kalman filters, the state transition matrix is often a function of time, computed by applying a polynomial expansion or a best-fitting technique over a consistent set of data [178]. For our purposes, dealing with discrete processes, we can compute the state transition matrix in a variety of ways, depending on the number of considered channels as well as their correlation, i.e. whether considering cross-channel relationships would increase robustness or not. Generally speaking, the state transition matrix can be obtained by exploiting a-priori models already available or exploiting pixel observation models characterizing the nominal behavior of a certain observed scenario. Of course, a mix of the two approaches can also be considered for some applications, i.e. physically-based models which need a set of nominal observations to fine-tune their trend.

In many applications, the fully-empirical approach is the only possible one, especially for global-scale applications in which a global applicable physical model is a challenging and hazardous choice. We can therefore exploit a background model vector of the considered scenario $\boldsymbol{m}_k$ (n×1), describing what one would expect if the observed scenario were nominal. The background model is to be intended as an independent source of information, which can be generally applicable, as a global-scale generic model, or even more accurate, e.g. seasonal pixel models for given geographical areas. A nominal scenario is identified as, for instance, a set of measurements converging to a well-defined mean value (e.g. radiances in clear air conditions) with as little associated noise as possible. In an ideal world, the background model vector corresponds to both actual and true observation vectors if the scenario is nominal.
For the scope of this work, let us suppose a linear relationship between two consecutive states and consider the relationship between the representations i of two consecutive states k and (k-1), i.e. $\boldsymbol{A}_k$ is a diagonal matrix. So doing, the elements of the state transition matrix depend on the background model vectors as follows:

$$\begin{cases} \{A_{ii}\}_k = \dfrac{\{m_i\}_k}{\{m_i\}_{k-1}} \\ \{A_{ij}\}_k = 0 \end{cases} \tag{6.4}$$

with $i = 1 \div n$, $j = 1 \div n$ and $i \neq j$. The state transition matrix is therefore strictly dependent on the considered timeslot, as it is directly related to the ratio between the background model m_i at a given discrete time k and its previous value at (k-1). This approach is considered robust when the time resolution of the background model is dense enough to get an advantage in supposing a linear relationship among consecutive values. If this is not the case, the state transition matrix shall be expressed as a function of time, by adopting a polynomial relationship which best represents the model of interest.

The process noise covariance matrix $\boldsymbol{Q}_k$ (n×n) is directly linked to the state transition matrix and it is a measure of the associated noise to each state transition. If a physical model is used, the matrix should be retrieved from its mathematical formulation. If the fully-empirical approach in (6.4) is adopted, $\boldsymbol{Q}_k$ can be retrieved making use of the noise associated to the background model vector by applying the error propagation theory. If the aforementioned assumptions (and therefore (6.4)) hold, $\boldsymbol{Q}_k$ is also diagonal with $\{Q_{ij}\}_k = 0$ and its diagonal elements correspond to the estimated system variance, dependent on both background model and its standard deviation as:

$$\begin{cases} \{Q_{ii}\}_k = |\{A_{ii}\}_k|^2 \left[\left(\dfrac{\{\sigma^m{}_i\}_k}{|\{m_i\}_k|} \right)^2 + \left(\dfrac{\{\sigma^m{}_i\}_{k-1}}{|\{m_i\}_{k-1}|} \right)^2 \right] \\ \{Q_{ij}\}_k = 0 \end{cases} \tag{6.5}$$

with $i = 1 \div n$, $j = 1 \div n$ and $i \neq j$, whereas the elements of $\boldsymbol{\sigma}_k^m$ are the standard deviation of the corresponding elements of $\boldsymbol{m}_k$. The equation above corresponds to the computation of the variance

associated to $\{A_{ii}\}_k$, retrieved by adopting the uncertainty propagation theory applied to the ratio model [190].

6. II.B. Kalman a-priori states and residuals

The Kalman a-priori state vector approximates the observed scenario by only using a-priori information available from the previous time-slot. It describes the equivalent nominal expected scenario one would observe if no perturbations are present. The Kalman a-priori state vector $\boldsymbol{x}_k^-$ (n×1) at time k is defined as follows [178]

$$\boldsymbol{x}_k^- = \boldsymbol{A}_k \, \boldsymbol{x}_{k-1}^+ \tag{6.6}$$

where $\boldsymbol{x}_{k-1}^+$ is the Kalman a-posteriori state vector (n×1) of the previous timeslot k-1. Similarly, the Kalman a-priori error covariance matrix gives an estimate of the achieved accuracy for a given state at time step k by means of [178]

$$\boldsymbol{P}_k^- = \boldsymbol{A}_k \, \boldsymbol{P}_{k-1}^+ \, \boldsymbol{A}_k^T + \boldsymbol{Q}_k \tag{6.7}$$

where $\boldsymbol{P}_{k-1}^+$ is the Kalman a-posteriori covariance matrix of the previous time step k-1. The process noise covariance matrix $\boldsymbol{Q}_k$, representing the noise associated to the state transition matrix at a given timestamp, is added on top to account for the uncertainty introduced by the state propagation among consecutive discrete timeslots. It is to be noted that, the a-priori quantities described in this section are an important add-on information often not provided by classic spatial-based remote sensing algorithms. Possible usages of these parameters are described in the conclusion.

Once computed the a-priori states, we focus on the computation of the so-called residual quantities. These are simply a measure of how large is the discrepancy between the actual observed values and the a-priori estimates. In many practical remote sensing applications, having large residual quantities does not mean the algorithm is not working correctly, contrary to the classic Kalman filtering theory.
Indeed, when observing a real physical phenomenon, we are actually interested in studying situations which go beyond the expected behavior and the presented algorithm aims at detecting and studying these phenomena. The residuals associated to the observation and covariance can be evaluated as follows

$$\begin{aligned} &\text{Observation residual:} \quad \hat{\boldsymbol{z}}_k - \boldsymbol{x}_k^- \\ &\text{Covariance residual:} \quad \boldsymbol{P}_k^- + \boldsymbol{R}_k \end{aligned} \tag{6.8}$$

6. II.C. Anomaly detection

We are here introducing the concept of anomaly intended as an observed scenario not complying with the nominal behavior of interest. In other words, our goal is to perceive if the actual observation vector can be classified as useful information for the filter propagation or it somehow deviates in such a way not to be beneficial to the following Kalman state. By only exploiting the a-

priori estimates and the background model, we consider a condition defining an anomaly-free region, which a nominal scenario must satisfy. If the scenario is a non-nominal state, then it is classified as an anomaly. A nominal scenario is detected if the following condition on the observation $\hat{\boldsymbol{z}}_k$ is verified:

$$\hat{\boldsymbol{z}}_k \in [\min(\boldsymbol{m}_k, \boldsymbol{x}_k^-) - \boldsymbol{t}_k, \max(\boldsymbol{m}_k, \boldsymbol{x}_k^-) + \boldsymbol{t}_k\ ] \tag{6.9}$$

the observation must reside within the region delimited by the background model and the Kalman a-priori estimate plus or minus a dynamic threshold value, which once again depends on the difference between the background model and the a-priori estimate. The single element $\{t_i\}_k$ of the threshold vector $\boldsymbol{t}_k$ vector is given by

$$\{t_i\}_k = t_{mi}\, e^{-\frac{\left(\{x_i\}_k^- - \{m_i\}_k\right)^2}{2\,\sigma_i^t}} \tag{6.10}$$

where t_{mi} is the maximum threshold assigned to the channel i and σ_i^t represents the confidence interval in which the a-priori state can still be representative of a nominal situation. Reasonable approximation is to consider $\sigma_i^t \cong t_{\mathrm{m}i}$, as in most of the cases they physically represent the same quantity, and cannot exceed the latter by definition.

Figure 6-1 provides a graphical representation of (6.9) and (6.10) in order to clarify the rationale behind such formulation. As evident in Figure 6-1, (6.9) defines an anomaly-free region where a given observation $\hat{\boldsymbol{z}}_k$ can be considered nominal (i.e. not an anomaly). Such a region varies dynamically with time and exclusively depends on the a-priori Kalman estimate and the background model, at a given timeslot. For instance, the timeslot k=1 in Figure 6-1 refers to a case where the a-priori estimate is below the actual pixel model (fixed) at the same timeslot. In this particular case, as the difference between the two is relatively large, the dynamic threshold in equation (6.10) results being small (value $\boldsymbol{t}_1$ in the figure). All new observations falling within the anomaly-free region (green area) would therefore be classified as nominal and exploited by the filter to update its status. The same considerations hold for the timeslot k=3, where the only differences reside in: a) the a-priori state estimate is above the relevant background model value, b) the difference between $\boldsymbol{m}_k$ and $\boldsymbol{x}_k^-$ is smaller and the $\boldsymbol{t}_3$ value is indeed larger. The timeslot k=2 presents a slightly different scenario, as the a-priori Kalman estimate corresponds to the background model (ideal situation); hence the value of $\boldsymbol{t}_2$ is the maximum possible ($\boldsymbol{t_2} = \boldsymbol{t}_m$) and defines fully by itself the anomaly-free region.

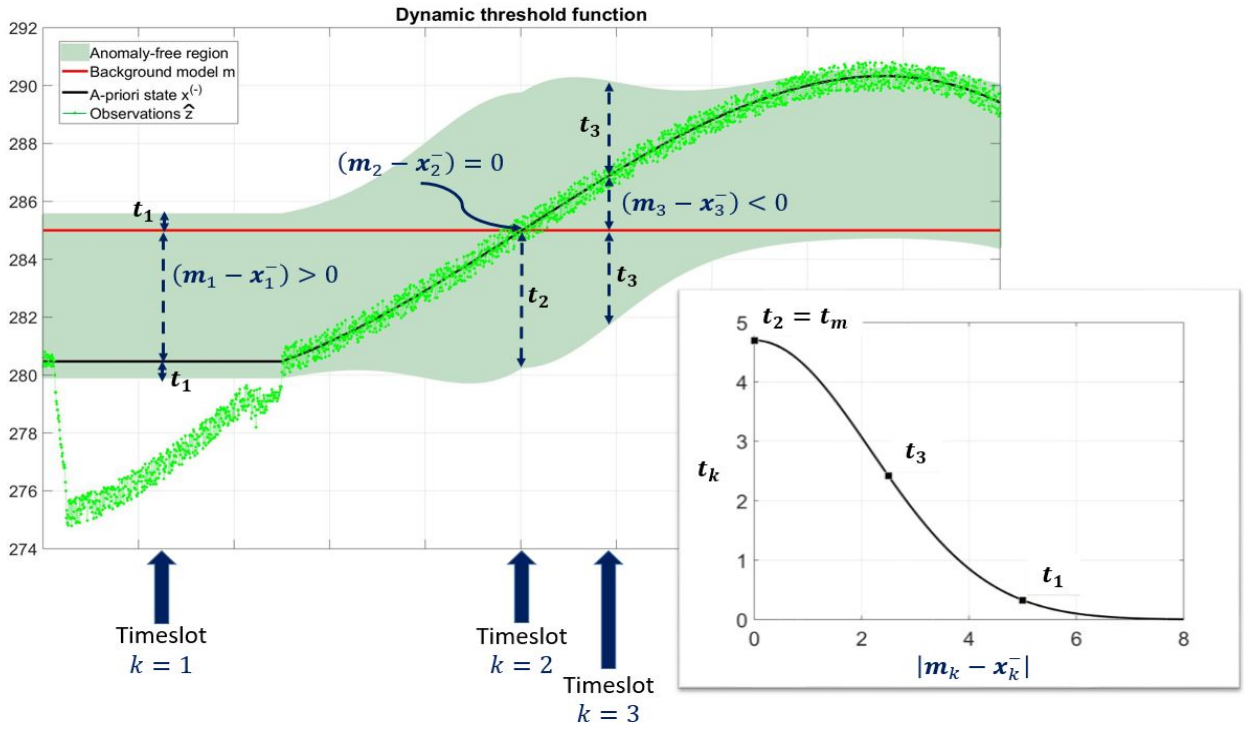

Figure 6-1. Dynamic threshold function, example. Graphical representation of the equations (6.9) and (6.10). The green dots correspond to the observations $\hat{\boldsymbol{z}}_{\boldsymbol{k}}$, the black curve is the a-priori estimate $\boldsymbol{x}_{\boldsymbol{k}}^{-}$ and the red curve represents the background model $\boldsymbol{m}_{\boldsymbol{k}}$. The green area corresponds to the anomaly-free region. A detailed description is provided in the text. The lower left figure shows an example of equation (6.10), using the values in Table 6-3 for the IR039 channel.

The Gaussian function in (6.10) is selected to allow smooth transitions among time steps, and to guarantee a continuous behavior of the dynamic threshold function (as evident in Figure 6-1). Moreover, a Gaussian expression allows the KAM algorithm to be easily tailored for any application, as the only necessary pre-defined (input) vector is $\boldsymbol{t}_m$ (e.g. using a triangular function would need a re-tuning of the whole threshold function formulation depending on the application, other than provoking possible discontinuities in the anomaly-free region trend). Also, it is to be noted how the Kalman status would change only when an observation is accepted as anomaly-free: in the example in Figure 6-1, some measurement examples (close to the timeslot k=1) are identified as anomalies. Due to this, the filter does not change its status and continue propagating the relevant information maintained from the last useful nominal timeslot (however adding a-posteriori noise to the error covariance, not visible in this figure). Further details are provided in the following paragraphs and in the chapter devoted to the application. The definition of the dynamic threshold (and associated anomaly-free region) for anomaly detection is one of the elements of novelty of the proposed technique.

6. II.D. Kalman gain computation and a-posteriori state

The Kalman gain $\boldsymbol{K}_k$ at time step k is then computed depending on the outcome of the anomaly detection. Practically speaking, the information provided by the actual observation is taken into account only if conditions were nominal. Contrary, the associated a-priori information is exclusively propagated to compute a-posteriori estimates, i.e. the boundary conditions for the next timeslot. The Kalman gain matrix $\boldsymbol{K}_k$ (n×n) is defined as follows

$$\begin{cases} \boldsymbol{K}_k = \boldsymbol{P}_k^- (\boldsymbol{P}_k^- + \boldsymbol{R}_k)^{-1} & \text{if nominal state} \\ \boldsymbol{K}_k = \underline{0} & \text{if anomaly state} \end{cases} \tag{6.11}$$

The a-posteriori state vector and covariance matrix are obtained by combining all the considered quantities. They provide the initial conditions for the timeslot k+1 by properly weighing the available information depending on the associated noise. The a-posteriori state vector $\boldsymbol{x}_k^+$ (n×1) and the a-posteriori error covariance matrix $\boldsymbol{P}_k^+$ (n×n) are computed by means of [178]:

$$\begin{cases} \boldsymbol{x}_k^+ = \boldsymbol{x}_k^- + \boldsymbol{K}_k (\hat{\boldsymbol{z}}_k - \boldsymbol{x}_k^-) \\ \boldsymbol{P}_k^+ = (\boldsymbol{I} - \boldsymbol{K}_k) \boldsymbol{P}_k^- (\boldsymbol{I} - \boldsymbol{K}_k)^T + \boldsymbol{K}_k \boldsymbol{R}_k \boldsymbol{K}_k^T \end{cases} \tag{6.12}$$

where I is the identity matrix. The $\boldsymbol{P}_k^+$ expression is known as the Joseph form of the covariance update equation and can be applied with any value of $\boldsymbol{K}_k$. Such formulation comprises other simplified forms and provides the best numerical computation properties as well as it helps with reducing numerical errors [179].

6. III. Geostationary Multispectral Data Processing

The proposed KAM algorithm is based on the temporal Kalman filter, used as a detection system, with the main goal of developing a nearly real-time operational application. The latter can be provided, for instance, by fixed-pointing ground-based multispectral video-cameras or by geostationary remote imaging sensors. The latter observation systems can guarantee a proper and recurrent time sampling and a fixed spatial characterization of the observed scenario.

In this work we use the geostationary Meteosat Second Generation (MSG) satellite with on-board SEVIRI, a 12-channel radiometer [184]. Earth imaging is obtained by a bi-dimensional Earth scan, combining the satellite spin and the scan mirror rotation. In this study, the rectified MSG SEVIRI image data are used. The SEVIRI Level 1.5 product is the result of a sequence of radiometric processing performed on the raw SEVIRI data such as linearization, conversion into radiances, calibration and linear scaling [196]-[197]. SEVIRI observes the Earth-atmosphere system with a spatial sampling distance of 3 km at the equator. The actual Instantaneous Field of View of the channels is about 4.8 km (11 channels) at nadir. The spatial resolution degrades as one moves further from the sub-satellite point. In particular for the chosen area of study in Western Africa the ground resolution of the SEVIRI's 12-channel imager range from 3.1 Km to 4 Km in both N-S and E-W directions [184]. SEVIRI takes images of the Earth at regular intervals, during a 15-minute repeat cycle (12 min 30 sec Earth imaging and up to 2 min 30 sec calibration and retrace phase);

thus resulting in a 15-min temporal resolution (corresponding to time interval in between two consecutive timeslots of the KAM).

Data are acquired in near real-time under the High Rate Information Transmission (HRIT) format which is the standard adopted by EUMETSAT to encode Level 1.5 SEVIRI image data [193]. Such HRIT files are ordered via the EUMETSAT Data Centre [200], in a lossless wavelet compressed file format. The wavelet decompression is then performed by using the "Public Wavelet Transform Decompression software" provided under license by EUMETSAT. Concerning the navigation of image data, the conversion of image coordinates into geographical ones is performed through the combination of a linear scaling function and a non-linear projection function [192]. Such procedure is solved through the creation of a "Navigation" GeoTIFF file starting from the border pixels of the MSG SEVIRI Native grid with the use of coefficients for the conversion in GEOS projection [194]. In this way the resulting latitude and longitude of a pixel centroid referring to image coordinates of the original MSG grid (full-disk) are directly obtained.

Five out of the 12 spectral SEVIRI channels are adopted here, namely the VIS 0.6 μm and the IRs at 3.9 μm, 10.2 μm, 12.0 μm and 13.4 μm. All spectral measurements have been calibrated. For the visible channel, the radiance has been converted in [mW m-2 sr-1 (cm-1)-1], while all infrared channels have been treated in K. The radiance R_{λ_i} expressed in [mW m-2 sr-1 (cm-1)-1] can be converted in radiance R_{m_i} in [W m-2 sr-1 μm-1] by means of $R_{m_i} = \left(10/\lambda_i^2\right) R_{\lambda_i}$. Furthermore, in order to mask out the twilight effect in visible channels a dedicated masking procedure has been implemented by setting a limit into the solar zenith angle θ_s. In particular, to filter out reflectance anomalies over the day–night transition area of a particular scene, only pixels having sun zenith angle θ_s lower than 80 degrees are taken as valid by the algorithm [194]. The solar zenith angle θ_s is function of time and location can be estimated by using the following equation:

$$\cos\theta_s = \sin\phi \sin\delta + \cos\phi \cos\delta \cos h_a \tag{6.13}$$

in which δ is the declination of the Sun, ϕ is the latitude and h_a is the hour angle.

The period of analysis goes from December 2015 to the end of February 2016. The dataset is uniformly sampled every 15 minutes. The algorithm has been applied on the countries of the Economic Community of West African States (ECOWAS) plus Mauritania and Chad. The area of interest has an upper-left corner of 1.355°N, 24.725°E and lower-right corner of 27.027°N, 20.942°W. MSG image segments 5, 6 of MSG full-disk product are processed to cover such area. In order to characterize SEVIRI data only over land, a water mask in MSG full disk grid has been derived for the entire area of interest using the Cloud Mask (CLM) product provided by EUMETSAT in GRIB2 format [191]. In particular, the resulting water mask binary GeoTIFF file is derived by extracting all pixels classified as "Clear sky over water" from all CLM products available over the same grid in the entire period of analysis. Note that the observed scene is kept under the original geostationary grid and covers 1530x880 pixels for each considered timeslot, i.e. 1346400 pixels. Water pixels constitute the 18.12% (243967 pixels) of the entire scene and are discarded for our purposes. The total number of pixels over land is indicated with N_{pixel}, equal to 1102433 pixels. The

number of timeslots per day for the entire period is indicated with D_{day}, where maximum D_{day}=96. Only 5 timeslots have been discarded after a proper data quality assessment due to Sun collinearity with the MSG satellite (2016-02-27 12:00, 2016-02-28 12:00, 2016-02-28 12:15, 2016-02-29 12:00, 2016-02-29 12:15).

6. IV. Application of Kalman-based Clear-Air masking

The KAM approach is here fine-tuned and applied to identify scenarios of clear-air conditions, i.e. defining the anomaly as anything that cannot be categorized as clear sky.

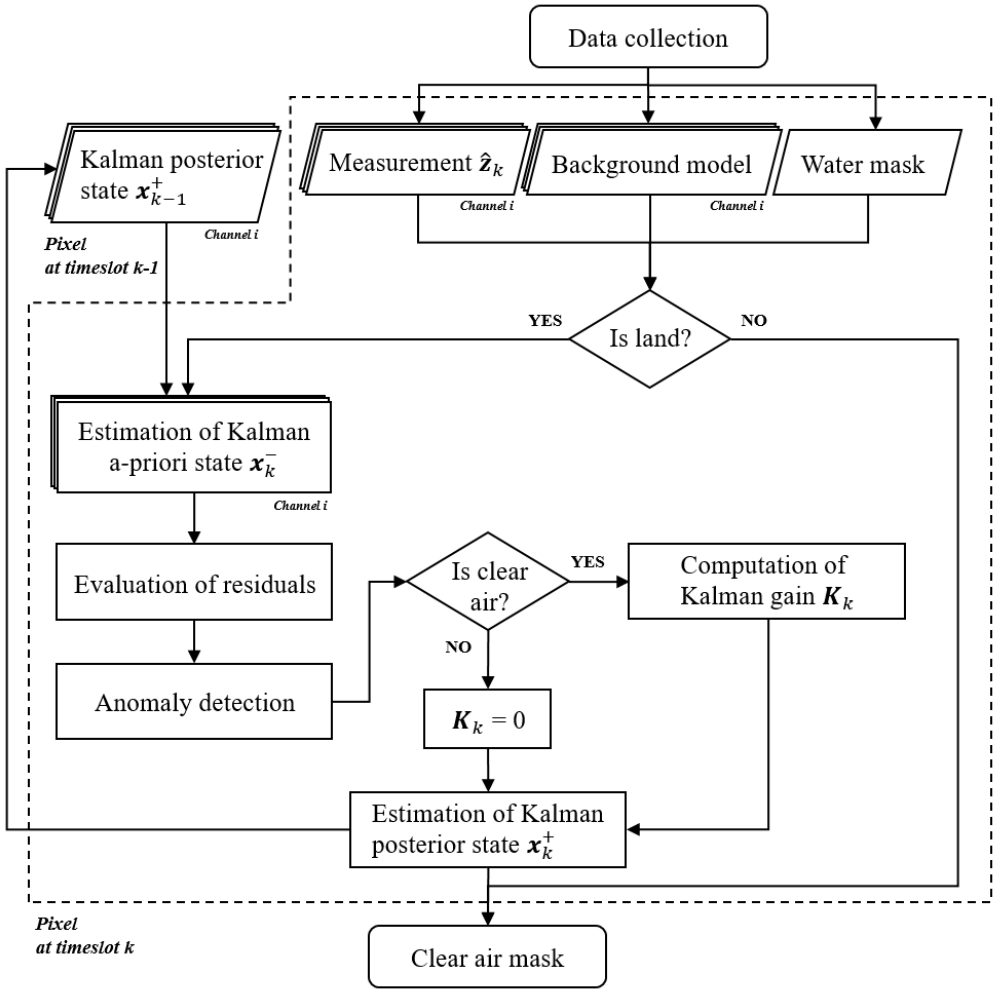

Figure 6-2. Scheme of the multi-spectral Kalman-based clear-air masking (KAM) filter. Each module corresponds to a software component developed for nearly real-time applications of the algorithm for clear-air masking.

Figure 6-2 shows the overall filter architecture going from the available dataset (described in Section 6. III). The clear-air KAM workflow follows the step defined in Section 6.II and provides the information whether the observed pixel is in pure clear air condition or an anomaly is detected.

This application represents the initial step in many space-borne remote sensing applications. A future effort may be devoted in performing a classification of the detected anomaly making use of the Kalman states complemented by the information provided by the background model. Applications can be manifold, as fire detection, volcanic ash detection or any other phenomenon that presents a distinct spectral behavior at the wavelengths of interest.
The next sections describe the tailoring of the KAM filter for the clear air masking application.

6. IV.A. Observations and noise covariances

As mentioned, the actual observation vector $\underline{\hat{z}}_k$ (n×1) describes a scenario characterized by several representations (multispectral observations). In particular, it is formed by the following MSG-SEVIRI channels (as described in 6. III): the VIS 0.6 μm and the IRs at 3.9 μm, 10.8 μm, 12.0 μm and 13.4 μm; i.e. $\hat{\boldsymbol{z}}_k = \left(\hat{z}_{0.6\mu m}, \hat{z}_{3.9\mu m}, \hat{z}_{10.8\mu m}, \hat{z}_{12.0\mu m}, \hat{z}_{13.4\mu m}\right)_k^T$. Visible channel measurements are expressed in terms of reflectance in [W m^{-2} sr^{-1} μm^{-1}], while all infrared channels are converted in K. The index k indicates the considered timeslot.

TABLE 6-2: SEVIRI NOISE BUDGETS AS MEASURED AT THE BEGINNING OF LIFE, EXPECTED AT THE END OF LIFE AND THE SPECIFICATIONS [184]-[186].

Channel	VIS06 0.6 μm [W m^{-2} sr^{-1} μm^{-1}]	IR039 3.9 μm [K]	IR108 10.8 μm [K]	IR120 12.0 μm [K]	IR134 13.4 μm [K]
Measured noise at the beginning of life	0.39	0.24	0.13	0.21	0.29
Expected noise at the end of life	0.59	0.36	0.20	0.32	0.44
Noise (specification)	**0.53**	**0.35**	**0.25**	**0.37**	**1.80**

The co-variances among noise pairs at the timeslot k form the observation noise covariance matrix R_k (n×n). Practically speaking, the latter matrix describes the correlation among errors associated to the various SEVIRI channels, see (6.3). It is common practice in data assimilation to treat observation errors as uncorrelated, i.e. inter-channel error correlations can be assumed null ($\boldsymbol{R}_k$ diagonal matrix). This is often an instrument design specification and, in the case of SEVIRI, studies have been performed to better characterize this aspect [170]. On the other hand, it is clear that the elements on the principal diagonal correspond to the error variance associated to each of the SEVIRI channels [185]-[186].

The variance can be computed as the square of absolute radiometric accuracy, as given by the instrument specifications [184]-[186] and reported in Table 6-2. The three rows correspond to the SEVIRI measurement uncertainty predicted at the beginning and at end of the mission life, as well as the imposed specifications at design level. The specifications were considered as baseline in the KAM application (worst-case scenario).

6. IV.B. Background model characterization

One of the essential steps of the KAM algorithm is the background model characterization for each of the employed MSG SEVIRI channel. A good channel-background model of a certain pixel must be purely representative of a clear-air situation with as less as possible associated noise, which is necessary for an accurate anomaly detection. In this work, we adopted static background models only and future studies are foreseen to refine the approach and consider a dynamic update of the model (through a combination of static models and a time-based moving average system).

Cloud-free scenes are identified by using the Cloud Mask product [191] projected in MSG full disk grid over the period going from December 2015 to the end of March 2016. For each of the considered timeslots (96 timeslots in a day) and relevant channel, an image stack was considered after filtering out cloudy scenarios. Average and standard deviation (1-sigma) are then computed for each stack at pixel level to obtain the background model quantities, $\{m_i\}_k$ and $\{\sigma^m{}_i\}_k$, respectively; one for each of the five SEVIRI channels and for each of the 96 timeslots. It is to be noted that the computed background models are completely general and mediated over the period and do not represent the specific daily trend to be expected over a certain period (i.e. they do not include any short-term effect). The background model vector of the considered scenario $\boldsymbol{m}_k$ (n×1) is formed by the mean values of the stacks (one per channel) at a given timeslot k (i.e. 15-min sampling). While the associated noise vector $\boldsymbol{\sigma^m}_k$ (n×1) is formed by the standard deviations of the stacks (one per channel) at a given timeslot k and quantifies the expected variations of the channel radiances under clear sky conditions on the long-term.

6. IV.C. Kalman-based filter tailoring

Referring to the KAM filter depicted in section 6.II, the clear-air anomaly detection is the only module that needs to get tailored for the adopted instrument. In particular, we would need to define the proper elements of the $\boldsymbol{t}_m$ vector (nx1) to be used in (6.10). Generally speaking, the smaller the t_{mi} values are, the more stringent the anomaly detection algorithm is. Small t_{mi} values would therefore make the Kalman algorithm very selective in accepting a clear-air condition, which would be anyway the preferred option for a filter propagation perspective. If the t_{mi} values are too large, the filter would wrongly associate an anomaly scenario as clear air, resulting in a propagation of the wrong information to the a-posteriori status and therefore to the following timeslot.

The applied solution was to compute the t_{mi} values making use of the information provided by the background model associated noise, hence becoming the only element needed to run the algorithm. In particular, the standard deviations $\{\sigma^m{}_i\}_k$ associated to the background models were exploited to compute the $\boldsymbol{t}_m$ vector (nx1). For each SEVIRI channel i=1,…,n (n=5) , the t_{mi} value was computed as follow:

$$t_{mi} = \frac{1}{(D_{day} + N_{pixel})} \sum_{N_{pixel}} \left[\sum_{k=1}^{D_{day}} \{\sigma^m{}_i\}_k \right] \tag{6.14}$$

where D is the number of timeslots per day (D_{day}=96 in this application) and N_{pixel} is the total number of pixels over land composing the observed scene. The $\boldsymbol{t}_m$ vector is therefore independent of time. Table 6-3 recaps the parameters of interest used in (6.10).

TABLE 6-3: THRESHOLD VALUES FOR ANOMALY DETECTION WHEN USING MSG-SEVIRI.

Channel	VIS06 0.6 μm [W m^{-2} sr^{-1} μm^{-1}]	IR039 3.9 μm [K]	IR108 10.8 μm [K]	IR120 12.0 μm [K]	IR134 13.4 μm [K]
t_{mi}	2.3	4.7	4.5	3.9	3.5

It is worth noting that such thresholds are applied indistinctively over the whole scene, and only depends on:

- the considered wavelength and its sensitivity to the considered anomaly, as well as the a-priori estimate deviation in clear sky conditions – meaning that the values represent the expected maximum interval within which we can still consider the observed scenario being in clear-air conditions;
- the adopted instrument, and therefore its sensitivity to the scene at a given wavelength, other than the considered spatial resolution.

The most important asset of the proposed KAM approach is the possibility to define a set of thresholds to be independently applied. The pixel-specific information is completely absorbed by the a-priori Kalman estimate by exploiting the background model (e.g. no need of having different thresholds to be applied in daily or night conditions as in most of the contextual-spatial detection algorithms).

6. IV.D. Clear-air KAM application

The algorithm described in the section 6.II has been applied to the available dataset presented in section 6. III over land pixels. The entire computation relies on a chain developed in Python, which has been developed by Progressive Systems in the context of the PROBA-V MEP TPS research project funded by the European Space Agency (ESA) [202]. I mainly focused on the theoretical formulation and the definition of the algorithm, as well as supporting the fine-tuning and the validation, so providing inputs for the code implementation. The implementation was together with the The processing here presented has been performed in the computer resources offered within the RSS Cloud Toolbox service [201] managed by the ESA's Research and Service Support (RSS) [195].

We report here some examples of temporal trends, with the description of the time evolution of the associated key-quantities governing the KAM algorithm. Figure 6-3 shows the KAM filter behavior during a clear-air day (December 9, 2015) for a sample pixel in the Senegal area and for all adopted MSG-SEVIRI channels. In such example, the measurements (observations $\hat{\boldsymbol{z}}_k$, red curves) clearly

describe clear-air conditions over the whole day. Hence, the a-priori estimates ($\boldsymbol{x}_k^-$, black dotted lines) tend to follow the measurements by exploiting the state transition matrix computed from the background model values ($\boldsymbol{m}_k$). Small signal variations of the a-priori estimates can be observed and such differences are sequentially corrected when updating the a-posteriori estimates (not shown) with the actual measurements so that, at the next state, the most reliable information is used to propagate the filter status. This is the best possible situation as the KAM is relying on useful measurements to continuously update its status with the minimum possible associated noise (basically corresponding to the instrument noise exclusively). We can also observe how, around 10:00 PM, the presence of a light cloud decreases the brightness temperatures for some of the considered channels. The KAM filter is able to detect an anomaly behavior thanks to the information provided by the channels at 12 and 13 μm (most affected), confirming the importance of having a multi-spectral anomaly detection module. The a-priori estimate maintains the information provided by the a-posteriori one and does not follow the non-clear air observed value, i.e. the filter does not exploit the actual measurements but rather propagates the estimates available from the previous slot adding a higher associated noise (making use of the process noise covariance matrix).

Figure 6-4 better highlights the mentioned behavior, where the daily trend of the same pixel is analyzed for the following day (December 10, 2015). The first half of the day is characterized by a discontinuous presence of light cloudy conditions, several anomalies are identified and the a-priori estimates always provide a consistent clear-air-like trend as they should (by correctly ignoring the measurements that do not fall within the multispectral anomaly-free region). When a clear-air observation is available (few timeslots during the first part of the day), clear-air scenarios are detected and used by the filter to update the a-posteriori estimate accordingly. In the afternoon, all considered channels reflect a persistent and heavier cloud coverage, making the information coming from the actual observation vector useless for what concerns the filter propagation. Nevertheless, the KAM filter continues providing an equivalent clear-air estimate basing the calculation on the last available measurements accepted by the filter and by sequentially adding the associated noise to the a-posteriori estimate (i.e. taking into account the noise associated to the state transition matrix).

As already mentioned, the KAM detection module is applied by looking at all available channels simultaneously, making the filter able to sound the atmosphere at different wavelengths and account for all possible anomaly scenarios. This allows excluding several false alarms or missed detections, since one channel may be less sensitive than others to an anomaly situation (or vice-versa). The continuous availability of the a-priori estimates $\boldsymbol{x}_k^-$ of the observed scene (computed exploiting the previous Kalman filter states and the pixel models) allows having an equivalent clear-air radiance for all channels, expected to be measured in absence of anomaly (could coverage). Exploiting this information may be beneficial for retrieval methods of secondary products associated to the observed scenario, being therefore able to isolate the contribution of the nominal radiance. Future works will specifically address this aspect.

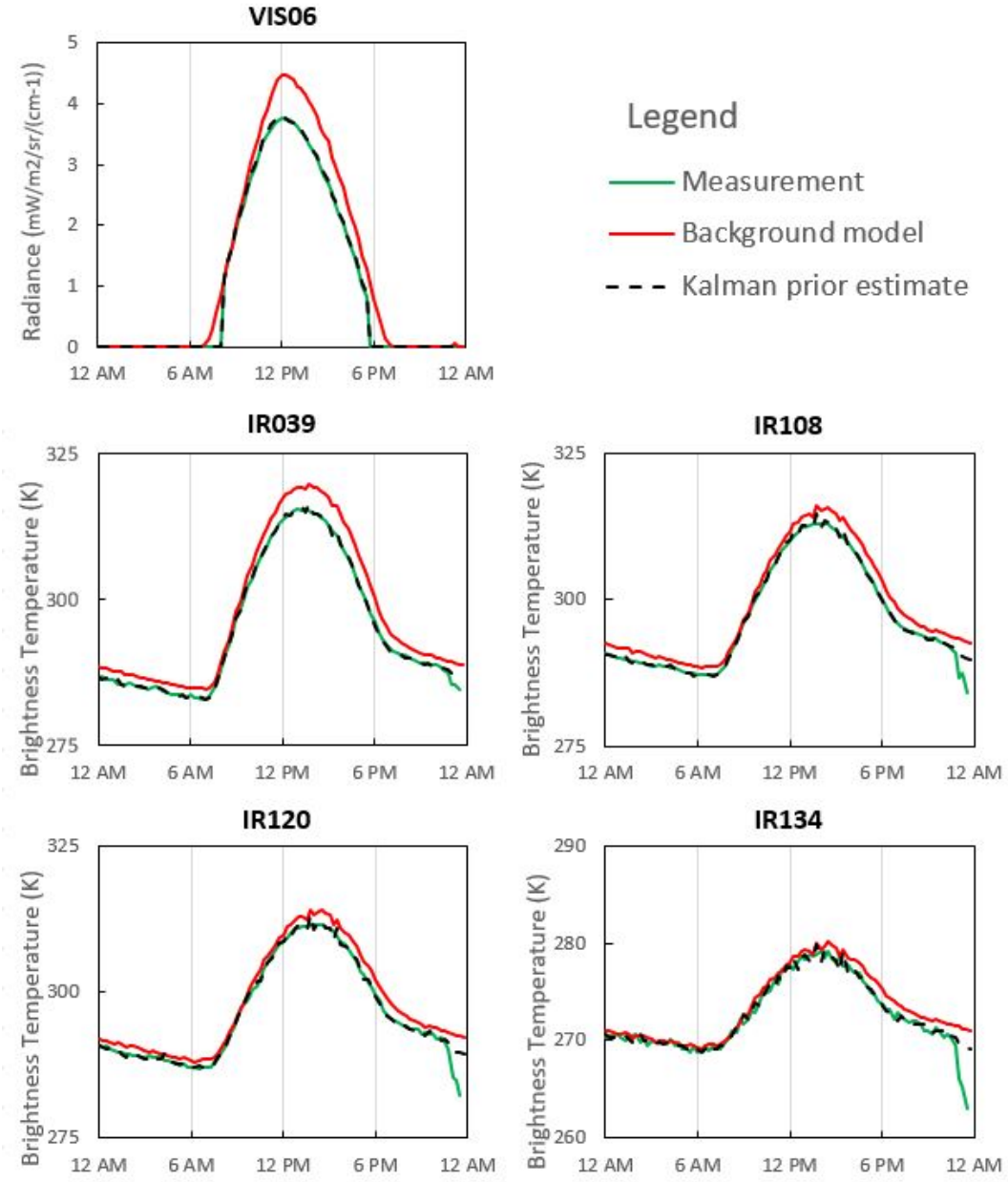

Figure 6-3: Example of clear-air day (December 9, 2015) for all considered channels of the MSG-SEVIRI instrument. The green curves represent the actual observation vector $\hat{\boldsymbol{z}}_k$, the black dotted curve is the a-priori estimate $\boldsymbol{x}_k^-$ and the red curve represents the background model $\boldsymbol{m}_k$. A detailed description is provided in the text.

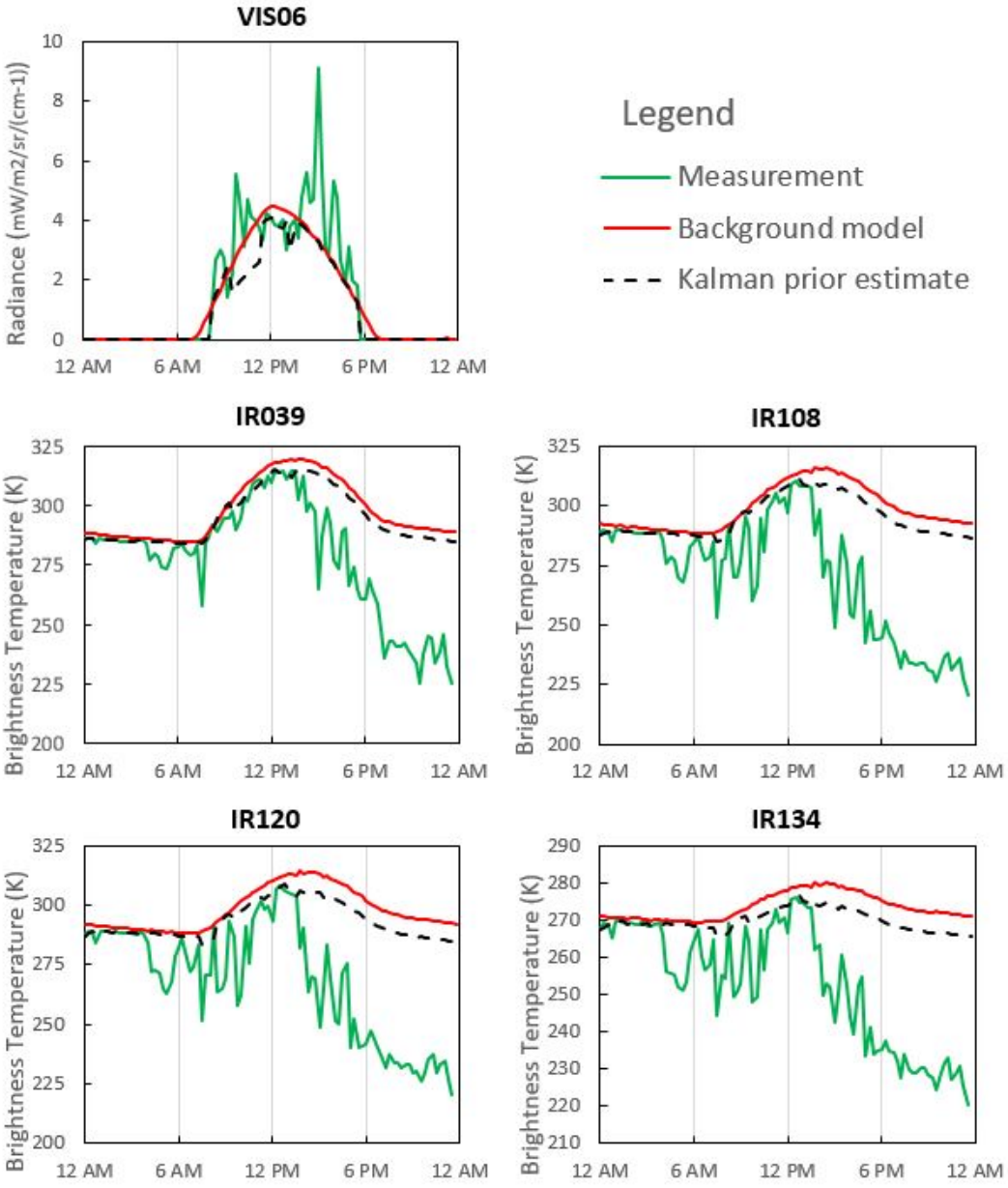

Figure 6-4. Example of "anomaly" day (December 10, 2015) for all considered channels of the MSG-SEVIRI instrument. The green curves represent the actual observation vector $\hat{\boldsymbol{z}}_k$, the black dotted curve is the a-priori estimate $\boldsymbol{x}_k^-$ and the red curve represents the background model $\boldsymbol{m}_k$. A detailed description is provided in the text.

6. V. Validation

In this section we present an inter-comparison of the presented algorithm with respect to the EUMETSAT cloud masking product. The latter has been extensively validated and operationally used in several real-time applications over the last decade; it therefore provides a solid comparison term for the validation [191]. Moreover, the selected comparison allows validating the clear-air KAM filter using the same input data (the same MSG SEVIRI geostationary grid is considered) in order to minimize any resampling of the product which may cause a loss of useful information. There is a fundamental difference between the two datasets: while the KAM approach is entirely temporal-based, the EUMETSAT cloud masking algorithm is spatially-based, by setting several thresholds and referring them to the "mean" value of a moving spatial average window centered at the pixel of interest [191].

The period of analysis goes from December 2015 to the end of February 2016. The dataset is uniformly sampled every 15 minutes. The observed scene is kept under the original geostationary grid and covers 1530x880 pixels for each considered timeslot, i.e. 1346400 pixels. Water pixels constitute the 18.12% of the entire scene and are discarded for our purposes. 96 timeslots per day are available for the entire period. For the validation, we define 4 classes: i) blue and cyan dots refer to situations of matching in clear-air and anomaly conditions, respectively; ii) yellow dots indicate missing detections of clear-air by the KAM filter with respect to the EUMETSAT cloud mask; iii) finally, red dots show false alarms of clear-air.

In some conditions, the KAM and EUMETSAT algorithms may lead to different results because the Kalman-based technique only exploits image temporal changes and is therefore independent of common biases potentially affecting the spatial pixel grid used by EUMETSAT. Moreover, while we aim at detecting situations of clear-air conditions (clear-air masking), the EUMETSAT product is intended to provide a cloud-masking product. Practically speaking, it is much more important for our validation purposes to minimize the missed detections of clear-air conditions, i.e. cases when the KAM algorithm indicates clear-air whereas the EUMETSAT one indicates cloud presence. False alarms are less critical: as the EUMETSAT product may flag a certain pixel as cloud free, but the Kalman-based detection system could classify that particular condition as a scenario not purely clear-air representative. It is also important to underline that both algorithms do not provide any ground truth and differences may be related to stricter or larger thresholds other than limits linked to such approaches.

Figure 6-5 shows an example of comparison for the whole area under analysis and for a single timeslot (December 13, 2015 h 12:00). For visual interpretation, Figure 6-6 provides the corresponding composite RGB image derived from the visible and near-infrared SEVIRI channels. A fairly good agreement is globally reached and yellow/red areas mainly correspond to borderline situations. Some mismatches, especially false alarms, are geographically grouped in the lower part of Figure 6-5/Figure 6-6. On top of the above mentioned considerations, this particular behavior

might be related to a relatively poor characterization of the background pixel models. Exploiting longer time series may overcome the issue and improve the final result.

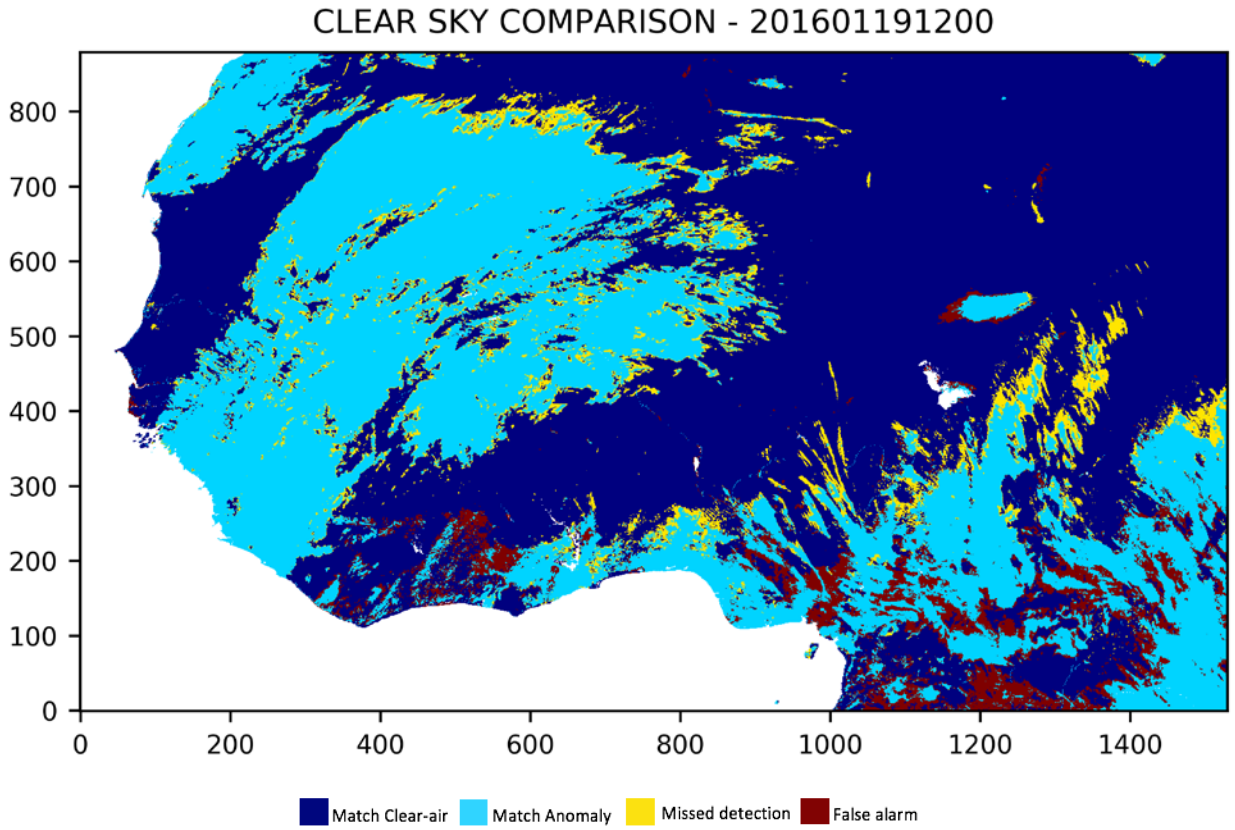

Figure 6-5: Inter-comparison with respect to EUMETSAT Cloud Mask product for a single timeslot (January 19, 2016 h 12:00). Blue and cyan points correspond to pixels for which the two algorithms provide the same result (clear-air and anomaly, respectively). Yellow points represent missed detections of the KAM algorithm with respect to the EUMETSAT masking product, while brown pixels indicate false alarms.

Table 6-4 provides the percentages of matching, missed detection and false alarm over the entire test period. The percentages take into account the whole scene, as well as differentiating the calculations on clear-air and anomaly scenarios. The table also reports the total number of pixels considered for the validation. The missed detections are very limited to about 3 % over the entire period and mainly due to mischaracterizations of the background models. False alarms are more often registered, however less critical for the reasons explained above.

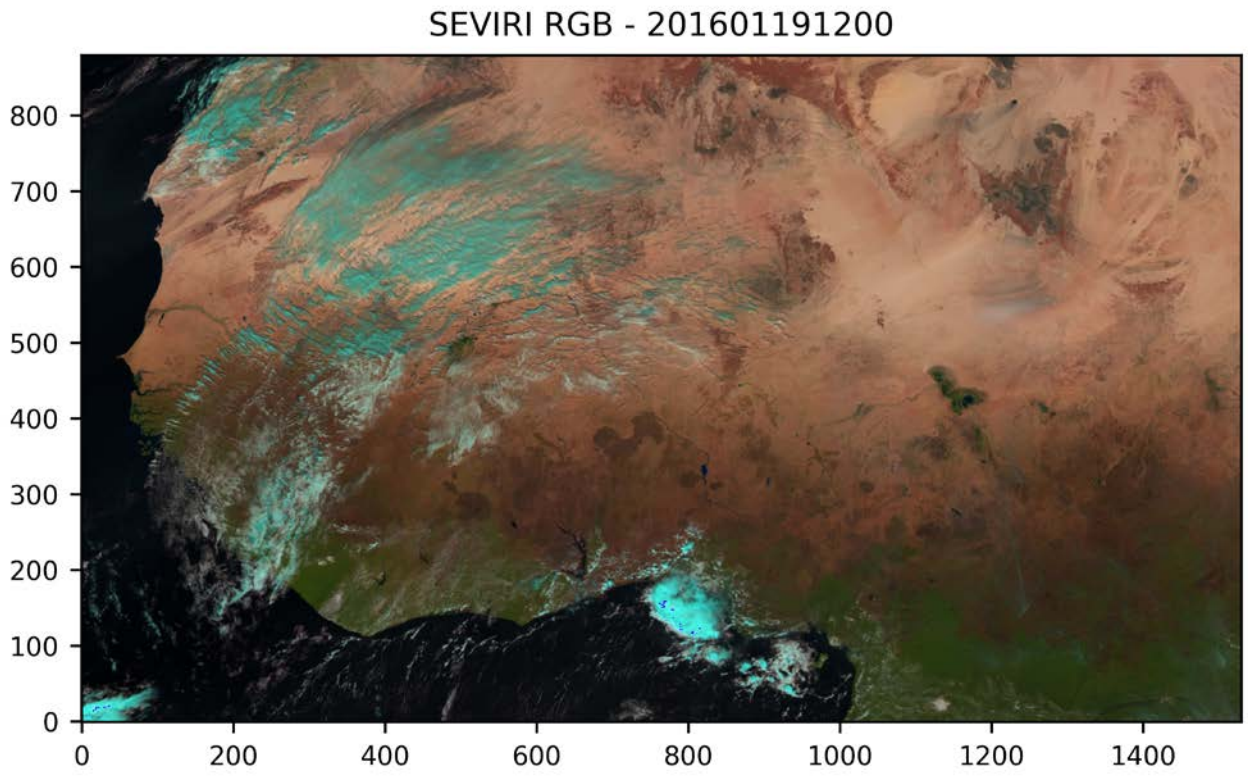

Figure 6-6: Composite RGB image from the MSG-SEVIRI instrument for the considered timeslot in Figure 6-5 (January 19, 2016 h 12:00).

TABLE 6-4: INTER-COMPARISON WITH RESPECT TO EUMETSAT CLOUD MASK PRODUCT.

CLEAR-AIR PIXELS (N. SAMPLES = 6.8407E+09)		CLOUDY/ANOMALY PIXELS (N. SAMPLES = 2.7843E+09)	
MATCH	MISSED DETECT.	MATCH	FALSE ALARMS
95.72 %	4.28 %	74.99 %	25.01 %

ALL PIXELS (N. SAMPLES = 9.6250E+09)		
MATCH	MISSED DETECTIONS	FALSE ALARMS
89.73 %	3.04 %	7.23 %

Figure 6-7 shows the same comparison in terms of temporal trend of both the percentages and number of pixels for each single timeslot. The same color legend is adopted: dark blue refers to clear-air situations, light blue to anomaly situations, yellow to missed detections and brown to false alarms. It can be seen how the total matching (dark blue plus light blue) is mainly constant over the whole period of analysis with a percentage of absolute matching placed around 90%.

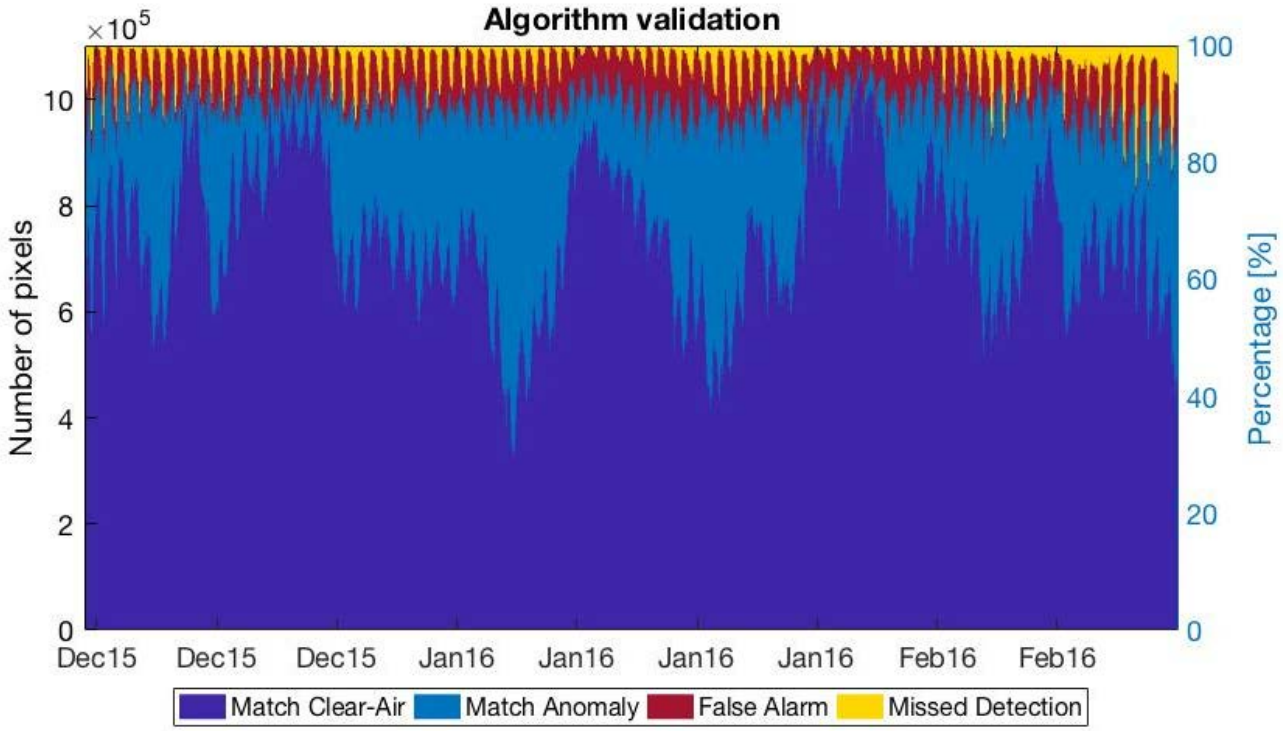

Figure 6-7: Inter-comparison (temporal trend) between the KAM algorithm and the EUMETSAT Cloud Mask product over the whole analyzed period for all pixels composing the scene. Blue and cyan points correspond to pixels for which the two algorithms provide the same result (clear-air and anomaly, respectively). Yellow points represent missed detections of the KAM algorithm with respect to the EUMETSAT masking product, while brown pixels indicate false alarms.

Chapter 7. Conclusions

Several techniques and applications in the field of the atmospheric remote sensing and radio-propagation have been shown, at both microwave and optical wavelengths.

In chapter 3, the Sun-Tracking technique has been introduced to estimate the Sun brightness temperature at K, Ka, V and W band. Two methods have been applied, the elevation-scanning Langley method and surface meteorological data method. The two techniques showed comparable results, but the first one need a careful selection of candidate clear-air days whereas the second one is depending on the external weather station data. Both techniques are affected by the daily variability of clear air extinction. The use of the two methods allowed us to give an uncertainty indication related to different adopted techniques. Since ST measurements are currently still being collected, it is intriguing to speculate the possibility of observing solar cycles in the retrieved Sun brightness temperature, although such variability is partly masked by the intrinsic accuracy of the estimates. Sun-tracking microwave radiometry has been also applied to estimate the atmospheric path attenuation in all-weather conditions at K, Ka, V and W band. In the presence of precipitating clouds, the technique allowed the estimate of the atmospheric extinction up to about 25 dB at K-band and up to about 30 dB at V- and W-band. The method has been applied, as a source of validation, for estimating the accuracy of the multi-frequency PPM-*PolDEx* model, showing a very good agreement with the ST retrievals in cloudy and rainy conditions, with an rms agreement of about 0.2 dB at K-band and 0.7 dB at V-band. With the availability of a larger dataset of measurements, the ST-MW radiometry technique will be useful in further developing the physically oriented parametric models. In particular, open issues are related to the analysis of cloudy and rainy events at low elevation angles, where prediction models generally have large errors, as well to the discrimination between heavy clouds and light rain. In case of precipitation, ST-MWR can be also used to assess the capability of microwave radiometer to estimate rainfall rate and to relate the latter to atmospheric path attenuation.
In the same chapter, an additional parametric prediction model approach was shown, for the retrieval of the atmospheric integrated path attenuation only exploiting channel brightness temperatures. Radiometric measurements available from the RPG-HATPRO MWR located at the ESA Cebreros deep space antenna premises in Spain were used. By exploiting well-known radiative transfer models for retrieving the equivalent clear air attenuation contribution, the cloud specific attenuation contribution was modelled with a stochastic process well defined in both amplitude and time domains. Such cloud attenuation results being log-normal distributed. Future studies will address the possibility of using such modelling to synthetize time series of cloud attenuation to be applied in situations with low data availability as first assessment of the propagation conditions at millimeter bands. Observation continuity is the key to improve the long-term statistical characterization of the atmospheric behavior and such modelling has proved to be crucial in assessing and completing attenuation estimate datasets, whenever solid path attenuation estimates were not available for relatively long periods.

Chapter 4 showed a model chain for the prediction of the tropospheric channel for the downlink of interplanetary missions operating above Ku band. The chain has been already tested within a feasibility study applied to the BepiColombo mission to Mercury operated by the European Space Agency (ESA) and by exploiting the JAXA Hayabusa-2 mission Ka-band data thanks to the ESA cross-support service. The model-chain is composed by three modules. A weather forecast module for the prediction of the atmospheric state expected during the downlink transmission. A radiopropagation module to simulate radiopropagation variables generated by the predicted atmospheric state. A downlink budget module for the statistical optimization of the satellite-to-Earth link. The latter exploits the spatial grid domain and the temporal evolution of the predicted radiopropagation variables to compute statistics and uncertainties of the outputs operational parameters to use during the transmission. A preliminary validation of the model-chain has been carried out by comparing the simulated signal-to-noise ratio with the one received from Hayabusa-2, showing an average error within 0.2 dB. Finally, a statistical approach has been proposed for the downlink optimization, allowing to overpass potential double-penalty errors due to the space-time mislocalization of predicted meteorological phenomena. The model-chain will be tested extensively making use of the Hayabusa-2 mission data, and systematic online operations are planned for future K- and Ka-band missions.

Chapter 5 recaps some studies performed in the context of International Telecommunication Union (ITU) activities of ESA. In particular, at the next ITU World Radiocommunication Conference 2019, Agenda Item 1.13 will address the identification and the possible additional allocation of radio-frequency spectrum to serve the future development of the International Mobile Telecommunications (IMT) for 2020 and beyond, mainly focused on systems supporting the fifth generation of cellular mobile communications. The chapter shows the potential impact of IMT deployments in terms of received radio frequency interference by ESA's telecommunication links in frequency bands allocated to the Earth Exploration-Satellite Service and to the Space Research Service. Received interference can derive from several propagation mechanisms including line-of-sight propagation, diffraction, scatter, ducting, reflection/refraction, etc. which strongly depend on climate, radio frequency, link availability, distance and path topography; at any time a single mechanism or more than one may be present. Particular focus is given to the ESA's tracking network and to the earth stations located in New Norcia (Australia), Cebreros (Spain), Malargüe Sur (Argentina) and Kiruna (Sweden). Several dynamic scenarios have been simulated to understand the most critical parameters which would contribute to situations of harmful received interference. Results point out the need of having separation distances up to 100 km depending on the station and frequency band under consideration.

Finally, in chapter 6 an anomaly detection and estimation technique has been presented, using a modified version of Kalman filter on a pixel basis in the temporal domain. Advantages of using a time-based KAM approach have been discussed, blazing a trail to many applications in detecting and monitoring natural and environmental phenomena around the world. After presenting the KAM system in a general framework, an application of the latter has been shown to prove its performance in detecting clear-air scenarios. The clear-air KAM algorithm has been applied to multispectral observations available from geostationary visible-infrared radiometric

measurements coming from SEVIRI instrument on-board of the Meteosat satellite. The area of interests covers the whole West Africa, for a test period of three months from December 2015 until the end of February 2016. This results in a large amount of processed pixels having 96 timeslots per day. A validation of the clear-air algorithm has been presented by inter-comparing the detection results with the well-known EUMETSAT cloud mask product. This has ensured to have the same input data processed by a completely different algorithm approach. The validation has shown constant percentages of matching around 90% over the entire period of analysis.

The add-on value of the Kalman approach is to be able to provide a-priori estimates of the scenario, exploiting the previous Kalman filter states and making use of the pixel models. This allows to have an equivalent clear-air radiance which is expected to be measured in absence of anomaly (for instance, in absence of cloud coverage). In such a way, the KAM algorithm can be globally applied, since the estimates are computed from the pixel models and the thresholds can be set independently from the area of interest.

Future work will address the use of the available a-priori states of the Kalman filter to develop atmospheric correction methods through the estimation of the atmospheric optical thickness. Moreover, efforts will be devoted to fine tuning of the KAM algorithm to add robustness (e.g. including channel weights in the anomaly detection) as well as to extending the application over other regions for further validation.

References

[1] D. Solimini, "Understanding Earth Observation: The Electromagnetic Foundation of Remote Sensing", Volume 23 of Remote Sensing and Digital Image Processing, Springer, 2016

[2] Demetrius T Paris and F. Kenneth Hurd, Basic Electromagnetic Theory, McGraw Hill, New York 1969 ISBN 0-07-048470-8

[3] J.A. Richards and X. Jia, "Remote Sensing Digital Image Analysis – 4th edition", Springer, ISBN-10 3-540-25128-6 (2005).

[4] Born M, Wolf E, Bhatia AB (2002) Principles of optics: electromagnetic theory of propagation, interference and diffraction of light. Cambridge University Press. ISBN:9781139643405

[5] Liebe HJ, Hufford GA, Cotton MG (1993) Propagation modeling of moist air and suspended water/ice particles at frequencies below 1000 GHz". In: NATO/AGARD Wave Propagation Panel, 52nd Meeting Atmospheric Propagation Effects Through Natural and Man-Made Obscurants for Visible to MM-Wave Radiation, Palma de Mallorca, 17–20 May 1993, vol AGARD-CP-542. ISBN:9283507274

[6] McClatchey RA, Burch DE, Rothman LS, Benedict WS, Calfee RF, Garing JS, Clough SA, Fox K (1973) AFCRL atmospheric absorption line parameters compilation. Technical report AFCRL-TR-73-0096. U.S. Air Force Cambridge Research Laboratories

[7] Liebe HJ (1989) MPM – an atmospheric millimeter-wave propagation model. Int J Infrared MillimWaves 10:631–650. doi:10.1007/BF01009565

[8] Brussaard G, Watson PA (1994) Atmospheric modelling and millimetre wave propagation. Springer. ISBN:9780412562303

[9] Liebe HJ (1981) Modeling attenuation and phase of radio waves in air at frequencies below 1000 GHz. Radio Sci 16(6):1183–1199. doi:10.1029/RS016i006p01183

[10] Pickett HM, Poynter RL, Cohen EA, Delitsky ML, Pearson JC, Müller HSP (1998) Submillimeter, millimeter and microwave spectral line catalog. J Quant Spectrosc Radiat Transf 60:883–890. doi:10.1016/S0022-4073(98)00091-0

[11] Liebe HJ (1984) The atmospheric water vapor continuum below 300 GHz. Int J Infrared MillimWaves 5(2):207–227. doi:10.1007/BF01417651

[12] Aplin KL, McPheat RA (2005) Absorption of infra-red radiation by atmospheric molecular cluster-ions. J Atmos Solar-Terr Phys 67(8–9):775–783. doi:10.1016/j.jastp.2005.01.007

[13] Saykally RJ (2013) Simplest water cluster leaves behind its spectral fingerprint. Physics 6(22). doi:10.1103/Physics.6.22

[14] Tretyakov MYu, Serov EA, Koshelev MA, Parshin VV, Krupnov AF (2013) Water dimer rotationally resolved millimeter-wave spectrum observation at room temperature. Phys Rev Lett PRL 110:093001. doi:10.1103/PhysRevLett.110.093001

[15] Yang Y, Mandehgar M, Grischkowsky D (2014) Determination of the water vapor continuum absorption by THz-TDS and molecular response theory. Opt Exp 22(4):4388–4403. doi:10.1364/OE.22.004388

[16] Liebe HJ, Rosenkranz PW, Hufford GA (1992) Atmospheric 60-GHz oxygen spectrum: new laboratory measurements and line parameters. J Quant Spectrosc Radiat Transf 48(5–6):629–643. doi:10.1016/0022-4073(92)90127-P

[17] Bernath PF (2002) The spectroscopy of water vapour: experiment, theory and applications. Phys Chem Phys 4:1501–1509. doi:10.1039/b200372d

[18] Ciddor PE (1996) Refractive index of air: new equations for the visible and near infrared. Appl Opt 35(9):1566–1573. doi:10.1364/AO.35.001566

[19] Rüeger JM (2002) Refractive indices of light, infrared and radio waves in the atmosphere. Technical report UNISURV S-68. School of Surveying and Spatial Information Systems University of New South Wales

[20] COST Action ES0702 EG-CLIMET – Final Report, Illingworth A.J., D. Ruffieux, D. Cimini, U. Löhnert, M. Haeffelin, and V. Lehmann (Eds.), doi:10.12898/ES0702FR, 2013.

[21] Westwater, E. R., S. Crewell, and C. Mätzler, 2004: A review of surface-based microwave and millimeter-wave radiometric remote sensing of the troposphere. Radio Science Bulletin, No. 3010, September 2004, 59-80.

[22] Westwater, E. R., S. Crewell, C. Mätzler, and D. Cimini, 2006: Principles of Surface-based Microwave and Millimeter wave Radiometric Remote Sensing of the Troposphere, Quaderni Della Societa Italiana di Elettromagnetismo, 1(3), September 2005, 50-90.

[23] Maetzler, C., Thermal Microwave Radiation: Applications for Remote Sensing, The Institution of Engineering and Technology, ISBN 0 86341 573 3.

[24] F.T. Ulaby, R.K.Moore and A.K.Fung, Microwave Remote Sensing Active and Passive, Vol.1, Addison-Wesley, 288-302, 1981.

[25] Goody R. M. and Y. L. Yung , Atmospheric Radiation, Theoretical Basis, Oxford University Press, Second Edition, 1995.

[26] C.F. Bohren and E. Clothiaux, "Fundamentals of Atmospheric Radiation: An Introduction with 400 Problems" Wiley, 2006. ISBN: 978-3-527-40503-9

[27] Janssen, M., "Atmospheric Remote Sensing by Microwave Radiometry", John Wiley, New York, 1993.

[28] G.W. Petty, "A First Course in Atmospheric Radiation", Sundog Publishing; 2nd edition, 2006.

[29] D. Deirmendjian, "Electromagnetic Scattering on Spherical Polydispersions", United States Air Force Project Rand, Report R-456-PR, April 1969

[30] T. Oguchi, "Scattering properties of Pruppacher-and-Pitter form raindrops and cross-polarization due to rain: Calculations at 11, 13, 19.3 and 34.8 GHz" Radio Sci., 12 (1977), pp. 41-51

[31] A. J. Gasiewski, "Atmospheric Remote Sensing By Microwave Radiometry", Wiley, New York, NY, 1993. ISBN # 0471628913. P. 91, 1993.

[32] F.S. Marzano, E. Fionda, P. Ciotti, A. Martellucci, "Ground-based multifrequency microwave radiometry for rainfall remote sensing", IEEE transactions on geoscience and remote sensing 40 (4), 742-759

[33] M.I. Mishchenko, L.D. Travis, and A.A. Lacis, "Scattering, Absorption, and Emission of Light by Small Particles", Cambridge University Press, 2002.

[34] Czekala, H. and C. Simmer, 1998, Microwave radiative transfer with non-spherical precipitating hydrometeors, J. Quant. Spectros. Radiat. Transfer, 60, 365-374.

[35] Czekala, H., S. Crewell, A. Hornbostel, K. Schroth, C. Simmer, and A. Thiele, 2001: Interpretation of polarization features in ground based microwave observations as caused by horizontally aligned oblate rain drops. J. Appl. Meteorol., 40, 1918-1932.

[36] Xie, X., U. Löhnert, S. Kneifel, and S. Crewell, 2012: Snow particle orientation observed by ground-based microwave radiometry, J. Geophys. Res., 117, D02206, 12 pp., doi:10.1029/2011JD016369

[37] T. Rose, S. Crewell, U. Loehnert, C. Simmer, "A network suitable microwave radiometer for operational monitoring of the cloudy atmosphere", Elsevier Atmospheric Research 75 (2005) 183 – 200.

[38] Knupp, K. R.; Ware, R.; Cimini, D.; Vandenberghe, F.; Vivekanandan, J.; Westwater, E.; Coleman, T.; Phillips, D, 2009, Ground-Based Passive Microwave Profiling during Dynamic Weather Conditions, Journal of Atmospheric and Oceanic Technology, vol. 26, issue 6, p. 1057.

[39] Ware, R., R. Carpenter, J. Güldner, J. Liljegren, T. Nehrkorn, F. Solheim, and F. Vandenberghe (2003), A multichannel radiometric profiler of temperature, humidity, and cloud liquid, Radio Sci., 38(4), 8079, doi:10.1029/2002RS002856.

[40] Kadygrov, E. N. and Pick, D. R. (1998), The potential for temperature retrieval from an angular-scanning single-channel microwave radiometer and some comparisons with *in situ* observations. Met. Apps, 5: 393-404. doi:10.1017/S1350482798001054.

[41] Crewell, S., and U. Löhnert, 2007: Accuracy of boundary layer temperature profiles retrieved with multi-frequency, multi-angle microwave radiometry, *IEEE Trans. Geosci. Rem. Sens.*, Vol. 45, 3, 2195-2201, DOI10.1109/TGRS.2006.888434.

[42] M. Schneebeli and C. Matzler, "Spatiotemporal Behavior of Integrated Water Vapor," in *IEEE Geoscience and Remote Sensing Letters*, vol. 8, no. 5, pp. 948-952, Sept. 2011. doi: 10.1109/LGRS.2011.2144562.

[43] J. H. Schween, S. Crewell and U. Löhnert, "Horizontal-Humidity Gradient From One Single-Scanning Microwave Radiometer," in *IEEE Geoscience and Remote Sensing Letters*, vol. 8, no. 2, pp. 336-340, March 2011. doi: 10.1109/LGRS.2010.2072981.

[44] N. Skou, Microwave Radiometer Systems: Design and Analysis, Norwood, MA, Artech House, Inc., 1989

[45] McGrath, A. and T. Hewison, 2001: Measuring the Accuracy of MARSS—An Airborne Microwave Radiometer. J. Atmos. Oceanic Technol., 18, 2003–2012, https://doi.org/10.1175/1520-0426(2001)018.

[46] Y. Han and E. R. Westwater, "Analysis and Improvement of Tipping Calibration for Ground-Based Microwave Radiometers," IEEE Transactions on Geoscience and Remote Sensing, 38, 2003, pp. 1260-1277.

[47] D Cimini, F Nasir, ER Westwater, VH Payne, DD Turner, EJ Mlawer, "Comparison of ground-based millimeter-wave observations and simulations in the Arctic winter", IEEE Transactions on Geoscience and Remote Sensing 47 (9), 3098-3106

[48] D Cimini, ER Westwater, AJ Gasiewski, "Temperature and humidity profiling in the Arctic using ground-based millimeter-wave radiometry and 1DVAR", IEEE Transactions on Geoscience and Remote Sensing 48 (3), 1381-1388

[49] M. Klein, A. J. Gasiewski, "Nadir sensitivity of passive millimeter and submillimeter wave channels to clear air temperature and water vapor variations", Journal of Geophysical research, vol. 105, no. D13, pages 17,481-17,511, July 16, 2000

[50] J. H. Van Vleck, "The Absorption of Microwaves by Oxygen", Physical Review Volume 71, Number 7, April 1, 1947.

[51] J. H. Van Vleck, "The Absorption of Microwaves by Uncondensed Water Vapor", Physical Review Volume 71, Number 7, April 1, 1947.

[52] H. J. Liebe, D. H. Layton, "Millimeter-Wave Properties of the Atmosphere: Laboratory Studies and Propagation Modeling", NTIA Report 87-224, U.S. DEPARTMENT OF COMMERCE, October 1987.

[53] H.J. Liebe, G.A. Hufford, and M.G. Cotton, "Propagation modeling of moist air and suspended water/ice particles at frequencies below 1000 GHz", AGARD Conf. Proc. 542, 3.1-3.10, 1993.

[54] P.W. Rosenkranz 1993, CHAP. 2 and appendix, in ATMOSPHERIC REMOTE SENSING BY MICROWAVE RADIOMETRY (M.A. Janssen, ed., 1993).

[55] P. W. Rosenkranz, "Water vapor microwave continuum absorption: A comparison of measurements and models", Radio Science, Volume 33, Number 4, Pages 919-928, July-August 1998.

[56] P.W. Rosenkranz, "Correction to water vapor microwave continuum absorption: a comparison of measurements and models", Radio Sci., vol. 34, n. 4, pp. 1025, 1999.

[57] Rosenkranz, P. W.: Line-by-line microwave radiative transfer (non-scattering), Remote Sens. Code Library, https://doi.org/10.21982/M81013, 2017.

[58] Cimini, Rosenkranz et al., "Uncertainty of atmospheric microwave absorption model: impact on ground-based radiometer simulations and retrievals", Atmos. Chem. Phys., 18, 15231–15259, 2018

[59] D. D. Turner, S. A. Ackerman, B. A. Baum, H. E. Revercomb, and P. Yang, "Cloud phase determination using ground-based AERI observations at SHEBA", J. Appl. Meteor., 42, 701–715, 2003.

[60] S. A. Clough, M. W. Shephard, E. J. Mlawer, J. S. Delamere, M. J. Iacono, K. Cady-Pereira, S. Boukabara, and P. D. Brown, "Atmospheric radiative transfer modeling: A summary of the AER codes", J. Quant. Spectrosc. Radiat. Transfer, 91, 233–244, 2005.

[61] ITU-R Rec P.452-16, Prediction procedure for the evaluation of interference between stations on the surface of the Earth at frequencies above about 0.1 GHz, 2015

[62] R.M. Hoffer, "Biological and Physical Considerations in Applying Computer-Aided Analysis Techniques to Remote Sensor Data", in P.H. Swain and S.M. Davis, Eds., Remote Sensing: The Quantitative Approach, N.Y., McGraw-Hill, 1978.

[63] Manual of Remote Sensing, Remote Sensing for the Earth Sciences, A.N. Renez and R.A Ryerson (Eds.), 3rd ed., NY,Wiley, 1999.

[64] M.T. Chahine, "Interaction Mechanisms within the Atmosphere. In Manual of Remote Sensing", R.N. Colwell (Ed). 2e. American Society of Photogrammetry, Falls Church, Va, 1983.

[65] H.C. Van de Hulst, "Light scattering by small particles", Dover Publications, Inc., New York, 1981.

[66] C. F. Bohren and D. R. Huffman, "Absorption and Scattering by a Sphere. In Absorption and Scattering of Light by Small Particles", 2007. doi:10.1002/9783527618156

[67] Debye, P. (1929) Polar Molecules. The Chemical Catalogue Company, New York.

[68] W. Ellison, "Permittivity of Pure Water, at Standard Atmospheric Pressure, over the Frequency Range 0–25 THz and the Temperature Range 0–100 °C" in Journal of Physical and Chemical Reference Data, March 2007.

[69] Ray, P. S. (1972). Broadband complex refractive indices of ice and water. Applied optics, 11(8), 1836-1844.

[70] Rasmussen, R., M. Politovich, J. Marwitz, W. Sand, J. McGinley, J. Smart, R. Pielke, S. Rutledge, D. Wesley, G. Stossmeister, B. Bernstein, K. Elmore, N. Powell, E. Westwater, B.B. Stankov, and D. Burrows, 1992: Winter Icing and Storms Project (WISP). Bull. Amer. Meteor. Soc., 73, 951–976.

[71] Kneifel, S., U. Löhnert, A. Battaglia, S. Crewell, and D. Siebler (2010), Snow scattering signals in ground-based passive microwave radiometer measurements, J. Geophys. Res., 115, D16214, doi:10.1029/2010JD013856.

[72] L. J. Ippolito, "Radio propagation for communications", IEEE Proc., vol. 69, pp. 697-727, 1981.

[73] G. Maral, M. Bousquet, and Z. Sun (Contributing Editor), Satellite Communications Systems: Systems, Techniques and Technology, 5th Edition, ISBN: 978-0-470-71458-4, 742 pages, Wiley (Hoboken, NJ, USA) Dec. 2009.

[74] A. Dissanyake, J. Allnut, and F. Haidara, "A prediction model that combines rain attenuation and other propagation impairments along Earth-satellite paths," IEEE Trans. Antennas Propagat., vol. 45, no. 10, pp. 1546–1558, Oct. 1997.

[75] A. Papoulis, S. U. Pillai, "Probability, Random Variables and Stochastic Processes," 4th eds., McGraw-Hill, 2002.

[76] G. Maral, M. Bousquet, Z. Sun (Contributing Editor), "Satellite Communications Systems: Systems, Techniques and Technology", 5th Edition ISBN: 978-0-470-71458-4, 2009

[77] J.W. Waters, "Absorption and emission by atmospheric gases", Methods of Experimental Physics: Astrophysics, vol. 12, part B, edited by M. L. Meeks, pp. 142-175, Academic, San Diego, Calif., 1976.

[78] M.L. Meeks, and A. E. Lilley, "The microwave spectrum of oxygen in the Earth's atmosphere", J. Geophys. Res., 68(6), 1683–1703, 1963, doi:10.1029/JZ068i006p01683.

[79] V. Mattioli, F. S. Marzano, N. Pierdicca, C. Capsoni, A. Martellucci, "Sky-Noise Temperature Modelling and Prediction for Deep Space Applications from X Band To W Band" IEEE Trans. of Antennas and Propagation, Volume: 61 , Issue: 7 Page(s): 3859 – 3868, 2013

[80] F.S. Marzano, L. Milani, V. Mattioli, K. M. Magde and G. A. Brost, "Retrieval of precipitation extinction using ground-based sun-tracking millimeter-wave radiometry," 2016 IEEE International Geoscience and Remote Sensing Symposium (IGARSS), Beijing, China, 2016, pp. 2162-2165. doi: 10.1109/IGARSS.2016.7729558

[81] R.J. Coates, "Measurements of Solar Radiation and Atmospheric Attenuation at 4.3-Millimeters Wavelength", Proc. of the IRE, pp. 122-126, Jan. 1958.

[82] Shannon C. E., "Communication in the Presence of Noise," in *Proceedings of the IRE*, vol. 37, no. 1, pp. 10-21, Jan. 1949. doi: 10.1109/JRPROC.1949.232969

[83] Pereira M., O. Postolache and P. Girao, "Spread spectrum techniques in wireless communication," in IEEE Instrumentation & Measurement Magazine, vol. 12, no. 6, pp. 21-24, December 2009.

[84] M. Biscarini, M. Montopoli, F. S. Marzano, "Evaluation of High-Frequency Channels for Deep-Space Data Transmission Using Radiometeorological Model Forecast", Antennas and Propagation, IEEE Transactions on, DOI: 10.1109/TAP.2017.2653420.

[85] S.M. Adler-Golden and J. R. Slusser, "Comparison of Plotting Methods for Solar Radiometer Calibration", J. Atmos. Oceanic Technol., vol. 24, pp. 935–938, 2007.

[86] C.U. Keller, and S.Krucker, "Radio Observations of the Quiet Sun", Chapter 14, Solar and Space Weather Radiophysics, Vol. 314, pp 287-303, 2005. DOI10.1007/1-4020-2814-8_14.

[87] M. Biscarini, F. S. Marzano, M. Montopoli, K. De Sanctis, L. Iess, M. Montagna, M. Mercolino and M. Lanucara, "Optimizing data volume return for Ka-band deep space links exploiting short-term radiometeorological model forecast", Antennas and Propagation, IEEE Transactions on, DOI: 10.1109/TAP.2015.2500910.

[88] F.S. Marzano, L. Milani, V. Mattioli, K. M. Magde and G. A. Brost, "Retrieval of precipitation extinction using ground-based sun-tracking millimeter-wave radiometry," 2016 IEEE International Geoscience and Remote Sensing Symposium (IGARSS), Beijing, China, 2016, pp. 2162-2165. doi: 10.1109/IGARSS.2016.7729558

[89] S.M. White, and M.R. Kundu, "Solar observations with a millimeter-wavelength Array," Solar Physics, Volume 141, Issue 2, pp 347-369, October 1992.

[90] H. Nakajima et al., "The Nobeyama radioheliograph," Proc. IEEE, vol. 82(5), pp. 705 - 713, 1994.

[91] K. Shibasaki, "Microwave Observations of the Quiet Sun", Proceedings of the Nobeyama Symposium, Eds., T. S. Bastian, N. Gopalswamy & K. Shibasaki, NRO Report No. 479, p.1-9, Kiyosato (Japan), Oct. 27-30, 1998.

[92] K. Shibasaki, C.E. Alissandrakis, S.Pohjolainen,, "Radio Emission of the Quiet Sun and Active Regions (Invited Review)", Solar Physics, Vol.273, Issue 2, pp 309-337, November 2011.

[93] C. Lindsey, Kopp, G., Clark, T. A., & Watt, G., "The Sun in Submillimeter and Near-Millimeter Radiation", Astrophysical Journal v.453, pp.511-516, Nov. 1995.

[94] D.L. Croom, "Sun as a broadband source for tropospheric attenuation measurements at millimetre wavelengths," in Electrical Engineers, Proceedings of the Institution of, vol.120, no.10, pp.1200-1206, October 1973, doi: 10.1049/piee.1973.0244.

[95] D.C. Hogg and Ta-Shing Chu, "The role of rain in satellite communications," in Proceedings of the IEEE, vol.63, no.9, pp.1308-1331, Sept. 1975, doi 10.1109/PROC.1975.9940.

[96] K. Shimada, M. Higashiguchi, Y. Otsu, "Characteristics of Atmospheric Attenuation at 35 GHz Obtained by Sun Track Measurements", Electronics and Communications in Japan, Vol. 67-B, No 2, pp. 26-36, 1984.

[97] F.S. Marzano, V. Mattioli, L. Milani, K. M. Magde and G. A. Brost, "Sun-Tracking Microwave Radiometry: All-Weather Estimation of Atmospheric Path Attenuation at Ka-, V-, and W-Band," in IEEE Transactions on Antennas and Propagation, vol. 64, no. 11, pp. 4815-4827, Nov. 2016. doi: 10.1109/TAP.2016.2606568

[98] F.S. Marzano, E. Fionda, P. Ciotti and A. Martellucci, "Ground-based multi-frequency microwave radiometry for rainfall remote sensing", IEEE Trans. Geosci. Rem. Sens., ISSN: 0196-2892, vol. 40, pp. 742-759, 2002.

[99] F.S. Marzano, E. Fionda, and P. Ciotti, "A neural network approach to precipitation intensity and extinction retrieval by ground-based passive microwave technique", J. Hydrology, ISSN: 0022-1694, DOI: 10.1016/j.hydrol.2005.11.42, vol. 328, pp. 121-131, 2006.

[100] F.S. Marzano, D. Cimini, P. Ciotti and R. Ware, "Modeling and measurements of rainfall by ground-based multispectral microwave radiometry", IEEE Trans. Geosci. Rem. Sens., ISSN: 0196-2892, vol. 43, pp. 1000-1011, 2005.

[101] F.S. Marzano, "Predicting antenna noise temperature due to rain clouds at microwave and millimeter-wave frequencies", IEEE Trans. Antennas and Propagat., ISSN: 0018-926X, vol. 55, n. 7, pp. 2022-2031, 2007.

[102] C. Ho, S. Slobin, A. Kantak, and S. Asmar, "Solar Brightness Temperature and Corresponding Antenna Noise Temperature at Microwave Frequencies", JPL IPN Progress Report, Vol. 42-175 • November 15, 2008.

[103] W. Graf, R. Bracewell, J. Deuter, and J. Rutherford, "The sun as a test source for boresight calibration of microwave antennas," IEEE Transactions on Antennas and Propagation, Vol. 19, Issue 5, pp. 606 - 612, Sept. 1971, DOI:10.1109/TAP.1971.1139996.

[104] J.C. Liljegren, E. E. Clothiaux, G. G. Mace, S. Kato, and X. Dong, (2001), "A new retrieval for cloud liquid water path using a ground-based microwave radiometer and measurements of cloud temperature. J. Geophys. Res., Vol. 106, pp. 14 485–14 500.

[105] V. Mattioli, "Alphasat TDP5 GS G/T measurement campaign and IOT GS4-MWR, Graz, Austria. Definition of radiometric coefficients", under ESA/ESTEC Contract Number 4000102639/10/NL/CLP, Nov 11, 2013.

[106] Radiometer Physics GmbH, "Technical Instrument Manual", Code: RPG-MWR-STD-TM, Issue: 01/02, Sept. 2013, pp.41.

[107] U.S. Standard Atmosphere, 1962, U.S. Government Printing Office, Washington, D.C., 1962.

[108] J.E. McKay, D.A. Robertson, P.A.S. Cruickshank, D.R. Bolton, R.I. Hunter, R. Wylde, G.M. Smith, "Compact wideband corrugated feedhorns with ultra-low side lobes for very high performance antennas and quasi-optical systems". IEEE Trans. Antennas and Propagat., Vol. 61, n. 4, pp. 1714-1721, 2013. DOI: 10.1109/TAP.2013.2243097

[109] M.M. Franco, S.D. Slobin, C.T. Stelzried, "20.7 and 31.4-GHz Solar Disk Temperature measurements", TDA progress Report 42-64, pp. 140-168, 1981.

[110] J.L. Linsky, "A recalibration of the quiet Sun millimeter spectrum based on the Moon as an absolute radiometric standard", Sol Phys, Vol 28, pp 419-424, 1973.

[111] Ko, H. C., "On the analysis of Radio Astronomical Observations made with high resolution Radio Telescope Antennas", The Ohio State University, Columbus, Radio Observatory Rept. No. 21, 1961.

[112] T. Rose, ESA ATPROP System (RPG-HATPRO & RPG-15-90), Version 2.00, Radiometer Physics GmbH (www.radiometer-physics.com), pp. 190, 2008.

[113] V. Mattioli, A. Graziani, P. Tortora, A.V. Bosisio, L. Castanet, "Analysis and improvements of methodologies for discriminating atmospheric conditions from radiometric brightness temperatures" Proc. of the 7th European Conference on Antennas and Propagation (EuCAP), pp. 1392 – 1396, 2013.

[114] A.V. Bosisio, G. Graziani, V. Mattioli, P. Tortora, "On the Use of Microwave Radiometers for Deep Space Mission Applications by Means of a Radiometric-Based Scalar Indicator", IEEE Journal of Selected Topics in Applied Earth Observations and Remote Sensing, Vol.8 issue 9, pp. 4336-4344, 2015.

[115] J.A. Schroeder, and E. R. Westwater, Users' guide to WPL microwave radiative transfer software, NOAA Tech. Rpt. ERL-219 WPL-213, 84 pp., NOAA/Environmental Research Laboratories, Boulder ,CO, 1991.

[116] V. Mattioli, P. Basili, S. Bonafoni, P. Ciotti, E. R. Westwater, "Analysis and improvements of cloud models for propagation studies", Radio Sci., 44, RS2005, Mar 2009, doi:10.1029/2008RS003876

[117] G. Brost and K.M. Magde, "On the Use of the Radiometer Formula for Atmospheric Attenuation Measurements at GHz Frequencies", European Conference on Antennas and Propagation (EuCAP), Davos , April 11-14, 2016.

[118] J.E. Vernazza, E. H. Avrett, and R. Loeser, "Structure of the solar chromosphere. III. Models of the EUV brightness components of the quit Sun", The Astrophysical Journal Supplement Series, 45:635-725, April 1981.

[119] V. Mattioli, F. S. Marzano, N. Pierdicca, C. Capsoni, and A. Martellucci, "Sky-Noise Temperature Modelling and Prediction for Deep Space Applications from X Band To W Band" IEEE Trans. of Antennas and Propagation, Volume: 61 , Issue: 7 Page(s): 3859 – 3868, 2013

[120] F.S. Marzano, "Modeling antenna noise temperature due to rain clouds at microwave and millimeter-wave frequencies", IEEE Trans. Antennas and Propagat., ISSN: 0018-926X, vol. 54, pp. 1305-1317, 2006.

[121] C.J. Willmott, S.M. Robesonb and K. Matsuura, "A refined index of model performance," Int. J. Climatol. vol. 32, pp. 2088–2094, 2012.

[122] V. Meunier, U. Lohnert, P. Kollias and S. Crewell, "Biases caused by the instrument bandwidth and beam width on simulated brightness temperature measurements from scanning microwave radiometers", Atmos. Meas. Tech., Vol 6, pp. 1171–1187, 2013, doi:10.5194/amt-6-1171-2013.

[123] V. Mattioli, E. R. Westwater, D. Cimini, A. J. Gasiewski, M. Klein, V. Y. Leuski, "Microwave and Millimeter-Wave Radiometric and Radiosonde Observations in an Arctic Environment", AMS Journal of Atmospheric and Oceanic Technology, Vol. 25, No. 10, pp. 1768–1777, 2008, doi:10.1175/2008JTECHA1078.1.

[124] H Brogniez et al., A review of sources of systematic errors and uncertainties in observations and simulations at 183 GHz, Atmos. Meas. Tech., 9, 2207–2221, 2016, doi:10.5194.

[125] X. Zou, L. Lin and F. Weng, "Absolute Calibration of ATMS Upper Level Temperature Sounding Channels Using GPS RO Observations," in IEEE Transactions on Geoscience and Remote Sensing, vol. 52, no. 2, pp. 1397-1406, Feb. 2014. doi: 10.1109/TGRS.2013.2250981.

[126] G. Brost and K. M. Magde, "On the use of the radiometer formula for atmospheric attenuation measurements at GHz frequencies," in Proc. 10th Eur. Conf. Antennas Propag., Davos, Switzerland, Apr. 2016, pp. 1–5.

[127] V. Mattioli, L. Milani, K. M. Magde, G. A. Brost, and F. S Marzano, "Retrieval of Sun Brightness Temperature and Precipitating Cloud Extinction Using Ground-Based Sun-Tracking Microwave Radiometry", IEEE J. Sel. Topics Appl. Earth Observ. in Remote Sens., vol. 10, no. 7, July 2017.

[128] Rose, T., S. Crewell, U. Löhnert, and C. Simmer, "A network suit-able microwave radiometer for operational monitoring of the cloudy atmosphere", Atmos. Res., vol. 75, no. 3, pp.183–203, 2005

[129] V. Mattioli, F. S. Marzano, N. Pierdicca, C. Capsoni and A. Martellucci, "Modeling and Predicting Sky-Noise Temperature of Clear, Cloudy, and Rainy Atmosphere From X- to W-Band," in *IEEE Transactions on Antennas and Propagation*, vol. 61, no. 7, pp. 3859-3868, July 2013. doi: 10.1109/TAP.2013.2254434

[130] Matsui, T., J. Santanello, J. J. Shi, W.-K. Tao, D. Wu, C. Peters-Lidard, E. Kemp, M. Chin, D. Starr, M. Sekiguchi, and F. Aires, (2014): "Introducing multisensor satellite radiance-based evaluation for regional Earth System modeling", J. Geophys. Res. Atmos., vol. 119, pp. 8450–8475, doi:10.1002/2013JD021424

[131] M. O. García, N. Jeannin, L. Féral, and L. Castanet, "Use of WRF model to characterize propagation effects in the troposphere," in Proc. Eur. Conf. Antennas Propag. (EuCAP), Apr. 2013, pp. 1377–1381.

[132] Radiometer Physics GmbH, "Technical Instrument Manual", Code: RPG-MWR-STD-TM, Issue: 01/02, Sept. 2013, pp.41.

[133] T. Rose, ESA ATPROP System (RPG-HATPRO & RPG-15-90), Version 2.00, Radiometer Physics GmbH (www.radiometer-physics.com), pp. 190, 2008.

[134] J. Zhang, K. Howard, C. Langston, B. Kaney, Y. Qi, L. Tang, H. Grams, Y. Wang, S. Cocks, S. Martinaitis, A. Arthur, K. Cooper, J. Brogden, and D. Kitzmiller, "Multi-Radar Multi-Sensor (MRMS) Quantitative Precipitation Estimation: Initial Operating Capabilities". Bull. Amer. Meteor. Soc., vol. 97, pp. 621–638, https://doi.org/10.1175/BAMS-D-14-00174.1, 2016.

[135] J. Zhang, K. Howard, S. Vasiloff, C. Langston, B. Kaney, Y. Qi, L. Tang, H. Grams, D. Kitzmiller, J. Levit, "Initial Operating Capabilities of Quantitative Precipitation Estimation in the Multi-Radar Multi-Sensor System", 2014 28th Conf. on Hydrology, Amer. Meteor. Soc.

[136] J. Zhang, K. Howard, S. Vasiloff, C. Langston, et al., "National Mosaic and multi-sensor QPE (NMQ) system: description, results and future plans". 2011 Bull. Amer. Met. Soc., 92, 1321-1338.

[137] Grell, G. A.: Prognostic evaluation of assumptions used by cumulus parameterizations within a generalized framework, Mon. Weather Rev., 121, 764-787, 1993.

[138] Shamarock et al. A Description of the Advanced Research WRF Version 3, NCAR TECHNICAL NOTE, 2008, NCAR/TN–475+STR.

[139] Reisner, J., R. J. Rasmussen, and R. T. Bruintjes, 1998: Explicit forecasting of supercooled liquid water in winter stroms using the MM5 mesoscale model. Quart. J. Roy. Meteor. Soc., 124B, 1071-1107.

[140] Mlawer, E. J., S. J. Taubman, P. D. Brown, M. J. Iacono, and S. A. Clough, 1997: Radiative transfer for inhomogeneous atmosphere: RRTM, a validated correlated-k model for the long-wave. J. Geophys. Res., 102(D14), 16663-16682.

[141] Troen, L., and L. Mahrt, 1986: A simple model of the atmospheric boundary layer: Sensitivity to surface evaporation. Bound.-Layer Meteor., 37, 129–148.

[142] Thompson, G. and T. Eidhammer, 2014: A study of aerosol impacts on clouds and precipitation development in a large winter cyclone. J. Atmos. Sci., 71, 3636–3658.

[143] Grell, G. A. and S. R. Freitas, 2014: A scale and aerosol aware stochastic convective parameterization for weather and air quality modeling, Atmos. Chem. Phys., 14, 5233-5250.

[144] Mellor, G. L. and T. Yamada, 1982: Developement of a turbulence closure model for geophysical fluid problems. Rev. Geophys. Space Phys., 20, 851-875.

[145] Kummerow, C., "On the accuracy of the Eddington approximation for radiative transfer in the microwave frequencies", J. Geophys. Res., 98, 2757-2765, 1993.

[146] Borysow, A, and L. Frommhold, Astrophysical Journal, v.311, pp.1043-1057 (1986) with modification to account for O2-O2 and O2-N2 collisions, as suggested by J.R. Pardo, E.Serabyn, J.Cernicharo, J. Quant. Spectros. Radiat. Trans. v.68, pp.419-433 (2001).

[147] Liebe H. J., G. A. Hufford and T. Manabe, "A model for the complex permittivity of water at frequencies below 1 THz," Int. J. IR & MM Waves, vol. 12, pp. 659-675, 1991.

[148] J.H. van Vleck, "The Absorption of Microwaves by Oxygen", Phys. Rev. vol. 71, iss. 7, 413-424, Apr 1947, doi: 10.1103/PhysRev.71.413.

[149] World Meteorological Organization, "General meteorological standards and recommended practices. Corrigendum to 1988 edition." WMO-No. 49. 2000, Geneva, Switzerland.

[150] S. Shambayati, "On the benefits of short-term weather forecasting for Kaband (32 GHz)," inProc. IEEE Aerosp. Conf., Mar. 2004, pp. 1489–1498.

[151] G. Brussaard and P.A. Watson, Atmospheric Modelling and Millimetre Wave Propagation. London, U.K.: Chapman & Hall, 1995.

[152] E. Matricciani, "An optimum design of deep-space downlinks affected by tropospheric attenuation,"Int. J. Satell. Commun. Netw., vol. 27, no. 6, pp. 312–329, 2009, doi: 10.1002/sat.942.

[153] M. Montagna, M. Mercolino, M. Arza, M. Lanucara, E. Montagnon, and E. Vassallo, "Maximization of data return at Ka-band for interplanetary missions," inProc. 18th Ka Broadband Commun. Navig. Earth Observ. Conf., Sep. 2012, pp. 24–27.

[154] M. O. García, N. Jeannin, L. Féral, and L. Castanet, "Use of WRF model to characterize propagation effects in the troposphere," inProc. Eur. Conf. Antennas Propag. (EuCAP), Apr. 2013, pp. 1377–1381.

[155] F. Davarian, S. Shambayati, and S. Slobin, "Deep space Ka-band link management and mars reconnaissance orbiter: Long term weather statistics versus forecasting," Proc. IEEE, vol. 92, no. 12, pp. 312–329,Nov./Dec. 2004.

[156] Biscarini M., F. S. Marzano, M. Montopoli, K. De Sanctis, L. Iess, M. Montagna, M. Mercolino and M. Lanucara, "Optimizing data volume return for Ka-band deep space links exploiting short-term radiometeorological model forecast", Antennas and Propagation, IEEE Transactions on, DOI: 10.1109/TAP.2015.2500910.

[157] J. Benkhoffet al., "BepiColombo comprehensive exploration of mercury: Mission overview and science goals", Planet. Space Sci., vol. 58, no. 1–2, pp. 2–20, 2010.

[158] Biscarini M., K. De Sanctis, S. Di Fabio, M. Montopoli, L. Milani, and Frank S. Marzano, "Assessment and uncertainty estimation of weather-forecast-driven data transfer for space exploration at Ka and X band", Antennas and Propagation, IEEE Transactions on, doi: 10.1109/TAP.2019.2899041

[159] A. Grell, J. Dudhia, and D. R. Stauffer, "A description of fifth-generation Penn State/NCAR mesoscale model (MM5)," National Center for Atmospheric Research, Boulder, CO, US, NCAR Tech. Note NCAR/TN-398+STR, 1994

[160] H. Masunaga et al., "Satellite Data Simulator Unit (SDSU): A multisensor, multi-spectral satellite simulator package," Bull. Amer. Meteorol. Soc., vol. 91, pp. 1625–1632, 2010.

[161] Shamarock et al. A Description of the Advanced Research WRF Version 3, NCAR Technical note, 2008, NCAR/TN–475+STR

[162] Matsui, T., J. Santanello, J. J. Shi, W.-K. Tao, D. Wu, C. Peters-Lidard, E. Kemp, M. Chin, D. Starr, M. Sekiguchi, and F. Aires, (2014): "Introducing multisensor satellite radiance-based evaluation for regional Earth System modeling", J. Geophys. Res. Atmos., vol. 119, pp. 8450–8475, doi:10.1002/2013JD021424

[163] Rec. ITU-R SA.1027-5, "Sharing criteria for space-to-Earth data transmission systems in the Earth exploration-satellite and meteorological-satellite services using satellites in low-Earth orbit", 2017

[164] Rec. ITU-R SA.609-2, "Protection criteria for radiocommunication links for manned and unmanned near-Earth research satellites", 2006

[165] Rec. ITU-R SA.1157-1 "Protection criteria for deep-space research", 2006

[166] Rec. ITU-R SA.1396 "PROTECTION CRITERIA FOR THE SPACE RESEARCH SERVICE IN THE 37-38 GHz AND 40-40.5 GHz BANDS", 1999

[167] ITU-R Recommendation M.2120-0, Modelling and simulation of IMT networks and systems for use in sharing and compatibility studies, 02/2017

[168] "Determination of a supplementary contour using the time-variant gain (TVG) method", Appendix 7, Annex 6.4, ITU Radio Regulations, Appendices, Edition 2016

[169] ITU-R, 5D/TEMP/265-E rev. 3, SWG Work for TG 5/1: Characteristics of terrestrial IMT systems for frequency sharing/interference analyses in the frequency range between 24.25 GHz and 86 GHz, 22 February 2017.

[170] E. M. Prince and W. P. Menzel, "Geostationary satellite detection of biomass burning in South America," Int. J. Remote Sens., vol. 13, no.15, pp. 2783–2799, 1992.

[171] Freeborn, P.H.; Wooster, M.J.; Roberts, G.; Xu, W. Evaluating the SEVIRI Fire Thermal Anomaly Detection Algorithm across the Central African Republic Using the MODIS Active Fire Product. Remote Sens. 2014, 6, 1890-1917. doi: https://doi.org/10.3390/rs6031890

[172] E. M. Prins, and W. P. Menzel, "Trends in South American biomass burning detected with GOES visible infrared spin scan radiometer atmospheric sounder from 1983 to 1991" J. Geophys. Res., vol. 99, no. 8, pp. 16.719–16.735, 1994.

[173] Platnick, et al, "The MODIS cloud products: Algorithms and examples from Terra", IEEE Transactions on Geoscience and Remote Sensing, vol. 41, no. 2, pp. 459-473, Feb. 2003. doi: 10.1109/TGRS.2002.808301

[174] K. D. Hutchison, J. K. Roskovensky, J. M. Jackson, A. K. Heidinger, T. J. Kopp, M. J. Pavolonis & R. Frey (2005) Automated cloud detection and classification of data collected by the Visible Infrared Imager Radiometer Suite (VIIRS), International Journal of Remote Sensing, 26:21, 4681-4706, DOI: 10.1080/01431160500196786.

[175] M Kordestani, MF Samadi, M Saif, and K Khorasani, "A New Fault Prognosis of MFS System Using Integrated Extended Kalman Filter and Bayesian Method", IEEE Transactions on Industrial Informatics PP, 1-11 (2018).

[176] Soltani, M. Kordestani, P Karim Aghaee, and M Saif, "Improved Estimation for Well-Logging Problems Based on Fusion of Four Types of Kalman Filters", IEEE Transactions on Geoscience and Remote Sensing 56, 647-654 (2018).

[177] P. Zarchan and H. Musoff, "Fundamentals of Kalman Filtering: A Practical Approach, Third Edition", Progress in Astronautics and Aeronautics, Vol. 232, ISBN 978-1-60086-718-7 (2009).

[178] C.D. Rodgers, "Inverse methods for atmospheric sounding – theory and practice", Series on Atmospheric, Oceanic and Planetary Physics – Vol.2, University of Oxford, ISBN 981-02-2740-X (200).

[179] R. S. Bucy and P. D. Joseph, Filtering for Stochastic Processing with Applications to Guidance. Providence, RI: AMS Chelsea Publishing, 2nd ed., 2005, pp 55–57.

[180] M. J. Wooster, G. Roberts, G. Perry, and Y. J. Kaufman, "Retrieval of biomass combustion rates and totals from fire radiative power observations: FRP derivation and calibration relationships between biomass consumption and fire radiative energy release", J. Geo. Res. Atm., 110, D24311, 2005.

[181] R. E. Kalman, "A New Approach to Linear Filtering and Prediction Problems", ASME. J. Basic Eng. 1960;82(1):35-45.

[182] M. Diagne, M. Drame, C. Ferrao, P. G. Marchetti, S. Pinto and G. Rivolta, "Multisource Data Integration for Fire Risk Management: The Local Test of a Global Approach," in IEEE Geosc & Remote Sen. Letters, vol. 7, no.1, pp. 93-97, Jan. 2010.

[183] L. Milani, M. Arcorace, R. Cuccu, G. Rivolta and F. S. Marzano, "Clear-Air Anomaly Detection Using Modified Kalman Temporal Filter from Geostationary Multispectral Data," 2018 IEEE International Geoscience and Remote Sensing Symposium, Valencia, 2018, pp. 6879-6882. doi: 10.1109/IGARSS.2018.8517396.

[184] J. Schmid, "The SEVIRI Instrument", ESA/ESTEC

[185] D. M. A. Aminou, B. Jacquet and F. Pasternak 'Characteristics of the Meteosat Second Generation Radiometer/Imager: SEVIRI' Proceedings of SPIE, Europto series, Vol. 3221 pages 19-31.

[186] D. M. A. Aminou, A. Ottenbacher, B. Jacquet and A. Kassighian 'Meteosat Second Generation: On-ground Calibration, Characterisation and Sensitivity Analysis of the SEVIRI Imaging Radiometer'. Proceedings of SPIE « Earth Observing Systems IV », Vol. 3750, page 419-430.

[187] L. Giglio, W. Schroeder, C.O. Justice, "The collection 6 MODIS active fire detection algorithm and fire products", Rem. Sens. of Env., Vol. 178, 2016, Pages 31-41, ISSN 0034-4257.

[188] Van den Bergh and P. E. Frost, "A multi temporal approach to fire detection using MSG data," International Workshop on the Analysis of Multi-Temporal Remote Sensing Images, 2005., Biloxi, MS, USA, 2005, pp. 156-160. doi: https://doi.org/10.1109/AMTRSI.2005.1469861

[189] I. Lira, Evaluating the Uncertainty of Measurement. Fundamentals and Practical Guidance. Institute of Physics, Bristol, UK, 2002.

[190] JCGM 100:2008. Evaluation of measurement data - Guide to the expression of uncertainty in measurement, Joint Committee for Guides in Metrology.

[191] EUMETSAT, "MTG-FCI: ATBD for Cloud Mask and Cloud Analysis Product", Doc.No. EUM/MTG/DOC/10/0542, 17 January 2013

[192] EUMETSAT, "MSG Ground Segment LRIT HRIT Mission Specific Implementation", v7, Code: EUM/MSG/SPE/057, 30 Nov. 2015.

[193] EUMETSAT, "MSG Level 1.5 Image Data Format Description", v8, Code: EUM/MSG/ICD/105, 26 Sep. 2017.

[194] EUMETSAT LSA SAF Product User Manual FUM FRP, Version 2.1, Appendix C, Ref. SAF/LAND/IM/PUM_FRP/2.1, 10 March 2016.

[195] P.G. Marchetti, G. Rivolta, S. D'Elia, J. Farres, G. Mason, and N. Gobron, "A Model for the Scientific Exploitation of Earth Observation Missions: The ESA Research and Service Support." IEEE Geoscience and Remote Sensing Society Newsletter, Vol. 162, pp. 10-18, March 2012.

[196] EUMETSAT, "Radiometric Calibration of MSG SEVIRI Level 1.5 Image Data in Equivalent Spectral Blackbody Radiance", Code: EUM/OPS-MSG/TEN/03/0064, January 2007

[197] EUMETSAT, "The Conversion from Effective Radiances to Equivalent Brightness Temperatures", v1, Code: EUM/MET/TEN/11/0569, October 2012.

[198] Roberts and M. J. Wooster, "Fire Detection and Fire Characterization Over Africa Using Meteosat SEVIRI," in IEEE Transactions on Geoscience and Remote Sensing, vol. 46, no. 4, pp. 1200-1218, April 2008. doi: https://doi.org/10.1109/TGRS.2008.915751

[199] J. Waller, S. Ballard, S. Dance, G. Kelly, N. Nichols, and D. Simonin, "Diagnosing Horizontal and Inter-Channel Observation Error Correlations for SEVIRI Observations Using Observation-Minus-Background and Observation-Minus-Analysis Statistics," Remote Sensing, vol. 8, no. 7, p. 581, Jul. 2016.

[200] EUMETSAT Data Centre, Data access [Online]. Available: https://www.eumetsat.int/website/home/Data/DataDelivery/EUMETSATDataCentre/index.html. [Accessed: 30- Jan- 2019].

[201] ESA RSS Cloud Toolbox Service [Online]. Available: https://eogrid.esrin.esa.int/cloudtoolbox/ [Accessed: 30- Jan- 2019].

[202] M. Arcorace, R. Cuccu, G. Rivolta, C. Orrù, L. Milani & J.M. Delgado Blasco, "Near Real Time Fire Detection Service via the PROBA-V Mission Exploitation Platform", The ESA Earth Observation Φ-week, 12-16 Nov. 2018, Frascati, Italy.

[203] M. Derrien and H. Le Gléau "Improvement of cloud detection near sunrise and sunset by temporal-differencing and region-growing techniques with real-time SEVIRI", International Journal of Remote Sensing, Vol. 31, No. 7, Pag. 1765-1780

[204] Y. Han, E. R. Westwater, and R. A. Ferrare, "Applications of Kalman Filtering to Derive Water Vapor from Raman Lidar and Microwave Radiometers," Journal of Atmospheric and Oceanic Technology, 14, 3, 1997, pp. 480-487.

APPENDICES

A. Sun-Tracking Microware Radiometry: Error sensitivity analysis

The sensitivity analysis of Sun brightness temperature estimate to residual errors or uncertainty of ST-MWR measurements is fundamental to understand the expected accuracy of the technique. The following section A.I of this Appendix is devoted to this analysis. Further considerations are also provided in the next sections A.II and A.III where the impact of the instrument spectral response and the radiometer antenna side lobes is discussed, respectively.

A.I. Theoretical sensitivity analysis and error budget

Several sources of uncertainty in ST-MW radiometry can be identified: i) different adopted techniques; ii) beam filling factor; iii) antenna pattern; iv) elevation scanning. In order to perform this error budget analysis, we can use the first-order error propagation theory by assuming a statistical independence among the error sources.

Primarily, uncertainties of the beam-filling factor f_Ω have to be considered to evaluate its impact in the T_{Bsun} estimation, considering that $T_{Bsun} = T^*_{Bsun}/f_\Omega$. In a general way, these are related to errors associated to the Sun radiation solid angle Ω_{Psun} and the antenna radiation solid angle Ω_{Pant}. Starting from (3.II.7), the uncertainty in T_{Bsun} because of variation in Ω_{Pant} is given by $\delta T_{Bsun} = (T^*_{Bsun}/\Omega_{Psun})\delta\Omega_{Pant}$, where the variations in Ω_{Pant} are mainly due to the knowledge of the antenna radiation pattern and the half-power beamwidth values. Analogously, T_{Bsun} uncertainty because of variations in Ω_{Psun} can be obtained from (3.II.7) leading to $\delta T_{Bsun} = -T^*_{Bsun}(\Omega_{Pant}/\Omega^2_{Psun})\ \delta\Omega_{Psun}$ and variations in Ω_{Psun} shall be computed considering the simplified expression in (3.II.17) or the general expression for a Gaussian beam in (3.II.19). The latter depends on both Sun disk diameter and half-power beamwidth values. For this reason, a more general sensitivity analysis can be achieved from (3.II.21) considering δT_{Bsun} because of variation in Θ_{ML}, which yields the following uncertainty:

$$\delta T_{Bsun} = \frac{2\ln(2)\ \eta_{ML}\ T^*_{Bsun}}{f^2_\Omega}\frac{\Theta^2_{sun}}{\Theta^3_{\mathrm{ML}}}e^{-\ln(2)\left(\frac{\Theta_{sun}}{\Theta_{\mathrm{ML}}}\right)^2}\delta\Theta_{\mathrm{ML}} \tag{A.1}$$

Figure A-0-1a shows the previous expression using the AFRL half-power beamwidth values and the Sun zenithal plane angle described in Section II.C and using T^*_{Bsun} values in Table A-0-1. It can be noted that the uncertainty in the value of Θ_{ML} provides a large source of error for the estimate of T_{Bsun}. For an uncertainty of Θ_{ML} up to 0.3°, the error in estimating T_{Bsun} goes from 1424 K at Ka band up to 2888 K at W band. In a more quantitative way, δT_{Bsun} has been be evaluated from (A.1) considering a difference of 11% in Θ_{ML} (worst case at 31.4 and 72.5, as the differences among AFRL values described in II.B and RPG LPW-U72-82 Θ_{ML} values from manufacturer specification). The

results are given in Table A-0-1 (left side). Furthermore, starting from (3.II.21), errors in T_{Bsun} due to main beam efficiency η_{ML} variation have to be taken into account according to:

$$\delta T_{Bsun} = -\frac{T^*_{Bsun}}{\eta_{ML} \cdot f_\Omega} \delta\eta_{ML} \tag{A.2}$$

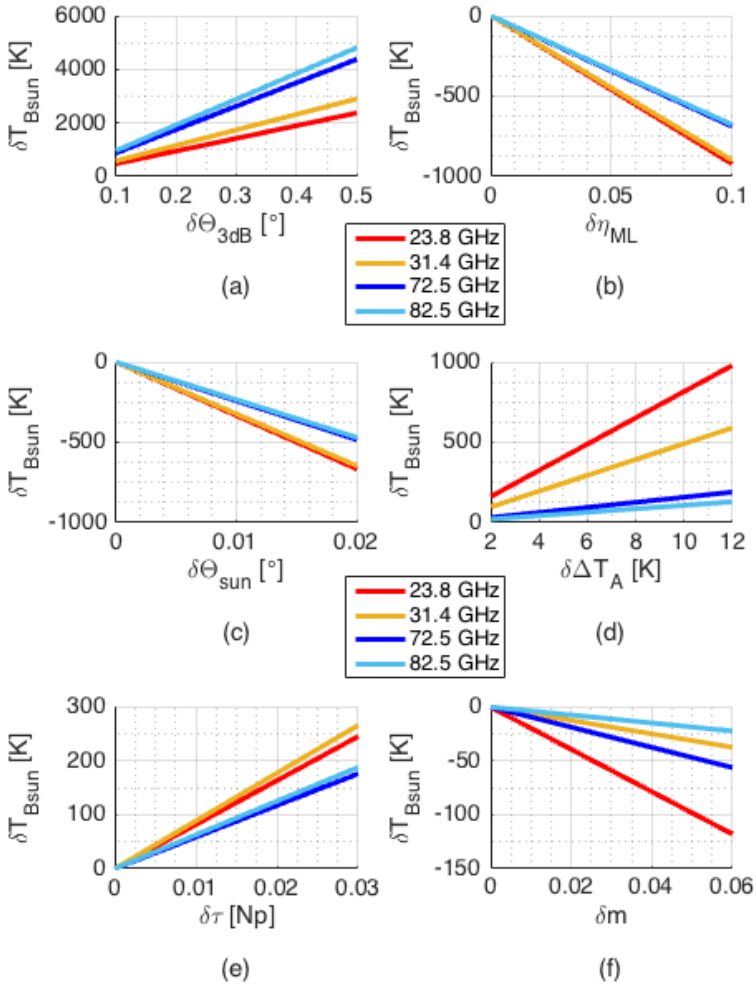

Figure A-0-1: Sensitivity analysis of ST-MWR performances for a set of values which are those expected between Ka and W band.

Figure A-0-1b shows the previous expression using values of interest in Table 3-4 and η_{ML} described in Section II.B. For an uncertainty of η_{ML} up to 0.05, δT_{Bsun} goes from -330 K at W band up to -450 K at Ka band. Error sources in both (A.1) and (A.2) imply that the AFRL-MWR antenna pattern should be known with a high degree of accuracy.

Analogously, the uncertainty in T_{Bsun}, because of variations in Θ_{sun}, can be computed from (3.II.21) yielding the following uncertainty:

$$\delta T_{Bsun} = \frac{-2\ln(2)\ \eta_{ML}\ T^*_{Bsun}}{f_\Omega^2}\frac{\Theta_{sun}}{\Theta_{\mathrm{ML}}^2}e^{-\ln(2)\left(\frac{\Theta_{sun}}{\Theta_{\mathrm{ML}}}\right)^2}\delta\Theta_{sun} \tag{A.3}$$

Since the Earth-Sun distance changes over the year, the disk angle subtended by the Sun varies between 0.526° and 0.545°. This leads to a maximum Θ_{sun} variation of 0.019°.

TABLE A-0-1: EXPECTED ERRORS IN T_{Bsun} DUE TO FILLING FACTOR VARIATIONS

	δT_{Bsun} vs $\delta\Theta_{\mathrm{ML}}$		δT_{Bsun} vs $\delta\Theta_{sun}$	
f [GHz]	$\delta\Theta_{\mathrm{ML}}$[°]	δT_{Bsun}[K]	$\delta\Theta_{sun}$[°]	δT_{Bsun}[K]
23.8	0.41	1946	0.0019	-63.3
31.4	0.33	1915	0.0030	-97.0
72.5	0.17	1489	0.0119	-287.5
82.5	0.14	1348	0.0152	-356.9

Figure A-0-1c shows (A.3) using the same values of the previous analyses, for Θ_{sun} variations of about 0.01° (maximum deviation from the value reported in Section II.B), the error in estimating T_{Bsun} is relatively small and it goes from -240 K at 82.5 GHz up to -340 K at 23.8 GHz. Table A-0-1 (right side) reports the uncertainty in T_{Bsun} because of Θ_{sun} variations in more detail, considering $\delta\Theta_{sun}$ values obtained by calculating the difference between the general formulation in (3.II.19) and the approximation in (3.II.17). This approximation leads to small errors in T_{Bsun} with respect to previous sources, especially at lower frequencies where the effect of the radiometer antenna pattern can be neglected in (3.II.16). Secondly, error analyses with respect to radiating quantities have to be carried out. Sensitivity δT_{Bsun} with respect to $\delta\Delta T_A$ is obtained from the governing equations (3.II.11) and (3.II.15) of Sun-tracking microwave radiometry leading to:

$$\delta T_{Bsun} = \frac{1}{f_\Omega}\ e^{\tau}\ \delta\Delta T_A \tag{A.4}$$

Figure A-0-1d shows the sensitivity to ΔT_A, in which τ values expected in clear-sky situations between K and W band were used (τ=0.10, 0.05, 0.30, and 0.15 Np for the four available frequencies, respectively). Since ΔT_A values are much smaller at K band with respect to V band, $\delta\Delta T_A$ uncertainties have larger effects at lower frequencies with respect to higher frequencies. Uncertainties are due to calibration errors and antenna mispointing during Sun tracking and atmospheric variability. The first is estimated to be less than 0.5 K at K and Ka band and about 1 K at W and V-band, whereas the latter goes from 4 K to 10 K with increasing frequency, whose reduction has suggested the filtering approach used in Section II.B. For an uncertainty in ΔT_A of about 8 K, the error in T_{Bsun} goes from 86 K at 82.5 GHz up to 652 K at 23.8 GHz. Quantitative analysis of (3.II.34) is reported in the left side of Table A-0-2, considering T_{Bsun} uncertainties for typical ΔT_A in clear air. The latters have been derived from the variability of AFRL-MWR data during the ooS and twS switching. In this case, δT_{Bsun} are less than 4% at all frequencies with respect to the absolute values (worst case at 23.8 GHz).

Furthermore, we can obtain the uncertainty in T_{Bsun} due to atmospheric extinction variations $\delta\tau$ from the same equations as before:

$$\delta T_{Bsun} = \frac{1}{f_\Omega}\, \Delta T_A\, e^{\tau}\, \delta\tau \tag{A.5}$$

Figure A-0-1e shows the relation for the same set of τ values and for ΔT_A values expected in clear-sky situations (ΔT_A = 100, 180, 370, and 580 K for the four available frequencies, respectively). For an uncertainty in τ of about 0.02 Np, the error in T_{Bsun} goes from 117 K at 72.5 GHz up to 176 K at 31.4 GHz. The two considered techniques use different methods to evaluate the atmospheric extinction: i) Langley technique estimates τ_z through the slope of the linear regression in (3.II.13), representing a daily average atmospheric extinction (the associated error is mainly due to the attenuation variability during the day and Sun tracking antenna mispointing); ii) Meteorological technique needs an estimate of τ to be computed according to (3.II.14). This means that both mean radiating temperature and antenna noise temperature ooS errors have to be taken into account. Note that for the meteorological technique we can provide a daily averaged value of Sun brightness temperature in order to mitigate the punctual T_{Bsun} uncertainties due to $\delta\tau$. Starting from (3.II.14), the uncertainty in τ because of variation in T_{AooS} is given by:

$$\delta\tau = -\frac{\delta T_{AooS}}{(T_{mr} - T_{AooS})} \tag{A.6}$$

Considering a fixed mean radiating temperature of 270 K and typical T_{AooS} values expected in clear-air situations (T_{AooS} = 35, 20, 100, and 60 K for the four available frequencies, respectively), we can estimate $\delta\tau$ associated to the δT_{AooS} absolute accuracies (equal to 0.5 K at K-band and 1 K at W-band according to the manufacturer specifications). Resulting $\delta\tau$ values are relatively small and they go from -0.0021 Np at 23.8 GHz up to -0.0059 Np at 72.5 GHz.
Furthermore, $\delta\tau$ uncertainty due to errors in estimating T_{mr} leads to:

$$\delta\tau = \frac{T_{cos} - T_{AooS}}{(T_{mr} - T_{cos})\,(T_{mr} - T_{AooS})}\, \delta T_{mr} \tag{A.7}$$

Since T_{AooS} assumes smaller values at K band with respect to V band, $\delta\tau$ uncertainties have larger effects at higher frequencies. This behavior is the opposite of what happens in (A.5), where δT_{Bsun} grows with decreasing frequency. For an uncertainty in T_{mr} of 3 K, the error in τ goes from -0.0008 Np at 31.4 GHz up to -0.006 Np at 72.5 GHz, using the same clear-air values of the previous analysis.

On the right side of Table A-0-2, the error budget analysis of T_{Bsun} is shown with respect to uncertainties $\delta\tau$. The latter have been derived from both τ_z confidence intervals of the linear regression slope in (3.II.13) and the standard deviation of the estimated atmospheric extinction time series in (3.II.14). The resulting values are very similar for both techniques. Errors in Sun brightness temperature are less than 2% at all frequencies with respect to the absolute values (worst case at 82.5 GHz).

TABLE A-0-2: EXPECTED ERRORS IN T_{Bsun} DUE TO RADIATING QUANTITY VARIATIONS

	δT_{Bsun} vs $\delta \Delta T_A$		δT_{Bsun} vs $\delta\tau$	
f [GHz]	$\delta \Delta T_A$[K]	δT_{Bsun}[K]	$\delta\tau$[Np]	δT_{Bsun}[K]
23.8	4	326	0.019	155
31.4	5	245	0.009	79
72.5	8	126	0.015	87
82.5	10	108	0.021	131

Further error should be considered whether different elevation angles are assumed between off-the-Sun and toward-the-Sun observations in the computation of the antenna noise temperature difference. Considering an ooS observation in (3.II.9) performed at an elevation angle θ_1, the antenna noise temperature difference in (3.II.10) depends on both elevation angles (or air-masses). The T_{Bsun} uncertainty due to the air mass variation δm between the two observations is given by:

$$\delta T_{Bsun} = \frac{(T_{cos} - T_{mr})\ \tau}{f_\Omega}\ \delta m \tag{A.8}$$

Note that the atmospheric transmittance ratio has been truncated to the first order the Taylor expansion. Figure A-0-1f shows the previous equation for the same set of values used before for the four AFRL-MWR frequencies. For an air-mass uncertainty of about 0.4 (worst case corresponding to a variation of about 3° from the minimum admitted elevation angle of 20°), the error in estimating T_{Bsun} increases with the frequency decrease and goes from -14 K up to -79 K.
Finally, we estimated the error in assuming the horizontal homogeneity in clear sky through the analysis of the estimated atmospheric extinction time series in (3.II.14) at the same elevation and different azimuths. Uncertainties of τ were estimated as 0.0039, 0.0016, 0.0053, and 0.0062 Np for an average azimuth distance of 5 deg. As such, the assumption holds.

A.II. Impact of radiometer spectral response

Radiometer characteristics, such as antenna pattern and receiver bandwidth, are relevant aspects to be considered when dealing with the development of algorithms, inter-comparisons with radiative transfer model simulations and data assimilation [122]. In order to rigorously approach these issues, the expression in (3.II.1) needs to be generalized to include the dependency on frequency so that the band-averaged antenna noise temperature is given by:

$$T_A(\theta_0, \varphi_0) = \int_B \frac{\int_{4\pi} T_{Bf}(\theta, \varphi, f) F_{nf}(\theta_0, \varphi_0, \theta, \varphi, f) d\Omega}{\int_{4\pi} F_{nf}(\theta_0, \varphi_0, \theta, \varphi, f\ ) d\Omega} H_n(f) \mathrm{d}f \tag{A.9}$$

where $H_n(f)$ is the normalized spectral response function (SRF) of the instrument within the bandwidth B so that

$$\int_B H_n(f)df = 1 \tag{A.10}$$

The band-averaged T_A in (A.9) is now expressed, with respect to (3.II.1), as the filtering of the spectral brightness temperature T_{Bf} through the instrumental SRF within the frequency bandwidth B. Moreover, in (A.9) the antenna power radiation pattern F_{nf} is also dependent on frequency.

Generally speaking, instrument narrow bandwidths allow to apply the approximation that spectral functions T_{Bf}, F_{nf} and H_n can be considered constant over B so that (A.9) reduces to (3.II.1). The impact of such approximation in our model development is analyzed in this section. Note that the frequency dependence of F_{nf} can be usually neglected without loss of accuracy for the window frequencies, but for high-frequency double-sideband channels around the absorption peak frequencies, it may not be negligible and F_{nf} should be possibly measured for the low and high sidebands.
In our work we should consider that AFRL-MWR channels at K-band at 23.8, 31.4 center frequency have relatively narrow bandwidths of 230 MHz, but the V- and W-band channels at 72.5 and 82.5 GHz have a bandwidth as large as 2 GHz. As recognized in [122], the errors associated to receiver channel bandwidth are less important in K-band and W-band, but this is not necessarily true for channels in the V-band or higher frequencies in the wings of absorption lines. On the one hand, highly asymmetric SRF can change the effective frequency of a radiometric channel, whereas on the other hand, spectral brightness temperature T_{Bf} due to the atmosphere can significantly vary within the same bandwidth B [123], [124].
Regarding the SRF characterization of AFRL-MWR, the receivers are tuned by the manufacturer as a complete system so that the radiometer channel central frequency is a good representation of the filter response [112]. For filter tuning a calibrated monochromatic input signal is swept over the spectrum, the digital radiometer output is monitored and the effective central frequency calculated. This implies that in our case the use of the effective central frequency is a good approximation for our purposes, provided that actual SRFs were not available from the manufacturer.
Indeed, the spectral variability of T_{Bf} within the assigned bandwidth B needs to be quantified to estimate the error due to monochromatic approximation at effective central frequency. To examine the SRF impact, we have simulated monochromatic brightness temperatures T_{Bf} in (A.9) with steps of 200 MHz at V and W band and performed several band-averaging summing them according to specific weights. We have modeled the SRF weights H_n in (A.9) in order to reproduce the shapes of realistic asymmetric spectral response functions, similar to those found in literature (e.g. as in [125]). Differences between monochromatic and band-averaged simulations can be up to 1.5 K at 72 GHz and 0.1 K at 82.5 GHz. As previously stated, this result is expected being the spectral variability more relevant for the 72.5 GHz channel as it is closer to the oxygen absorption wing. According to our evaluations, it is highly advisable that the radiometer characteristics, such as SRF and antenna patterns, are made available to users, especially in future applications at millimetre-wave frequency channels, as recommended in [124].

A.III. Impact of radiometer antenna side lobes

As described in Section II.A, the approximation of an antenna Gaussian beam has been used for computing f_Ω. Provided that actual antenna patterns of AFRL-MWR were not available from the manufacturer, the Gaussian shape antenna proposed here has been favored with respect to other possible approximations, such as a pattern described by Bessel functions, since: i) the main lobe of AFRL-MWR is well characterized by the Gaussian shape, as suggested by the manufacturer [112]; ii) the side-lobe levels produced by the feed-horn/parabola system are below -30 dB at 23.8 and 31.4 GHz and below -40 dB at 72.5 and 82.5 GHz [106]. This limits the use of Bessel functions which generally provide higher side lobes unless additional tapering by other functions is introduced.

The antenna radiation pattern is, however, characterized not only by the main lobe. In this section the effect of neglecting antenna pattern side lobes is evaluated. In our retrievals and in clear sky conditions, the effect of side lobes may be relevant: i) at very low elevations when side lobes can pick up ground radiation (but typically the radiometer is not operated below 10°); ii) during the switch when the Sun can be picked up by the side lobes (at least the first one) when observing in the "off the sun" mode.
In order to take into account the side lobe contributions and to evaluate them quantitatively, a Gaussian-shape has been also employed to model both the main lobe and the side lobes centered in $\theta_{i=1,\dots,m}$ in the radiometer antenna normalized pattern F_n:

$$F_n(\theta,\varphi) = F_{nML}(\theta,\varphi) + \sum_{i=1}^{m} F_{nSLi}(\theta,\varphi) = e^{-\ln(2)\left(2\frac{\theta}{\Theta_{\mathrm{ML}}}\right)^2} + \sum_{i=1}^{m} A_i\, e^{-\ln(2)\left(2\frac{\theta-\theta_i}{\Theta_{\mathrm{SL}i}}\right)^2} \tag{A.11}$$

considering m side lobes in the general expression above, θ_i, φ_i as the side lobe pointing angles and Θ_{ML} and $\Theta_{\mathrm{SL}i=1,\dots,m}$ as the half-power beamwidth values for the main lobe and the side lobes, respectively. In (A.11), it is reasonable to assume negligible the tails of the Gaussian pattern shapes outside of each respective beam, with an impact generally less than 0.1%. The antenna radiation-pattern solid angle Ω_{Pant} can be obtained from (3.II.2) using (A.11):

$$\Omega_{Pant} = \Omega_{PML} + \sum_{i=1}^{m} \Omega_{PSLi} \tag{A.12}$$

where Ω_{PML} and Ω_{PSLi} stand for antenna main lobe radiation-pattern solid angle and the antenna side lobe radiation-pattern solid angles, respectively. By properly evaluating the integrals, the following expressions have been obtained for the aforementioned antenna radiation-pattern solid angles:

$$\Omega_{PML} \cong \frac{\pi}{4\ln(2)}\Theta_{\mathrm{ML}}^2\left[1 - e^{-\ln(2)\left(\frac{2\pi}{\Theta_{\mathrm{ML}}}\right)^2}\right] \tag{A.13}$$

$$\Omega_{PSLi} \cong 2\pi\, A_i \left\{ \frac{\Theta_{\mathrm{SL}i}^2}{8\ln(2)} \left(e^{-\,{a_i}^2} - e^{-\,{b_i}^2} \right) + \frac{\sqrt{\pi}\,\Theta_{\mathrm{SL}i}\theta_i}{4\sqrt{\ln(2)}} \left[\mathrm{erf}(b_i) - \mathrm{erf}(a_i) \right] \right\} \tag{A.14}$$

where

$$a_i = \frac{2\sqrt{\ln(2)}}{\Theta_{\mathrm{SL}i}}\theta_i \quad ; \quad b_i = \frac{2\sqrt{\ln(2)}}{\Theta_{\mathrm{SL}i}}(\pi + \theta_i) \tag{A.15}$$

As described in [108], corrugated feedhorns have traditionally used a linearly tapered internal profile with main-beam efficiencies even greater than 98%. By including the parabola spillover, we can estimate an overall main-lobe efficiency by means of

$$\eta_{ML} = \eta_s \eta'_{ML} = \eta_s \frac{\Omega_{PML}}{\Omega_{Pant}} \tag{A.16}$$

where η_{ML} is the overall efficiency, η_s is the spillover efficiency and η'_{ML} is the feedhorn main lobe efficiency. By properly evaluating (A.12) and (A.13) we can retrieve a reasonable value of $\eta'_{ML} = \Omega_{PML}/\Omega_{Pant}$ for each considered frequency. In the radiometer antenna normalized pattern F_n, we have considered equally spaced side lobes with constant half-power beamwidth values $\Theta_{\mathrm{SL}i}$, equal to $\Theta_{\mathrm{ML}}/2$. Furthermore, in order to have an upper boundary condition, we have assumed that the 99.9% of the total power is received within 30° from the pointing angle of the main lobe. The values of A_i have been set to -30 dB (10^{-3}) at 23.8 and 31.4 GHz and to -40 dB (10^{-4}) at 72.5 and 82.5 GHz, according to [106]. Considering spillover efficiencies η_s of 0.98 at Ka band and 0.99 at V-W bands, we have obtained η_{ML} values equal to 0.969, 0.969, 0.979, 0.979 at 23.8, 31.4, 72.5 and 82.5 GHz, respectively. The effect on T_{Bsun} estimates due to uncertainty in η_{ML} is also analyzed in (A.2) (see Figure A-0-1b). By considering the side lobe contributions in (3.II.1), we obtain:

$$\begin{aligned} T_A(\theta_0, \varphi_0) &= \eta_s \frac{\Omega_{PML}}{\Omega_{Pant}} T_{BML}(\theta_0, \varphi_0) + \eta_s \frac{\sum_{i=1}^{m} \Omega_{PSLi} T_{BSL_i}(\theta_i, \varphi_i)}{\Omega_{Pant}} + (1 - \eta_s) T_{BSpill} \\ &= \eta_s \eta'_{ML} T_{BML}(\theta_0, \varphi_0) + \eta_s (1 - \eta'_{ML}) \overline{T_{BSL}} + (1 - \eta_s) T_{BSpill} \end{aligned} \tag{A.17}$$

where θ_i, φ_i represent the pointing angles of the side lobes, $\overline{T_{BSL}}$ is the averaged contribution of side lobes and T_{BSpill} is the spillover brightness contribution. By supposing $T_{BSpill} \cong \overline{T_{BSL}}$, we can retrieve from (A.17) the deviation δT_A due to side lobe and spillover effects:

$$\delta T_A = \eta_s (1 - \eta'_{ML}) \overline{T_{BSL}} + (1 - \eta_s) T_{BSpill} \cong (1 - \eta_{ML})\, \overline{T_{BSL}} \tag{A.18}$$

Referring to (A.17), the impact of an additive side lobe radiation is negligible in (3.II.6) since, when the main lobe is pointing toward the sun $T_{BML} = T_{BtwS}$, all the side lobes are pointing toward the same clear-air scenario $\overline{T_{BSL}} \cong T_{BooS}$. This condition gives brightness contributions from 20 K at 31.4 GHz up to 100 K at 72.5 GHz, corresponding to δT_{AtwS} going from 0.6 K to 2 K. Considering the same analysis carried out for (3.II.5), we have to take into account the possibility that, during

the switch, the Sun can be picked up by one of the side lobes when observing "off the Sun", i.e. the contribution of the side lobes is not uniform. We can rewrite (A.18) as

$$\delta T_A = (1 - \eta_{ML})[w_{SL}\, T_{BtwS} + (1 - w_{SL})\, \overline{T_{BSL}}\,] \tag{A.18}$$

where w_{SL} is the weight of the side lobe picking up the Sun radiation. To evaluate a worst-case scenario, we have supposed to have the sun precisely centered by the first side lobe that contributes for the 80% (w_{SL} =0.8) with respect to the other side lobes. Using typical clear-air T_{BtwS} values from 150 K at 23.8 GHz to 600 K at 82.5 GHz, we can obtain δT_{AooS} values going from 4 K to 10 K. These values of δT_A lead to ΔT_A errors that affect the T_{Bsun} estimates as discussed in detail in (A.4) of this Appendix A.

B. Sun-Tracking Microware Radiometry: radiative transfer modelling inter-comparison and validation

In this work, we focus on the following frequencies: 23.80 (K band), 31.40 (Ka band), 72.50 (V band) and 82.50 GHz (W band), corresponding to wavelengths from 12.6 to 3.6 mm, where radiometric measurements where available. In particular, 23.8 and 31.4 GHz are used to estimate integrated water vapor and liquid water in atmospheric remote sensing. While K and Ka band are actually adopted in recent satellite missions [87], the potential advantages of using V and W band are under investigation [84]. In this sense, the atmospheric channel characterization at such frequencies assumes a great importance and is the aim of this work in order to provide a valid reference to evaluation of propagation models and measurements in both atmospheric remote sensing and satellite communications fields. We characterize A and TB using both data derived by direct measurements and data simulated by radiative transfer models. As concerning the measurements, we have considered two ground based microwave radiometers: a Sun tracking [126], [127] and a humidity and temperature profiler radiometer [128] (ST-MWR and PRO-MWR, respectively). As concerning the radiative transfer models, we have adopted a one-dimensional (1D) stochastic model, based on the sky-noise Eddington method (hereafter termed as 1D-RTM) [129] and the pseudo three-dimensional (3D) radiative transfer module within the Goddard Satellite Data Simulator Unit suite [130], fed by numerical weather predictions (NWP) performed by the weather research and forecasting system [131] (hereafter termed as 3D-RTM).

We have also exploited data from weather radar networks and radio sounding observations to validate the NWP model. Both measurements and simulations analyzed in this work are co-located in space and time and they are performed in the area of Rome, NY, USA, within the Air Force Research Laboratory facility for a period of roughly one year between 2015 and 2016. With respect to previous works on the same subject, the original aspect highlighted in this study is in the use of unconventional tools like ST-MWR and 3D-RTM. The former is a radiometer that uses the Sun as reference of stable radiance source with a special antenna pointing system which is able to continuously perform observations toward-the-Sun and out-of-Sun while tracking the Sun path [127]. So doing, ST-MWR is able to simultaneously derive both TB and A, with a single receiver, in all-weather conditions and along different slant directions, thus allowing the statistical characterization of the propagation channel for several elevation angles. The shortage of high-frequency observations makes the statistical characterization of the channel one of the most primary interests of the scientific community, especially at millimetre waves. On the other hand, investigate the reliability of 3D-RTM model simulations of TB and A is an important task because it could open the way to the possibility of performing deterministic forecasts of the atmospheric channel. This work is organized into five sections. Available measurements and simulations are described in Section B.I and Section B.II, respectively. Comparisons among the various sources of A and TB are shown in Section B.III, where also a model for the computation of the probability of A conditioned to the elevation angle in continental climate areas is presented.

B.I. Available measurements in Rome, NY.

The following sections provide a complete overview of all the input data and actual measurements adopted in this appendix B to train, tune and validate the proposed weather forecast and radiative transfer models.

➢ *Ground-based Sun-tracking microwave radiometer*

The ground-based Sun-Tracking Microwave Radiometer (ST-MWR) is a Radiometer Physics GmbH-Liquid Water Path (RPG-LWP-U72+82) water-vapor and cloud-liquid microwave radiometer with four channels at 23.8, 31.4, 72.5 and 82.5 GHz. It is described in detail in section 3.II.B.

As detailed in chapter 3, section 3.II, the Sun-tracking operation mode allows tracking the Sun motion along the ecliptic (Figure 3-1). The available dataset consists of measurements collected by the ST-MW radiometer from May 2015 to December 2016 in Rome, NY, USA (43.2°N, 75.4°W) at elevation angles varying between 20° and 70° (with some missing data days due to maintenance and calibration operations on the radiometer).

➢ *Ground-based profiler microwave radiometer*

The second source of radiometric measurements is available for the whole year 2016 in Rome, NY (43.2°N, 75.4°W) from RPG humidity and temperature profiler microwave radiometer (PRO-MWR) with 7 channels from 22.24 GHz to 31.4 GHz and 7 channels from 51 GHz to 58 GHz [132], [133]. PRO-MWR provides TB measurements that are always taken at zenith, even though the radiometer is provided with an azimuth positioner allowing a scan step of 0.15° in elevation and 0.1° in azimuth. Time resolution and integration time are set to 1 second. In this work we only use the frequency channels overlapping with the ones of the ST-MWR that are: 23.8, 26.25 and 31.4 GHz.

➢ *Weather radar*

We use the Radar Archive of the National Severe Storms Laboratory (NSSL), including the Next Generation Weather Radar System and Terminal Doppler Weather Radar (NEXRAD) network [134] - [136], to assess the reliability of the 2-dimensional precipitation fields simulated by the NWP model. In particular, we have compared the precipitation accumulations derived from the summation of the Surface Precipitation Rate (SPR) product over a specified time interval with the precipitation forecasted by NWP model [135]. The one-hour Quantitative Precipitation Estimation (QPE) – Radar Only product is an aggregation of the SPR field, which is updated every 2 minutes. The SPR fields from the previous 60 minutes are summed to create the one-hour QPE – Radar Only field. The QPE is post-processed by a Gauge Bias Correction [136]. Values at or below 0.25 mm are removed to reduce the areal coverage of what is most likely false light precipitation. Radar data have been taken for a test period going from May to December 2015 and covering various weather conditions.

➢ *Radiosounding observations*

The closest radiosounding site to Rome, NY, is located at Albany County Airport, NY, USA (World Meteorological Organization station Identifier code: 72518, Weather Bureau Army Navy Identifier code: 14735; lat/lon 42.69/-73.83). Radiosounding data belonging to the period 2007-2016 have been collected for this study to compare and validate the outputs of the NWP models.

B.II. Simulating brightness temperature and optical thickness at centimeter and millimeter wave

This section is devoted to the description of the radiative transfers models used to simulate T_B and A: 3D-RTM and 1D-RTM. Since the 3D-RTM is driven by weather forecasts, in the first paragraph of this section we describe the numerical weather prediction models considered in this work.

➢ *Numerical Weather Prediction models*

Several numerical weather prediction models are designed to simulate mesoscale atmospheric circulation. In this work we have considered the Fifth-Generation Penn State University/National Center for Atmospheric Research Mesoscale Model (MM5) [137], and the Weather Research and Forecasting (WRF) system [138], developed by the National Oceanic and Atmospheric Administration and by the National Center for Environmental Prediction, are used.

MM5 is a non-hydrostatic, terrain-following sigma-coordinate model, designed to simulate or predict mesoscale and regional-scale atmospheric circulation. It includes:

- a multiple-nest capability;
- non-hydrostatic dynamics, which allows the model to be used at a few-kilometer scale;
- multitasking capability on shared and distributed-memory machines;
- a four-dimensional data-assimilation capability;
- more physical options.

WRF model system is designed to be a flexible atmospheric simulation system, efficient on available parallel computing platforms. It represents:

- the state-of-the-art model that has good conservation characteristics (e.g., conservation of mass);
- an easy to modify model, that could well parallelize on many processors;
- plug-compatible physics to support improvements in model physics;
- designed for grid spacing of 1-10 km.

We have initialized both regional models (MM5 and WRF) with data from the global-scale model of the European Center for Medium-range Weather-forecast performing two-way nested domains simulations centered on Rome, NY (Figure B-0-2). We have compared the performances of the models for different resolutions of the initialization data.

After a climatological analysis of the target area of Rome, NY, we have defined the setup for the physical parameterizations for the considered models. The MM5 setup considers Reisner II for microphysics [139], Grell for cumulus [137], Rapid Radiative Transfer Model for radiations [140] and Medium Range Forecast for planetary boundary layer [141]. WRF setup includes Thompson for microphysics [142], Grell-Freitas for cumulus [143], Rapid Radiative Transfer Model for radiations and Mellor-Yamada-Janjic for planetary boundary layer [144].

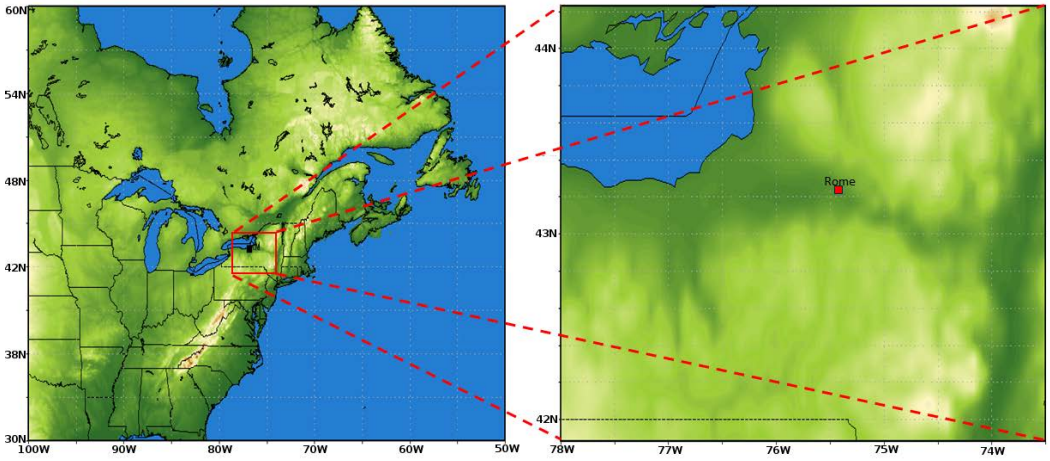

Figure B-0-2: Two nested domains of the NWP models centered on the target area of Rome, NY: (a) domain 1 at 18 km (and 9 km) resolution; (b): domain 2 at 6 km (and 3 km) resolution.

➢ *Radiative transfer models from three-Dimensional weather forecast and one-Dimensional stochastic clouds*

As previously stated, in this work we consider two radiative transfer models, both focused on the area of Rome, NY, were ST-MWR measurements are available.

The first is a pseudo three-dimensional radiative transfer model (3D-RTM) included in the Goddard Satellite Data Simulator Unit suite [130]. The 3D-RTM is based on the two-stream model with Eddington's Second Approximation using bulk single-scattering properties along selected slant paths [145]. These slant-paths mimic rigorous 3D microwave radiative transfer approach by using a 1D radiative transfer model and for this reason it is referred as "pseudo" 3D-RTM. It takes into account the gas absorption (i.e. nitrogen, cloud water, oxygen and water vapor) and the single-particle single-scattering due to five hydrometeors species (cloud, rain, ice, snow, graupel). Consequently, values of downwelling T_B and A are produced at several frequencies and elevation angles for a period going from 1 August 2015 to 31 July 2016 (according to ST-MWR availability). Input scenarios in terms of spatial and temporal hydrometeor and background gases distributions are derived by WRF simulation forecasts at the temporal sampling of one hour. Single-particle single-scattering properties are computed at each WRF grid point and subsequently integrated over the explicit particle size distribution for the various species (e.g. rain, ice, snow, graupel etc.) to represent bulk single scattering properties. Lorenz-Mie method is used to calculate single scattering properties in rain regimes whereas for ice and snow, discrete dipole approximation or T-matrix calculations are selected. Polarization is not taken into account in our simulations. Effective refractive indices needed to calculate single scattering properties are obtained through

the Maxwell-Garnett method that accounts for bin-by-bin particle effective density (riming fraction) and melting fraction. The absorption coefficients for water vapor, oxygen, nitrogen and cloud water are calculated using formulas from [56], [54], [146] and [147], respectively. Figure B-0-3 shows the statistics of *A* for the target period obtained from the 3D-RTM at the zenith view.

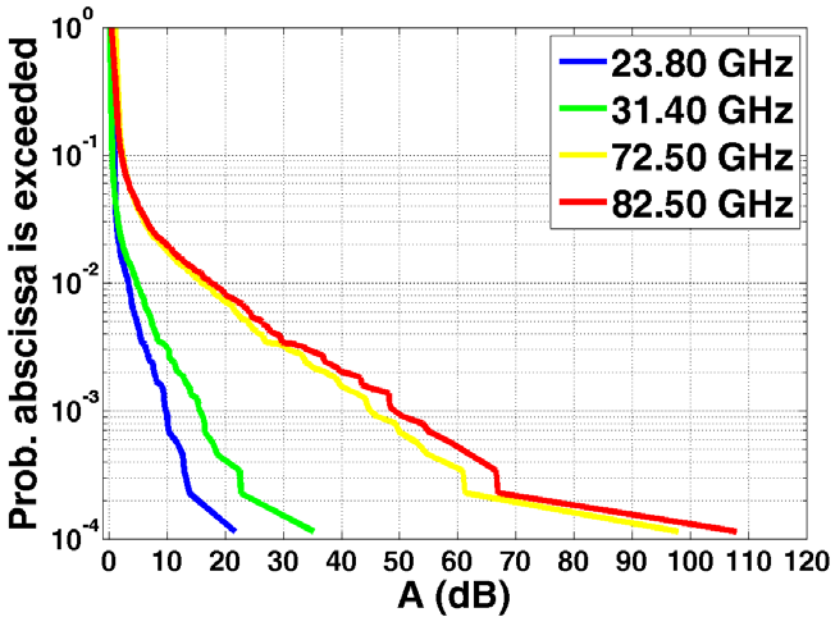

Figure B-0-3: Complementary cumulative distribution function of A computed from 3D-RTM simulations from 1 August 2015 to 31 July 2016 for the frequencies of interest.

The second model that we consider is a sky noise Eddington model that was developed and described in [129]. It is a 1Dimensional radiative transfer model (1D-RTM) that gives an Eddington-based analytical approximation of the solution of the radiative transfer equation [120]. The input of 1D-RTM is a synthetic clouds dataset for the random generation of seasonal-dependent and time-decorrelated radiometeorological variables at the desired frequencies and elevation angles, with statistics driven by radiosounding profiles in clear sky [129] available from the World Meteorological Organization. The simulated variables are relative to ten clouds classes (including the clear air): cumulonimbus, cumulonimbus with incus, cumulus, cumulus congestus, altocumulus, altostratus, nimbostratus, stratus, cirrus and clear air. Each cloud class has 500 realizations per each season (winter, spring, summer, autumn) for a total of 20000 realizations per each considered frequency and elevation angle.

Both 3D-RTM and 1D-RTM simulations are obtained at several elevation angles (i.e., 10°, 20°, 30° 36°, 40°, 50°, 54°, 60°, 70°, 80, 90°) for the frequencies at 23.8, 31.4, 72.5 and 82.5 GHz where ST-MWR measurements are available.

B.III. Validation and comparison

This section shows the validation of weather forecast and radiative transfer models considered in this work. For the validation process we have exploited data available from several measurements described in section B.I.

➢ *Validation of numerical weather prediction model*

We have performed quantitative analysis using some statistical parameters: bias (Bias), standard deviation (STD) and correlation coefficient (Corr) calculated on the vertical profiles of humidity and temperature between simulations and observations according to the following definitions:

$$Bias = \langle x_{sim} - x_{obs} \rangle \tag{B.1}$$

$$STD = \sqrt{\langle [(x_{sim} - x_{obs}) - \langle (x_{sim} - x_{obs}) \rangle]^2 \rangle} \tag{B.2}$$

$$Corr = \frac{\sigma_{(x_{sim}, x_{obs})}}{\sigma_{x_{sim}} \sigma_{x_{obs}}} \tag{B.3}$$

where x represent the considered variable (humidity or temperature) and the subscripts sim and obs stand for simulations and observations, respectively. In this case, simulations are from Numerical Weather Predictions and observations are from radio soundings or weather radar measurements.
First, we have explored the sensitivity of MM5 and WRF to different initialization data and we have found that the best configuration is represented by WRF model initialized with data from the European Center for Medium-range Weather-forecast at 0.125° resolution.

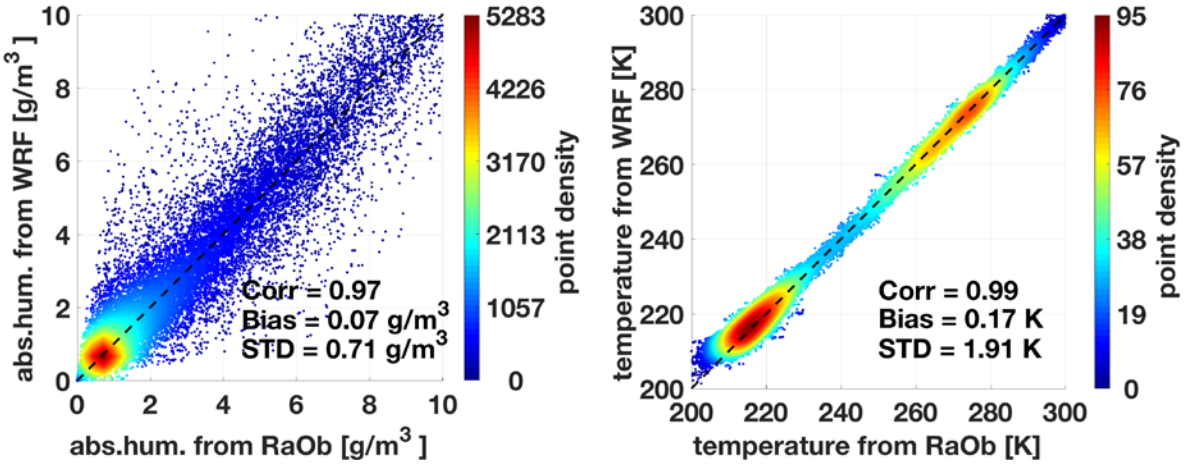

(a) (b)

Figure B-0-4: Numerical weather predictions validation with radiosounding data: (a) absolute humidity, (b) temperature.

Then, we have validated the WRF best configuration performing a long run in the analysis period using two domains, at 12 km and 4 km horizontal spatial resolution, one hour of temporal resolution and daily forecast. The run was from 1 August 2015 to 31 July 2016 (according to ST-MWR availability) on a volume with a base of 4x4 km2 and height ranging from surface to ~ 12 km centered on Albany, NY, where radiosounding data were available for the validation. Figure B-0-4 a and b reports the scatter plot of absolute humidity and temperature, respectively, with respective values of bias, correlations and standard deviation.
To quantify the capability of WRF setup to reproduce radio soundings at every altitude, the Index of Agreement (IA) has been adopted [121]. IA is a standardized measure of the degree of model prediction error that varies between 0 and 1. An agreement index score of 0 suggests little or rather no agreement between weather forecast simulations and radiosounding data, while an agreement score of 1 suggests complete match. An IA less than 0.5 suggests a diversity (between forecast and observation).
The results are reported in Figure B-0-5. Humidity content profile (red curve in Figure B-0-5 obtained from the dataset in Figure B-0-4a) shows an IA ranging between ~ 1 (around surface) and ~ 0.8 (around 12 km). The IA of temperature profiles (blue curve in Figure B-0-5 obtained from the dataset in Figure B-0-4b) ranges between ~ 1 (around surface) and ~ 0.9 (around 12 km).

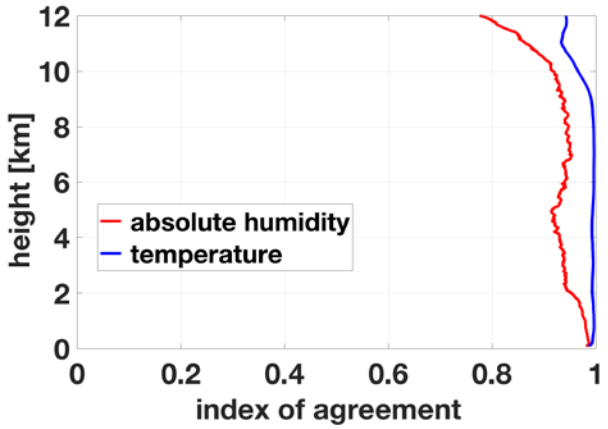

Figure B-0-5: Vertical profile of Index of Agreement between WRF and radiosounding data for absolute humidity and temperature profiles.

We have accomplished a further comparison using hourly surface precipitation, which can mainly affect the atmospheric optical thickness A, to evaluate the NWP performances close to the surface level. We have compared the output of the NWP model with measurements available from a radar-gauge mosaic on an area of 4 km x 4 km centered on Albany site (Figure B-0-6). The distribution of points density shows a correlation coefficient of 0.44, a bias of -0.09 mm and a standard deviation of 0.93 mm. The evaluation scores for the precipitation are sensibly worse than those obtained for temperature and humidity previously discussed but, given the large spatial and temporal variability of precipitation, they can be considered satisfactory.

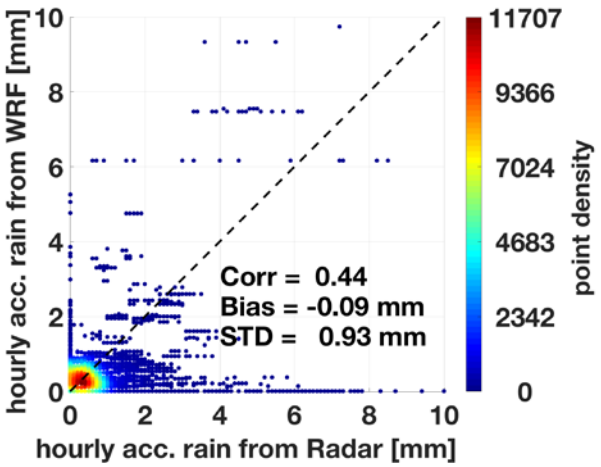

Figure B-0-6: Comparison between WRF and Radar Data in terms of rain accumulated in 1 hour on a domain centered on Albany site.

➢ *Comparison between radiative transfer models and radiometric measurements*

In this section we show several validation comparisons of both 1D-RTM and 3D-RTM with available radiometric measurements (ST-MWR and PRO-MWR).

Figure B-0-7 shows T_B scatterplots comparing data from 3D-RTM simulations with ST-MWR measurements available from 1 August 2015 to 31 July 2016 for the four radiometric channel frequencies. Due to the Sun-tracking operation mode, ST-MWR acquires measurements at continuously varying elevation angles (from about 20° to about 70°). The comparisons in Figure B-0-7 are done considering all the points within the elevation-angle range covered by ST-MWR measurements performing a time-matching between the two datasets. Because of the different time sampling between 3D-RTM and ST-MWR (1 hour vs few seconds, respectively) we have averaged ST-MWR measurements over 1 minute around each nominal hour of 3D-RTM simulations. We have done the same plots of Figure B-0-7 in terms of A and listed the error scores in Table B-0-3 for both T_B and A. Error scores between radiometric measurements and radiative transfer model are presented in terms of correlation, bias, standard deviation and root mean square error. Both Figure B-0-7 and Table B-0-3 show a general agreement between model and measurements although, from Figure B-0-7 we note a larger point dispersion at high T_B values, i.e. where rainy events likely occur. In addition, from Table B-0-3 we observe an underestimation bias of 3D-RTM in terms of T_B of the order of 11 K to 18 K depending on the frequency. Such biases could be ascribed to several factors: inaccuracies in the 3D-RTM routines of the radiative transfer, errors introduced by the slant path interpolation implemented within 3D-RTM [130] or to possible calibration biases of the ST-MWR [127]. We have also accomplished the same comparison of Figure B-0-7 but at a fixed elevation angle of 36° (which is one of the most frequent value during the Sun-tracking antenna motion). Results in terms of error scores were promising: correlations always larger than 0.74 and 0.68 for T_B and A, respectively, and biases ranging from 6 K to 11 K and from 0.13 dB to 0.49 dB.

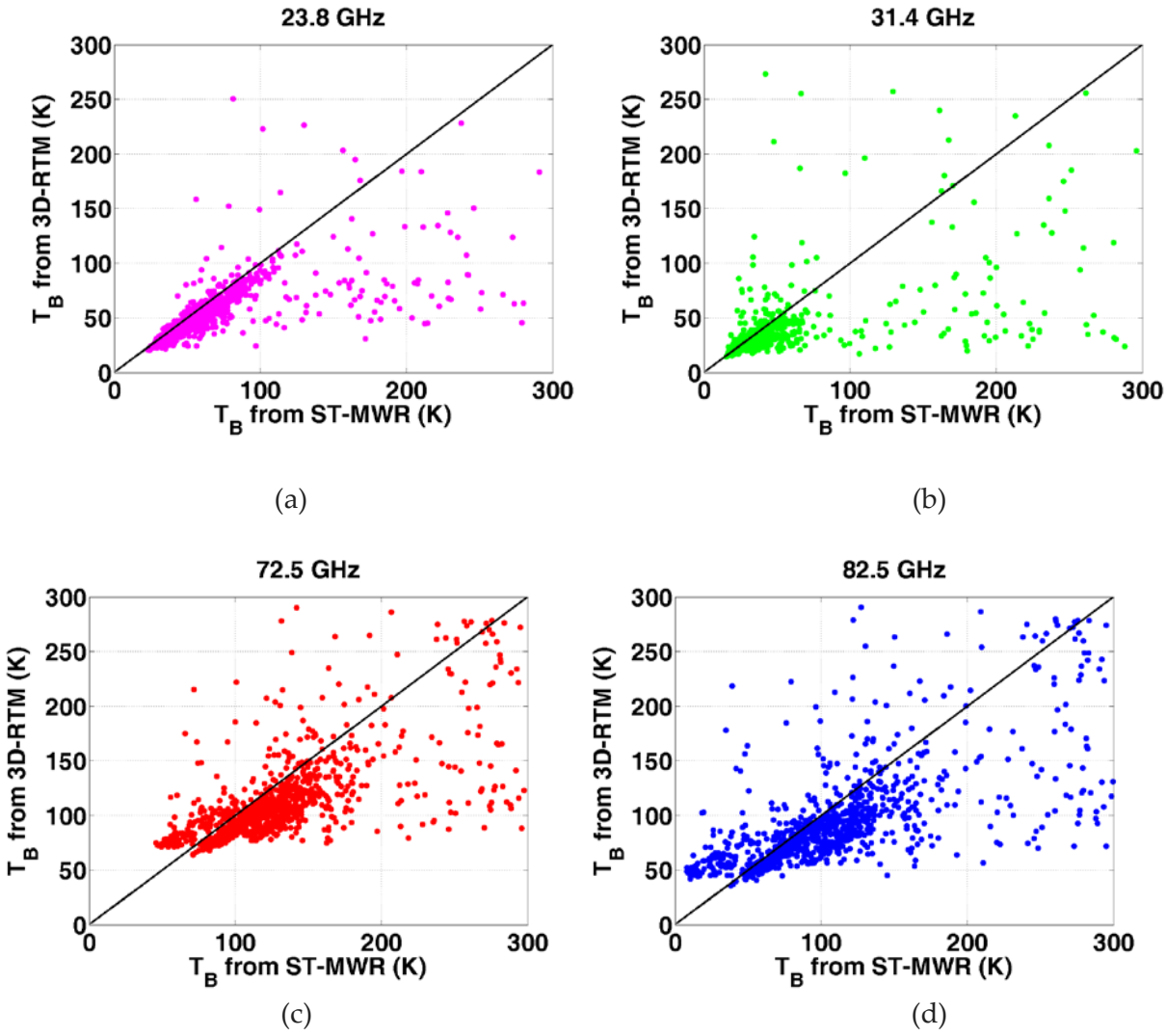

Figure B-0-7: TB scatterplot for the period from 1 August 2015 to 31 July 2016: 3D-RTM vs ST-MWR after time-matching at all elevation angles interested by the ST-MWR measurements.

TABLE B-0-3: T_B AND A ERROR SCORES FROM 1 AUGUST 2015 TO 31 JULY 2016: 3D-RTM VS ST-MWR AFTER TIME-MATCHING AT ALL ELEVATION ANGLES OBSERVED BY ST-MWR

	Freq. (GHz)	**23.80**	**31.40**	**72.50**	**82.50**
T_B	**Corr.**	0.65	0.56	0.68	0.70
	Bias (K)	-13.40	-10.83	-17.48	-14.03
	Std (K)	31.42	39.00	36.63	43.04
	RMSE (K)	34.14	40.46	40.57	45.25
A	**Corr.**	0.52	0.40	0.43	0.43
	Bias (dB)	-0.34	-0.34	-0.58	-0.46
	Std (dB)	1.12	1.73	3.30	3.62
	RMSE (dB)	1.17	1.76	3.35	3.65

To partially check the origin of the biases listed in Table B-0-3, we have compared 3D-RTM simulations with PRO-MWR in the period of interest (1 August 2015 - 31 July 2016) after a time-matching between the two sources of information. Figure B-0-8 and Table B-0-4 show the results of the comparison in two cases of all-weather and clear-sky conditions. The clear-sky identification is accomplished using the sky status indicator [113],[114]. However, it should be noted that with respect to the previous comparison between 3D-RTM and ST-MWR, where data were compared along the direction of 36° elevation angle, in the case of 3D-RTM vs PRO-MWR, the comparisons are at 90° since PRO-MWR is a zenithal-pointing radiometer.

From Table B-0-4 we note that the bias in terms of T_B sensibly reduces with respect to those listed in Table B-0-3 and this lead to conclude that most of the bias in the 3D-RTM vs ST-MWR comparisons could be ascribed to ST-MWR calibration issues. Inaccuracies in the 3D-RTM routines of the radiative transfer still play a role, especially in clear-sky, as highlighted by the overestimation of T_B of 3D-RTM with respect to PRO-MWR (look at the lower left tail in Figure B-0-8 panels *b*, *d*, *f*). The impact of 3D-RTM overestimation of T_B in clear-sky is larger at 31.4 GHz than at 23.84 GHz (see biases in Table B-0-4 in clear-sky). This behavior suggests that the water vapor representation in 3D-RTM is not able to accurately reproduce PRO-MWR observations. In all weather conditions (i.e. clear-sky+ cloud-sky and precipitation, Figure B-0-8, panels *a*, *c*, *e*), the overestimation previously noted in 3D-RTM simulations in clear-sky is masked by the variability of cloud and precipitation events.

TABLE B-0-4: T_B ERROR SCORES FROM 1 AUGUST 2015 TO 31 JULY 2016: 3D-RTM VS PRO-MWR AFTER TIME-MATCHING AT ZENITH VIEW (SEE FIGURE B-0-8)

	Freq. (GHz)	**23.84**	**26.24**	**31.4**
All-weather	**Corr.**	0.70	0.56	0.52
	Bias (K)	-1.48	-0.15	0.07
	Std (K)	17.44	20.02	23.63
	RMSE (K)	17.50	20.02	23.62
Clear-sky	**Corr.**	0.97	0.97	0.95
	Bias (K)	0.60	0.51	0.74
	Std (K)	2.06	1.32	1.17
	RMSE (K)	2.14	1.42	1.38

Figure B-0-9 shows the correlation between brightness temperatures at the four channel frequencies comparing 1D-RTM, 3D-RTM and ST-MWR. These scatterplots are often exploited for data-quality check and for calibrating and validating both measurements and models. Indeed, anomalies in the channel correlation can help to find if a channel is unreliable (e.g., due to calibration errors) or a simulation is inaccurate (e.g., due to radiative model under or over estimation). Due to the variation of the elevation-angle of the ST-MWR measurements and in order to have a robust comparison, in Figure B-0-9 we have considered all the elevation angles within the range of the ST-MWR data (20°-70°). The figure highlights as the 3D-RTM is able to well reproduce the overall statistical trend of ST-MWR measurements. Moreover, the two radiative transfer models (3D-RTM and 1D-RTM) are in quite excellent agreement. From Figure B-0-9 we note a considerable T_B underestimation of the 3D-RTM in the right flank region of the "banana" shape shown in panels

a and b. Interestingly both 1D-RTM and 3D-RTM models fails in reproducing lower TB values in the 82.5 vs 23.8 GHz plane.

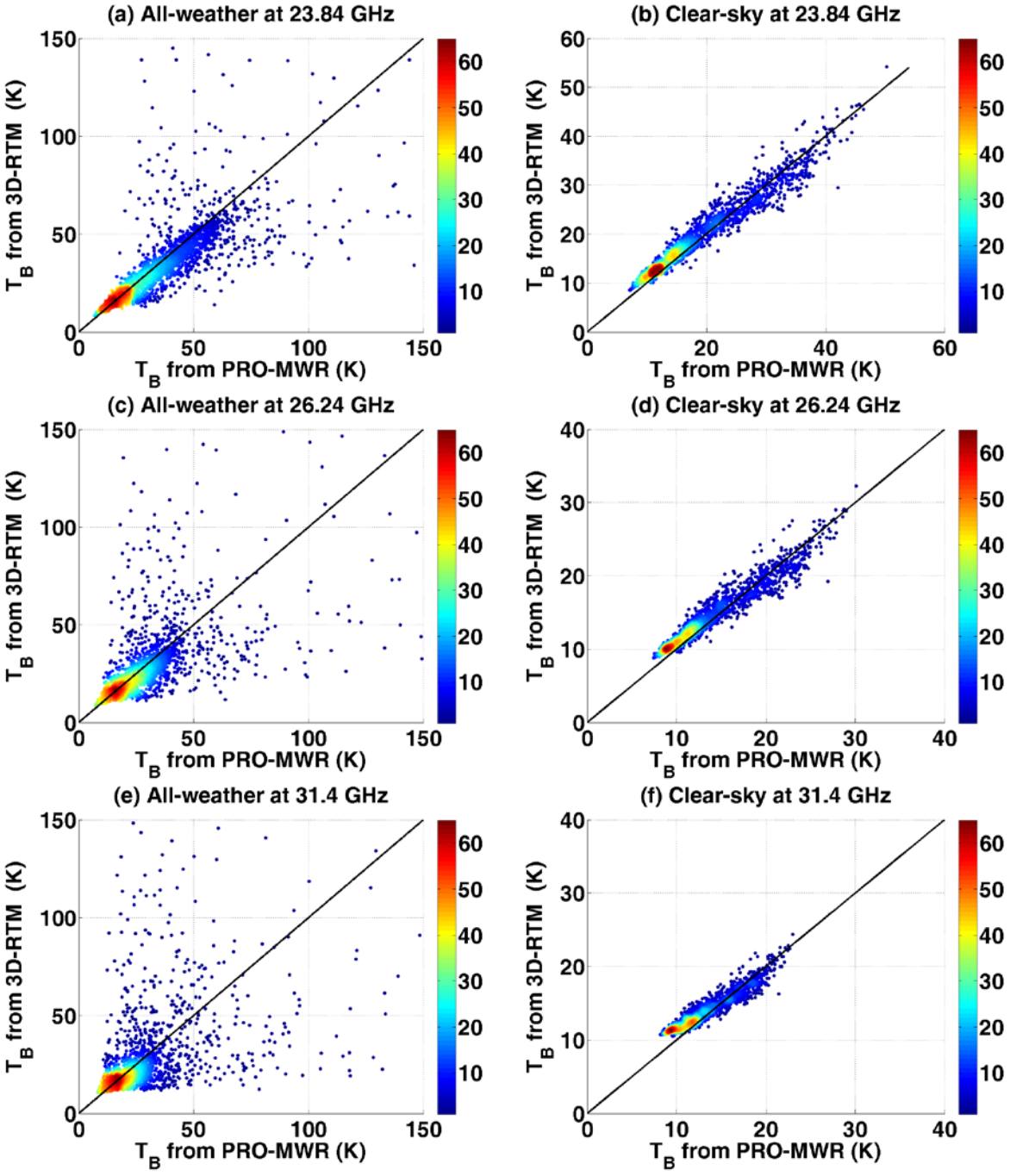

Figure B-0-8: T_B scatter density plot for the period from 1 August 2015 to 31 July 2016: 3D-RTM vs PRO-MWR after time-matching at zenith view.

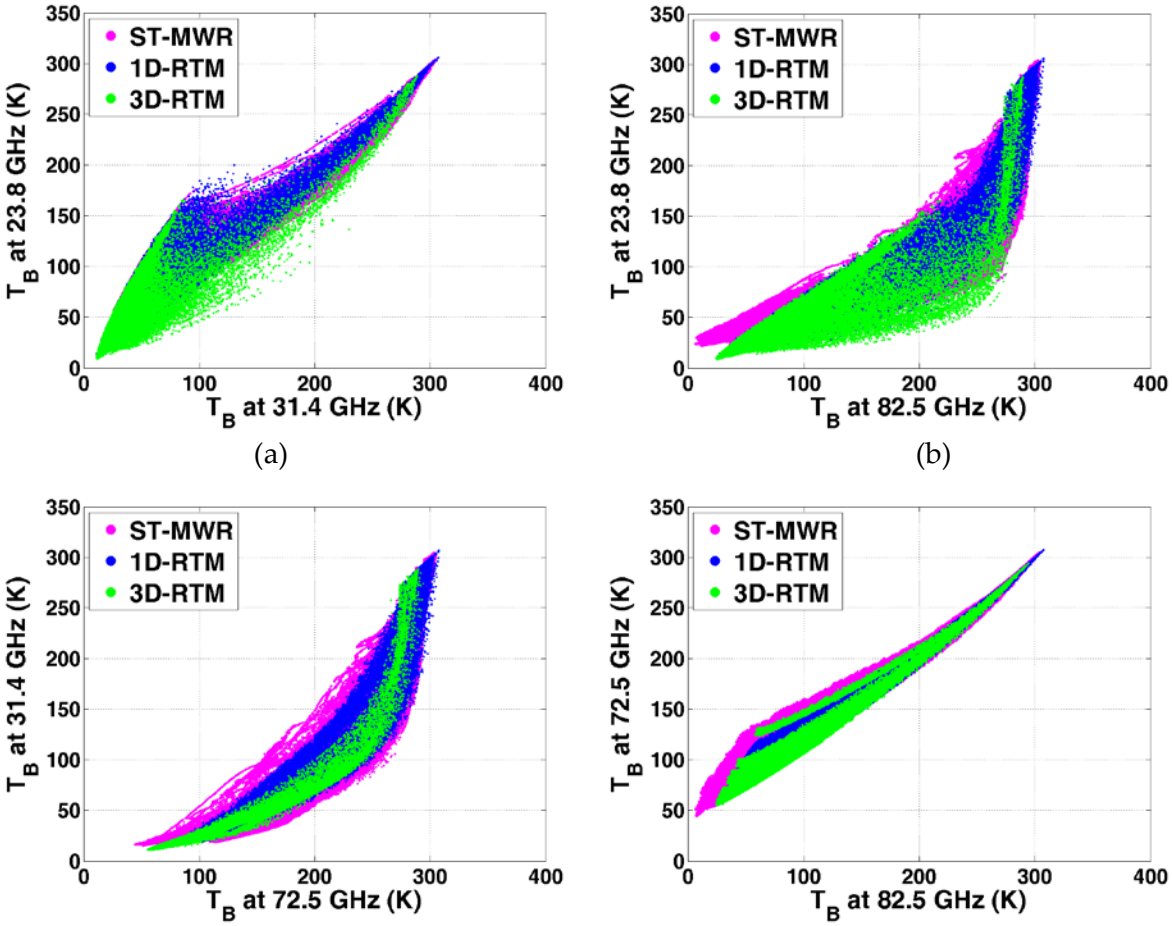

Figure B-0-9: TB - TB channel correlation of ST-MWR, 1D-RTM and 3D-RTM at the ST-MWR frequency channels. All the elevation angles are included.

Similar considerations can be done looking at the TB-A correlation scatterplots reported in Figure B-0-10 with ST-MWR, 1D-RTM and 3D-RTM data. Figure B-0-10 also highlight the saturation occurring at high values of A measured by ST-MWR. This behavior is expected because in strong rain condition (i.e., for high values of A), the atmosphere appears as a screen from the radiometer point of view and obstructs the sight of the Sun preventing the Sun-tracking operation.

Figure B-0-11 reproduces the same quantities as in Figure B-0-9 except that in this case ST-MWR is replaced by PRO-MWR and the plots are realized at zenith view. We note a general agreement among the three dataset except for the region T_B<150 K where 3D-RTM is not totally superimposed to 1D-RTM and PRO-MWR.

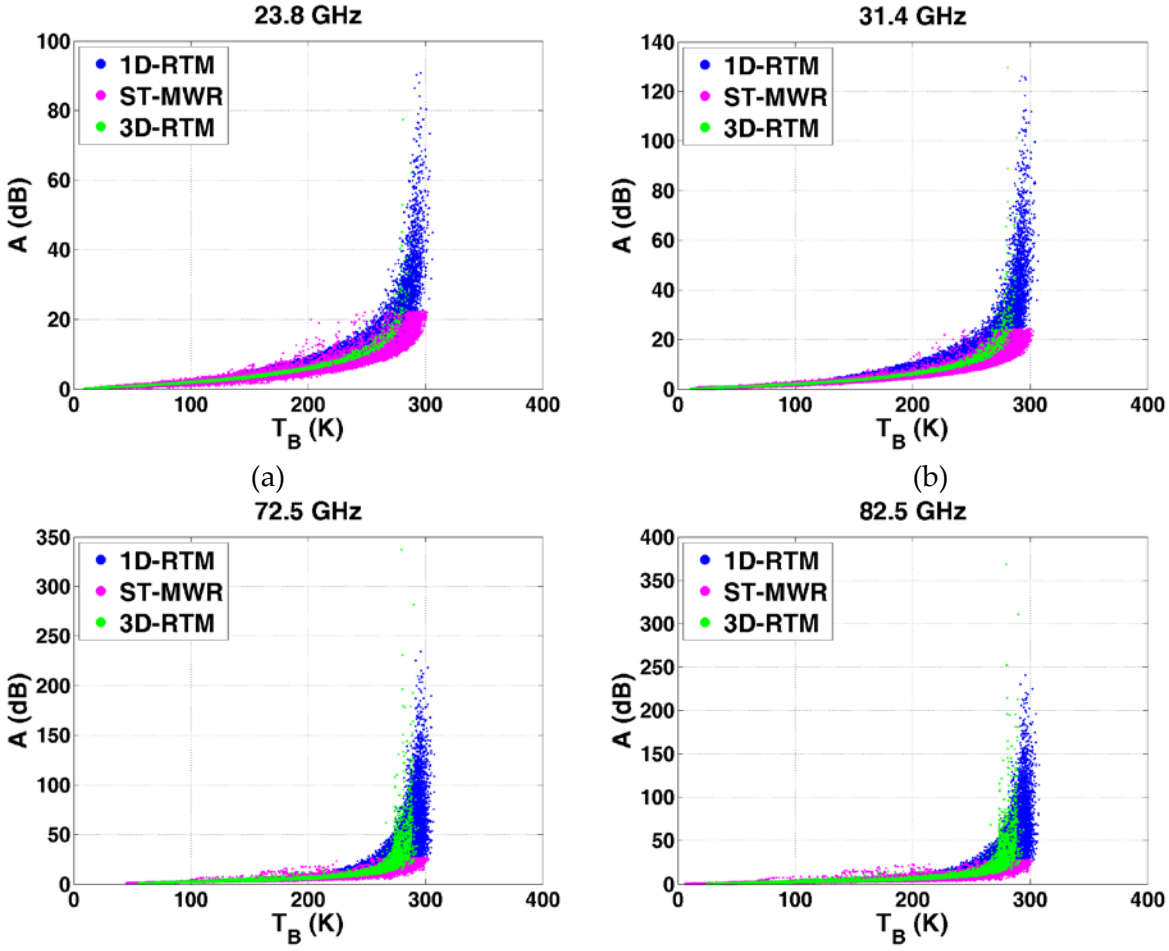

Figure B-0-10: TB - A correlation of ST-MWR, 1D-RTM and 3D-RTM at the four ST-MWR frequency channels. All the elevation angles are included.

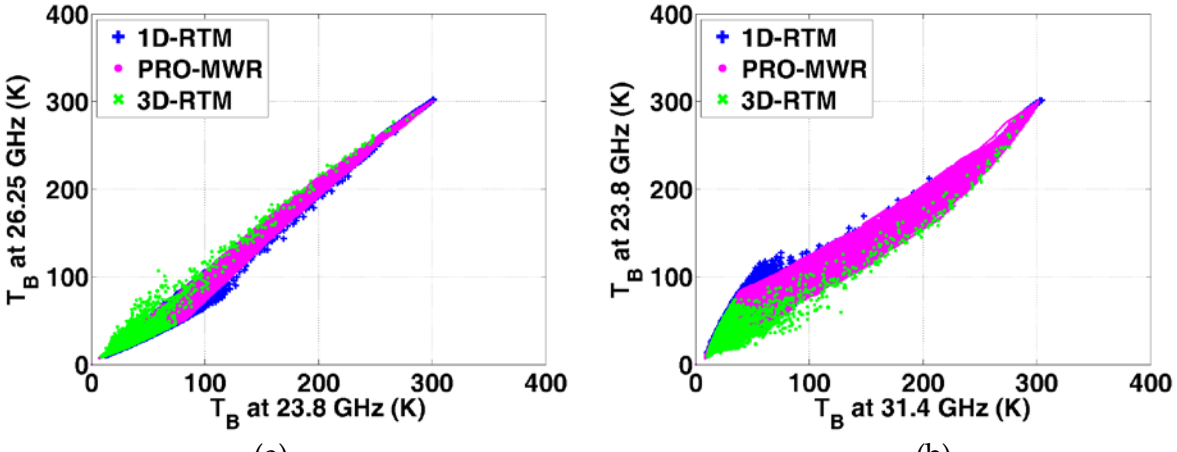

Figure B-0-11: T_B - T_B channel correlation of PRO-MWR, 1D-RTM and 3D-RTM at the PRO-MWR frequency channels, zenith view.

➢ *Probabilistic characterization of Sun-tracking data*

In this section we perform a probabilistic analysis of the 3D-RTM simulations through a comparison with the available radiometric measurements. 3D-RTM is the result of coupling a numerical weather prediction model with a physically-based pseudo-3D radiative transfer model. A probabilistic analysis is useful to evaluate the capacity of the 3D-RTM to reproduce the statistical trend of the atmospheric radiometeorological parameters. Such statistics can be exploited within several contexts (e.g., satellite communications) to characterize the atmospheric channel at millimeter wave frequencies.

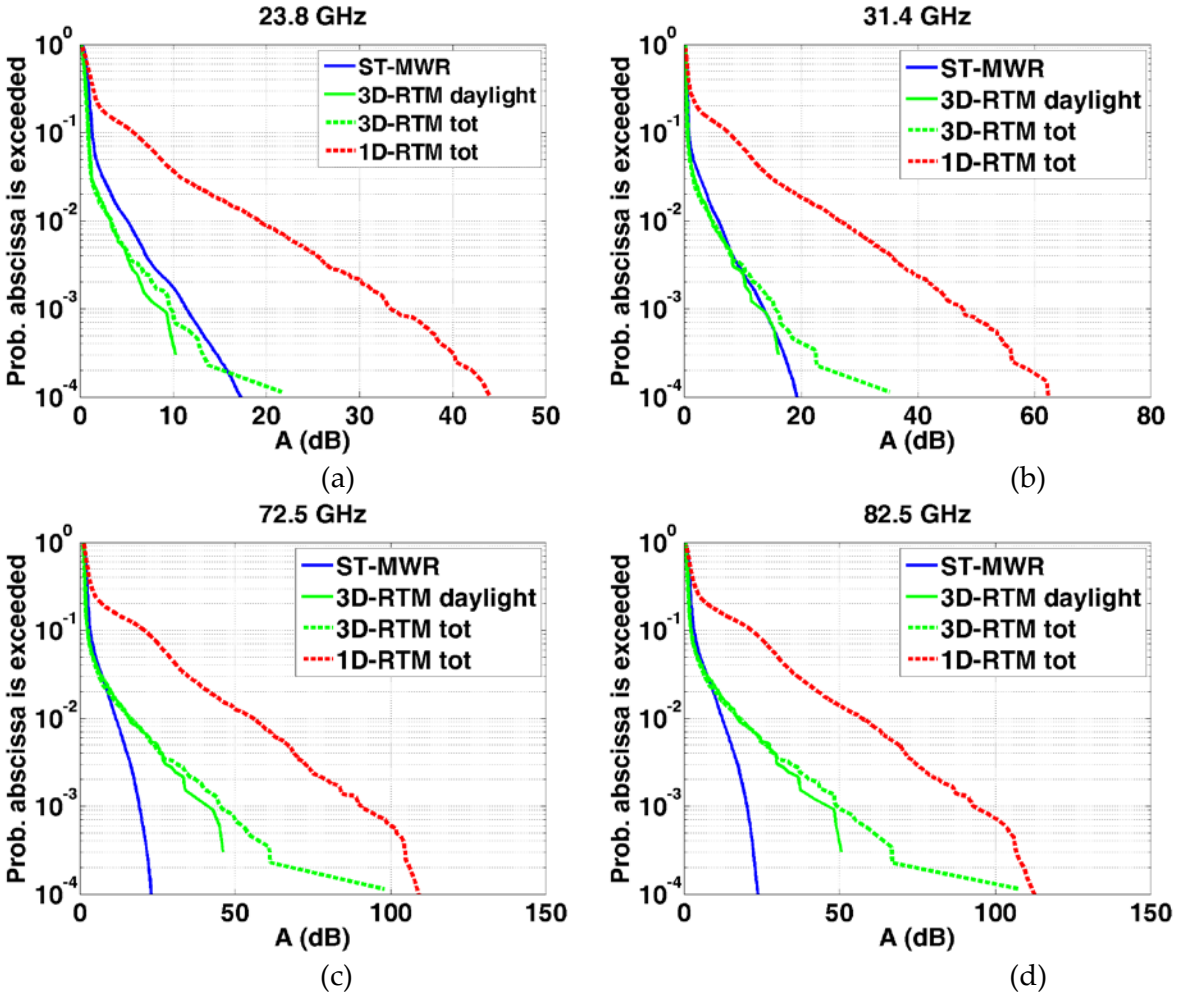

Figure B-0-12: Complementary cumulative distribution function of A from 3D-RTM, 1D-RTM, and ST-MWR, zenith view. ST-MWR measurements have been reported to the zenith via the cosecant law.

Figure B-0-12 shows the complementary cumulative distribution function of A computed from 3D-RTM simulations (green line) and 1D-RTM (red line) and compared with the one computed from ST-MWR (blue line) measurements at the zenith. Note that ST-MWR measurements have been reported to the zenith via the cosecant law, this allows to exploit all the available ST-MWR measurements to realize a robust statistic. Due to the fact that ST-MWR measurements are acquired

only during daylight, in order to make a homogeneous comparison we have distinguished daylight (solid lines) from total (i.e., daylight + night, dashed lines) data for 3D-RTM data. This procedure is not possible for 1D-RTM being such data time decorrelated.
The first thing that leaps out from Figure B-0-12 is the overestimation of A from 1D-RTM model with respect to both 3D-RTM and ST-MWR. Since 1D-RTM is a stochastic model driven by a synthetic clouds dataset, such overestimation suggest that, before running the 1D-RTM, a climatological adaptation should be done by conveniently selecting the clouds classes which are more frequent in the area of Rome, NY, for the target period.
Comparing ST-MWR (blue solid line) with 3D-RTM (green solid line) in Figure B-0-12, we note a general agreement between the two dataset. At 23.8 GHz (Figure B-0-12a), as already observed in previous figures, 3D-RTM exhibits a slight underestimation which increase at high values of A. The error between 3D-RTM and ST-MWR is of the order of 2-3 dB reaching a maximum of 5 dB for probability values approaching 10-4. At 31.4 GHz (Figure B-0-12b) we observe an excellent agreement between 3D-RTM and ST-MWR (with the green and blue solid lines almost superimposed). At 72.5 and 82.5 GHz (Figure B-0-12c and d) we note a very good agreement between 3D-RTM and ST-MWR for A values up to about 10 dB. Above 10 dB the lines separate reaching a maximum error of about 15 dB and of more than 20 dB at 72.5 and 82.5 GHz, respectively. The underestimation of ST-MWR with respect to 3D-RTM at high attenuation values can be ascribed to saturation effects already observed in Figure B-0-10. Similar plots to those in Figure B-0-12 can be realized in terms of TB.

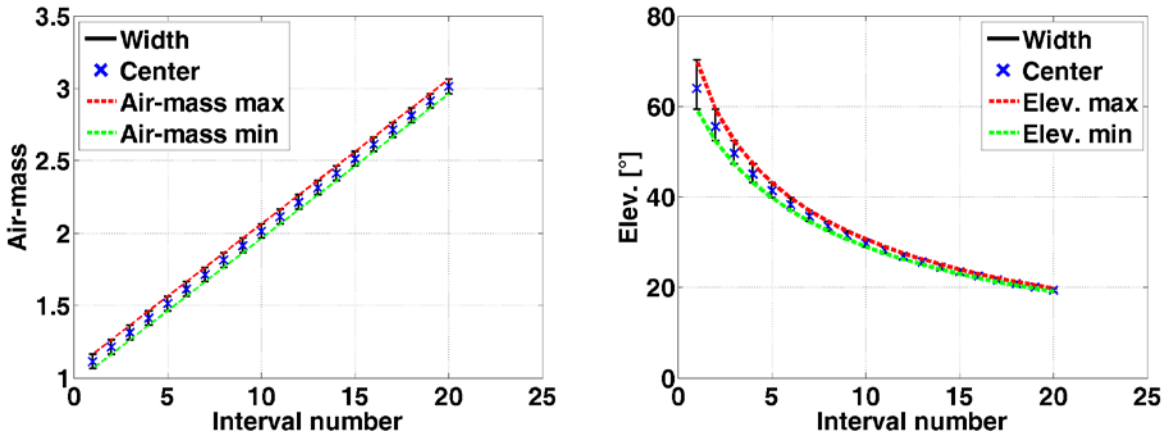

Figure B-0-13: (a) Division of the ST-MWR dataset into air-mass intervals and (b) corresponding elevation-angles intervals.

PhD Candidate – List of publications

International journals:

[J.1] F.S. Marzano, V. Mattioli, L. Milani, K.M. Magde, and G.A. Brost, "Sun-Tracking Microwave Radiometry: All-weather Estimation of Atmospheric Path Attenuation at Ka-, V- and W- band", in IEEE Transactions on Antennas & Propagation, vol. 64, no. 11, pp. 4815-4827, Nov. 2016. doi:10.1109/TAP.2016.2606568.

[J.2] V. Mattioli, L. Milani, K.M. Magde, G.A. Brost, and F.S. Marzano, "Retrieval of Sun brightness temperature and precipitating cloud extinction using ground-based Sun-tracking microwave radiometry", in IEEE Journal of Selected Topics in Applied Earth Observations and Remote Sensing, vol. 10, no. 7, pp. 3134-3147, July 2017. doi:10.1109/JSTARS.2016.2633439.

[J.3] M. Biscarini, K. De Sanctis, S. Di Fabio, M. Montopoli, L. Milani, and F.S. Marzano, "Assessment and uncertainty estimation of weather-forecast-driven data transfer for space exploration at Ka and X band", in IEEE Transactions on Antennas and Propagation, vol. 67, no. 5, pp. 3308-3322, May 2019. doi: 10.1109/TAP.2019.2899041.

[J.4] M. Biscarini, L. Milani, M. Montopoli, K. De Sanctis, S. Di Fabio, K.M. Magde, G.A. Brost and, F.S. Marzano, "Exploiting Tropospheric Measurements From Sun-Tracking Radiometer for Radiopropagation Models at Centimeter and Millimeter Wave," in IEEE Journal of Selected Topics in Applied Earth Observations and Remote Sensing, vol. 12, no. 6, pp. 1697-1708, June 2019. doi: 10.1109/JSTARS.2019.2916372.

[J.5] L. Milani, M. Arcorace, G. Rivolta, R. Cuccu, F. S. Marzano, "Clear-Air Anomaly Masking by Kalman Temporal Filter from Geostationary Multispectral Imagery", in IEEE Transactions on Geoscience and Remote Sensing (accepted for publication)

[J.6] M. Biscarini, A. Vittimberga, K. De Sanctis, S. Di Fabio, M. Montagna, L. Milani, Y. Tsuda and F. S. Marzano, "Optimal stochastic prediction and verification of signal-to-noise ratio and data rate for Ka-band spaceborne telemetry" in IEEE Transactions on Antennas and Propagation (submitted)

Conferences:

Year 2016

[C.1] M. Biscarini, M. Montopoli, D. Cimini, L. Milani, F.S. Marzano, K. De Sanctis, S. Di Fabio, M. Montagna, M. Mercolino, and M. Lanucara, "Microwave radiometric characterization of deep space Ka-band channel from numerical models and experimental ground data", 14th Specialist Meeting on Microwave Radiometry and Remote Sensing of the Environment (MICRORAD), April 11-14, 2016, Espoo, Finland.

[C.2] M. Montopoli, F.S. Marzano, M. Biscarini, L. Milani, D. Cimini, K. De Sanctis, and S. Di Fabio, "Evaluation of Deep Space Ka-Band Data Transfer using Radiometeorological

Forecasts and radiometer measurements", European Geosciences Union General Assembly (EGU), April 17-22, 2016, Vienna, Austria.

[C.3] F.S. Marzano, L. Milani, V. Mattioli, K. M. Magde, and G.A. Brost, "Retrieval of precipitation extinction using ground-based sun-tracking millimeter-wave radiometry", Proc. 2016 IEEE International Geoscience and Remote Sensing Symposium (IGARSS), Beijing, China, 2016, pp. 2162-2165. doi:10.1109/IGARSS.2016.7729558.

[C.4] M. Biscarini, F.S. Marzano, L. Milani, M. Montopoli, K. De Sanctis, S. Di Fabio, D. Cimini, M. Montagna, M. Mercolino, and M. Lanucara, "Optimizing X and Ka band data volume return for BepiColombo mission using Cebreros and Malargüe data and weather-forecast based methodology", Proc. ESA International Workshop on Tracking, Telemetry and Command Systems for Space Applications (ESA-TTC), Noordwijk, The Netherlands, 2016, pp. 1-5. (on IEEE Xplore, INSPEC Accession Number: 16579068).

Year 2017

[C.5] M. Biscarini, F.S. Marzano, L. Milani, M. Montopoli, K. De Sanctis, S. Di Fabio, D. Cimini, M. Montagna, M. Mercolino, and M. Lanucara, "Improving Weather-Forecast Based Model Chain to Optimize Data-Volume Transfer for Ka-band Deep-Space Downlinks", 11th European Conference on Antennas and Propagation (EuCAP), 19-24 March 2017, Paris, France. doi:10.23919/EuCAP.2017.7928744.

Year 2018

[C.6] M. Biscarini, L. Milani, F.S. Marzano, M. Montopoli, K. De Sanctis, S. Di Fabio, and G.A. Brost, "Predicting Mean Radiative Temperature at Millimiter Wavelenghts in Continental Climate Areas", 12th European Conference on Antennas and Propagation (EuCAP), 9-13 April 2018, London, UK. doi:10.1049/cp.2018.0591.

[C.7] M. Biscarini, M. Montopoli, L. Milani, K. De Sanctis, S. Di Fabio, F.S. Marzano, and G.A. Brost, "Exploiting Sun-tracking Microwave Radiometers for testing Radiative Transfer Models of Precipitating Clouds", 15th Specialist Meeting on Microwave Radiometry and Remote Sensing of the Environment (MICRORAD), March 27-30, 2018, Cambridge, MA, USA.

[C.8] M. Arcorace, L. Milani, R. Cuccu, G. Rivolta, J.M. Delgado Blasco, and C. Orru, "Enabling Enhanced Support in Forest Fires Monitoring and Management to Western Africa Countries through Multisource EO Data Integration and Analysis", ESA PROBA-V Symposium 2018, May 29-31, 2018, Ostend, Belgium.

[C.9] M. Biscarini, M. Montopoli, L. Milani, K. De Sanctis, S. Di Fabio, F.S. Marzano, and G.A. Brost, "Assessing radiative transfer models trained by numerical weather forecasts using Sun-tracking radiometric measurements for satellite link characterization up to W band", 2nd URSI Atlantic Radio Science Meeting (AT-RASC), 28 May - 1 June 2018, Gran Canaria, Spain. doi:10.23919/URSI-AT-RASC.2018.8471535.

[C.10] L. Milani, M. Arcorace, R. Cuccu, G. Rivolta, and F.S. Marzano, "Clear-Air Anomaly Detection using Modified Kalman Temporal Filter from Geostationary Multispectral

Data", IEEE International Geoscience and Remote Sensing Symposium 2018 (IGARSS), July 23-27, 2018, Valencia, Spain. doi:10.1109/IGARSS.2018.8517396.

[C.11] M. Biscarini, F.S. Marzano, M. Montopoli, K. De Sanctis, S. Di Fabio, L. Milani, K. Magde, and G.A. Brost, "Coupling numerical weather prediction and radiative transfer models for tropospheric radiocommunications", First National Congress of the Italian Association of Atmospheric Science and Meteorology, September 10-13, 2018, Bologna, Italy.

[C.12] D. Cimini, F. S. Marzano, L. Luini, C. Riva, M. Biscarini, L. Milani, K. De Sanctis, S. Di Fabio, F. Di Paola, E. Ripepi, E. Ricciardelli, and F. Romano, "WRad: a long-term radiometric field campaign for characterizing W-band attenuation of precipitating clouds", 9th International Precipitation Working Group (IPWG) Workshop, 5-9 November, 2018, Seoul, Korea.

[C.13] M. Arcorace, L. Milani, R. Cuccu, G. Rivolta, J.M. Delgado Blasco, and C. Orru, "Near Real Time Fire Detection Service via the PROBA-V Mission Exploitation Platform", The ESA Earth Observation Phi-week, 12-16 November 2018, ESA/ESRIN Frascati (Rome), Italy. DOI: 10.13140/RG.2.2.14004.71045

Year 2019

[C.14] M. Biscarini, L. Milani, M. Montopoli, K. De Sanctis, S. Di Fabio, K.M. Magde, G.A. Brost, and F.S. Marzano, "Statistical characterization of slant-path atmospheric channels exploiting microwave Sun-tracking radiometer", 13th European Conference on Antennas and Propagation (EuCAP), 31 March - 5 April 2019, Krakow, Poland. (on IEEE Xplore, Electronic ISBN: 978-88-907018-8-7).

[C.15] L. Milani, M. Biscarini, S. Di Fabio, K. De Sanctis, M. Montopoli, K.M. Magde, G.A. Brost, and F.S. Marzano, "Validating weather-forecast-driven propagation models at high frequency using multisource ground-based radiometric data", 13th European Conference on Antennas and Propagation (EuCAP), 31 March - 5 April 2019, Krakow, Poland. (on IEEE Xplore, INSPEC Accession Number: 18775556).

[C.16] M. Biscarini, A. Vittimberga, S. Di Fabio, K. De Sanctis, L. Milani, M. Montagna, and F.S. Marzano, "Modeling and Predicting Down-link Tropospheric Channel above Ku Band for Interplanetary Exploration", 41st PhotonIcs and Electromagnetics Research Symposium (PIERS), 17 - 20 June 2019, Rome, Italy (on IEEE Xplore).

[C.17] L. Milani, M. Biscarini, and F.S. Marzano, "Cloud attenuation stochastic characterization from ground-based microwave radiometric data at Ka-band", 41st PhotonIcs and Electromagnetics Research Symposium (PIERS), 17 - 20 June 2019, Rome, Italy. (on IEEE Xplore).

[C.18] L. Milani, E. Vassallo and M. Arza, “Evaluating the radio frequency interference potential of 5G mobile networks on space links at millimeter waves” Proc. 8th ESA International Workshop on Tracking, Telemetry and Command Systems for Space Applications (ESA-TTC 2019), ESA-ESOC, Darmstadt, Germany, 24-27 Sep 2019. (on IEEE Xplore).

[C.19] M. Biscarini, A. Vittimberga, S. Di Fabio, K. De Sanctis, L. Milani, M. Montagna, M. Lanucara, G. Ravera, T. Yamada and F. S. Marzano, “Weather-Forecast-Based Ka-Band Telemetry Optimization with Hayabusa-2 Cross-Support Data”, Proc. 8th ESA

International Workshop on Tracking, Telemetry and Command Systems for Space Applications (ESA-TTC 2019), ESA-ESOC, Darmstadt, Germany, 24-27 Sep 2019.

Year 2020

[C.20] G. Lorenzo, L. Milani, Y. Doat, P.M. Besso, M. Lanucara, S. Martí, F. Pelorossi, K. Krekula, A. Paajarvi and P. Bargellini, "Kiruna, ESA Polar Station Evolution Roadmap", The 16th International Conference on Space Operations (SpaceOps 2020), 18-22 May 2020, Cape Town, South Africa.

[C.21] M. Montagna, M. Lanucara, G. Ravera, L. Milani, J. Reynolds, M. Biscarini, F.S. Marzano, K. De Sanctis, S. Di Fabio, A. Fujii, Y. Takei, Y. Tsuda, "Ka-band operations at ESA with Hayabusa-2", The 16th International Conference on Space Operations (SpaceOps 2020), 18-22 May 2020, Cape Town, South Africa.

[C.22] M. Biscarini, A. Vittimberga, K. De Sanctis, S. Di Fabio, L. Milani, M. Montagna and F. S. Marzano, "Satellite Link-Budget Statistical Prediction from Weather Forecast Models: Verification with Hayabusa-2 Ka-band Data", 14th European Conference on Antennas and Propagation (EuCAP), March 15-20, 2020, Copenhagen, Denmark.

[C.23] L. Milani, M. Biscarini, K.M. Magde, G.A. Brost, F.S. Marzano, "Estimating tropospheric extinction due to Clouds and Precipitation using Sun-tracking Microwave and Millimeter-wave Radiometers", 16th Specialist Meeting on Microwave Radiometry and Remote Sensing of the Environment (MICRORAD), 23-27 March 2020, Florence, Italy.